Universitat Autònoma de Barcelona
Institut National des Sciences Appliquées de Toulouse

Tesis

Presentado para obtener el titulo

Doctor de Física

por

Ulrike Anne Lüders

Development and integration of oxide spinel thin films into heterostructures for spintronics

Directores:
Josep Fontcuberta Griñó
Jean-François Bobo

20 de mayo 2005

Universitat Autònoma de Barcelona
ICMAB Departament de Física
INSA TOULOUSE
CNRS CENTRE NATIONAL DE LA RECHERCHE SCIENTIFIQUE
ONERA
Laboratoire de Nano Magnétisme pour l'Hyperfréquence

Jury:

Jean-Claude Ousset	president	
Josep Nogues Sanmiquel	secretary	(Rapporteur)
Rudolf Gross	vocal	(Rapporteur)
Jacobo Santamaria	vocal	
Marie-José Casanove	vocal	
Agnés Barthélémy	vocal	
Manuel Bibes	vocal	

This thesis was supported by a
Marie Curie Fellowship of the European Community program Human potential
I3P fellowship of the Consejo Superior de Investigaciones Cientificas of Spain
the THIOX program of the European Science Foundation
and
the Centre National de la recherche Scientifique of France.

Development and integration of oxide spinel thin films into heterostructures for spintronics

Ulrike Anne Lüders

20 May 2005

Resumen

En esta memoria se describe el crecimiento, mediante pulverización catódica rf, de capas delgadas de $NiFe_2O_4$ y $CoCr_2O_4$ sobre distintos substratos y la subsiguiente caracterización magnética y eléctrica. El objetivo es integrar dichas capas en dispositivos magnetoelectrónicos tales como uniones túnel o filtros de spin.

Hemos descubierto que el crecimiento epitaxial permite estabilizar fases nuevas del óxido $NiFe_2O_4$, fases que no existen en la forma másiva, y que tienen propiedades remarcablemente distintas. Como por ejemplo: un aumento dramático de la magnetización o la posibilidad de modificar drásticamente sus propiedades de transporte, pudiéndose obtener capas aislantes -como es en forma cerámica- o conductivas. Se ha realizado un estudio sistemático de los efectos del espesor de la capa y de las condiciones de crecimiento sobre las propiedades de magnetotransporte y los mecanismos de crecimiento.

Argumentamos que el aumento de la magnetización es debido a la estabilización de una fase $NiFe_2O_4$ espinela que es parcialmente inversa, en la que los iones Ni^{2+} están distribuidos entre las dos posiciones disponibles (tetraédrica y octaédrica) de la estructura. La introducción adicional de vacantes de oxígeno es probablemente la causa de la existencia de una configuración electrónica mixta $Fe^{2+/3+}$ en la subred octaédrica.

Hemos aprovechado la capacidad de obtener epitaxias de $NiFe_2O_4$ ferrimagnéticas conductivas o aislantes para integrarlas en dos distintos dispositivos magnetoelectrónicos: una unión túnel magnética y un filtro de spin.

Las capas conductivas de $NiFe_2O_4$ se han empleado como electrodos ferrimagnéticos-metálicos en uniones túnel. Se ha podido medir una magnetoresistencia túnel importante hasta temperaturas tan altas como 280K. Los valores de magnetoresistencia corresponden a una polarización de spin del $NiFe_2O_4$ de aproximadamente un 40%, que es prácticamente independiente de la temperatura. Estos resultados sugieren que la nueva fase conductiva que hemos estabilizado es un candidato interesante como fuente de corriente polarizado en spin.

Por otra parte, el $NiFe_2O_4$ aislante se ha implementado, por primera vez, como barrera túnel en una heteroestructura de filtro de spin. Hemos observado una magnetoresistencia túnel que alcanza valores de hasta un 50%. A partir de estas medidas, hemos deducido detalles relevantes de la estructura electrónica de la fase parcialmente inversa de $NiFe_2O_4$.

Hemos crecido el óxido $CoCr_2O_4$ sobre distintos substratos, tales como MgO(001) y $MgAl_2O_4$(001). Hemos podido comprobar que este óxido presenta una pronunciada tendencia a un crecimiento 3D. Por esta razón, las superficies de la capa no son nunca suficientemente planas y no se pueden usar en heteroestructuras túnel. Sin embargo hemos podido aprovechar esta característica para controlar el crecimiento de estas estructuras 3D y hemos conseguido la formación de objetos submicrónicos, autoorganizados con for-

mas piramidales muy bien definidas. El estudio detallado del efecto de los parámetros de crecimiento nos ha permitido por una parte, dilucidar cuales son los mecanismos que llevan a una autoorganización tan perfecta y por otra determinar que, en las condiciones adecuadas, se pueden obtener templates totalmente faceteados con múltiples posibilidades para futuras aplicaciones.

Contents

Resumen **3**

1 Motivation **9**

2 Introduction **11**
2.1 Introduction to tunneling transport 11
2.1.1 Theory of the magnetic tunnel junction 12
2.1.2 Spin filter 17
2.2 Introduction to transition metal oxides 21
2.2.1 Crystal field theory 21
2.2.2 Magnetic coupling and transport properties 22
2.3 Spinel oxides 25
2.3.1 Structure 25
2.3.2 Magnetic properties 26
2.3.3 Transport properties 29
2.4 Thin film growth 30
2.4.1 Macroscopic model 30
2.4.2 Microscopic model 31
2.4.3 Accommodation of lattice misfit 33
2.4.4 Growth of complex oxides 34

3 State of the art: Recent research on spinel oxides **35**
3.1 Research on bulk properties 35
3.1.1 Nanoparticles 37
3.2 Research on thin films 38
3.2.1 Structural properties 38
3.2.2 Magnetic properties 40
3.2.3 Transport properties and magnetoresistance 41

4 Experimental procedures **43**
4.1 Sample preparation 43
4.1.1 Deposition of $CoCr_2O_4$ 44
4.1.2 Deposition of $NiFe_2O_4$ 46
4.2 Structural characterization 48
4.2.1 X-Ray diffraction 48

4.2.2 Reflection high energy electron diffraction (RHEED) 52
4.2.3 Transmission electron microscopy 53
4.3 Magnetic characterization 54
4.3.1 SQUID 54
4.4 Surface characterization 54
4.4.1 Scanning electron microscopy 54
4.4.2 Atomic Force Microscopy 55
4.4.3 Resiscope 55
4.5 Magnetoresistive characterization 55
4.5.1 Optical lithography 56
4.5.2 Nanoindentation 58
4.5.3 Transport measurements 59

5 Characterization of $NiFe_2O_4$ films **61**
5.1 $NiFe_2O_4$ grown in an Ar/O_2 atmosphere 62
5.1.1 Structural properties 63
5.1.2 Surface morphology 68
5.1.3 Magnetic properties 69
5.1.4 Electric properties 72
5.2 $NiFe_2O_4$ grown in pure Ar 74
5.2.1 Structural properties 74
5.2.2 Morphology 79
5.2.3 Composition 81
5.2.4 Magnetic properties 82
5.2.5 Electric properties 85
5.3 Postannealing experiments on $NiFe_2O_4$ films grown in pure Ar 89
5.3.1 Structural properties 89
5.3.2 Morphology 90
5.3.3 Magnetic properties 93
5.4 $NiFe_2O_4$ grown on Pt(001) in pure Ar 96
5.4.1 Structural properties 96
5.4.2 Magnetic properties 99
5.4.3 Electric properties 99
5.4.4 Discussion 100

6 Spin-dependent transport of conductive and insulating $NiFe_2O_4$ **101**
6.1 Conductive $NiFe_2O_4$: Magnetic tunnel junction 103
6.1.1 Dependence on bias voltage 105
6.1.2 Temperature dependence 109
6.2 Insulating $NiFe_2O_4$: Spin filter 110
6.2.1 Dependence on bias voltage 113
6.2.2 Temperature dependence 115

7 Self-organized islands in spinel oxides **119**
7.1 Epitaxial islands of $CoCr_2O_4$ . . . 120
7.1.1 Structural properties . . . 121
7.1.2 Magnetic properties . . . 124
7.1.3 Surface morphology . . . 125
7.1.4 Discussion . . . 136
7.1.5 Other phenomena and open questions . . . 141
7.2 Islands in $NiFe_2O_4$ . . . 144
7.3 Comparison to Si/Ge . . . 146
7.4 Discussion . . . 149

8 Main results and remaining questions **151**
8.1 Properties of $NiFe_2O_4$ thin films . . . 151
8.1.1 Magnetic structure of ultrathin $NiFe_2O_4$ films . . . 151
8.1.2 Conducting phase of $NiFe_2O_4$ . . . 152
8.2 Spin-dependent transport measurements of $NiFe_2O_4$ thin films . . . 153
8.2.1 Magnetic tunnel junction containing conductive $NiFe_2O_4$ . . . 153
8.2.2 Spinfilters with a spinel barrier . . . 154
8.3 Self-organized growth of spinel islands . . . 155

Résumé **175**

List of Publications **177**

Gracias! Merci! Thanks! **181**

A1 Appendix 1: Properties of the $(La, Sr)MnO_3$ base layer **185**
A1-1 Introduction to $La_{2/3}Sr_{1/3}MnO_3$ . . . 185
A1-2 Properties of the LSMO(/STO) base . . . 187

A2 Appendix 2: Results on $CoCr_2O_4$ based spin filter heterostructures **193**
A2-1 Characterization of $(La, Ca)MnO_3$ single films . . . 193
A2-2 Characterization of $(La, Ca)MnO_3/CoCr_2O_4$ bilayer . . . 197

1 Motivation

Spintronics has received a strong interest in the last years by the scientific community due to the possibility to develop new electronics, which are faster and show interesting features in comparison with the classical electronics, for example a non-volatility of stored information [1–3]. The base of this new electronics is the use of highly spin-polarized currents. The current of spin-up and spin-down electrons behave independently from each other with separate conduction channels, having an asymmetric behavior due to a different carrier density and/or mobility. One of the spintronic devices has already made the way to applications, namely the Giant Magnetoresistance read head, which detects the magnetically stored data by a change of resistance in the read head originated by the magnetic field of the bit. Another application is the storage of data itself with the Magnetic Random Access Memory based on magnetic tunnel junctions, which is a non-magnetic thin insulating layer sandwiched by two magnetic electrodes. The resistance of the device can be manipulated by a magnetic field and is kept also when the electricity is switched off.

The experimental part of the development of spintronics is first of all a challenge for materials scientist, as a source of highly spin-polarized current can be found in magnetic conductors. The exchange splitting of the bands leads to different carrier densities of the two spin channels, so that the ideal materials used as a source of spin-polarized current are the half-metals, which show a metallic behavior for one spin direction, while it is semiconducting for the other one [4]. One of the examples are the manganites [4, 5], showing a nearly total spin-polarization of the conduction electrons [6, 7].

Another approach to the generation of highly spin-polarized current is the filtering of one of the two spin channels. If a device can be fabricated, which has a much higher resistance for one spin channel than for the other, a source of non-polarized current together with the filtering device can act as an artificial half-metal, generating a fully spin-polarized current. Such a filtering device can be for instance the tunnel spin filter, which is a magnetic thin insulating film, acting as a tunnel barrier between two non-magnetic electrodes. The exchange split bands of the barrier leads to a spin-dependent gap and so a spin-dependent barrier height of the tunnel barrier. The tunnel current in turn is exponentially dependent on the barrier height, so that the exchange splitting of the magnetic barrier leads to a high resistance of one of the spin channels which will be filtered.

The advantage of this source of highly spin-polarized current is that a non-magnetic electrode can be used and thus a spin-polarization can be injected easily into semiconductors, linking the well-known logical devices of the classical electronics to the advantages of spintronics. The drawback is the small choice of magnetic, insulating materials. These can be found only in materials which have a magnetic coupling which is not transmit-

ted by the itinerant electrons as for example in Ni, Fe or Co, but an indirect magnetic coupling of ionic bindings. A group of such materials are the complex oxides like the manganites [8] or the spinels [9].

However, the preparation of thin films of complex oxides for the application in spintronics with bulk properties is difficult, as in these materials the transport and magnetic properties are closely related to the structural properties of the film. Structural defects introduced in the growth process will change significantly the functionality of the films.

The objective of this thesis is the fabrication of tunnel junctions and spin filters with spinel oxides. The materials investigated are $NiFe_2O_4$ and $CoCr_2O_4$. The first aim is to control the growth of these materials, which are prepared by sputtering on different oxide substrates. Once reproducible flat and magnetic single films are grown, the spinel thin film is introduced into a heterostructure based on the perovskite $(La, Sr)MnO_3$ to build spin filters or magnetic tunnel junctions. Due to the high Curie temperature of the $NiFe_2O_4$ of around $850K$ [10] it should be possible to develop a spin filter working at room temperature and to overcome some of the actual problems of spintronics.

In chapter 2 the fundamental theoretical aspects of this thesis are introduced. A part on spin-dependent transport will treat the basics of magnetic tunnel junctions and spin filters. Another part will deal with the description of the magnetism and transport of magnetic oxides, especially the spinels. In the end a short introduction to the growth of thin films is given. Chapter 3 is a short review on the state of the art of the research on spinel materials, including bulk and film research of the last years.

Chapter 4 consists of the description of the deposition process and the experimental techniques used in this thesis. The emphasis is put on the experimental procedure and the treatment of data.

The results of the experimental work carried out during this thesis are described and discussed in chapters 5, 6 and 7. Chapter 5 treats the growth and properties of single $NiFe_2O_4$ films and integrated into heterostructures, which were afterwards used to measure their spin-dependent transport properties as described in chapter 6. The growth of $CoCr_2O_4$ and the appearing self-organization of three dimensional islands is discussed in chapter 7.

In chapter 8 the results are summarized and remaining questions are discussed.

The appendices 1 and 2 report some supplementary experimental results. In Appendix 1 a short introduction to the properties of manganite perovskites is given and the characterization of the $(La, Sr)MnO_3$ base layers used for the heterostructures in chapter 6 is found. Appendix 2 summarizes the results obtained for $(La, Ca)MnO_3$ / $CoCr_2O4$ bilayers.

2 Introduction

In this chapter the basic ideas and theories important for this thesis are introduced. To motivate the choice of materials which was made, first the spintronic devices to be developed (magnetic tunnel junctions and spin filters) will be described and an outline of the theories dealing with spin transport will be given. Then some aspects of the physics of transition metal oxides will be introduced, ending in the discussion of the spinel oxide group, the main material treated in this thesis.

In the last ten years the research concentrated very strongly on the properties of ferromagnetic and metallic manganese perovskites and much experimental and theoretical work was done on these materials. I will discuss the manganites only shortly in section A1-1, but the experimental data is vast in this field. An extensive review on the spin transport was published by M. Ziese [11] and an introduction to the transport properties can be found in 'Spin Electronics' [12].

2.1 Introduction to tunneling transport

In spin electronics a spin-polarized current must be generated, manipulated and detected again. For the generation, normally, highly spin-polarized materials are used as a source. For the manipulation and detection the magnetic tunnel junction is used. It consists of a non-magnetic barrier sandwiched between two magnetic electrodes. The device relies on the quantum mechanic tunnel effect, where electrons tunnel through the barrier from one electrode to the other at the application of a bias voltage.

The manipulation of the spin is in this case related to the difference in magnetization direction of the electrodes, so that one spin direction will tunnel preferably. The detection of the state of the magnetic tunnel junction is carried out by the measurement of the resistance of the trilayer. In Figure 2.1 the schematic magnetization of the trilayer for a cycle of the magnetic field is shown, together with the resistance of the junction. One can distinguish two different resistance levels, connected to the parallel (low resistance) and antiparallel (high resistance) alignment of the magnetization of the electrodes. Turning back to spin electronics, these two different resistance states will be denoted as state '0' and '1'.

Due to the immense development of thin film growth and vacuum techniques in the last twenty years the study of thin films and multilayers is now better controllable. Also characterization techniques like X-ray diffraction, electron microscopy and the magnetic characterization get more and more sensitive so that very few amount of material is detectable. However, the film thickness involved (few nanometers for the barrier and tens of nanometers for the electrodes) is still at the limit of sensitivity. The first publications

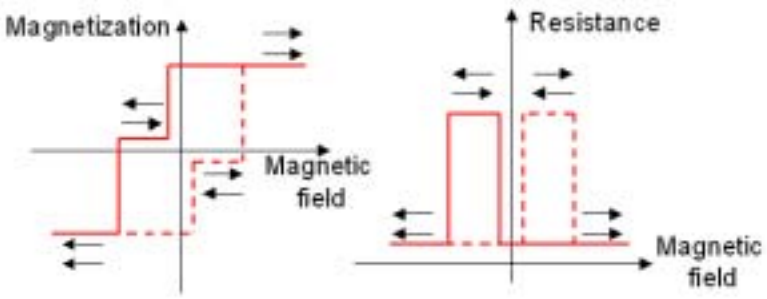

Figure 2.1: Schematic hysteresis loop (left side) and resistance loop (right side) of an ideal magnetic tunnel junction.

of magnetic tunnel junction date back to the end of the sixties and the seventies [13], showing a very small effect. The first breakthrough was made by Moodera et al. in 1995 with a 10% of magnetoresistance at room temperature [14], involving a magnetic tunnel junction made of 3d transition metals and an oxide barrier. Following this approach intense studies on magnetic tunnel junctions were done, for a review see [11, 12, 15].

2.1.1 Theory of the magnetic tunnel junction

The non-magnetic tunnel effect is a classical problem of quantum mechanics, to be found in every textbook. The starting point is the time-independent free-electron Hamiltonian:

$$H_x = -\frac{\hbar^2}{2m}\left(\frac{d^2}{dx^2}\right) + U(x) \tag{2.1}$$

where the first term describes the kinetic energy of an electron with the energy E_x, the second one the potential energy. $U(x)$ is the potential wall of the barrier with the height U_0 for $0 \leq x \leq d$ (with d being the barrier thickness) and m the free electron mass (see Figure 2.2). The problem is treated in one dimension and the basic assumption is that the electrons are incoming with a moment purely perpendicular to the interfaces. With an *ansatz* for the wave functions in the three different parts (electrode(1)/barrier(2)/electrode(3)) as follows

$$\psi_1(x) = Ae^{ikx} + Be^{-ikx} \quad x < 0 \tag{2.2}$$
$$\psi_2(x) = Ce^{-i\kappa x} + De^{i\kappa x} \quad 0 \leq x \leq d \tag{2.3}$$
$$\psi_3(x) = Fe^{ikx} \quad x > d \tag{2.4}$$

with the wave vectors $k = \sqrt{2mE_x}/\hbar$ and $\kappa = \sqrt{2m(U_0 - E_x)}/\hbar$. The transmission coefficient T, defined as the ratio of the transmitted flux to the incident flux, can be written as

$$T(E) = \left|\frac{F}{A}\right|^2 \tag{2.5}$$

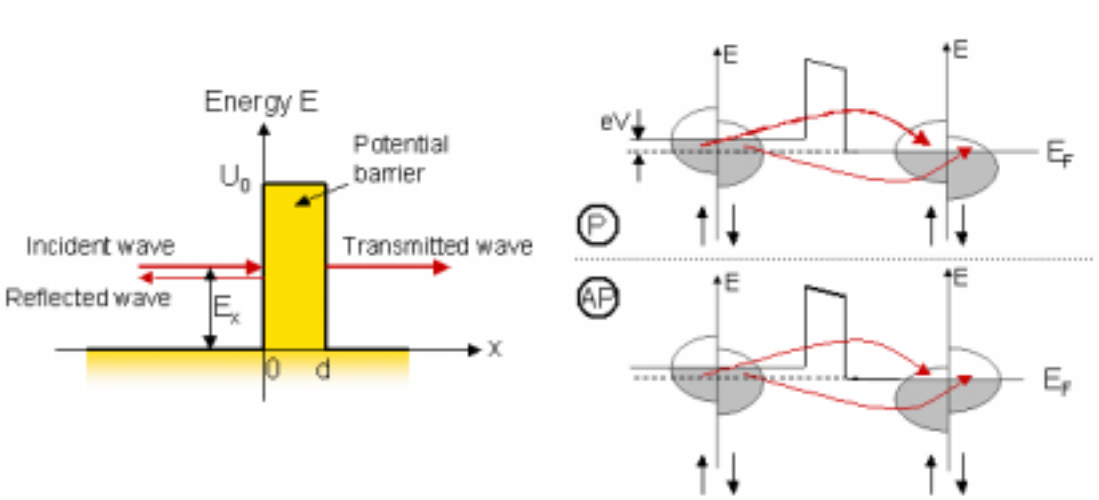

Figure 2.2: Schematic representation of the tunnel effect (left side) and the magnetic tunnel effect (right side, parallel configuration on top, antiparallel in the bottom).

Matching the boundary conditions for the wave functions and their derivatives at the interfaces $x = 0$ and $x = d$, and with the assumption of a sufficiently thick barrier, the transmission coefficient can be expressed as

$$T(E) \propto \exp(-\frac{2d}{\hbar}\sqrt{2m(U_0 - E_x)}) \tag{2.6}$$

This result, which describes the fraction of the incident electrons tunneling through the barrier and so essentially the tunnel current, reveals an interesting dependence of the tunnel current on the barrier height and width. Both of them are of an exponential nature, and are the most important factors governing the electron transmission.

But the more interesting case is the tunnel effect involving two magnetic electrodes. Slonczewski was the first theoretician proposing a model of the spin-dependent tunnel resistance effect [16], basing on the above approach of the tunnel effect. The difference to equation (2.1) is an additional energy term, which describes the internal exchange energy of the ferromagnetic electrodes. So the modified Hamiltonian is

$$H_x = -\frac{\hbar^2}{2m}(\frac{d}{dx})^2 + U(x) - \mathbf{h}(x)\sigma \tag{2.7}$$

Here, -**h** is the molecular field and σ is the conventional Pauli spin operator with the equivalent notation $\sigma = \pm 1 = \uparrow, \downarrow$. **h** is restricted only to the two magnetic electrodes and vanishes for $0 \leq x \leq d$, i.e. in the non-magnetic barrier. However, the magnitude of **h** as well as the direction can differ between the two electrodes, the angle between the direction of the two magnetizations is named θ. As the energy term of the electron in the electrodes are changed and will depend on the spin direction, the *ansatz* of the wave

functions will be more complex. Equation (2.3) splits up into two equations, assuming that the incident electrons all are spin-up:

$$\psi_1^{\uparrow}(x) = A^{\uparrow}e^{ik^{\uparrow}x} + B^{\uparrow}e^{-ik^{\uparrow}x}, \psi_1^{\downarrow}(x) = B^{\downarrow}e^{-ik^{\downarrow}x} \tag{2.8}$$

Also k is now spin-dependent and is changed to $k^{\sigma} = \sqrt{2m(E_x + \sigma\mathbf{h})}/\hbar$. The same change holds for the area of the second electrode, there one finds

$$\psi_3^{\sigma}(x) = F^{\sigma}e^{ik^{\sigma}x}, \sigma = \uparrow, \downarrow \tag{2.9}$$

The wave functions ψ_2^{σ} are similar to equation (2.4), as the barrier is non-magnetic.

Nine parameters must now be determined by the continuity of the wave functions and their derivatives at $x = 0$ and $x = d$. The angle θ between the magnetization of the two electrodes requires a spinor transformation at $x = d$, which results in two more equations. Of the resulting coefficients, only F is interesting in this case, as it is related to the tunneling electrons. This is now spin- and angle-dependent:

$$F^{\uparrow} = f(k^{\uparrow}, \kappa, d) \cdot \cos(\theta/2), F^{\downarrow} = f(k^{\uparrow}, k^{\downarrow}, \kappa, d) \cdot \sin(\theta/2) \tag{2.10}$$

where f is a function of k^{σ}, κ and d. Here, one of the basic observation of the magnetic tunnel junction is represented, the tunnel current is strongly dependent on θ. In the case of a parallel alignment of the magnetizations of the two electrodes ($\theta = 0$), $F^{\downarrow}$ is vanishing, while in the case of antiparallel alignment ($\theta = \pi$), $F^{\uparrow}$ is vanishing. Calculating the transmission coefficient T^{σ} spin-independently, one can get directly the total conductance of the tunnel barrier with the expression

$$\frac{I_e}{V} = G = \frac{e^2}{8\pi^2\hbar}\frac{\kappa T}{d} \tag{2.11}$$

under the assumption that the applied voltage V is small and the current is carried predominantly by electrons with an energy around the Fermi energy. e is the electron's charge and I_e the total charge current. The conductance for the case that the second electrode is a half-metal is again a function of $\cos\theta/2$, so no current flows in the antiparallel state. However, for a normal ferromagnet, the conductance shows two contributions

$$G = G_0(1 + P_{fb}^2 \cos\theta) \tag{2.12}$$

where G_0 denotes a mean conductance and P_{fb} the spin-polarization of the electrode-barrier interface:

$$P_{fb} = \frac{k^{\uparrow} - k^{\downarrow}}{k^{\uparrow} + k^{\downarrow}}\frac{\kappa^2 - k^{\uparrow}k^{\downarrow}}{\kappa^2 + k^{\uparrow}k^{\downarrow}} \tag{2.13}$$

The first term is the typical expression of the spin-polarization of the electrode, while the second term describes the polarization connected to the electrode-barrier interface, thus in the experiments the spin-polarization of this interface influences the results strongly. Another result, which can be drawn from this equation, is that the penetration of the wave function into the barrier depends on k^{σ}. Thus the tunnel current does not depend

on the electrodes alone, but is very sensitive on the barrier height ($\propto \kappa^2$). A sufficiently small barrier height can result in a negative sign of the conductance.

However, this model by Slonczewski has important drawbacks. It does not take into account the effective electron mass and depends on a band model involving parabolic bands. The barrier is thought to be square and symmetric. But most important: the model is depending on the free single electron approach of the problem, although magnetism is a many-body effect.

A many-particle approach was done by Meservey and Tedrow [17] and applied by Jullière to experiments [13]. Here, the current through the tunnel junction is described by Fermi's golden law:

$$I \propto \frac{2\pi}{\hbar} |M|^2 N(E) \tag{2.14}$$

where I is the tunnel current (or the number of tunneling electrons),$N(E)$ the density of the final states and $|M|^2$ the transmission matrix element, comparable to the transmission coefficient in Slonczewski's theory. The current for an applied bias voltage V for a tunnel junction can be expressed as (with $e1$ denoting the first electrode and $e2$ the second one)

$$I^{e1\to e2} \propto N_{e1}(E-eV) f(E-eV) |M|^2 N_{e2}(E) [1-f(E)] \tag{2.15}$$

$$I^{e2\to e1} \propto N_{e1}(E-eV) [1-f(E-eV)] |M|^2 N_{e2}(E) f(E) \tag{2.16}$$

and so the resulting tunnel current $I = I^{e1\to e2} - I^{e2\to e1}$ is

$$I(E) \propto |M|^2 N_{e1}(E-eV) N_{e2}(E) [f(E-eV) - f(E)] \tag{2.17}$$

To calculate the tunnel current independent of the energy, the above expression must be integrated over all the energies. Bardeen [18] showed that the transmission matrix $|M|^2$ is independent on the energy, so it can be ignored in the integration. With the assumption, that the tunnel current is governed by electrons around the Fermi energy E_F, the Fermi function can be approximated by the delta function $eV\delta(E-E_F)$ and integration results in

$$\frac{I}{V} \propto |M|^2 N_{e1}(E_F) N_{e2}(E_F) \tag{2.18}$$

In the 2-current-model, i.e. that the current of the spin-up electrons and that of the spin-down electrons can be described independently from each other, the current for each spin channel can be expressed as follows

$$\frac{I^{\pm\sigma}}{V} \propto |M|^2 N_{e1}^{\pm\sigma}(E_F) N_{e2}^{\pm\sigma}(E_F) \tag{2.19}$$

for the parallel alignment of the two magnetic electrodes, and

$$\frac{I^{\pm\sigma}}{V} \propto |M|^2 N_{e1}^{\pm\sigma}(E_F) N_{e2}^{\mp\sigma}(E_F) \tag{2.20}$$

for the antiparallel case. Now the total current of the parallel (antiparallel) case is the sum of the two different spin-currents, and again with the assumption, that essentially

electrons at E_F are the tunneling electrons, the density of states N_i^σ at E_F can be substituted by the number of electrons in the i-th electrode n_i^σ and so the total current for the parallel ($\uparrow\uparrow$) and the antiparallel ($\uparrow\downarrow$) case, respectively, is:

$$I^{\uparrow\uparrow} \propto n_{e1}^{\uparrow} n_{e2}^{\uparrow} + n_{e1}^{\downarrow} n_{e2}^{\downarrow} \tag{2.21}$$

$$I^{\downarrow\uparrow} \propto n_{e1}^{\uparrow} n_{e2}^{\downarrow} + n_{e1}^{\downarrow} n_{e2}^{\uparrow} \tag{2.22}$$

Introducing the definition of the spin-polarization of a material

$$P \equiv \frac{n^{\uparrow} - n^{\downarrow}}{n^{\uparrow} + n^{\downarrow}} \tag{2.23}$$

one finds an easy formula to estimate the expected effect (or the polarization of the electrodes) as follows

$$\frac{\Delta G}{G} = \frac{I^{\uparrow\uparrow} - I^{\uparrow\downarrow}}{I^{\uparrow\uparrow}} = \frac{2P_{e1}P_{e2}}{1 - P_{e1}P_{e2}} \tag{2.24}$$

Although the Jullière formalism just takes into account the spin-dependent density of states, and not the effect of the barrier or the interface contributions like the description of Slonczewski, this formula is very successful in predicting the amplitude of the tunnel magnetoresistance, especially for tunnel junctions made of transition metals.

Simmons [19, 20] developed the V dependence of the tunnel current density J on the basis of the Wentzel-Kramers-Brillouin (WKB) approximation. The derived formulas are for the non-magnetic tunnel effect, but are used widely to describe the tunneling also in magnetic tunnel junctions. Simmons discusses the tunneling between dissimilar electrodes with two different work functions. The resulting trapezoidal barrier shape is approximated by the mean barrier height. For bias voltages, where the only transport is tunneling (i.e. $V \leq U_0/e$) he finds the following relationship:

$$J = \theta_S(V + \gamma_S V^3) \tag{2.25}$$

with θ_S and γ_S a function of the barrier height and width. This equation provides a way to extract the mean barrier height and width from the experimental data.

To access also the barrier asymmetry, Brinkmann developed a model of the V dependence of the conductance $G = dI/dV$, also basing on the WKB approximation, resulting in a parabolic behavior:

$$\frac{G(V)}{G(0)} = 1 - \alpha eV + \beta(eV)^2 \tag{2.26}$$

with α and β again constants depending on the barrier height and width, but also on the barrier asymmetry.

However, voltage or temperature dependences derived from this description are not too reliable [11], as the tunneling is described for non-magnetic electrodes and ideal tunnel junctions. Typical effects changing the V dependence of the experimental magnetic tunnel junctions are firstly impurity states in the barrier, so that sequential tunneling is possible, reducing the effective barrier thickness. Even more, inelastic effects can take place. This case described by Xu et al [21] leads to a dependence like $V^{4/3}$.

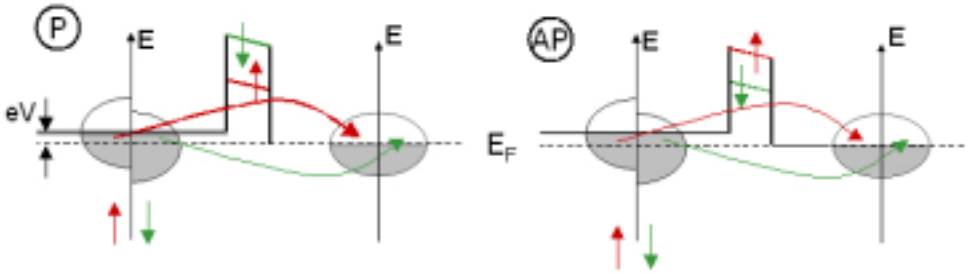

Figure 2.3: Schematic representation of the spin filter effect from a magnetic to a non-magnetic electrode. The parallel alignment between the magnetic electrode and the barrier is shown on the left side (P) and the antiparallel on the right side (AP).

Also the magnetic character of the electrodes can change the ideal V dependence. In the magnetic tunnel junction the emission and absorption of magnons in the electrodes are possible. While in transition metals this effect is reduced to the interface regions, the magnons can move through the electrode in case of an indirect magnetic coupling [22], changing the Vdependence strongly.

2.1.2 Spin filter

A source of spin-polarized current based on the tunnel effect was found in the seventies by different groups, measuring the field emission of tungsten tips coated with EuS [23–25]. A new design was proposed by Moodera et al [26], introducing a magnetic barrier between two non-magnetic electrodes. The transport mechanism, leading to a spin-polarized tunnel current without a magnetic electrode, is due to the preferred tunneling of one spin direction. As the tunnel barrier is magnetic, the electronic states are exchange split, so that the barrier height is different for a spin-up and a spin-down electron (see Figure 2.3). The tunnel current on the other hand is depending exponentially on the barrier height (Equation (2.6)), so that the electrons with the majority spin will tunnel more easily than the minority spins. This means, that the spin dependence of the transport is not due to non-available states in the second electrode (like in the case of magnetic tunnel junctions), but due to different tunnel probability of the two spin directions.

The theoretical description of the spin filter effect for a tunnel junction with a magnetic barrier and one magnetic electrode was done by Saffarzadeh [27]. His model is based on the model introduced by Slonczewski (see Section 2.1.1), making the same basic assumptions of an electron wave vector perpendicular to the interfaces and the conservation of the spin direction in the tunneling process. Besides taking into account a non-symmetrical barrier shape and an effective mass for the electrons m^*, the changes concentrate on an additional term of the Hamiltonian describing the spin-dependent potential of the interaction of the tunneling electrons with the localized moments of the

barrier material (V^σ):

$$H = -\frac{\hbar^2}{2m_j^*}\frac{d}{dx^2} + U(x) + V^\sigma - \mathbf{h}(x)\sigma \tag{2.27}$$

with the same nomenclature like in Section 2.1.1 and $V^\sigma = -I\sigma < S_z >$, being I the exchange constant and $< S_z >$ the thermal average of the spins. This additional potential takes place only inside the barrier, so it modifies the *ansatz* of the wave functions only in the barrier. Introducing Airy functions for the electron's energy leads to a quite complex transmission coefficient, which cannot be solved analytically. In the article the model was applied to the special case of a Fe/EuS spin filter and the formulas were solved numerically. The dependence of the TMR on the barrier thickness and the bias voltage is calculated, leading to a very distinct dependence of the TMR on the bias voltage, which shows a peak at a finite voltage and afterwards a monotonous decrease. This is in contrast to the voltage dependence of the tunnel junction as discussed in the previous section.

For an estimation of the expected effect in the spin-dependent transport measurements, a modified Jullière's model can be used [26]. Regarding the dependence of the barrier height on the spin direction of the tunneling electrode, the tunnel probability of the tunnel effect (Equation (2.6)) must be expressed in terms of a spin-dependent tunnel current $J_\uparrow$ and $J_\downarrow$ for the two spin directions with the different barrier heights $U_\uparrow$ and $U_\downarrow$:

$$J_{\uparrow(\downarrow)} = \frac{e}{2\pi h d^2} U_{\uparrow(\downarrow)} \cdot \exp(-\frac{2d}{\hbar}\sqrt{2m(U_{\uparrow(\downarrow)} - E_x)}) \tag{2.28}$$

with

$$U_{\uparrow(\downarrow)} = \phi \mp \Delta E_{ex} \tag{2.29}$$

where ϕ is the mean gap of the insulator and ΔE_{ex} the exchange splitting of the states. This difference in tunnel probability leads to a tunnel efficiency

$$P_{barrier} = \frac{J_\uparrow - J_\downarrow}{J_\uparrow + J_\downarrow} \tag{2.30}$$

equivalent to the expression of the spin-polarization given in Equation (2.23). Interpreting this tunnel efficiency now as a 'polarization' of the barrier, the modified Jullière's formula will be

$$\Delta R/R = \frac{2P_{e1}P_{barrier}}{(1 - P_{e1}P_{barrier})} \tag{2.31}$$

giving a rough guide of the effect's magnitude expected.

As can be deduced by this short description of the spin filter effect, the important property of the barrier to show a high filter efficiency is the difference in the barrier height, i.e. the exchange splitting ΔE_x, and the average barrier height ϕ, and not the difference of the density of states at a given energy. This is the important difference to a magnetic tunnel junction, where the amplitude of the effect is governed strongly by the spin-polarization of the electrodes. A non-magnetic electrode in connection with the magnetic barrier serves as a artificial half-metal in the ideal case.

Besides the work on the EuS-coated tungsten tips, the spin filter effect of a tunnel current through a magnetic barrier was investigated experimentally by Moodera et al. [26, 28, 29]. A tunnel junction of the structure Au/EuX/Al (with X = O, S, Se) was fabricated and spin-dependent transport measurements were carried out using the superconducting Al as a spin detector. The highest spin-polarization of the current was found to be up to 80% for a EuS barrier [26]. To investigate the role of the magnetic state of the barrier, antiferromagnetical EuSe was used, leading to a spin filter effect only when a slight canting of the antiferromagnet was introduced by an external magnetic field [28]. Recent work on a EuO barrier shows a maximum filter efficiency of 29% for a Al/EuO/Y heterostructure [29].

The first spin filter using a ferromagnetic electrode as a spin detector was developed in 2002 by LeClair et al. [30]. Also they used EuS as a magnetic barrier, but the second electrode was Gd instead of Au. They observed a tunnel magnetoresistance of 120% at 4K and calculated from this a tunnel efficiency of nearly 90%. Parallel to this experimental paper, several theoretical papers were published, confirming the idea of the transport mechanism proposed by the experimentalists [27, 31, 32] and proposing even more efficient devices including a spin filter [33, 34].

Apart from the work on spin filters including Eu chalcogenides as a barrier, no further experimental work was reported. There is one major reason: the choice of magnetic insulators is rather limited, only two groups of magnetic insulators (or semiconductors) exist. First of all the semiconductors with Eu, showing a spontaneous magnetization at low temperatures, the Curie temperature is lower than some ten K. The other group of magnetic insulators is to be found in the transition metal oxides, especially in the group of spinel oxides and also in the group of manganites.

No work was reported on the spinel insulators, although the dielectric properties of the spinel ferrites are well-known and widely used for wave guides etc., and the only magnetic insulator in the group of the manganites $(La, Bi)MnO_3$ raised recently more interest for its multiferroic properties. The spinel ferrites with the formula AFe_2O_4 show very interesting properties, which is a high Curie temperature above room temperature, an insulating behavior due to their ionic bonding character and a large exchange splitting. But on the other hand, these materials have also an important experimental drawback: high quality films with bulk properties of these transition metal oxides are rather difficult to make, as the structural and physical properties show a close relationship (see Section 2.2). As their magnetic interaction is an indirect interaction, the magnetic properties are expected to be influenced strongly by the reduced dimension of the thin film. In the non-insulating spinel ferrite Fe_3O_4, for instance, ultrathin films tend to be superparamagnetic instead of ferromagnetic [35]. Taking all this together, the complex oxides are not a very convenient material to be employed as a magnetic barrier, but due to the limited choice, the spinels are the only materials so far to develop a spin filter working at room temperature.

Another reason of the low amount of the reported work is a basic experimental problem of the spin filters: the crystal and interfacial quality of the heterostructure must be very good. And in the special case of a spin filter with a magnetic electrode as the spin polarizer (instead of a superconducting one), the magnetic barrier is in close contact to

the magnetic electrode, the first being much thinner than the latter. It is not obvious that in a configuration like that a decoupling and so an antiparallel state of the two magnetic films is possible.

2.2 Introduction to transition metal oxides

The family of transition metal oxides show a big variety of magnetic and transport properties, although the binding character is predominantly ionic and thus the electrons are localized. However, the absence of itinerant electrons does no inhibit long range interaction like ferromagnetism. Also some conductive oxides can be found.

In the following, a small introduction to the magnetic and electric properties of transition metal oxides will be given. More literature on the exchange interactions in this kind of material can be found in [12, 36]. This chapter will concentrate on the spinels, neglecting the rest of the big universe of transition metal oxides.

2.2.1 Crystal field theory

In the transition metal (TM) oxides the electrons are strongly localized and the electronic states can be considered as atomic like, in contrast to, for example, metals or semiconductors. When a free TM ion is located in a crystal lattice, the degenerate d-orbitals split into two different energy states due to the reduced symmetry of the crystal lattice. In the easiest case of a cubic, octahedral surrounding the coulomb repulsion by the surrounding atoms will give rise to a splitting into the so-called t_{2g} and e_g states, the first including three of the five possible $3d$ lobes d_{xy}, d_{xz} and d_{yz} and the latter the other two: $d_{x^2-y^2}$ and d_{z^2} (see Figure 2.4). The reason for this is obvious regarding the spatial orientation of these orbitals. While the e_g lobes (represented in red) are oriented along the crystal axes, showing a big overlap with the neighboring oxygen $2p$ orbitals (represented in white), the t_{2g} orbitals are oriented between the crystal axes, pointing away from the neighboring oxygen ions. Thus the coulomb repulsion between the electrons of the two ions is smaller for the lobes included in the t_{2g} orbitals and the formerly (i.e. in the free atom) degeneration of the $3d$ states is lifted. The difference in energy between the t_{2g} and the e_g orbitals is called the crystal field splitting. Changing the crystal symmetry from octahedral to tetrahedral, the neighboring atoms are distributed between the crystal axes with an angle of 120°. In this case the t_2 orbitals get energetically less favorable than the e orbitals and the latter lie lower in energy.

Now that the $3d$ orbitals are only partially degenerate, the electrons in an atom with more than three electrons occupying the d-orbitals have different ways to distribute over the orbitals. Following the first Hund's rule, the spin of the system should be maximum, which means that the electrons are distributed in that way, that first each of the five levels will be filled with a spin-up electron, and only afterwards the levels will be filled with an electron with the opposite spin. This, the so-called high spin state, is observed in nearly all the transition metal ions with some exceptions. The other way, where first the lower lying levels are filled with two electrons and afterwards the higher lying levels, can be energetically more favorable (although the first Hund's rule will be violated), if the crystal field splitting is very large. The low spin state was for example observed for Ni^{3+} [12].

Just taking into account the crystal field splitting, the magnetic moment and the transport properties of the materials treated in this thesis can be well understood. But

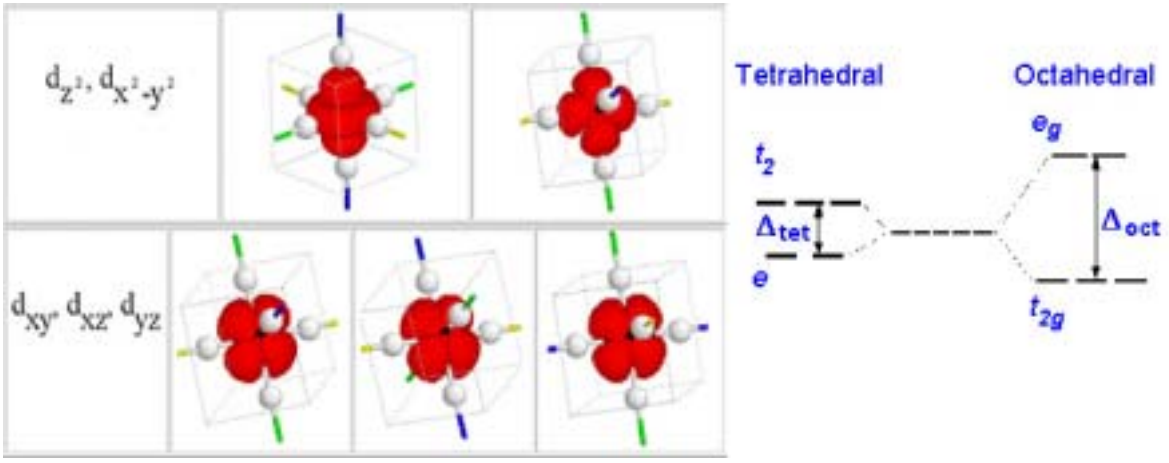

Figure 2.4: Left part: Schematic view of the different 3d orbitals of transition metals (red). The oxygen $2p$ lobes are depicted in white. Right part: Crystal field splitting for different geometries.

there are more effects involved in the description of TM oxides, as for example the hybridization between the TM $3d$ and the O $2p$ orbitals, leading to an additional energy splitting of the t_{2g} and e_g orbitals. As this splitting is in the same direction like the crystal field splitting, i.e. increasing the energy of the e_g orbitals in respect to the t_{2g} orbitals, it will not be discussed further.

The degeneration of the $3d$ levels can be pushed even further in splitting the t_{2g} and e_g itself as a result of the Jahn-Teller-effect. This effect is only strong for the d^4 and d^9 ions in the octahedral surrounding (d^3 and d^8 for the tetrahedral coordination), as the last electron has different energetically equivalent possibilities to fill the levels. By distorting the crystal lattice around the ion, the degeneracy of the t_{2g} or e_g orbitals will be relieved, resulting in a macroscopic distortion of the crystal lattice.

2.2.2 Magnetic coupling and transport properties

The base of the theoretical description of the transport properties is the Hubbard-model, described by the Hamiltonian

$$H = -\sum t_{ij} c^{+}_{i\sigma} c_{j\sigma} + U \sum n_{i\uparrow} n_{i\downarrow} \tag{2.32}$$

where the first term describes the hopping of one electron to the neighboring ion with the hopping parameter t and the creation and destruction tensors $c^{(+)}_{i\sigma}$, and the second term the coulomb repulsion with the parameter U. It depends on the ratio of t and U, if the material is a conductor or not. If the Coulomb repulsion is bigger than the hopping parameter t, the electron will be localized at the ion and the material is an insulator. If $t >> U$, the electron can hop easily and the material is a conductor. However, also these materials are hopping conductors and do not have itinerant electrons, so the resistivity is enhanced compared to the metals. High conductivity and even itinerant bands as

observed for certain complex oxides like the spinel Fe_3O_4 or some perovskites are due to magnetic effects. In the following I will describe only the insulating case, as the spinels are insulators.

For a transition metal oxide one has to take into account that the hopping does not take place between two TM ions, but there is an oxygen ion in between. In this case another parameter must be introduced, which is the charge transfer energy D, describing the energy for an electron hopping from a filled O $2p$ orbital to a $3d$ orbital of the neighboring TM ion. In case that $D > U$ the insulator is a Mott-Hubbard insulator, where the oxygen ions have only a small influence on the properties. For $D < U$ the insulator is called a charge transfer insulator.

Also the magnetic coupling in this kind of oxides is indirect involving the $3d$ orbitals of the transition metal ion and the $2p$ orbitals of the O ion. The transition metal ions are too far away from each other to show a direct coupling, but the oxygen ion acts as an intermediary. This indirect exchange interaction was first proposed by Néel and later described theoretically by Anderson [37]. The description involves only the TM $3d$ and the O $2p$ electrons. In the ground state the O $2p$ orbitals are filled with two electrons of opposite spin. In Figure 2.5 a schematical drawing of the situation is shown. Due to the Heisenberg uncertainty principle the localized electrons can decrease their energy by virtual hopping. However, the Pauli principle is obeyed: the electron can hop only into orbitals which are not occupied by an electron with the same spin.

In the case of the transfer of one O $2p$ electron to one of the two neighboring TM ions, the O $2p$ orbital will be left with only one electron with the opposite spin than that of the hopped electron. Involving the direct exchange of the left O $2p$ electron and the overlapping TM $3d$ orbitals, the other neighboring TM ion will couple antiferromagnetically to the left electron of the O $2p$ orbital. Taken the virtual hopping and the antiparallel direct exchange together, one can see, that the two TM ions are coupled antiparallel. As both lobes of one $2p$ orbital are involved, the superexchange interaction is strong only in the case that all three ions lie on one axis, i.e. the coupling angle is 180°.

In the oxides with a mixed valence of one TM ion, a second interaction takes place. The so-called double exchange interaction applies in the case of a 90° coupling angle and

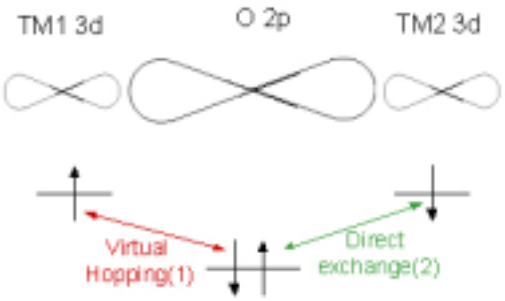

Figure 2.5: Scheme of the superexchange interaction process. TM1 and TM2 denote transition metal ions. Only one lobe of the $3d$ orbitals is shown.

two TM ions with a mixed valence, for example in Fe_3O_4 for the interaction of the Fe^{2+} and Fe^{3+} ions. Here the case is more complicated as two O $2p$ orbitals must be involved for the explanation of the coupling. Virtual hopping takes place between one electron of one of the completely filled O $2p$ orbitals and the Fe^{3+} ion, as the first spin-down electron. Then the left O $2p$ electron is polarized and if now one electron of the other completely filled O $2p$ changes the orbital, the direct exchange with the Fe^{2+} ion leads to a parallel coupling of the two Fe ions. This coupling leads not only to a parallel magnetic coupling of the B-sites, but also to a high conductivity of Fe_3O_4, as a chain of ferromagnetically Fe^{3+} and Fe^{2+} ions serve as hopping chains for the first spin-up electron of Fe^{3+}. There are other mixed valence oxides, one of the most investigated are the doped Manganites ($(La, A)MnO_3$ where A is an element of the IIA group, typically Ca or Sr). Here the Mn is in two different valence states, namely Mn^{3+} and Mn^{4+} (see also Section A1-2). A strong interaction between the magnetic and the electric properties was observed, becoming manifest in the so-called colossal magnetoresistance [12].

2.3 Spinel oxides

The spinel oxides XY_2O_4, where X and Y are typically transition metals, is a wide group of materials with various physical properties. Magnetite Fe_3O_4 is one of the oldest known and still investigated magnetic materials, and it is one of the few conductive materials in this group. The spinel ferrites (Y=Fe) are used very successfully in microwave devices as dielectric materials. Their Curie temperature is typically above room temperature and the magnetic moment is high. But in thin films the research and the application of these materials is still rare, due to the fact that they have a complex crystal structure with a big unit cell and many unoccupied interstitial sites, which makes them hard to synthesize in thin film form with the bulk properties (see Section 3.2).

2.3.1 Structure

The spinel crystal structure can be described as a close-packed face-centered cubic oxygen lattice with cations at the interstitial octahedral and tetrahedral sites (see Figure 2.6). The unit cell contains 32 oxygen anions and 24 cations. 8 of the cations are distributed on the 64 available tetrahedral sites (A-sites) and 16 on the 32 available octahedral sites (B-sites). The cations are distributed in that way, that B-site cations form a chain along the [111] direction of the lattice. Every B-site ion has six nearest neighbors, while every A-site ion has four nearest neighbors. The distance between the ions and their nearest neighbors is the smallest for the B-B neighbors, then A-B neighbors and the largest separation is between the A-A neighbors [9].

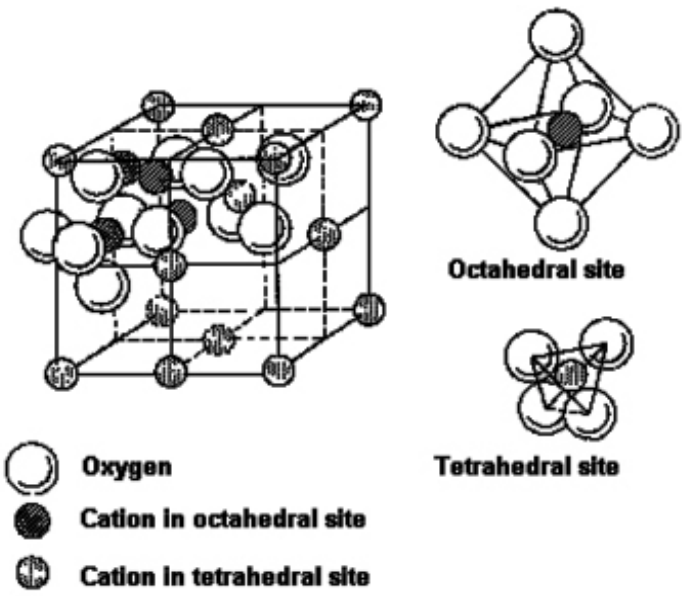

Figure 2.6: Schematic view of one unit cell of the spinel structure (left part) and the interstitial sites of the cations (right part).

The lattice parameter of the spinel oxides is usually larger than $0.8nm$. One of the smallest lattice parameters is found for $MgAl_2O_4$ ($a = 0.808nm$), while the ferrites and also the chromites show a larger lattice parameter of around 0.83 to $0.84nm$ ($CoCr_2O_4$: $a = 0.833nm, NiFe_2O_4 : a = 0.834nm$).

Considering the distribution of the cations over the two possible sites, three different spinel types have to be distinguished, the 'normal', the 'inverse' and the 'mixed' spinel structure. In the normal spinel structure the trivalent cations are found only on the B-sites, while the divalent cations occupy the A-sites (e.g. $MgAl_2O_4$, $CoCr_2O_4$ and other chromites due to the strong A-site preference of Cr^{3+}). In the other extreme, the inverse spinel structure, the divalent ions occupy half of the B-sites and the trivalent ions are distributed equally over half of the B- and over the A-sites (e.g. $NiFe_2O_4$, Fe_3O_4). The mixed structure is a mixture between the normal and the inverse spinel (e.g. $CoFe_2O_4$, $(Mn, Zn)Fe_2O_4$). The question how the 3+ and 2+ cations distribute over the A- and B-sites was addressed by theoreticians, who calculated the site preference of different transition metal ions taking into account the crystal field splitting and geometric considerations [38]. A quantitative measure is given by the stabilization energy Δ, which is the difference of energy between the normal and the inverse spinel structure. Δ ranges from some hundreds of meV to more than $1eV$. In the case of a small Δ a mixed inverse/normal structure can occur. The strongest B-site preference results for the Cr^{3+}-ions, which was experimentally verified in the normal spinel chromite group [39]. In case of the ferrites the situation is not as clear. The Fe^{3+} ions do prefer the octahedral sites, but when the other cation shows a stronger B-site preference (like for example Ni^{2+}), an inverse spinel structure is found. In $NiFe_2O_4$ the inverse spinel structure is more stable than the normal structure by $\Delta = 1.6eV$ [40], therefore deviations from a bulk-like cation distribution are less likely to occur than in other ferrites [41], for example $CoFe_2O_4$.

Another particularity of the spinels is the surface energy. Few theoretical work was done [42–44], especially due to the complex crystal structure and the lack of important parameters for the calculation. However, the both works predict the {111} surface to be of much less energy than the other surfaces being a factor of 4-5 lower than the e.g. the {100} surface energy. Experimental work confirms these predictions [45, 46].

2.3.2 Magnetic properties

The spinel oxides show a wide range of magnetic properties, depending on the TM ions involved. However, the application of the theory given in Section 2.2.2 is not straight forward, as the angle between the A- and the B-sites is around 125°, and the angle between two B-site ions is 90°. After L. Néel published a simple collinear and very successful model [47], in the fifties substantial theoretical work was done on the description of the magnetism in the spinel oxides. Wickham and Goodenough [48] gave some basic postulates referring to the magnetic coupling of the different sublattices, extracted just by electrostatical description of the e_g and t_{2g} orbitals. But also other - non collinear - magnetic structures where proposed by Yafet and Kittel [49] and later by Hastings and Lyons [50,51], triggered by the experimental observation [52] that some

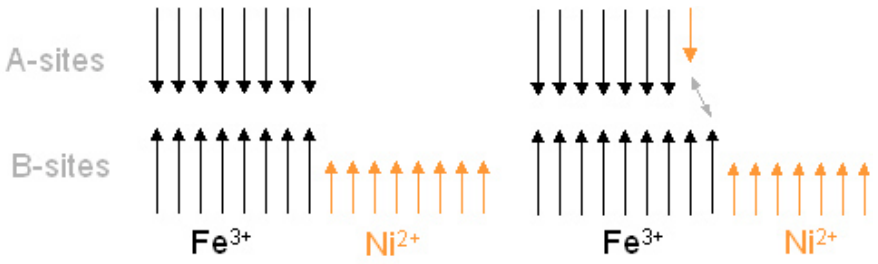

Figure 2.7: Illustration of the magnetic structure of $NiFe_2O_4$, the magnetic moment per ion is depicted as an arrow. On the right side the structure with one antisite is shown.

chromites showed a magnetic moment which could not be explained by the model of Néel. So first the Néel structure of the ferrites, in particular $NiFe_2O_4$, will be discussed, afterwards the more complicated case of $CoCr_2O_4$.

Ferrites show the collinear ferrimagnetic ordering of the Néel theory [47]. Here two ferromagnetically ordered sublattices are formed, one by the ions on the A-sites, one by those on the B-sites. The intersublattice coupling between the ions on the A- and the B-sites is antiferromagnetic and relatively strong, due to a superexchange interaction between these ions. The intrasublattice coupling between the different ions on B-sites is also an antiferromagnetic superexchange coupling (except Fe_3O_4 where the mixed valence of the Fe ions leads to a ferromagnetic double exchange interaction), which is weaker than the interlattice coupling due to the large distance between the B-site ions. The distance between A-site ions is even larger, and so the weak antiferromagnetic super exchange coupling of the A-site ions and of the B-site ions is covered by the strong intersublattice coupling and the intrasublattice ordering is forced to be ferromagnetic. In the case of the inverse ferrites including $NiFe_2O_4$(NFO) the moment of the Fe^{3+} ions ($5\mu_B/ion$) distributed over both sites cancels out and the overall magnetic moment is governed by the other A-site TM ion (see Figure 2.7, left side). For NFO the moment of the Ni^{2+} ion is $2\mu_B/ion$ and so the overall magnetic moment is $2\mu_B/f.u.$ ($f.u.$: formula unit). The experimental value is typically slightly higher [10], which is attributed incomplete quenching of the orbital magnetic moment. The Curie temperature (T_C) of the ferrites are typically above 700K, reflecting the very stable magnetic interaction in this system.

On the other hand, for the chromites the coupling between the Cr^{3+} ions on the B-sites is more important due to the half-filled t_{2g} orbitals of the B-site Cr^{3+} ions [48]. The coupling of the B-site ions is strong and antiferromagnetic, resulting in a non-collinear cone structure [51, 53], which is temperature dependent also below T_C and shows a very small magnetic moment per formula unit of 0.1 to $0.2\mu_B$ [54]. The propagation vector is along the [110] direction. As the ordering is less stable, the T_C is reduced with respect to the collinear ferrites and is around 100K for $CoCr_2O_4$.

As the spinel oxides are ferrimagnets involving two different sublattices, the resulting magnetic moment is strongly perturbed by defects in the structural lattice. In a film

deposition process many of these defects can be introduced. In the following some of them should be discussed and the magnitude of the change of the magnetic moment will be estimated for the case of $NiFe_2O_4$.

If antisites are introduced, this means that the TM ion formerly placed on B-sites (in the case of NFO the Ni^{2+}) occupies A-sites and so a higher number of Fe^{3+} ions is forced to be on B-sites, the moment of the Fe ions will not cancel out anymore (see Figure 2.7, right side). So the magnetic moment/$f.u.$ will be higher than the bulk moment. For the case of NFO the magnetic moment will increase by $0.75\mu_B/f.u.$ per antisite, leading to a magnetic moment for 100% Ni ions on A-sites (i.e. normal spinel structure) of $8\mu_B/f.u.$, a factor of four higher than the bulk moment of $2\mu_B$. Antisites or a metastable cation distribution were found for a row of ferrite systems (see Chapter 3).

If there is a deficiency of iron ions and those vacancies were preferably found on the A-site positions, the magnetic moment would increase also very strongly as again the Fe moments do not cancel out anymore. This effect can occur not only for a real Fe deficiency, but also in the case of iron ions situated on normally non-occupied A-sites in the spinel structure. In this structure only one eighth of the A-sites in a unit cell are actually occupied (see Section 2.3.1) and so some iron ions at these normally unoccupied sites will act as impurities and will not influence the crystallographic properties. However, they will lack in the A-sites, which will disturb the magnetic ordering although the stoichiometry of $NiFe_2O_4$ is preserved.

Another possibility to change the magnetic moment are oxygen vacancies. Some of the Fe^{3+} ions will be reduced to Fe^{2+} ions with a smaller moment of $4\mu_B/ion$. If those ions are not equally distributed over the A-and B-sites, the total magnetic moment will change. There will be a decrease in the case that the Fe^{2+} ions are found preferably on B-sites and an increase in magnetic moment, if the Fe^{2+} ions are located on the A-sites. However, the change will not be as big as for antisites, because per Fe^{2+} ion the magnetic moment will change by $0.125\mu_B/ion$.

A fourth possibility to change at least the saturation behavior and the coercive field is the formation of antiphase boundaries (APBs) [55]. When a spinel film is grown on a rock salt or perovskite substrate, the spinel film has a unit cell eight times larger. While the spinel material is growing, there are nine equal positions for the incoming TM ions on the surface of a rock salt or perovskite substrate. Neighboring islands will coalesce after a critical thickness of the film and the unit cell of each will be shifted or rotated in comparison to the other islands, and so APBs are formed. The coupling over an APB is antiferromagnetic and so the APB's build Bloch walls in the magnetic structure, though the crystal structure is not disturbed at these points. It was shown for Magnetite that the APB's change strongly the magnetic behavior, introducing very high saturation fields and superparamagnetic behavior for very thin films [35, 55, 56].

In the extensive studies on nanoparticles another effect was observed, altering the magnetic properties of the spinel nanoparticles: the surface spin disorder. At every surface the ion's surrounding is another than in the bulk, but as nanoparticles have a very high surface to volume ratio, the altered magnetic properties of the surface ions have an influence on the overall magnetic properties of the particle. In most of the spinel nanoparticle the effect was observed [57–63], reducing the saturation magnetiza-

tion, increasing the saturation field and shifting the hysteresis loop along the field axis. Kodama et al [58] gave a theoretical model, showing that missing superexchange bonds are the origin of this behavior. As the magnetic interaction in the spinel is an indirect interaction, missing oxygen or transition metal ions at the surface of the nanoparticle gives rise to a variation of exchange fields for the ions and a spin-glass like state is formed at the surface.

2.3.3 Transport properties

Many spinels, especially the ferrites (except magnetite) and chromites, are insulators in the sense of the formerly given description of the transition metal oxides. The exception of magnetite is due to the mixed valence Fe ions. The extra electron ($3d^6$) of the Fe^{2+} ions is the first spin-down electron. As the B-sites form a chain of ferromagnetically coupled Fe^{3+} and Fe^{2+}, the sixth electron can hop between the sites, the distances between the B-sites are small enough.

In case of $NiFe_2O_4$ a similar hopping mechanism like in Fe_3O_4 was found in bulk material: here a transfer of an electron between a Ni^{2+} and a Fe^{3+} can take place and a Ni^{3+} ion and Fe^{2+} ion is formed. A mixed valence of the Ni and Fe ions is produced locally, so that a hopping mechanism of the electron to the surrounding Fe^{3+} ions occurs, while the hole will hop to the neighboring Ni^{2+}. As the ion distances in the spinels are big and the overlap between the localized electron's wave functions is small, this hopping needs the assistance of phonons and is thermally activated with a typical activation energy of $0.45eV$ to $0.5eV$ [64, 65].

The typical resistance of bulk NFO at room temperature is around $1k\Omega cm$ [65]. The temperature (T) dependence of the resistivity due to the hopping mechanism is a logarithmic one:

$$\sigma T = \sigma_\infty \exp(q/k_B T) \tag{2.33}$$

where $\sigma = 1/\rho$ is the conductivity defined as the reciprocal of the resistivity, q is the activation energy and k_B the Boltzmann constant.

In conductivity measurements of nanoparticles by Ponpandian et al [64] the influence of antisites on the conductivity behavior was investigated. As the distance of the A-sites is larger than that of the B-sites, and the binding character is less covalent, the hole conduction between the Ni^{2+} ions on A-sites has a higher activation energy and the conductivity is small. It will be important only at temperatures above 500K. However, by the introduction of antisites, the Ni^{2+} ions on the B-sites is reduced, so that the hole hopping itself will be smaller on B-sites and hence the conductivity will decrease with increasing number of antisites.

An oxygen deficiency can also induce a conductivity in the NFO. Here a lack of oxygen ions will lead to a higher electron concentration on the sites of the transition metal ions. In the case of NFO, the Fe^{3+} ions will be reduced to Fe^{2+} and so again one spin-up electron can hop quite easily to the neighboring Fe^{3+}.

2.4 Thin film growth

In this chapter an overview of the phenomena of the epitaxial growth is given. A film growth on a substrate is called epitaxial, if the film grows oriented in-plane and out-of-plane on the substrate. In case of polycrystalline growth the interaction between substrate and film is not very important, so it will be excluded from this definition. If the film and the substrate are chemically identical, the growth is called homoepitaxy, while the heteroepitaxy describes the growth of a film on a substrate with a different structure.

In the following section a short overview of the basic phenomena of thin film growth on single crystalline substrates is given. First the macroscopic growth modes derived from thermodynamic considerations will be introduced, afterwards a more detailed, microscopic description of the film growth which includes also effects far away from the thermodynamic equilibrium.

2.4.1 Macroscopic model

In Figure 2.8 the three possible growth modes as distinguished by Bauer [66] are shown. In the two dimensional layer-by-layer (or Frank-van-der-Merwe) growth mode the substrate is completely covered. The interaction between the substrate and the adatoms is stronger than the interaction between the adatoms, so that a complete monolayer of the material is formed. After the deposition of more material a second layer covers the first one. The binding energy with the surface decreases monotonously with the volume of the film.

The other extreme is the island or Volmer-Weber growth mode (Figure 2.8 right side). Here the interaction between the adatoms is stronger than with the substrate, so that the surface is not completely covered. As the adatoms have a certain mobility on the surface, clusters are build and afterwards islands. The Stranski-Krastanov growth mode is the intermediate case: the growth starts as a layer-by-layer growth, but after a critical thickness islands are formed.

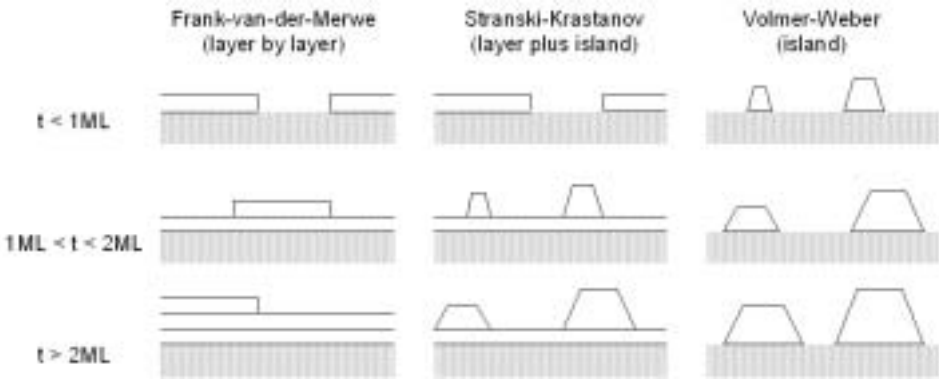

Figure 2.8: Schematic representation of the three growth modes after [66].

The thermodynamical basis for this classification is the interplay between the free surface energy of the adsorbate σ_{ad}, the substrate σ_{sub} and the energy of the interface between the substrate and the adsorbate σ_{int}. The energy of the system is calculated as the difference between the energy of the newly introduced surface of the adsorbate film and the interface ($\sigma_{ad} + \sigma_{int}$) and the free surface energy of the substrate σ_{sub}, thus $\Delta = \sigma_{ad} + \sigma_{int} - \sigma_{sub}$. If Δ is positive the Volmer-Weber growth mode will be observed, if it is zero or negative, the Stranski-Krastanov or Frank-van-der-Merwe mode is the preferred one. The latter case takes place, if $\Delta \leq 0$ for each layer.

The interface energy consists of the mechanical and chemical interactions in and at the interface with a finite thickness between the substrate and the film. The misfit, i.e. the difference of the lattice parameter of the substrate and the film, has a special importance. It is defined as $\delta = (c_f - c_{sub})/c_{sub}$, where c_f is the lattice parameter of the film material and c_{sub} that one of the substrate. If $c_f < c_{sub}$ the misfit results in a compressive strain of the film and if $c_f > c_{sub}$ the strain is tensile. The strain and eventual defects introduced in the film to relax the strain (see section 2.4.3) enter the interface energy.

The interface energy increases with δ and the thickness of the film, thus the growth mode is also dependent of the film thickness. Above a critical film thickness the increase of the interface energy leads to a change of sign of Δ and so a change from the layer-by-layer growth mode to an island growth mode. This behavior was observed for the growth of metals on metals and on semiconductors.

This model proposed by Bauer is only valid in the thermodynamic equilibrium of the system. Interdiffusion between the components or surface diffusion of the adatoms are neglected, as well as chemical reactions between the substrate and the film or kinetic effects resulting from the deposition process. For the sputtering or pulsed laser deposition technique the growth process includes processes away from the equilibrium, as the energy of the adatoms is higher than the thermal energy, so that the model is not sufficient for the description of the film growth in these cases. Here a miscroscopic picture of the growth is necessary, including kinetic processes.

2.4.2 Microscopic model

In the microscopic model the atomic processes on the surface are described which are responsible for the surface diffusion, the nucleation and the island formation (for a review see for instance [67]). These atomic processes are shown in Figure 2.9. After the adsorption of the atom on the surface, different processes are possible: the diffusion, the nucleation of identical adatoms (homogeneous nucleation), the adsorption at steps or other defects (heterogeneous nucleation) and the desorption into the vapor phase. The interdiffusion between the film and the substrate is neglected in the easy models of film growth.

The condition for the nucleation is a sufficient mobility of the adatoms on the surface. The transport of the adatom is governed by a hopping mechanism, as the substrate surface constitutes a two-dimensional periodic potential with binding states (valleys) and diffusion barriers (hills). When the thermic energy of the adatom is higher than the

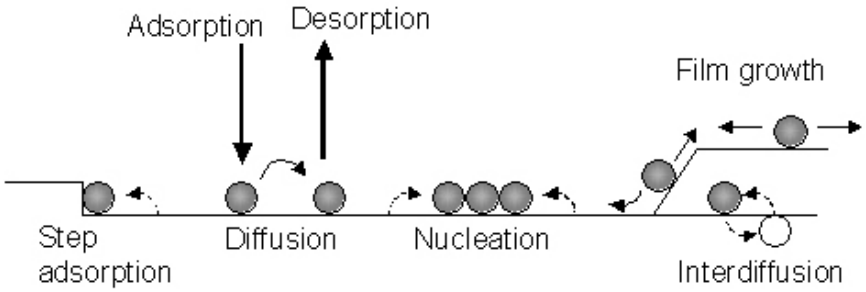

Figure 2.9: Schematic representation of the most important microscopic processes during the nucleation and the growth of thin films.

diffusion barriers, the adatom will diffuse on the surface until a stable state is found. Hereby the adatoms prefer the direction with the lowest corrugation height.

With increasing amount of the material on the surface, a two dimensional gas of single atoms is build, if the adatoms are able to move free on the surface. The probability that two diffusing atoms will meet and form a dimer increases with the adatom concentration, if the possibility of desorption is excluded. The dimer is a non-stable formation, it will disappear or incorporate another adatom. The nuclei build like this are stable only above a critical size, which is strongly dependent on the substrate temperature and the binding energy in the nucleus. The trapping of adatoms by the nuclei leads to a characteristic denudation zone around them, so when the adatom flow is interrupted before one monolayer is complete, islands are present. On the other hand, in the case of a supersaturation, i.e. a flux of adatoms incident on the surface, the islands grow laterally and a closed layer is formed by the coalescence of these nuclei in the Frank-van-der-Merwe growth mode, or the nuclei will grow also horizontally, so that islands are formed in the Volmer-Weber growth mode.

The diffusion, nucleation and island formation was described theoretically by Venables et al [68, 69] by a rate equation model. This model is very successful in describing the growth of metals on metals for example. However, effects like step or island edges or the reconstruction of the surface are not taken into account. This defects are often observed for the growth on semiconductors, so that in these systems the rate equations do not describe the growth in a correct way [70].

At steps for example the coordination of the adatom is higher and so the energy of the adatom can be decreased substantially by the nucleation at these sites. By the step adsorption the density of adatoms in the area adjacent to steps is reduced, so that here the homogeneous nucleation can be totally suppressed (for example in the case of high substrate temperatures or a low supersaturation), which leads to a growth mode called step-flow. The exclusive adsorption of the adatoms at a step results in a motion of the step over the terrace.

For the motion of an adatom across a step or the edge of an island the adatom sees an activation barrier, which is called Ehrlich-Schwoebel barrier and results from the changed coordination number at the step edge. Crossing the step the adatom has to

pass through a transition state of very low coordination, which implies poor binding and thus a higher energy. It has been first observed by Ehrlich [71] and later on described theoretically by Schwoebel [72]. If the incident atoms do not have enough thermal energy to cross the barrier, they are reflected at the barrier, so that the transport of mass between the higher lying and lower lying terrace is interrupted. As at step edges, the Ehrlich-Schwoebel barrier forms also at island edges, which hinders the adatom from leaving the island area, resulting in a three dimensional island growth.

2.4.3 Accommodation of lattice misfit

In heteroepitaxial systems the lattice parameters show a discrepancy between the film and the substrate expressed by the misfit δ. A consequence are homogeneous and inhomogeneous strains, which interact strongly with the film growth. The system tries to accommodate the strain in various manners.

Below a critical misfit, which is depending on the system, a coherently strained film can be formed. Here the film material takes the lattice parameter of the substrate (as for example Fe_3O_4 on MgO or $(La, Sr)MnO_3$ on $SrTiO_3$), called pseudomorphic growth. The strain energy, however, increases linearly with the film thickness, so that above a critical film thickness the pseudomorphic growth is not possible anymore.

As a possible way to release the strain, dislocations can be introduced into the film, which are line defects orthogonal to the direction of the substrate. In the dislocation area more atoms are introduced into the lattice ($\delta < 0$) or atoms are removed ($\delta > 0$). The plastic deformed areas will separate domains of a nearly pseudomorphic growth from each other. Inside the dislocation the atomic distances of the layer vary, but at the same time the film lattice parameter stays pseudomorphic for other directions of the substrate. This mechanism is called uniaxial expansion (compression) and the strain can be relieved at least in one direction.

Another possibility of stress relief is the introduction of islands. In the classical model of the Stranski-Krastanov growth the emergence of the islands is for example related to a misfit dislocation formation after a critical film thickness due to the accumulation of strain in the wetting layer. However, also coherently strained islands can accommodate stress, as the island can partially laterally relax due to the three dimensional growth, and furthermore an elastic local adjustment of the substrate lattice parameter can ocurr [73]. The strain leads to a roughening of the film surface with subsequent diffusive aggregation of adatoms at elevated points representing a lower total strain energy which outweighs the increased surface energy. The island's total energy has a minimum at a finite size when the elastic relaxation energy at the island edges exceeds the surface energy and the islands will resume the optimum size and do not have a propensity to grow [74, 75].

The stability window for coherent islands depends on the lattice mismatch, surface energy and total number of particles in the film. An important parameter is also the binding energy of the film material. In the case of a low mismatch, the coherent islands are stable up to a large amount of deposited material, while with increasing misfit this stability zone decreases and dislocated islands are introduced at already a low amount of deposited material [76].

Strain can be accommodated also by the rotation of the unit cell of the film on the substrate, resulting in the so-called Moiré pattern. In this way a different commensurability of the two lattices can be reached, lowering the misfit and so the strain. The placing of the adatoms between or on top of the substrate atoms leads to a vertically corrugated surface, as the atoms placed on top of the underlying atoms stands out of the surface, as observed in the growth of FeO on Pt(111) [77]. Other possibilities of strain accomodation in thin films include buckling of the film without the formation of three dimensional islands as for example observed in the growth of MgO on Ag(100) [78] and the formation of cracks perpendicular to the film plane [79].

2.4.4 Growth of complex oxides

The growth of oxides was investigated due to the importance of oxide films in technological applications. Different phenomena are observed and explained (for a review for instance see [80]), but it lacks a consistent theoretical description of the growth of the oxides as was achieved for the growth of metals. Though the microscopic processes will be similar to the ones shown in Figure 2.9, certain features of the oxides makes a modified description necessary.

The first point is the adsorption and diffusion of particles on the surface. In the oxides several ions are involved, i.e. the oxygen ion and at least one cation. As the binding character of the oxides is ionic, dimers and molecules are formed more readily. Depending on the deposition technique, not only atoms are incident on the surface, but also ions and molecules. The growth processes in turn are strongly influenced by the nature of the diffusing ions and their mobility. Even more, the growth of complex oxides demands the formation of a oxygen lattice with the right kind of ion at the interstitial sites, so that cations need a sufficient energy to mount steps and to find the adequate interstitial site. The microscopic mechanisms of these processes are not clear and require theoretical description.

Another particularity is the semiconducting or insulating character of oxides. Therefore also electric charges and fields in the film need to be integrated into the theory, as described by Atkinson [81]. Rate equations were formulated for the growth of oxide thick films on metal surfaces and the growth rate was found to be strongly dependent on the paths of charge and material transport in the films. However, the model does not allow a conclusion on the microscopic processes and leaves the existence of interface charges or space charges out of the discussion.

3 State of the art: Recent research on spinel oxides

Spinel oxides are a big group of materials and can be applied for different functionalities: catalysts for decomposition of gases [82, 83], magneto-optical storage media [84], flux guides and sensors in thin film recording heads [85], ferromagnetic semiconductors [86], magnetic fluids [87], multiferroic composites [88–91], transformer cores and microwave magnetic devices [92], and as magnetic nanoparticles in medical applications [93]. The spinel involved in most of the cases is a ferrite, as they are stable, have a high corrosion resistance and a high T_C combined with a high magnetic moment. The research in the last few years exploded on the nanoparticle field, as they are easy to produce and very promising for applications. However, this chapter will show that many basic questions of the ferrites are still unsolved, and that the research of thin films is hampered by the reproducibility of the results from one group to the other.

3.1 Research on bulk properties

Although the spinels are known for a long time, some basic features are discussed until know in the literature. Most research is concentrated on the ferrite group, especially magnetite Fe_3O_4, and one of the recently strongly discussed problem is the Verwey transition. It appears only in magnetite and is a metal-to-insulator transition at around 120K accompanied by a distortion of the cubic symmetry [94]. An interpretation was given already in the 40's [95]: The electron-hopping along the chains of B-sites is frozen out and the electrons get localized, forming a charge ordered state of Fe^{2+} and Fe^{3+} ions. The distortion of the lattice arises from the Coulomb repulsion.

This model was accepted and theoretical calculations were able to predict this charge ordered state at low temperature [96, 97], and even an orbital order [98, 99]. Recently the observation of a charge ordered state of a reconstructed magnetite(001) surface of an artificial crystal by scanning tunneling microscopy was reported [100], where Fe^{2+}-Fe^{2+} and Fe^{3+}-Fe^{3+} pairs were found. However, Subías et al [101, 102] carried out X-ray resonant scattering on an artificial crystal, and were not able to observe certain reflections, which are forbidden for high-temperature phase of magnetite, but which should appear for a charge-ordered state. Also Szotek et al concluded from their theoretical study [103] that the lattice distortions of the crystal are responsible for the insulator transition and not a charge ordering effect. This view of the Verwey transition was found experimentally in nanoparticles of $Fe_{2.75}Ti_{0.25}O_4$ [104]. Although the Verwey transition is known for around 60 years, the mechanism of this transition is not clear yet.

Another topic of research is the surface termination of magnetite (a short review of the state of the art is given in [105]). This is a very interesting topic also for the thin film community as the surface termination and especially the Fe/O ratio can strongly influence the magnetic and electronic properties and so the performance of magnetite in magnetic tunnel junctions. The (100) surface of magnetite is polar and has two possible terminations, so the history of the sample preparation has a strong influence [105]. Also the (111) surface was examined by scanning tunneling microscopy [106,107] and shows a strong dependence of the magnetoresistance of magnetite on oxygen vacancies [106] and of the electronic structure of the surface on stress [107]. In [108] the electronic structure of the (111) surface was investigated by angle-resolved photoelectron spectroscopy.

Recently a variety of scattering methods was used to investigate the magnetic circular dichroism [109–114] and to extract for example the spin- and the orbital moment of magnetite [114] and Ni- and $CoFe_2O_4$ [113]. But the interpretation of the measurements is very complicated and does not lead to results without extensive theoretical description. Some observation can be extracted: X-ray Magnetic Circular Dichroism was shown to be sensitive to the same TM ion on two different sites [110], although with a careful theoretical description needed. Van der Laan et al [113] investigated the spin- and the orbital moment of $NiFe_2O_4$ and $CoFe_2O_4$, showing that the orbital moment in $NiFe_2O_4$ is quenched as expected due to the crystal field, but they pointed out the difference of $CoFe_2O_4$, where the orbital moment is quite high. The same accounts for magnetite, where also an unquenched orbital moment was observed [114] due to spin-orbit interaction and electron correlation.

Band structure calculations faced a substantial problem: the calculated band structures of spinels [115–117] showed states at the Fermi energy, while the materials were experimentally known as insulators. Over the last years the modeling methods were refined, resulting in more reliable results. Fava et al [118] modeled the properties of $MnCr_2O_4$ with a periodic Hartree-Fock scheme. Zuo et al [119] used a modified local spin density approximation for $MnFe_2O_4$, comparable to Szotek et al [120] for Fe_3O_4 and $NiFe_2O_4$. The very interesting fact of the last two references is that the gap of the minority spins is much smaller than that of the majority spins, so that the valence band is strongly spin-polarized. Szotek at al [120] also include a study on a normal spinel $NiFe_2O_4$ cation distribution, leading to a decrease of the minority spin gap and an increase of the majority spin gap, so that the spin-polarization of the valence band is even stronger than in the inverse spinel cation distribution.

More general in the spinels the thermodynamics of the cation distribution was examined experimentally and theoretically. Warren et al [121] carried out ab-initio calculations of the cation ordering for spinel $MgAl_2O_4$ and claimed that this method can be used for other spinels, too. In the ferrite group the research was concentrated on $(Mn, Zn)Fe_2O_4$, as this system is a mixed spinel. The electronic properties [122, 123] and neutron diffraction [124] were used to investigate the thermodynamics of the reordering of the cations.

3.1.1 Nanoparticles

A very active part of the recent years is the investigation of nanoparticles of different ferrites. Nanoparticles are interesting for application as magnetic storage media, for magneto-optical application [84] or magnetic fluids and foams. From the point of view of fundamental research they are interesting due to the finite size effects, which one can expect. Nanoparticles of ferrites show two pronounced effects: a surface spin canting due to the broken bonds and disturbed superexchange interactions at the surface of the nanoparticles, as well as cation redistribution.

The first aspect was observed experimentally by an enhanced coercive field and even a shifted hysteresis loop along the field axis in $CoFe_2O_4$ [125], $CuFe_2O_4$ [59], $ZnFe_2O_4$ [60] and $NiFe_2O_4$ [57, 58, 61, 62, 126–128]. Also a lowered saturation magnetization was observed. Morrish and Hanada [57,125] were the first to interpret this behavior by a spin disorder in the shell of the nanoparticle and represented the nanoparticle with a core with bulk magnetic properties and a shell with strongly disordered spins. Kodama et al proposed a theoretical model for $NiFe_2O_4$ nanoparticles [58] and later generalized for the spinel ferrites [126], which takes into account the surface roughness of the nanoparticle and broken bonds due to the lower coordination at the surface. This model was very successful in describing the magnetic behavior of the nanoparticles.

Perriat [129] commented the core-shell model from a more chemical point of view and observed a strong interplay between strains in the shell and the chemical reactivity of the particles. Zhang et al [62] refined recently the Kodama model taking into account the change of the superexchange mechanism at the surface, and pointed out, that the magnetic shell (i.e. the region of magnetic disorder) can extend by far the structural shell (i.e. the region of structural disorder described by Kodama et al). Two groups including the nanoparticles in a matrix, Silica [130] and Polyol [63], did not observe a sign of surface spin disorder, which could propose a way of synthesizing nanoparticles with the bulk saturation magnetization.

On the other hand a very interesting behavior was observed in nanoparticles of $(Mn, Zn)Fe_2O_4$ [131], $NiFe_2O_4$ [61] and $CuFe_2O_4$ [59]: the nanoparticles showed a well-defined magnetization behavior, but they started to show a superparamagnetic behavior after post-annealing of the sample (or decreasing the milling time in the case of [59, 61]). The observation was interpreted by a cation redistribution. At low temperature the cations are not distributed like in the bulk, which leads to a 'blocking' of the particle. When the temperature is raised, the cations redistribute approaching the bulk distribution, which leads to a superparamagnetic behavior of the particle. This interpretation was consistent with the observation of an enhanced saturation magnetization in other particles, which was also attributed to a non-equilibrium cation distribution on the A- and B-sites. The presence of antisites were reported for a row of ferrite nanoparticles: $(Mn, Zn)Fe_2O_4$ [131–133], $ZnFe_2O_4$ [60, 134], $(Ni, Zn)Fe_2O_4$ [135], $CuFe_2O_4$ [59, 136] and $NiFe_2O_4$ [61, 63, 64, 127, 128, 130, 137]. It was proven directly by Mössbauer spectroscopy [59–61, 63, 128, 131, 136, 138] or by EXAFS [61, 133–135] and indirectly by the observation of T_C [127, 132]. The latter showed an increase for $NiFe_2O_4$ [127] and a decrease for $(Mn, Zn)Fe_2O_4$ [132]. Equally the influence on the electric properties was

investigated by [64,137] in $NiFe_2O_4$ nanoparticles, both observing a n-type conduction by formation of Fe^{2+} ions and a p-type conduction by the formation of Ni^{3+} ions. The redistribution of the disordered ions leads to a change of the slope of the Arrhenius-plot, as the hole- and electron mediated conduction is extremely sensible on the surrounding of the ions. Chinnasamy et al [60] observed that the number of antisites is increasing with decreasing particle size, indicating a surface mediated effect. The dependence of the cation distribution on the preparation was pointed out by [138, 139].

The nanoparticles made out of Fe_3O_4 do not fit into this picture. Surface spin disorder was only observed for non-stoichiometric $Fe_{3-\delta}O_4$ [140] or after a high-pressure compaction [141], possibly due to the compaction treatment. Antisites were not reported, the nanoparticles show a superparamagnetic behavior down to a blocking temperature of $20K$ [142]. A very interesting study was reported by Zeng et al [143], who managed to synthesize Fe_3O_4 nanoparticles with a $FePt$ shell and were able to tailor the magnetic properties of these particles by changing the core-shell ratio.

3.2 Research on thin films

The most important work done the last years on thin films of spinel materials was the influence of the substrate on the structural and physical properties of the films (for a review see [92]). In 1996 Margulies et al [55] showed that in magnetite thin films an abnormal saturation of the magnetization was found in films on various substrates, which was explained by the antiphase boundaries (see Section 2.3.2) originated in the principal stages of film growth. This triggered more work in the field, especially also because Fe_3O_4 was predicted to be a half-metal [5]. Due to its large coercive field $CoFe_2O_4$ is of interest for the perpendicular recording media and magneto-optical applications.

3.2.1 Structural properties

Spinel thin films were grown on a row of substrates, especially oxide substrates. The spinel structure is very flexible in accommodating misfit between the substrate and the film, so that fully epitaxial films can be grown up to a misfit of 6%.

The mostly used substrate is MgO. The close-packed oxygen structure allows an uninterrupted oxygen sublattice at the interface MgO/spinel and the lattice parameter of 0.42nm is nearly identical to that one of many ferrites. Most work was carried out on magnetite on MgO(001) substrates [55, 144–149] resulting in fully epitaxial films with a cube-on-cube epitaxial relationship, as observed also for $(Ni, Zn)Fe_2O_4$ [150]. The critical thickness, above which a relaxed growth is expected, was calculated to be $60nm$ [148]. However, two groups [145,151] found a substantial interdiffusion of Mg^{2+} into magnetite, forming the spinel $MgFe_2O_4$. The interdiffusion problem was also found for other spinel ferrite films. Venzke et al [152] grew $NiFe_2O_4$ films on a row of substrates and discard MgO due to the strong interdiffusion observed at already low deposition temperatures, as did Cillessen et al [153] for the deposition of $(Ni, Zn)Fe_2O_4$ films.

The use of a substrate with a unit cell that much smaller than the film, like for

example MgO, leads to antiphase boundaries. As they are structural defects, they show a temperature driven diffusive motion [154], but to remove them totally the temperatures involved are so high, that in the most studied case of magnetite it leads to the formation of a Fe_2O_3 parasite phase [92]. The antiphase boundaries are visible in dark field transmission electron micrographs [154, 155]. Eerenstein et al [156] also showed that the density of the antiphase boundaries can be decreased by using the isostructural $MgAl_2O_4$ as predicted by Margulies at al [55].

To avoid the existence of antiphase boundaries a spinel substrate or a spinel buffer on other substrates can be used. The only commercially available spinel substrate is $MgAl_2O_4$, which is a very stable material, but the mismatch with most of the ferrites and chromites is very large ($c = 0.804nm$). Although this substrate is the only one to diminish the density of antiphase boundaries, studies of the growth on $MgAl_2O_4$ are rare. For magnetite a recent study was carried out by Kale et al [148] and Krasnikov et al [147], but the structural data is spare. It was observed, that the magnetite grows relaxed on $MgAl_2O_4$, but with a cube-on-cube epitaxy. Two other studies on $NiFe_2O_4$ [152] and $(Mn, Zn)Fe_2O_4$ [153] do not give structural data, but discard this substrate because of strong Mg and Al interdiffusion.

As a substrate, where the interdiffusion will not play a role, $SrTiO_3$ was used. The mismatch is high (6%), so that it was used only by few groups. Suzuki et al [157, 158] made films of several ferrites on $SrTiO_3$ substrates. The films show a cube-on-cube epitaxy, but the rocking curves of the ferrite(004) peak are in the order of 1 to 2.5°. It was shown that the crystalline quality of the films can be substantially improved buy using a spinel buffer, for example $CoCr_2O_4$. Wakiya et al [150] prepared thin films of $(Ni, Zn)Fe_2O_4$ on $SrTiO_3$ and observed also an improvement of the film properties with the introduction of a spinel buffer.

Venzke et al [152] fabricated $NiFe_2O_4$ films on bare $SrTiO_3$ substrates, observing a width of the rocking curves comparable to that of Suzuki et al. Even more, they observed amorphous parts of the film between crystalline grains, which could be removed by a post-annealing treatment. In contrast to the before mentioned studies, which observed a cube-on-cube epitaxy, Cillessen et al [153] found for their $(Ni, Zn)Fe_2O_4$ films on $SrTiO_3(001)$ a (111) out-of-plane orientation, attributed to the absence of epitaxial growth as the {111} plane is the plane of lowest energy for the spinels. They introduced a buffer of $BaZrO_3$, which has a lower mismatch than $SrTiO_3$, and the films resulted to be fully cube-on-cube epitaxial. However, the growth of magnetite on $SrTiO_3$ with a high structural quality seems to be possible as reported by [148].

As can be deduced from the different studies on substrates, an ideal substrate for spinel films does not exist. Cillessen et al [153] report that the films with the highest structural quality were grown on spinel Zn_2TiO_4 single crystals, but this material is not available commercially and must be home-made. Other oxide substrates, which were studied, were $(La, Sr)(Al, Ta)O_3$ [150], resulting in a cube-on-cube epitaxy of the $(Ni, Zn)Fe_2O_4$ films. Also sapphire was tried for $NiFe_2O_4$ thin films by Johnsson et al [159]. The films showed a (111) out-of-plane orientation on a (0001) oriented substrates and the formation of twin boundaries.

Due to the predicted half-metallicity of Fe_3O_4, several groups studied the growth of

magnetite on semiconductor substrates [150, 160–164]. The most exhaustive study was done by Kennedy et al [160]. For films directly grown on bare Si(100) and GaAs(100) substrates they find a (111) out-of-plane oriented polycrystalline growth. Again, the origin is to be found in the {111} minimum energy plane. By introducing a MgO buffer layer they find cube-on-cube epitaxial growth of the MgO buffer and the magnetite film, as do Reisinger et al [161] for a TiN/MgO buffer. Other studies on Si(100) find a (001) out-of-plane textured polycrystalline [162] or an amorphous [163] growth, which could be changed to a (001) out-of-plane textured polycrystalline growth by introducing a Cu buffer layer. Wakiya et al [150] grew $(Ni, Zn)Fe_2O_4$ on CeO_2 or spinel buffered Si and observe in all cases a fully epitaxial, (111) out-of-plane oriented film. Another study on the growth of magnetite on GaAs [164] shows a polycrystalline growth on the untreated substrate, comparable to [160], but claim that on a pretreated substrate a preferential (111) orientation can be reached.

3.2.2 Magnetic properties

The most investigated topics in the magnetic properties of spinel thin films are the influence of stress and in magnetite the appearance of antiphase boundaries. The first topic was the point of interest of the work of Suzuki et al, who grew different spinel ferrites ($CoFe_2O_4$ [157, 158, 165–167], $(Mn, Zn)Fe_2O_4$ [157, 158, 165] and $NiFe_2O_4$ [158]) on various (buffered) substrates. They found a strong decrease of the saturation magnetization with the stress, and proposed to introduce a $CoCr_2O_4$ buffer in order to diminish the stress of the film and to allow a growth with few antiphase boundaries or other structural defects. This reduction of the saturation moment by stress was also found in $CoFe_2O_4$ films on SiO_2 [168] and for magnetite films on MgO [146]. Wakiya et al [150] made a study of $(Ni, Zn)Fe_2$0$_4$ on various bare and buffered substrates, showing a very interesting behavior of the films: for a window from 0% to 6% lattice mismatch resulting in compressive strain the films showed bulk magnetic behavior, but for a tensile strain the saturation magnetization decreases already for very small mismatches, notably on MgO (mismatch -0.3%) the magnetization is already reduced from the bulk value. Results reported in other work are consistent with this study. They invoke a concept of a stress-induced magnetization, but do not discuss in length the origin of these findings.

Magnetite thin films were studied to elucidate the appearance and influence of antiphase boundaries on the magnetic properties of the films. Kalev et al [169] tested a micromagnetic model of the antiphase boundaries by nuclear resonant scattering and verified the Bloch-wall-like spin orientation across the antiphase boundary. Recently Moussy et al [170] analyzed the hysteresis loops of their samples with a model of ferromagnetic grains separated by sharp antiferromagnetic interfaces and verified the model. They found a strong antiferromagnetic coupling across these areas, which explains the high saturation field of some magnetite films found in the experiments [55, 56, 171, 172]. Also the superparamagnetic behavior of ultrathin films was attributed to the antiphase boundaries [35, 173], but this was recently put into question by Eerenstein et al [155], who find the origin of the superparamagnetic behavior in the structural domains and not the magnetic ones. However, antiphase boundary free films were found by Kale et

al [148] on a row of substrates.

Due to the possible application of magnetite in magnetic tunnel junctions with for example a MgO barrier, the magnetism of the magnetite/MgO interface was studied [105,174]. Strijkers et al [174] introduced an enriched ^{57}Fe magnetite layer at different distances from the MgO interface in multilayers and measured the properties with Mössbauer spectroscopy. They do not find a deviation of the properties between the interfacial layers and the bulk-like ones. Kalev et al [105] had a closer look and measured the properties of monolayers of magnetite at the surface and the interface by soft-landing experiments and find a change of the properties only for the first four monolayers (at the surface) or less (at the MgO interface).

Negulescu et al [175] prepared NiO/$NiFe_2O_4$ bilayers by pulsed laser deposition to test the possibility of exchange biasing a ferrimagnet by an antiferromagnet. They found a hysteresis field offset up to -800Oe for field-cooled samples, but also an exchange bias in single $NiFe_2O_4$ films. They do not claim if it is an intrinsic behavior of thin ferrite films, or if it is due to some extrinsic effect.

3.2.3 Transport properties and magnetoresistance

Few work was done on the transport properties of ferrites as only magnetite is a conductor. The most important factor of the electric transport in ferrites seems to be the grain boundaries as pointed out by [176] on $ZnFe_2O_4$ polycrystalline films and Fe_3O_4 by [156,177]. The latter also measured the magnetoresistance of the films, finding a spin valve-like behavior due to the antiferromagnetically ordered antiphase boundaries.

The extrinsic magnetoresistance of magnetite was addressed by some groups recently due to the prediction of de Groot et al [5] and the experimental result [178] that magnetite is a half-metal. However, the experimental results do not hold the high expectation of the researchers. Magnetite was used as a magnetic electrode in tunnel junctions [179–182], but the typical spin-polarization at low temperature was found to be around 30% which decreases very fastly with increasing temperature until at room temperature a spin-polarization of only a few percent is left. The same feature was observed by Wei et al. [183], who measured the exchange splitting and the energy gap between majority and minority spins in magnetite. At low temperature they find evidence for half-metallicity, while at room temperature the energy gap between the spin bands was not observable anymore. They discuss that this is maybe due to the Verwey transition observed at 120K. If the Verwey transition is accompanied by a order-disorder transition, the energy gap would be smeared out due to the disorder. Another intrinsic possibility for the limitation of the spin-polarization of magnetite was found by Srinitiwarawong and Gehring [184], they deduce from their calculations that due to the ferrimagnetic ordering and the hopping mechanism 60% will be the highest spin-polarization possible. Also the sign of the magnetoresistance is not totally clear. While some groups find a positive magnetoresistance [179, 180], others find a negative one [177, 181, 182, 185]. The negative spin-polarization is the expected one as band calculations [5] show that magnetite is negatively spin-polarized.

4 Experimental procedures

In this chapter the experimental procedure for the film deposition is described. Afterwards the characterization techniques are shortly introduced. In the end the lithography procedure for the fabrication of the tunnel junctions and the resistance measurements are described.

4.1 Sample preparation

The film deposition was carried out using the radio frequency (RF) sputtering technique. Basically a plasma of the material to be deposited is generated from a target and the material vapor condenses on the substrate, which is collocated in the proximity of the plasma. To generate the plasma an inert gas (usually Ar) and a DC or RF electric field is used. In the DC mode the atoms of the Ar are ionized and are accelerated by the electric field versus the target, which acts as the cathode. The bombarded target emits atoms of the material in a wide solid angle, which now travel to the substrate. In case that a dielectric material is sputtered, a DC electric field would lead to massive positive charging of the target, so that the Ar ions do not reach the target anymore. For this reason RF sputtering is used for dielectric materials, where the electric field changes so quickly that the electrons of the plasma do follow the electric field, but not the ions. The target gets charged negatively, attracting the Ar ions itself.

As the anode normally the substrate holder is used. In case of the RF technique this leads to a bombardment not only of the target, but also of the substrate. This substrate bombardment can lead to the desorption especially of volatile elements present in the film, as for instance oxygen when oxides are deposited. Thus an off-axis geometry is more convenient, where the sample bombardment is avoided by applying the RF electric field between two facing targets and placing the sample perpendicular to the target-target axis.

The typical growth rate of RF sputtering are some nm/min. To enhance the sputtering rate magnetrons are used. These are target holders which comprise a permanent magnet. The static magnetic field at the location of the target acts on the charged particles bombarding the target, so that the sputtering velocity is enhanced.

The films of this thesis were done in two different sputtering setups, one located at the ICMAB in Barcelona, the other one at the LNMH at Toulouse. The CCO films were entirely deposited at Barcelona using RF magnetrons, while the NFO films were made in Toulouse, where a face-to-face RF sputtering is available, beneath DC magnetrons for the deposition of metals. The magnetrons were not used to allow RHEED imaging.

The typical deposition process is the same for the two sputtering setups. The substrate

is introduced into the vacuum chamber and mounted on a motor, which permits moving the samples in the chamber. The deposition takes place in a vacuum chamber, because a controlled atmosphere, which is as pure as possible, permits a high reproducibility of the properties of the sample. The substrate's surface is cleaned by a preannealing at high temperature or a prolonged annealing at the deposition temperature if underlying films are present. During the annealing a presputtering of the target is carried out in order to clean the target from surface contamination and to stabilize the stoichiometric ratio of the different ions in the plasma. After the presputtering the sample is held at the deposition temperature and is collocated next to the plasma for the deposition time. The atmosphere of the chamber during the deposition consists of Ar as the sputter gas and eventually some part of oxygen for the oxidization of the film during the growth process. After the deposition the sample is moved away from the plasma and the magnetron switched off. The sample is cooled down slowly to room temperature and withdrawn from the sputtering chamber. The deposition parameters differ between the two chambers and the samples to be prepared. They will be described with more detail in the following sections.

4.1.1 Deposition of $CoCr_2O_4$

All the samples of $CoCr_2O_4$ were made in the sputtering chamber of the ICMAB in Barcelona.

Deposition chamber

In Figure 4.1 a schematic drawing of the chamber is shown. The front window is a flange which can be opened, there the sample is introduced. The sample is mounted on $2mm$ thick Ni plate, which can be mounted on top of the heater. The heater itself is mounted on a step motor, which permits to move the sample between different horizontal positions in the chamber. The heater is a Khantal (a Fe-Cr alloy) wire or a commercial thermocoax heater, the substrate temperature is measured by a thermocouple inside the Ni plate. The substrate temperature is regulated by a PID controller with the substrate temperature as the feedback.

Up to four magnetrons can be mounted in this chamber. The magnetrons are Minimax guns from US Gun for a target diameter of $1.3inch$. They work with a self-regulating Hüttinger RF source, where the RF power is fixed and regulated with the bias voltage of the source.

The CCO target was made by solid state reaction mixing CoO and Cr_2O_3 in the stoichiometric amounts, involving three to four grinding and subsequent pressing and firing steps. The spinel structure of the target was proven by X-Ray diffraction, no other Cobalt or chromium oxides were found. The magnetic characterization shows bulk behavior. The targets are glued on a thin copper plate with a metallic ring on the back. The target is held in place by the static magnetic field of the magnetron.

The base vacuum before deposition is better than $1 \cdot 10^{-6} torr$. The pumps are a Alcatel turbopump connected to a prepump. The pressure is detected by three different

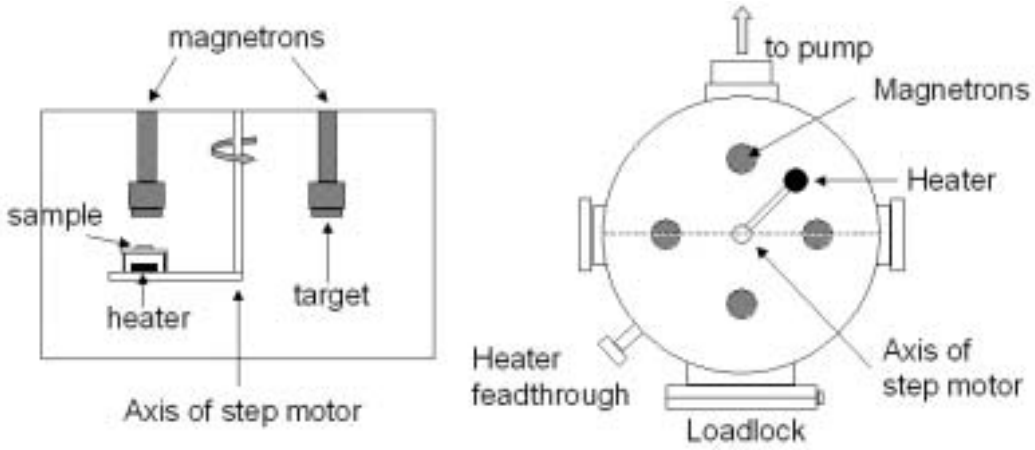

Figure 4.1: Schematic representation of the sputtering chamber at the ICMAB. The left panel shows a vertical cut of the chamber at a position indicated by the dashed line in the right panel.

pressure gauges. For atmospherical pressure down to $10^{-3}torr$ a Pirani gauge is used. For pressures between $1torr$ and $10^{-3}torr$, as well as for regulating the deposition atmosphere a Baratron gauge is attached. For the high vacuum a Penning gauge is installed, measuring in a range from $10^{-3}torr$ down to $10^{-10}torr$. N_2, Ar and O_2 can be introduced into the chamber, where the first is used to vent the chamber, while the latter two are used for the deposition atmosphere. The deposition pressure is regulated by two mass flow controller (for Ar and O_2, the latter one connected with a electric valve to permit a massive inflow of the gas) and the rotation velocity of the turbo pump.

The chamber is computer controlled. The substrate temperature, gas flow, pump speed and the motor are controlled via a LabView interface. This makes it possible to reproduce very well the deposition conditions as well as the monitoring and control of the major deposition parameters all along the deposition. During the deposition run a log-file is created, where the time, the pump speed, the temperature and the pressure is listed. For further details on the chamber and the controlling software, see [186].

CCO single films

For the single CCO films commercial one side polished $MgAl_2O_4(001)$ and MgO(001) substrates from the company CrysTec were used with the dimensions $5x5x0.5mm^3$. The substrates were cleaned in an ultrasonic bath with acetone, ethanol and water and afterwards sticked with silver paste on the Ni plate of the heater and dried in an oven at $100°C$ for at least four hours.

After introducing the substrate into the chamber, the chamber is pumped until a pressure better than $1 \cdot 10^{-6}torr$. The substrate is placed at 45° from the sputtering target. The chamber is pumped at the lowest pressure during 20min, afterwards the substrate is heated to the deposition temperature between 450 and $800°C$ in vacuum

with a speed of $30°C/min$. When the substrate has reached the target temperature, the deposition atmosphere is generated in the chamber. The typical mass flow parameters $F_{Ar} = 17.5cm^3/min$ and $F_{O_2} = 4.37cm^3/min$ with a turbo speed of $9750rpm$ leads to a pressure of $240mtorr$. The composition of the atmosphere is 75% Ar and 25% O_2. After stabilizing the deposition atmosphere the magnetron is switched on with a set point of $15W$, followed by a $20min$ sputtering period with the substrate placed away from the plasma. During this time the substrate is held at the deposition temperature and placed afterwards under the magnetron to initiate the deposition process.

For a distance of $3cm$ between the substrate and the target and the before mentioned deposition atmosphere the growth rate of CCO is around $1.7nm/min$. The growth rate could not be measured exactly. Due to the rough morphology of the films for long growth times, the determination by X-Ray Reflectivity was only possible for the sample deposited during $15min$ (see Section 7.1).

After the deposition time the sample is moved away from the target. The plasma is stopped and the Ar flow set to zero. The chamber is filled with oxygen to a pressure of $300mbar$ to allow an oxidization of the sample. Directly after reaching that pressure the sample is cooled down to room temperature with a velocity of $15°C/min$.

4.1.2 Deposition of $NiFe_2O_4$

All the $NiFe_2O_4$(NFO) samples were made in Toulouse, in the sputtering chamber of the LNMH.

Deposition chamber

The chamber of the LNMH is a commercial chamber Plassys MPU 600S. In Figure 4.2 a horizontal cut through the chamber is shown. There are two face-to-face sputtering and three DC magnetrons for the metals. Each sputter source is equipped with a shutter, so that the deposition times can be controlled with an accuracy better than $1s$. The NFO target is a stoichiometric target, made by solid state reaction from NiO and Fe_2O_3 with a similar procedure like the CCO target described in previous section. The chamber is also equipped with an electron gun and a fluorescent screen to carry out Reflection High Energy Electron Diffraction (RHEED) (described in detail in Section 4.2.2).

The sample is mounted on a sample holder which can be moved vertically and horizontally and allows as well planetary rotation around the sample normal. The sample holder includes also the heater, which is a commercial thermocoax heater. A close up of the sample holder is shown in Figure 4.2. The temperature is measured by a thermocouple on the back of the plate on which the sample is fixed.

The base vacuum of the system is between $5 \cdot 10^{-9}$ and $1 \cdot 10^{-8}torr$. The chamber is equipped with a cryogenic pump with a pumping speed of $3000l/s$. The sample is introduced via a load lock so that the vacuum does not have to be broken for changing the samples. The load lock and the electron gun are pumped by a turbopump connected with a dry pump. The pressure control is carried out by a Bayard-Alper ion gauge for the base pressure. The deposition pressure is controlled by a Baratron pressure gauge.

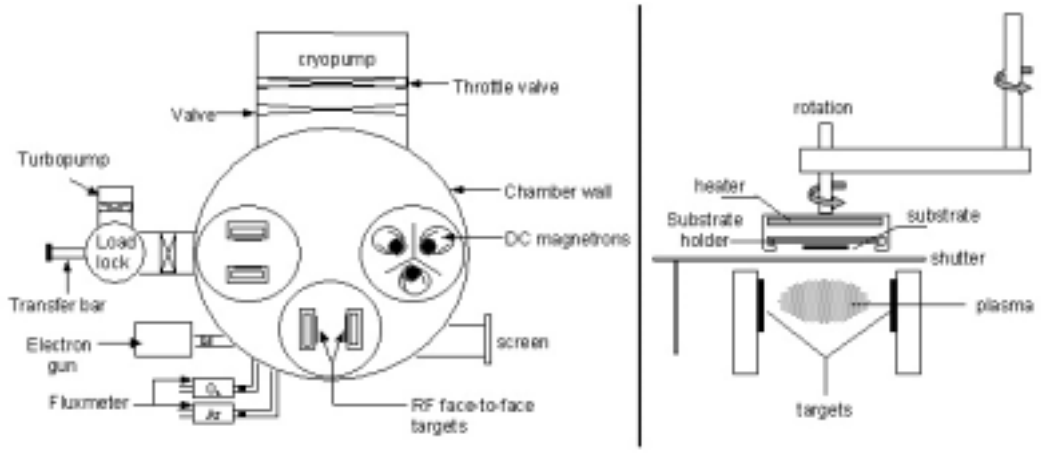

Figure 4.2: Horizontal cut through the sputtering chamber at the LNMH (left side) and a vertical cut through the substrate holder (right side).

Oxygen and Ar can be let into the chamber via a mass flow controller. Together with the throttle valve in front of the cryopump, the pressure can be controlled.

The sputtering chamber is fully automatized. All the important parameters are controlled by a computer and periodically saved in a log-file during the process.

Deposition procedure

For the preparation of NFO films, the samples are fixed on the sample holder with silver paste. The paste is dried for $15min$ on a $100°C$ plate. The sample holder is introduced into the load lock and mounted on the transfer stick. When the vacuum in the load lock is at least $1 \cdot 10^{-6}mbar$, the gate valve is opened and the sample holder transferred into the main chamber. Now the substrate is heated to $800°C$ or to the deposition temperature in case of a heterostructure. When the temperature is reached, the sample is moved to the RHEED position and patterns are collected. Now the temperature is lowered to the deposition temperature between 450 and $550°C$. Ar and O_2 are let in with a flux of $50sccm$ (standard cubic centimeter per minute) and $5sccm$, respectively, controlled by a mass flowmeter. The plasma is ignited at a high pressure, afterwards the pressure is regulated to $1 \cdot 10^{-2}mbar$. The output power of the RF source is fixed to $50W$ with a variable DC Bias. A short presputtering in the order of some minutes is carried out on the face-to-face target, before the substrate is moved on top of the plasma. The shutter is opened and the deposition time starts.

The deposition rate of NFO is around $0.2nm/min$ in a sputtering atmosphere of pure Ar and $0.075nm/min$ in a mixed Ar/O_2 atmosphere. This big difference in deposition rate for the same pressure and distance between the target and the substrate is due to the oxygen partial pressure in the plasma that absorbs a lot of free electrons and reduces the ionization of Ar. The deposition rate was determined by X-Ray reflectivity of the samples and shows a good reproducibility.

At the end of the deposition time, the shutter on top of the plasma is closed and the sample moved away. The RF source is switched off as well as the gas flows in order to reach back the chamber base pressure. The sample is moved to the RHEED place and pictures are taken with the sample being at the deposition temperature. The sample is cooled down in vacuum and afterwards removed from the chamber via the load lock.

In case of the deposition of a heterostructure the process does not change, as the underlying films are made ex-situ. They were deposited by pulsed laser deposition at the UMR Thales-CNRS-Université Paris-Sud by J.P. Contour and coworkers. For the details see [187, 188]. The only change is that the sample is heated directly to the deposition temperature and not kept at high temperature before the deposition of NFO to prevent intermixing of the underlayers.

For the deposition on Pt(001), a Pt film was deposited on a MgO(001) film. To achieve a single (001) orientation for the Pt layer, avoiding the presence of (111) crystallites, 0.5nm of $Ni_{80}Fe_{20}$ were deposited on the MgO before growing Pt [189]. Prior to deposition of the first layer, the substrates were heated in vacuum at $800°C$. The Pt film was deposited at $400°C$ by conventional on-axis DC sputtering from a $1.3inch$ target of Pt in a pure Ar atmosphere with a pressure of $0.005mbar$. The NFO films were deposited at $550°C$ in a pure Ar atmosphere.

4.2 Structural characterization

The structural characterization includes the characterization of the crystal structure, the lattice parameter, the composition of the samples, the thickness and the interface structure. X-ray diffraction is one of the basic tools of materials science, as it allows to distinguish between different phases and different orientations in the films, to determine the thickness of the film and it is non-destructive. On the other hand, at least for the surface characterization, electrons are very useful, too. By the diffraction of electrons on the surface of the sample information can be gained regarding the surface morphology (electron microscopy), the growth mode of the sample and the in-plane epitaxy (RHEED).

4.2.1 X-Ray diffraction

For X-ray measurements there exist typically two sorts of machines: the two-circle and the four-circle diffractometers. Depending on the kind of diffractometer, one can vary different angles of the sample and so one can get different information. A schematical view and the nomenclature of the angles in this thesis can be seen in Figure 4.3: θ denotes the angle of the incoming X-Ray beam and ω the one of the outgoing beam. ϕ denotes a rotation around the normal of the sample surface and ψ is a rotation around an in-plane axis of the film.

To get information about the different phases, the out-of-plane parameter c and the out-of-plane orientation of the films, θ-2θ scans in a range from 5° to 110° were made. A θ-2θ scan means that ω equals θ, so specular reflection. As the thin films are nearly

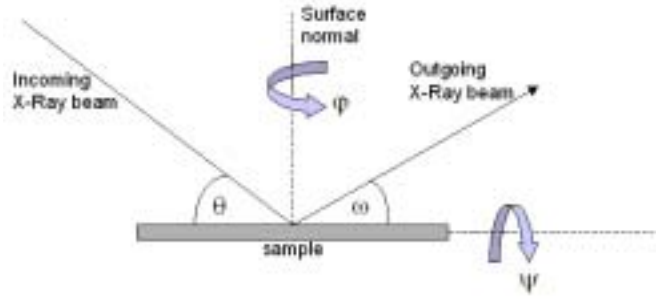

Figure 4.3: Schematic view of the different angles involved in a XRD measurement

single crystals, a possible ω-shift (due to for example a small misalignment of the sample or stress in the film) can lead to the depletion of the signal. So the angle ω was optimized by the intensity of the substrate peak or in certain cases the film peak. The θ-position of at least two film peaks was corrected by a possible θ-shift (also due to a misalignment of the sample), which was determined from the position of the substrate peaks. These corrected position were used to calculate the out-of-plane lattice parameter using the Bragg's equation:

$$2d \sin\theta = n\lambda \tag{4.1}$$

where d is the lattice plane spacing, θ is the position of the peak , n is the order of diffraction and λ is the wavelength of the X-rays.

For the spinel structure the most intense peak is the (113) peak, but as the films in this thesis were grown with a (001) out-of-plane orientation, only (00l) peaks with $l = N \cdot 4$ are visible in a θ-2θ scan. On the other hand, the lattice parameter of the spinels is around 2 times bigger than that ones of the oxides used as substrates, so that a substrate peak can be found in the vicinity of the film peaks with $1/2 \cdot l$.

The rocking curve, which is a scan in ω around the peak, gives valuable information about the orientation spread of the sample. The full width at half maximum (FWHM) $\Delta\omega$ of the rocking curve of a low indexed peak should be around 0.02° for a nearly ideal single crystalline sample (for example the substrate). For the film $\Delta\omega$ is indicative of the crystalline quality of the sample.

To examine the in-plane epitaxy ϕ-scans were carried out. Here a crystallographic axis, which is not parallel to the surface normal, was used. Having a single crystal, the peak corresponding to this direction can be found at a certain angle θ and ω depending on lattice spacing of the chosen direction, and at an angle ϕ and ψ depending on the geometry of the unit cell. Now a 360° ϕ-scan is made of the sample and the substrate. The relation between the peaks appearing for the substrate and the film shows the in-plane-epitaxy of the film. In case for example that the peaks corresponding to the same reflection are at the same positions, the unit cell of the film is oriented exactly like the unit cell of the substrate. In this case one speaks of a cube-on-cube epitaxy.

To determine the in-plane parameter a of the film two different methods can be used. One can use the θ-position of a normal-to-surface direction (to get the out-of-plane

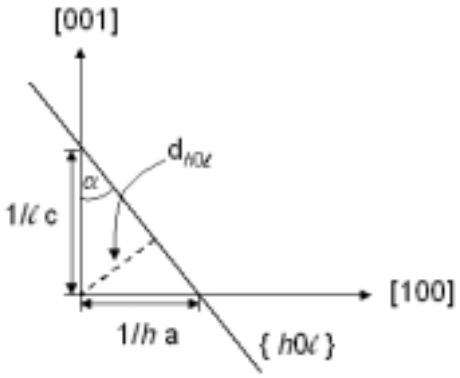

Figure 4.4: Schematic representation of the $(h0l)$ plane in a non-cubic crystal.

parameter) and combine it with the position of the peak of another direction, which includes a finite angle with the first one. For example in the case of an (001) out-of-plane oriented film, one can use the position of a $(00l)$ peak and the position of a $(h0l)$ or $(0kl)$ peak to deduce a. In case of a $(h0l)$ peak the situation in the crystal is represented in Figure 4.4: the $\{h0l\}$ plane cuts the [001] direction at $\frac{1}{l}c$ and the [100] direction at $\frac{1}{h}a$. d_{h0l}, the lattice spacing of the $\{h0l\}$ planes, forms a rectangular triangle with the [001] directions and the plane, including the angle α. This angle contains the information of the difference between a and c, as it is depending on the ratio of them. Knowing c from the position of a $(00l)$ peak, the angle α and so also a can be calculated with the following expression:

$$\sin\alpha = \frac{ld_{h0l}}{c} \Longrightarrow a = c\tan\alpha \tag{4.2}$$

To estimate the error of a, the most important factor is the error of c. The error of α will not be too important, as the tangent function around 45° has a small slope. So the error of a is estimated to be in the order of the error of c.

Another possibility of measuring a is the reciprocal space map. Here one takes a crystallographic direction with an angle to the out-of-plane direction. One can decouple ω and θ by using the equation $\theta - \psi = \omega$, as the chosen direction has an angle $\psi \neq 0$. The measurement involves a scan of a ω-θ region around the substrate and film peak. To get information about the parameters, the scan axis must be changed from θ and ω to the wave vectors parallel to the surface $Q_{||}$ and perpendicular to the surface $Q_{\perp}$ with the following relations:

$$Q_{||} \propto \sin(\theta)\sin(\theta - \omega) \tag{4.3}$$

$$Q_{\perp} \propto \sin(\theta)\cos(\theta - \omega) \tag{4.4}$$

When the measurement is represented with the two wave vectors as the coordinates, one can see immediately if the film is strained, i.e. it has the same a like the substrate. If it is so, the peak of the film will be located at the same $Q_{||}$ value like the peak of the substrate. Absolute values of a and c can be extracted from the position of the peak,

again corrected by an ω and/or θ shift deduced from the substrate peaks with

$$a = \frac{h}{Q_{||}} \tag{4.5}$$

$$c = \frac{l}{Q_{\perp}} \tag{4.6}$$

where h and l denote the Miller indices of the peak.

Another powerful tool in the X-ray family is the X-Ray reflectivity(XRR). Here a θ-2θ scan is carried out for very low angles, which is in the range of 0.5° to 7°. Using the Bragg equation these angles correspond to very high lattice spacings in the range of the layer thickness. Provided that the film has very smooth interfaces and surface, the outgoing X-rays will interfere and one can see oscillations in the intensity, which are called Kiessig fringes (see for example Figure 5.1).

The period of the oscillation corresponds to the film thickness, which can be shown by geometric considerations. The difference of the path length of the part of the beam reflected at the surface of the film and the beam reflected at the film/substrate interface is

$$\Delta l = 2d\sqrt{k^2 - \cos^2\theta} \tag{4.7}$$

where d is the thickness of the film, k the optic constant of the film and θ the angle of the incident beam. k can be expressed as

$$k = 1 - \delta - i\beta \tag{4.8}$$

δ denotes the term of refraction, while β that one of the absorption.

A maximum in the reflectivity curve corresponds to a constructive interference, thus

$$\Delta l = n\lambda \tag{4.9}$$

with n the order of diffraction of the fringe appearing at $\theta = \theta_M$, the position of the maximum. Inserting this into Equation 4.7, the following relation between d and θ_M is found:

$$\sin^2\theta_M = \frac{\lambda^2}{4d^2}n^2 + 2\delta \tag{4.10}$$

To derive d from a XRR measurement, $\sin^2\theta_M$ is plotted against n^2. The slope of the linear fit of the data is than proportional to d.

With more advanced fitting procedures, taking into account the optical density of the film material, additionally the surface and interface roughness can be calculated from the decay of the intensity. However, the involved film thicknesses must be between some ten nm to some hundred nm, otherwise the fringes are too wide or too narrow, respectively, to be properly analyzed.

The measurements shown in this work were done at different machines in Barcelona, Toulouse and Paris. All the CCO films as well as the target powder were measured at the two-circle Rigaku diffractometer located at the ICMAB. For the more detailed measurements an Philips MRD four-circle diffractometer was used located at the technical

service at the University of Barcelona. For the NFO films grown in an Ar/O_2 atmosphere the characterization was done with a Seifert four-circle diffractometer located at the CEMES in Toulouse and at a Panalytical X'pert system located at the Institut d'Electronique Fondamentale in Orsay.

All the measurements were done with the same wavelength, the Cu $K_{\alpha 1/2}$ of $0.15418nm$ [190]. The Philips MRD diffractometer used a Ni-filter to filter the K_β radiation, while the systems at Toulouse and Orsay use a monochromator, so that only $K_{\alpha 1}$ radiation is incident on the sample, so the wavelength is $0.15405nm$. These two systems are high-resolution systems.

4.2.2 Reflection high energy electron diffraction (RHEED)

The method of the RHEED relies on the wave character of the electrons. When the electrons are incident on the sample surface with a high energy between 5 and $100keV$, their wavelength is significantly smaller than the atomic distances and thus diffraction can ocurr at the sample surface for grazing incidence. The small angle of the incident electrons leads to a small penetration depth, so that the technique is surface sensitive. Due to the high energy the radius of the Ewald sphere of the electrons is very large and it intersects the reciprocal lattice in a plane instead of cutting it. This leads to smeared out diffraction points: streaks are seen on the fluorescent screen where the electrons are detected.

As the electron beam is diffracted from the lattice of the sample the distance between the streaks is a measure of a of the sample. But the calculation of absolute values is difficult and comprises normally a large error bar as the distance between the sample and the fluorescent screen is not well-defined. Due to the grazing incidence of the beam and the sample size of $1cm$, there is in a considerable difference in flight length for the electrons from the sample to the fluorescent screen (distance $30cm$). On the other hand the in-plane orientation of the sample can be very well measured. If the sample is mounted on a sample holder with a planetary rotation, the RHEED images can be taken with different azimuths. If this is done for the substrate with a known orientation of the crystal in respect to the incoming electrons, and compared with the film patterns at different azimuths, the in-plane orientation of the film can be deduced.

Due to their long free path, the incident electrons can go through a small island on the sample surface, thereby showing spots on the screen, as the diffraction becomes three dimensional, and the intensity of the outgoing beam is decreased. This feature can be used to get information on the surface morphology of the sample, as in case of a rough surface spots will appear in the diffraction image, while in case of a smooth surface streaks will be seen.

The variation of intensity of the RHEED pattern with increasing roughness is widely used to monitor the growth in-situ. In case of a layer-by-layer growth the coverage of the surface by adatoms will increase the steps on the surface and the intensity of the diffracted electron beam will decrease. When more material is deposited approaching one monolayer, the islands coalesce and the step density on the surface will go down again. So the intensity of the diffracted beam increases. During the film growth this leads to

oscillations in the diffracted beam intensity which have the period of one monolayer. Monitoring the intensity in-situ during the deposition process allows to determine very accurately the thickness of the film and the deposition can be controlled down to half a monolayer of material.

Unfortunately the electron beam needs a good vacuum to reach the sample. During the deposition with high gas pressures the electrons will be scattered before and no diffraction is visible. The maximum pressure of the LNMH chamber at which RHEED images can be captured in-situ is $5 \cdot 10^{-3} torr$, therefore in this thesis the RHEED is only used to characterize the surface morphology and the epitaxy, as the deposition pressure is $1 \cdot 10^{-2} torr$ (see Section 4.1.2). The measurements were carried out with a STAIB electron gun and an electron energy of $20 keV$. The images were taken with a $2 Mpixel$ digital camera located $0.2m$ in front of the fluorescent screen.

4.2.3 Transmission electron microscopy

Electron microscopes work exactly as their optical counterparts except that they use a focused beam of electrons instead of light to 'image' the specimen and gain information as to its structure and composition. A stream of electrons is formed by an electron source and accelerated toward the specimen using a positive electrical potential. This stream is confined and focused using metal apertures and magnetic lenses into a thin, focused, monochromatic beam, which is focused onto the sample using a magnetic lens. Interactions occurring inside the irradiated sample are affecting the electron beam, and so these interactions and effects are detected and transformed into an image.

For the transmission electron microscope (TEM) the sample is cut and polished until its thickness is only some hundred nm, so that the incoming electron beam is allowed to cross through the specimen, where the intensity of the outcoming electrons depends of the interaction between the electrons and the specimen. With TEM, information on morphology is gained, but in the case of a high resolution TEM also on crystallographic properties like lattice parameter or on atomic-scale defects.

If the microscope is also equipped with an energy detector for the outcoming electrons, Electron Energy Loss Spectroscopy (EELS) can be carried out. Here the energy of the outcoming electrons is detected and so the energy loss of them in the sample can be calculated. This loss is due to scattering effects, for instance plasmon or phonon excitations, and specific for the different elements of the sample, thus the composition of the bombarded area can be deduced.

The TEM measurements shown in this thesis were carried out by Thanh Trung Nguyen and Jean Luc Maurice from the UMR Thales-CNRS-Université Paris-Sud. The microscope is a scanning electron microscope with a spot width of $0.7nm$ and equipped with a CCD camera of 1043 x $100 pixel$ to detect the outcoming beam. The measurements were carried out with an electron voltage of $100 kV$.

4.3 Magnetic characterization

4.3.1 SQUID

The Superconducting Quantum Interference Device (SQUID) uses the Josephson effect to measure the magnetization of the sample. The device consists of a superconducting ring with two or more weak links, and the interference of the superconducting current flowing through the two halfs of the ring is used to measure the magnetic field produced by the sample. The SQUID has a high sensibility as the current has a periodic dependence on the magnitude of the applied field , with a period of variation of the quantized unit of magnetic flux Φ_0.

The measurements were carried out on a Quantumdesign MMPS system with a maximum applied field of $5T$. If not indicated differently all measurements were carried out with the following conditions: The measurements are done with the magnetic field applied in the film plane. The magnetization measurements were done heating up in temperature under an applied field of $5kOe$ to prevent effects due to an uncomplete saturation of the film. The hysteresis loops were done after zero field cooling.

The hysteresis loops showed normally a negative slope of the magnetization at high fields, due to the diamagnetic character of the substrate. This contribution was eliminated by fitting the data for fields above $3T$ with a linear fit and subtract a line with the same slope from the data. However, we cannot exclude that also a high field positive slope, for example due to spin disorder or antiphase boundaries was eliminated, too. The slope of the subtracted line was controlled to be in the range of the theoretical value for the different substrates.

4.4 Surface characterization

4.4.1 Scanning electron microscopy

The scanning electron microscope (SEM) has the same principle as the TEM, described in Section 4.2.3. In this case a focused beam of electrons is scanned over the surface and the different interactions of the beam with the surface are detected. The reflected electrons are used to image the surface, while the secondary electrons, which are electrons from the sample surface emitted after the interaction with the material, are used to investigate the homogeneity. If the SEM is equipped with a detector for x-rays, the composition of the surface can be studied as well. The incident electrons cause excitations in the sample atoms, which relax by emitting X-rays specific for the atoms.

As the thin films investigated in this thesis are insulating or semiconducting, the sample surface was metalized with a thin film of Au. The images were done on the SEM of the technical service of the Universitat de Barcelona on a Leica Cambridge Stereoscan model S-360. The electron energy is $15keV$.

4.4.2 Atomic Force Microscopy

Like all other scanning probe microscopes, the Atomic Force Microscope (AFM) uses a sharp probe moving over the surface of a sample in a raster scan. In the case of the AFM, the probe is a tip on the end of a cantilever which bends in response to the force between the tip and the sample. To measure the bend of the tip, an optical lever system is used. The beam of a laser, focused on the end of the tip, is reflected to a detector with four detection pads. The detector is capable of sub-angstrom resolution in x-, y- and z-directions. The z-axis is conventionally perpendicular to the sample.

The images in this thesis were collected with a Nanoscope III multimode AFM in the tapping mode. The cantilever is oscillated at its resonant frequency and positioned above the surface so that the interatomic forces influences the oscillations of the tip. By measuring the deviation from the resonance frequency a surface image can be calculated. One of the most important factors influencing the resolution which may be achieved with an AFM is the sharpness of the scanning tip. Tip broadening arises when the radius of curvature of the tip is comparable with, or greater than, the size of the feature trying to be imaged. As the tip scans over the specimen, the sides of the tip make contact before the apex, and the microscope begins to respond to the feature. The tips used for the imaging in this thesis have a nominal radius of less than $10nm$.

4.4.3 Resiscope

The resiscope is an AFM with a conducting tip. The image is taken in contact mode and so the surface morphology as well as the surface resistance can be monitored, when the tip is in electric contact with the film. The CTAFM located at the UMR CNRS-Thales-Université Paris-Sud is based on a Digital Instruments Nanoscope III multimode AFM. This apparatus was modified after [191] to perform local resistance measurements in the range of 100 to $10^{12}\Omega$ under a bias voltage ranging from 0.1 to 10 V, with 5% accuracy. Conductive tips are provided by Nanosensor. These tips are standard Si_3N_4 tips with spring constant ranging from 2 to 50 N/m coated by Boron-doped polycrystalline diamond. The macroscopic tip radius is about 100 nm, but the diamond crystallites induce a nanoroughness which leads to a local radius of less than $10nm$.

4.5 Magnetoresistive characterization

All magnetoresistive characterization were carried out in Orsay at the UMR Thales-CNRS-Université Paris-Sud. The two lithography processes were developed in that group before and I was kindly allowed to use the equipment and the knowledge for processing my samples.

For the transport measurements the thin films must be properly connected. As the measurements are done in the current-perpendicular-to-plane (cpp) configuration, lithography is necessary to contact the bottom electrode of the tunnel junctions. Two different definition processes were used. The first one is based on a optical lithography and leads

to junction areas in the order of some μm. To these samples will be referred with 'macro-junctions'. On the other hand a process based on nanoindentation was used, where the junction area is in the order of tens of nm. Junctions done in this way will be called 'nanojunctions'.

4.5.1 Optical lithography

The lithography process is a four step process in which first the junction pillars are defined, afterwards the shape and contacts of the bottom electrode. After the deposition of an insulating layer the top electrode is contacted. The masks allow to make 144 junctions of sizes ranging from $2\mu m^2$ to $6144\mu m^2$ on a sample of 0.7x1cm^2. For the preparation of the samples the surface is cleaned with acetone and ethanol.

- Step 1: A resist is deposited on the sample surface with a spin coater and heat-treated at $100°C$. Afterwards a mask is aligned with the sample edges and illuminated during a certain time with a fixed illumination power. The resist is developed and washed. The first mask defines the junction surface and with it the junction size, and the contact pads of the bottom electrode.

  After the resist is developed, Ar ion beam etching is carried out on the sample. The surface covered by the illuminated resist, i.e. the junction surface, is thereby protected and not etched. The etching is carried out just until the bottom electrode. The etching process is controlled by a mass spectrometer, so that the etching is stopped when elements contained in the bottom electrode emerge from the sample. Now the junction pillar is defined. In Figure 4.5 an image of the sample and a schematic view is shown.

  Now the sample surface is cleaned from the remaining resist by acetone, before proceeding with the next step.

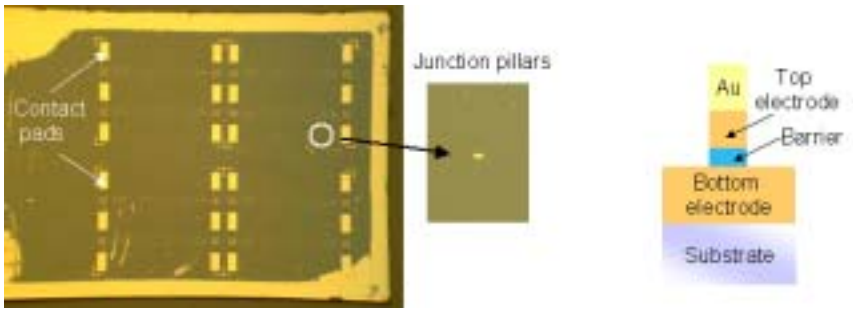

Figure 4.5: Left: Picture of a sample after the first lithography step, the large gold areas are the contact pads of the bottom electrode. Middle: Zoom on a junction pillar. Right: Schematic lateral view of the sample after the first lithography step.

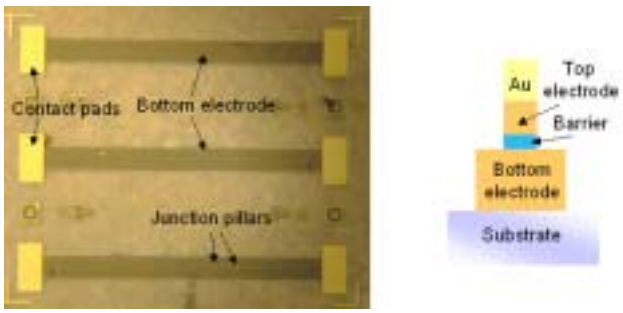

Figure 4.6: Left: Picture of a sample after the second lithography step, in the bottom bar the junction pillars can be seen very clearly. Right: Schematic lateral view of the sample after the second lithography step.

- Step 2: In step 2 the shape of the bottom electrode is defined. After depositing the resist like in step 1 without the heat treatment, the mask is aligned with the alignment marks defined in the first lithography step just on top of the predefined pattern. After illumination and development, the resist forms now bars between the contacting pads defined in the first step and covering the junction pillars. After etching, now until the substrate, 12 junction pillars are on top of one bottom electrode stripe (Figure 4.6).

  After this step all the surface is covered with insulating Si_3N_4 to avoid shortcuts between the bottom electrode and the top electrode, of which the contacting pads will be defined in the fourth lithography step.

- Step 3: After the deposition of the insulator, a hole must be made in the insulating film just on top of the junction pillar to be able to contact them (Figure 4.7) and the contacting pads for the bottom electrode must be freed again. As the junctions are very small, here the alignment process is extraordinarily important. To define the holes, the mask leaves free all the surface of the sample, just the pillars and the pads are covered. After removing the not-illuminated resist, reactive ion beam etching with SF_6 is carried out, so that only the Si_3N_4 is etched away.

- Step 4: In the last step of the lithography process the top electrode contact pads

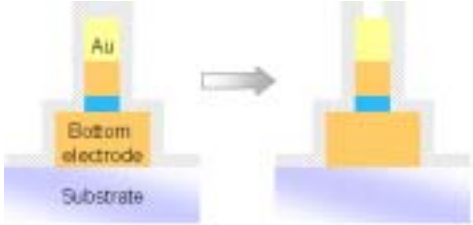

Figure 4.7: Schematic lateral view of the sample before (left) and after (right) the third lithography step.

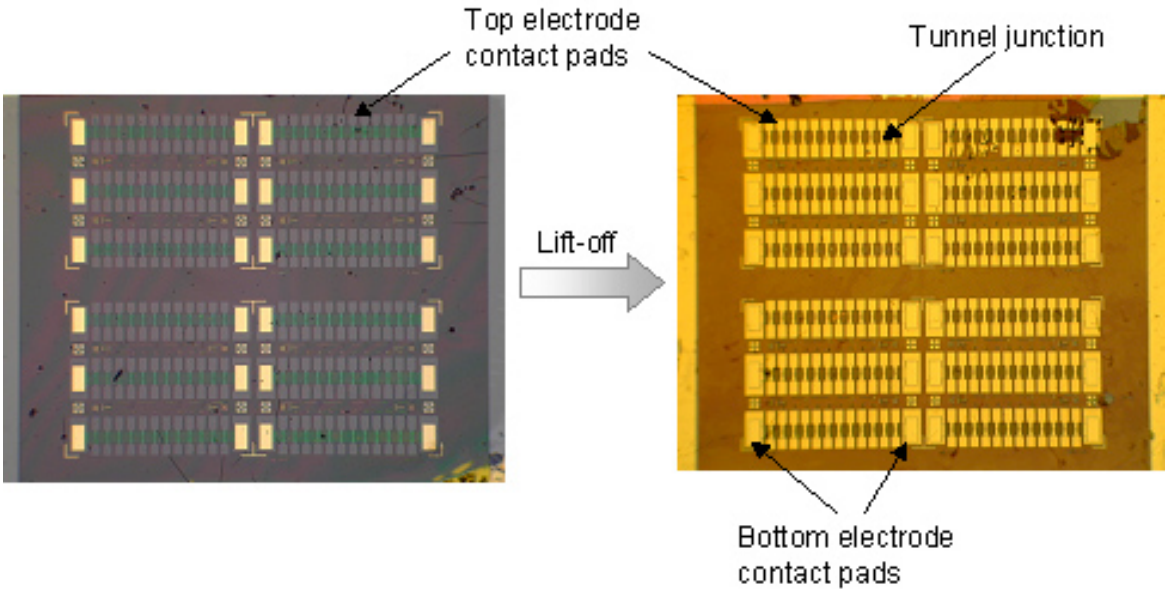

Figure 4.8: Images of the sample surface before (left) and after (right) the deposition of a Au layer and the final lift-off step.

are defined. This is done via the lift-off method, that means that the patterns are formed not by etching, but by depositing another layer on top of the resist and when the resist is released from the surface, the film only stays where there was no resist before. Therefore a mask is used which only covers the final top electrode contacts (see Figure 4.8 left side), so that after development the sample is entirely covered with resist except the top electrode contacts. On top a thin film of gold is deposited, and afterwards the resist is removed with acetone. The final sample can be seen in Figure 4.8 right side.

4.5.2 Nanoindentation

The nanoindentation is another possibility to form tunnel junctions [192]. The advantage to the optical lithography described in the last section is the very fast and easy lithography and the small junction size. This is a big advantage in case of inhomogeneous or very rough barriers. On the other hand, the small junction size makes the results extremely dependent on the local surrounding of the junction, for example grain boundaries, magnetic domain structure and local thickness, so that the reproducibility of the results is low. Another drawback of this method is that the heterostructure is only prepared until the barrier: the counterelectrode is deposited later. As the quality of the electrode-barrier interface is crucial for the magnetoresistance, a damaged surface of the barrier can influence the measurements substantially. Therefore it is important to treat the surface as soft as possible.

To make the junctions the surface resistance of the bottom electrode-barrier structure

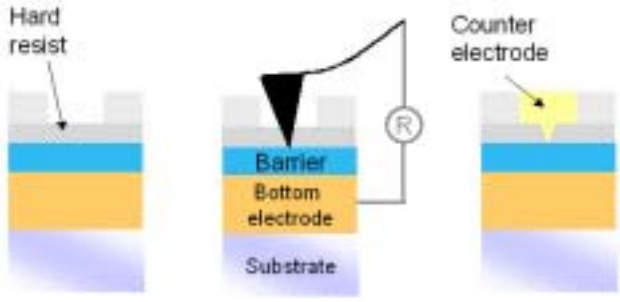

Figure 4.9: Schematic view of the indentation process: Deposition of the hard resist (left), indentation of the hole (middle) and the deposition of the counterelectrode (right).

is first measured by a resiscope scan (see Section 4.4.3). Afterwards a resist layer of around $40nm$ in thickness is spun over the surface and thermally treated. In this layer the holes to the barrier will be indented afterwards (see Figure 4.9 left side). Small squares of $30\mu m^2$ are defined on the surface into another resist layer just to mark the places of the hole.

Now the sample will be indented with the resiscope. The indentation process is controlled in-situ via the resistance between the tip and the bottom electrode (Figure 4.9 middle). When there is some resist between the tip and the barrier the resistance measurement is saturated as the resist has a high resistance. The tip is indented until the before measured resistance of the bilayer is reached. Like this the depth of the hole can be very well controlled as the resistance will rapidly decay if the tip has indented until the electrode.

When the hole is made, it will be widened with a short oxygen plasma to some $20nm$ in diameter at the barrier surface. This is the junction width. Afterwards Au as the counterelectrode material will be deposited by sputtering. Now the junctions are protected with a spot of silver paste on top and the remaining top electrode material between the junctions is etched with the ion beam etching, until the junctions are isolated from each other.

4.5.3 Transport measurements

The transport measurements are carried out with a Keithley electrometer for the nanojunctions and a Keithley 2400 for the macrojunctions, as the resistance is different due to the different junction area. For the nanojunctions only a two point measurement is possible due to the geometry of the junction. The junction's resistance was typically some tens of $M\Omega$, thus the measured current was in the range of nA. In case of the macrojunctions they are measured with the four point method. The resistance is typically in the range of some hundred $k\Omega$, resulting in a current of mA. The set-up is also equipped with a He cryostat which allows to go down to $4K$ and a electromagnets with a maximum field of $7kOe$. The samples are sticked into a sample holder, which allows

up to 10 contacts. The samples were contacted so that positive bias voltage corresponds to electrons tunneling from the top to the bottom electrode and vice versa.

5 Characterization of $NiFe_2O_4$ films

In the development of a heterostructure the growth of each component must be very well controlled. Even more so for heterostructures where the interplay between the different properties of the layers will be used to gain new functionalities as in magnetic tunnel junctions or spin filters. Especially for complex oxides, where the physical properties are strongly related to the structural properties and the deposition process (see Section 3.2.2), it is necessary to investigate the films carefully before integrating them into a stack with different materials.

$NiFe_2O_4$ (NFO) was chosen due to its high Curie temperature T_C of around $850K$, its insulating properties with a resistivity of $1k\Omega cm$ at room temperature [65] and the low probability of cation inversion [40]. At the same time it acts as a model system in the large group of magnetic insulators in the spinel oxide group.

To grow epitaxial NFO films, possible substrates from a structural point of view are $MgAl_2O_4$ and MgO. Although the misfit on $MgAl_2O_4$ is quite high (3.1%), the substrate is isostructural and allows thus the growth of spinel films with bulk magnetic properties (see Section 3.2.1). On the other hand, MgO is a rocksalt structure, but the low mismatch of the lattice parameter was found to promote a high crystal quality of the films. But both substrates contain Mg^{2+} ions, which are known to diffuse easily into the ferrite structure [145, 151–153]. Perovskite substrates on the other hand have a different crystal structure, thus they may provide a reduction of a possible atomic interdiffusion. Due to the high misfit[1], these substrates were not used to grow spinels until recently (see Section 3.2), but interestingly enough the films showed adequate properties. Furthermore the growth on such a substrate allows to transfer the film on manganites. Experiments with magnetite showed that Pt is also a possible template for the growth of spinels [193].

This chapter is organized in the following manner: first the growth and properties of NFO single films on STO(001) and on STO//$(La, Sr)MnO_3$(35nm)/STO(0.8nm) (001) heterostructures in an Ar/O_2 atmosphere is described. Afterwards the results for a series of films on both the bare substrate and heterostructure grown in a pure Ar atmosphere are discussed. Post-annealing experiments were carried out on the single films grown in pure Ar, described in Section 5.3. Finally, the growth of NFO films in pure Ar on Pt is described.

[1]For instance $SrTiO_3$(001) (STO) has a mismatch of 6.8% ($c_{STO} = 0.3905nm$)

5.1 $NiFe_2O_4$ grown in an Ar/O_2 atmosphere

The following series of films were made to investigate the growth and the properties of a magnetic insulator. A mixture of Ar and O_2 was chosen with 10% O_2 in order to have proper oxidation of the films.

The samples grown for this study (listed in Table 5.1) included basically a series of different deposition temperatures (T_{dep}) between 450 and 550°C with a fixed film thickness (t) of 14.3nm and 2.8nm, as well as a series of different film thickness between 3.6 and 14.3nm for a fixed deposition temperature of 550°C. Also samples on a perovskite heterostructure were made. In case of the sample NFOox-08 it was a STO(001)//$La_{2/3}Sr_{1/3}MnO_3$ (LSMO, 35nm)/STO(0.8nm) heterostructure and for the sample NFOox-09 STO(001)//LSMO(35nm). The properties of the base layers of heterostructure are described in the appendix A1-2.

The thickness of the films was measured by X-Ray Reflectivity (XRR, see Section 4.2.1). The curves of two films are shown in Figure 5.1. The θ positions of the well-defined Kiessig fringes were used to determine the film thickness as described in section 4.2.1. The $sin^2(\theta)$ plot is shown in Figure 5.1 on the right side. The slope of the fitted linear functions are $2.893(28)\times10^{-5}$ for NFOox-01 and $1.113(22)\times10^{-4}$ for NFOox-06, resulting in the thickness listed in Table 5.1. The thickness of NFOox-07 was not measured directly, but deduced from the mean deposition rate of $0.069(1)nm/min$ to be 3.6nm. As the samples were prepared with the same deposition parameters and without removing the targets the extrapolation of the thickness of other samples is possible.

Sample	Template	t (nm)	T_{dep} (°C)
NFOox-01	STO	14.3	450
NFOox-02	STO	14.3	500
NFOox-03	STO	14.3	550
NFOox-04	STO	2.8	450
NFOox-05	STO	2.8	500
NFOox-06	STO	7.3	550
NFOox-07	STO	3.6	550
NFOox-08	STO//LSMO/STO	12	450
NFOox-09	STO//LSMO	13.3	450
NFOox-10	STO//LSMO/STO	3	450
NFOox-11	STO//LSMO	3	450

Table 5.1: Table of the samples used for the investigation of the properties of $NiFe_2O_4$ films grown in an Ar/O_2 atmosphere. 'Template' denotes the growth template used for the sample (STO: $SrTiO_3$, LSMO: $La_{2/3}Sr_{1/3}MnO_3$), t the $NiFe_2O_4$ film thickness and T_{dep} the deposition temperature.

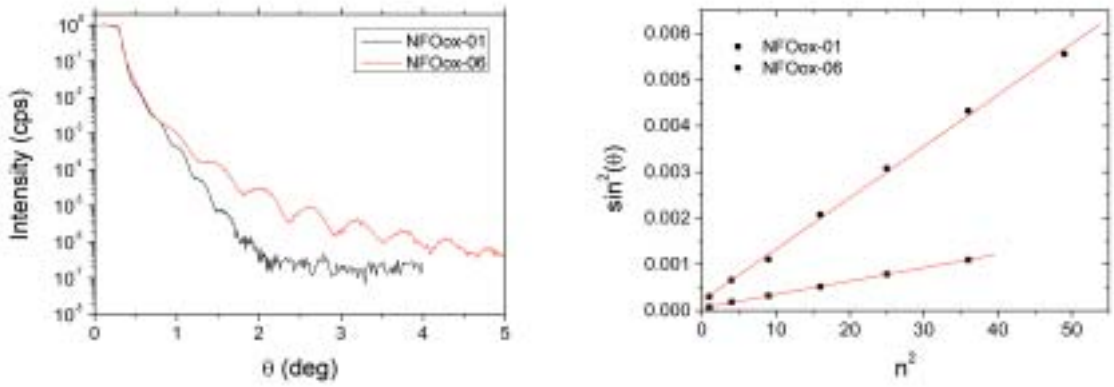

Figure 5.1: XRR curves for two NFO samples grown in an Ar/O_2 atmosphere and $sin^2(\theta)$ vs n^2 of the position of the maxima with the linear fits for the same samples.

5.1.1 Structural properties

X-ray diffraction

In Figure 5.2 a θ-2θ scan of the NFO(004) and the STO(002) reflections are shown for the samples NFOox-01 to 03 deposited at 450, 500 and 550°C and with a thickness of

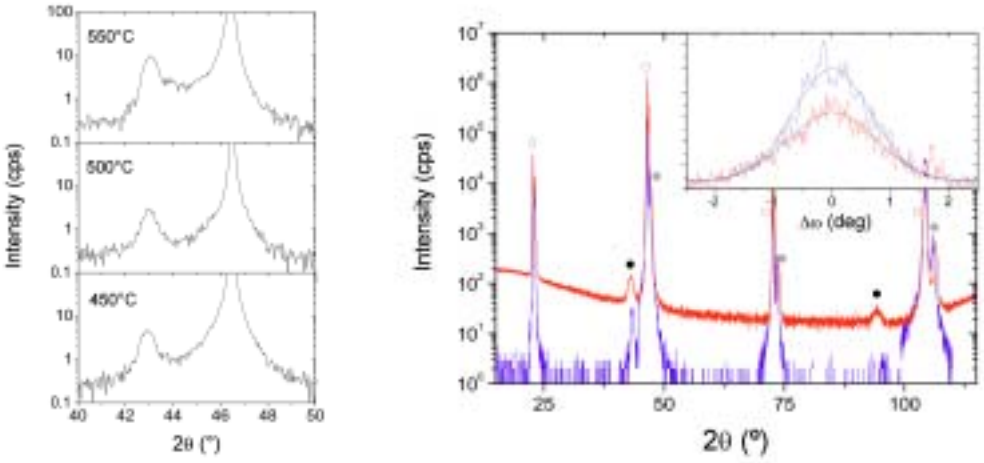

Figure 5.2: $\theta - 2\theta$ scans of single films of 14.3nm grown at three different temperatures (left side) and of a LSMO/STO/NFO (red line) and a LSMO/NFO (blue line) heterostructure (both in the right panel). The inset shows rocking curves applying the same color code. The black points indicate the reflections of NFO, the gray points of LSMO and the white points of the STO substrate.

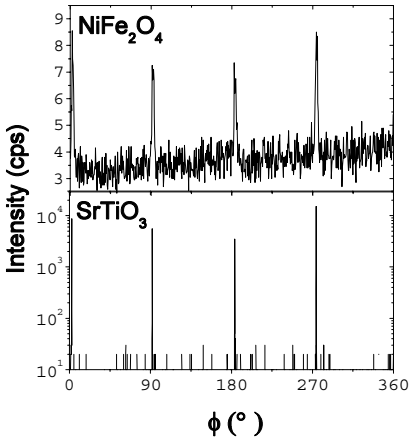

Figure 5.3: ϕ-scan of the STO(202) (bottom panel) and the NFO(404) (top panel) reflection of 14.3nm NFO grown at 550°C.

14.3nm. The measurement shows only NFO and STO (00l) reflections, thus the NFO films grows (001) textured out-of-plane as induced by the substrate. The absence of reflections, which cannot be attributed to a NFO(001) reflection, shows that the films grow single crystalline without the presence of parasite phases or differently oriented parts of the film.

The rocking curve of the NFO(004) reflection shows a $\Delta\omega$ of around 1.6°. The value for the film is high compared to typical values for epitaxial thin films, which is due to the high mismatch between the STO and the NFO. However, the values are comparable with those ones found by Suzuki et al [158] for NFO films grown directly on a STO(001) substrate, or by Venzke et al. [152] in a study on polycrystalline NFO films on STO(001).

At the right side the θ-2θ scans of a LSMO/STO/NFO and LSMO/NFO heterostructure are shown. Also here only one phase of NFO with a (001) out-of-plane texturing is detected. For the analysis of the LSMO reflections see appendix A1-2. The rocking curves shown in the inset have $\Delta\omega$ of 1.3° for the sample NFOox-08 (red line) and 1.5° for the sample NFOox-09 (blue line), thus the uniformity of the crystalline orientation is comparable to the single films. The NFO film grown on LSMO directly shows a slightly higher $\Delta\omega$, although the crystal structure and the lattice parameter of LSMO and STO is the same (see appendix A1-2).

In order to investigate the in-plane epitaxy, ϕ-scans were carried out on the STO(202) and NFO(404) reflection on the single films (see Figure 5.3). The four-fold symmetry of the ϕ-scan of the film reflects a well-oriented in-plane texture. As the reflections appear at the same ϕ-position as that ones of the STO, the orientation of the film is the same as that of the substrate, thus the film grows fully epitaxially on the STO. In the following this epitaxial relationship will be called cube-on-cube.

The out-of-plane parameters (c) were extracted from the position of the NFO(004)

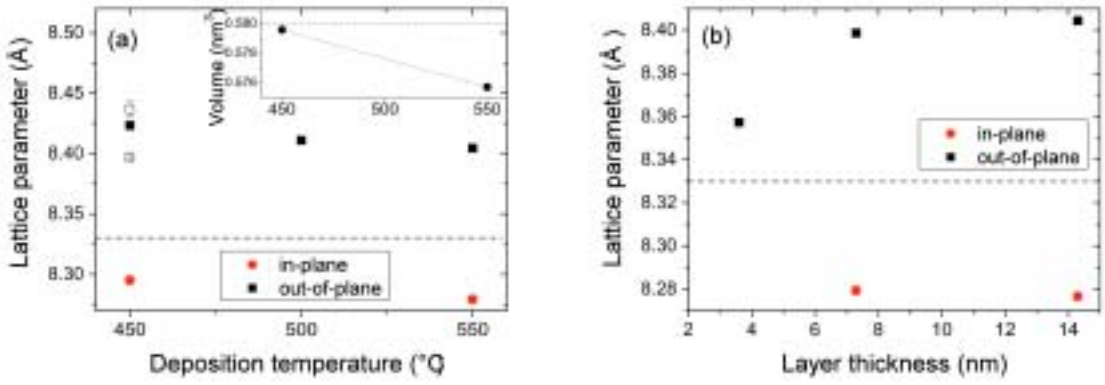

Figure 5.4: Out-of-plane and in-plane lattice parameter of samples NFOox01 to -03 (t = 14.3nm) as a function of the deposition temperature (a) and of samples NFOox06 and -07 (T_{dep} = 550°C) as a function of the film thickness (b). The open symbols in the left panel denote the values for films grown on heterostructures, the dashed line denotes the NFO bulk value.

and (008) reflection as described in Section 4.2.1. In Figure 5.4 the observed values for samples NFOox01 to -03, -06 and -07 are summarized as a function of the deposition temperature and the film thickness. For all samples they are larger than the bulk value of 0.833nm (indicated by a dashed line), including the values for the heterostructures denoted by open symbols.

The analysis of the in-plane parameter (a) was done by measuring the 2θ position of the NFO(404) reflection as described in Section 4.2.1, as the detection of reciprocal space maps was not possible. The problem arises from the doubled lattice parameter of the spinel unit cell in comparison to the perovskite unit cell. For the reciprocal space map a reflection of the substrate and the film must be found, which are intense and adjacent in the reciprocal space, so that it is possible to compare the position of the reflections. We found that for the case of a large distance of the two positions, the shift of the reflections due to the misalignment of the sample gets too important to extract reliable results. Thus the low index reflections of the spinel (like for example the (113) reflection) cannot be used as no reflection of the substrate in the same angle range can be found. Only the (*2h, 2k, 2l*) have an adjacent STO reflection, but the intensity of these reflections of the spinel is strongly reduced. Even with a careful study of the available reflections of the system, no appropriate reflection was found to collect reciprocal space maps of the NFO/STO system.

The values of a are also shown in Figure 5.4. For all samples a is smaller than c, forming a tetragonally distorted unit cell. The ratio of a over c is in the range above 0.98, so that the distortion is small. The origin is to be found in the compressive strain exerted on the film by the substrate with the smaller unit cell. To accommodate the strain at least partially, a of the film is reduced in comparison to the NFO bulk value.

The value of c is changed corresponding to the unit cell volume.

A decrease of the volume of the unit cell (see inset of Figure 5.4(a)) with increasing deposition temperature is found. At a deposition temperature of $450°C$ the unit cell volume of the film corresponds to the bulk value ($0.580nm^3$, indicated by the dashed line), but it decreases with increasing deposition temperature to a value of $0.576nm^3$, which is 1% smaller. As the oxygen partial pressure at the surface decreases with increasing deposition temperature [194], the variation of the unit cell volume is most likely connected to a change of oxygen stochiometry of the samples. This is consistent with a study carried out for polycrystalline films whose oxygen content was changed by the deposition in an Ar/O_2 atmosphere with changing oxygen partial pressure [195]. Here an increasing lattice parameter was found with increasing oxygen content.

The analysis was also done for different NFO film thickness (see Figure 5.4(b)). For a film thickness of $7.3nm$ and above the unit cell volume does not change, being somewhat smaller than the bulk unit cell volume as the deposition temperature was chosen to be $550°C$. Unfortunately it was not possible to measure a for the 3.6nm thick sample as the intensity of the NFO(404) reflection was too small. However, a decrease in c can be observed for this thickness in respect to the thicker films. If this is due to a change of the unit cell volume or a different strain state cannot be decided as a is unknown for this film.

RHEED imaging

The RHEED patterns of the samples grown in an Ar/O_2 deposition atmosphere (see Figure 5.5) show for all deposition temperatures smooth lattice streaks indicating a two dimensional growth mode of the film (see Section 4.2.2). The high number of visible

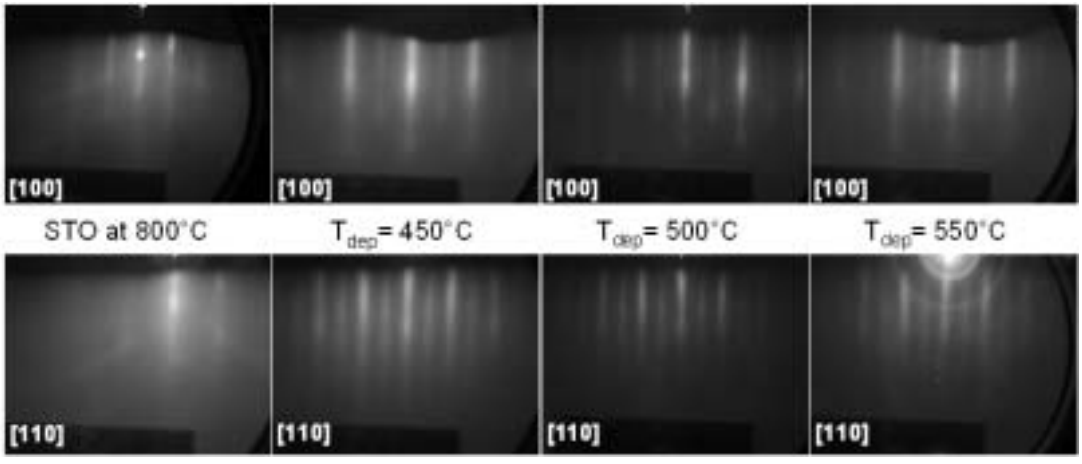

Figure 5.5: RHEED patterns for films grown at different deposition temperatures and a thickness of $14.3nm$. The first row shows the [100] azimuth, the second the [110] azimuth. The first column shows the pattern of the substrate at a temperature of $800°C$.

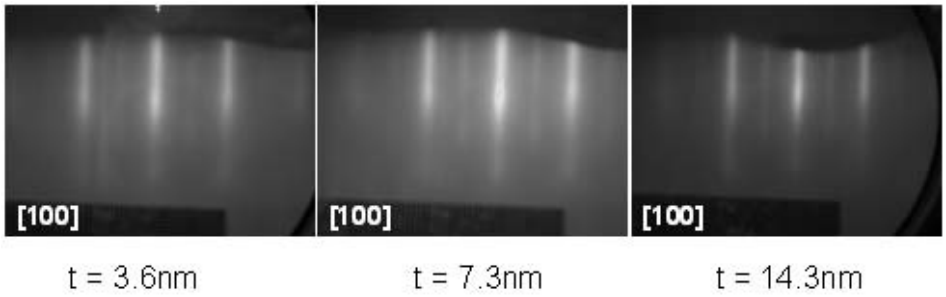

Figure 5.6: RHEED patterns for films with three different layer thickness, grown at $550°C$.

orders of diffraction reflects a smooth and well-ordered surface of the samples. A doubling of the diffraction streaks can be observed when the patterns collected of the substrate and those of the films are compared. This indicates that a unit cell with twice the size of the substrate unit cell is formed consistent with the formation of a spinel structure of the films.

To investigate the in-plane texture RHEED patterns were collected at different azimuths of the substrate and the films, namely 0° corresponding to the [100] direction of the substrate and 45° corresponding to the [110] direction. The spatial coincidence of the [100] and [110] azimuth for the film and the substrate confirms the cube-on-cube epitaxy found by X-ray diffraction.

The RHEED images for the thickness series at $550°C$ is shown in Figure 5.6. The patterns do not change with decreasing thickness, only the intensity of the additional

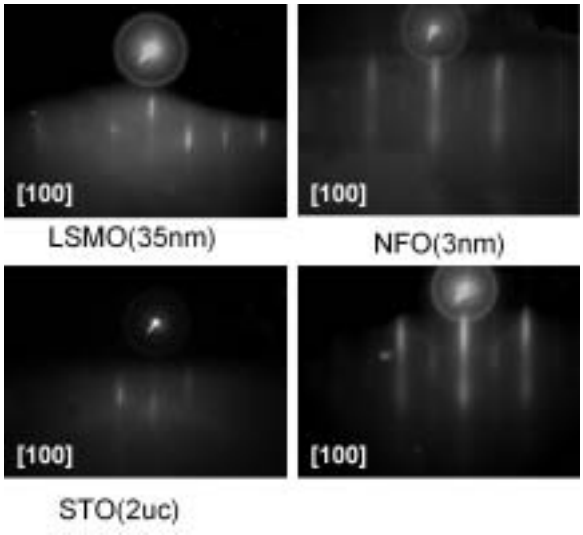

Figure 5.7: RHEED images of the surface of the LSMO (top left) and the LSMO/STO (bottom left) layers and after the deposition of a 3nm NFO film (right side).

spinel rods is decreasing. This can be understood taking into account the large unit cell of the spinel system: in the thinnest film the spinel order with $a = 0.833nm$ is disturbed, and the surface shows an order with a equal to a_{STO}, which could reflect the absence of an ionic long-range order.

RHEED images were also collected for the NFO films deposited on the heterostructures. In Figure 5.7 the patterns collected before the deposition (the left side on top for a bare LSMO film and in the bottom for a LSMO/STO bilayer) and after deposition (right side) are shown. It was observed that the RHEED images taken of the base heterostructure surface at room temperature were rather blurry, due to the covering of the surface by water, but increasing the temperature well-defined streaks appear and at the deposition temperature of $450°C$ a clean, smooth and well crystallized surface is observed as shown in Figure 5.7.

The RHEED images after the deposition of $3nm$ of NFO resemble the images taken of the single NFO films, showing well-defined spinel streaks indicating a two dimensional growth mode. Also in this case an angular coincidence of the [100] and the [110] azimuths of the substrate and the film was found, thus the NFO films grow also fully epitaxial on the heterostructures.

5.1.2 Surface morphology

The AFM images of a $3nm$ thick NFO film grown at $450°C$ (NFOox-04) and $500°C$ (NFOox-05) show a smooth surface (see Figure 5.8) as expected from the observation of two dimensional growth in the RHEED images. Wide ripples can be observed, which have a $700nm$ period for the sample grown at $450°C$ and $500nm$ for the sample grown at $500°C$. As the period of the ripples is depending on the growth temperature their origin is possibly kinetic. The rms values were calculated for a 1 x $1\mu m^2$ image, so that the ripples not contribute, and were found to be $0.5nm$ for the sample grown at $450°C$ and $0.3nm$ for the sample grown at $500°C$.

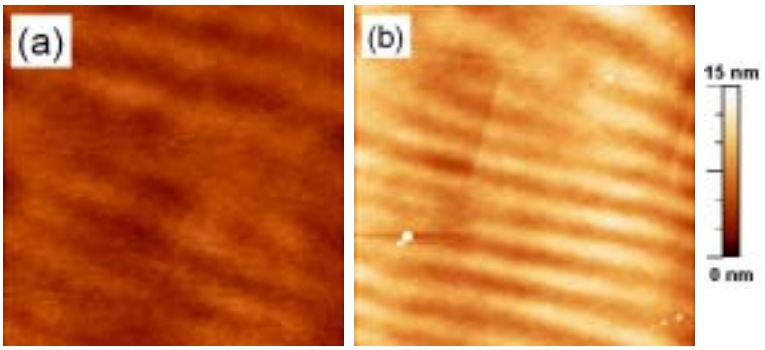

Figure 5.8: Planar view of an 5 x $5\mu m^2$ AFM image of a NFO film grown in a Ar/O_2 atmosphere at (a)$450°C$ and (b) $500°C$. The image edges correspond to the [110] directions.

5.1.3 Magnetic properties

The magnetic properties of the films were studied with SQUID magnetometry. In Figure 5.9 the hysteresis loops of the samples NFOox-03,-06 and -07 with a film thickness of $14.3nm$, $7.3nm$ and $3.6nm$, respectively, measured at 10K are summarized. A strong dependence of the magnetization on the layer thickness can be observed with increasing magnetic moment for decreasing layer thickness. Even more the magnetic moment for all the films is above the NFO bulk magnetic moment of $300emu/cm^3$.

Both of the features are in contrast to what is normally observed in thin films. In other oxide thin films the disorder and the reduced dimensions of the film lead to a magnetic moment somewhat lower than the bulk value [196], as the spins at the interface are disordered as a result of their lower coordination. This influence of the interface gets stronger with decreasing film thickness, so that normally in ferrites the magnetic moment decreases with film thickness [173]. An enhanced magnetic moment in comparison to the bulk value for NFO was already observed in nanoparticles [61] and homoepitaxial NFO films [152], but the effect observed here is more spectacular since it corresponds to an enhancement of up to 400% in comparison to 25% observed by Venzke et al [152]. Even more the effect is clearly promoted by the reduction of thickness. Several explanations can be invoked to account for our observation.

First, the large magnetic moment could be due to the presence of parasite phases. Possible candidates include Fe or Ni oxides and metallic alloys of Ni and Fe. However, no Fe or Ni oxide has a magnetic moment as large as that one which was measured for the thinner NFO films. Furthermore, XRD and RHEED (see Section 5.1.1) do not reveal the presence of parasite phases and in fact provide evidence that the largest fraction of the sample volume, if not all, corresponds to the spinel phase.

Second, one must consider Fe vacancies on A-sites as a factor resulting in an enhanced

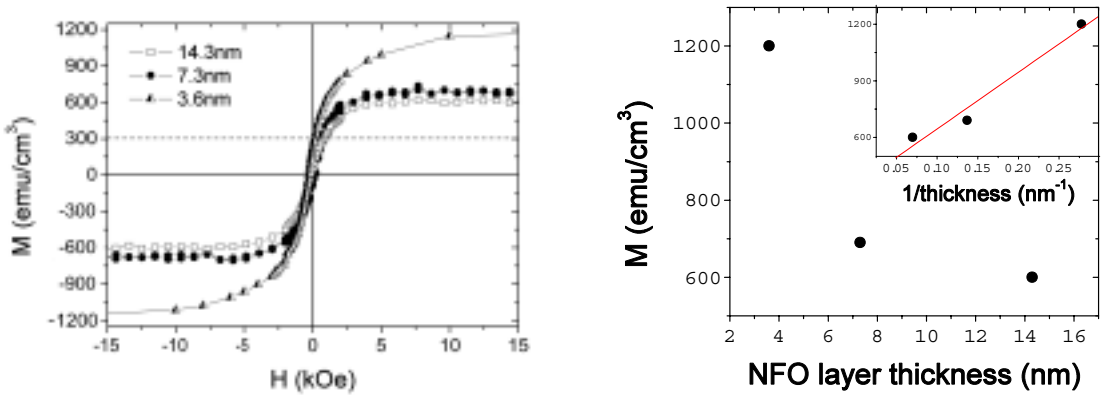

Figure 5.9: Right panel: Hysteresis loops of samples grown at $550°C$ for three different layer thicknesses. Left panel: Summary of the saturation magnetization vs. the layer thickness, in the inset: Magnetization vs reciprocal film thickness.

magnetic moment, for example in the case of a non-stoichiometry of the Fe content. Note that a concentration of 75% of Fe vacancies exclusively on the A-sites would be required to account for the observed saturation magnetization. Even though the films were grown using a stoichiometric target (see Section 4.1.2), the Fe content of the plasma can differ from this stoichiometry. XPS measurements were carried out in NFO films grown for the same deposition parameters but in a pure Ar atmosphere, and show that the Fe:Ni ratio corresponds to a stoichiometric NFO film (see Section 5.2.3), while the films show a comparable enhancement of the magnetic moment (see Section 5.2.4). Thus the formation of Fe vacancies due to a Fe deficiency can be ruled out. Even more, it was shown by Paladino [197] that neither NiO nor Fe_2O_3 can form a solid solution with NFO, so that a Fe deficiency would cause the formation of NiO, which was not detected in our films.

A third possibility could be the presence of oxygen vacancies in the films, although the films were grown in an Ar/O_2 atmosphere. In that case, the valence of some Fe ions would likely be 2+ instead of 3+, as Ni^+ is extremely improbable. In the picture of a bulk-like cationic distribution on the A and B sites and assuming that all the Fe ions situated at the A sites have a valence of 2+ with a moment of $4\mu_B$, the total magnetic moment rises to $3\mu_B/f.u.$ or $450emu/cm^3$, which is clearly not enough to explain our data.

A fourth possibility, already invoked by [152] and proved to be the origin of the elevated magnetic moment in NFO nanoparticles [61], is a change in the cation distribution. Indeed, if all the Ni^{2+} replace the Fe^{3+} at A-sites and vice-versa, ending up with an A-sublattice totally filled with Ni^{2+} and a B-sublattice fully consisting of Fe^{3+} (i.e. the normal spinel structure) the total magnetic moment increases up to $8\mu_B$/formula unit or $1200emu/cm^3$, which is the value found for the $3nm$ film. In this picture the bulk inverse spinel structure is changed to a non-equilibrium normal spinel structure in ultrathin films.

Although the energy difference between the normal and inverse spinel structure Δ is high in NFO (see Section 2.3.1), substantial levels of up to 10% of cation inversion have been reported in NFO quenched crystals [198]. This shows that in non-equilibrium conditions cations can be stabilized in energetically unfavorable sites. The films discussed here have been grown by RF sputtering and the ions in a RF plasma are usually highly energetic. Thus the material deposited onto the substrate is formed in conditions far from the thermodynamic equilibrium. As a result, one might expect Fe and Ni ions randomly distributed among the A- and B-sites, yielding a magnetic moment of $4\mu_B/f.u.$ or $600emu/cm^3$, which is very close to the value obtained for the 7.3 and $14.3nm$ films grown at $550°C$ (see Figure 5.9).

Besides, several studies on nanoparticles [61,130,199] have demonstrated that cationic inversion is promoted at surfaces. This might indicate that the value of Δ decreases at a surface and may even change sign. The magnetic moment increases as the thickness decreases with a linear dependence on the reciprocal film thickness (see inset in Figure 5.9 right side) indicating some interface effect. It can be therefore argued that the similar effect observed for nanoparticle surfaces is occurring at the STO/NFO interface, resulting in a large cationic disorder and a strongly enhanced magnetic moment.

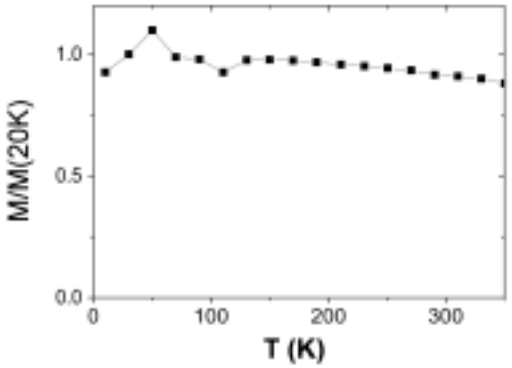

Figure 5.10: Magnetization vs temperature for a $7.3nm$ thick film.

The dependence of the magnetization on the temperature for the sample NFOox-06 ($550°C$, $7.3nm$) is shown in Figure 5.10. The magnetization stays roughly constant up to room temperature indicating a T_C far above room temperature, as expected for NFO.

The coercive field of the films showing a smaller fraction of cation inversion (i.e. 7.3 and $14.3nm$) is around $100Oe$, while the coercive field of the thinnest film is enhanced to $300Oe$. An equal variation of the coercive field was found for polycrystalline films [152]. In the cited study a small coercive field of around $100Oe$ was found for post-annealed films, which were claimed to be of good crystalline quality. An important dependence of the coercive field on the structural properties was observed for these films [152], as well as for nanoparticles due to surface spin disorder [58]. A similar mechanism can be the origin of the enhanced coercive field of the thinnest film. As here the interface has a strong influence, surface spin disorder will have an influence on the magnetic properties.

Another possibility as the origin for an induced magnetic anisotropy was proposed by Schnettler at al [200]. Theu conclude from their measurements on single crystals that the origin is a Jahn-Teller effect of Ni^{2+} ions located on A-sites. As the ion inversion is stronger for the $3nm$ film, a similar mechanism is possible.

In the case of the heterostructure, the magnetic properties of the NFO film on top of a much thicker LSMO film are difficult to measure. An estimation of the magnetic moment of a $35nm$ thick LSMO film gives a value of $10^{-4}emu$, while a $13.3nm$ thick NFO film (NFOox-09) leads to a magnetization of only $10^{-5}emu$ for the same sample size. Combined with the low remanence of the NFO films (as observed in Figure 5.9), the reversal of the NFO cannot be observed in a SQUID measurement performed on heterostructures.

The only possible way to measure the magnetization of the NFO film only is to pass the T_C of the LSMO layer. The M(T) measurement of samples NFOox-09 in Figure 5.11 shows that the T_C of the LSMO layer is around $350K$. In the right panel the hysteresis loops of the same sample for different temperatures are shown. In the hysteresis loops below $350K$, the reversal of the NFO cannot be observed, while for the hysteresis loop at

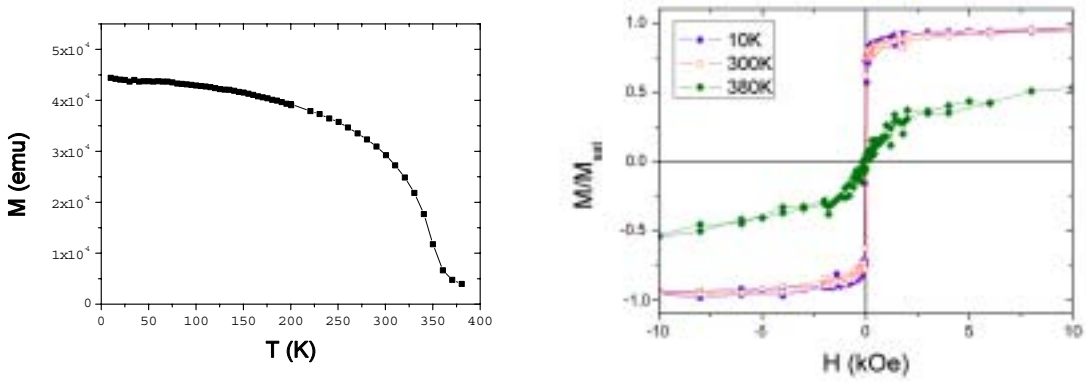

Figure 5.11: Magnetization vs temperature (left panel) and M(H)/M_{sat} vs magnetic field for different temperatures (right panel) for a LSMO($35nm$)/NFO($13.3nm$) bilayer.

$380K$ the LSMO is not magnetic anymore, but the loop shows still a (small) hysteresis, indicating a NFO still magnetic at $380K$. The calculated magnetization of $300emu/cm^3$, assuming that no LSMO contribution to the measured magnetization is left at $380K$, is similar to the bulk value. The strong enhancement of the magnetic moment is thus not observed for the films grown on heterostructures, possibly due to the important thickness and the relatively low deposition temperature. The coercive field is $75Oe$ and the remanence is 5% of the saturation magnetization.

For the application of the heterostructures as tunnel spin filter, the magnetic decoupling of the LSMO and the NFO layer is an important factor. However, in the hysteresis loops no sign of a decoupling, i.e. a magnetic reversal with two different coercive fields, can be observed. On the other hand as stated before, the contribution of the NFO layer to the overall magnetic moment is so small, that it cannot be observed. No conclusion can be drawn, whether the magnetic layers are decoupled or not.

5.1.4 Electric properties

It was not possible to carry out DC transport measurements of a $12nm$ NFO film grown in an Ar/O_2 atmosphere, as the resistance of the film was too high. However, a minimum resistivity of the sample can be estimated to be $200\Omega cm$ from the maximum resistance range of the setup, which is $200M\Omega$. The bulk NFO resistivity was found to be $1k\Omega cm$ [65].

Resiscope measurements were carried out for different thicknesses of the NFO film grown on a LSMO/STO heterostructure. The resiscope pictures shown in Figure 5.12 show a strong increase of the resistance already for a film of $5nm$ comparing to the STO layer. The resistance maps show a homogeneous resistance without hot spots or pin holes. The thickness dependence of the mean resistance is summarized on the right

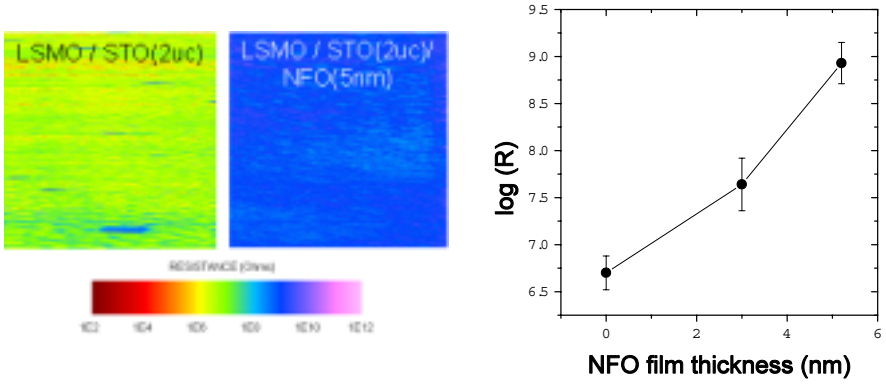

Figure 5.12: Resistance surface maps for a LSMO/STO bilayer (left) and the same LSMO/STO bilayer with $5nm$ NFO grown in an Ar/O_2 atmosphere (middle). At the right the mean resistance value is plotted vs the NFO film thickness.

of Figure 5.12, showing a exponential increase with increasing film thickness (note the logarithmic scale). For a film of $12nm$ the resiscope measurements were not possible due to a too high resistance. The exponential increase is a sign of a tunneling of the electrons through the NFO film, which is due to the insulating character of the NFO.

The surface of a NFO film grown directly on a LSMO film showed the same results. For the barrier material in the spin filter an NFO film grown in Ar/O_2 shows adequate properties, as it is insulating and magnetic.

5.2 $NiFe_2O_4$ grown in pure Ar

To investigate the influence of the oxygen content of the film on its properties, NFO films were also grown in a pure Ar atmosphere. Studies on the effect of an oxygen deficiency on the properties of spinel films or nanoparticles are scarce and concentrate on the structural properties. The only study on NFO is from Westwood et al [195], who sputtered polycrystalline NFO films in an Ar/O_2 atmosphere with different Ar/O_2 ratios. The structural properties showed an enhancement of the lattice parameter and a decrease of the saturation moment with increasing oxygen content.

For the study of thin films in a pure Ar atmosphere, films with different thickness and deposited at different temperatures were made, listed in Table 5.2. The thickness calibration was done by X-Ray Reflection, a typical curve is shown in Figure 5.13. The derived growth rate was $0.2nm/min$, thus much faster than the deposition rate in Ar/O_2 though the total deposition pressure and the RF output power were kept at the same value.

5.2.1 Structural properties

XRD measurements

The XRD studies show for all the films a single phase structure and (001) out-of-plane oriented films. In Figure 5.14 XRD spectra for samples on the bare substrate (a) and on a LSMO/STO heterostructure (b) are shown for samples with a $12nm$ layer thickness. The only peaks appearing can be identified as the STO($00l$), LSMO($00l$) and the NFO($00l$)

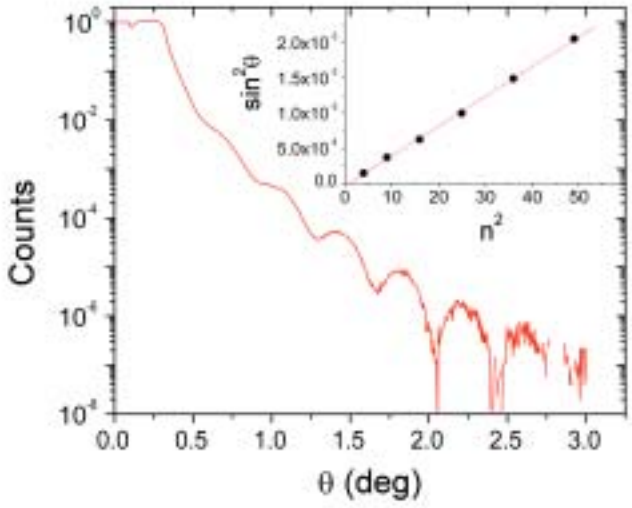

Figure 5.13: X-Ray Reflection measurement of sample NFOAr-01. The inset shows the $sin^2(\theta)$ vs n^2 of the position of the maxima with the linear fit.

Sample	Template	t (nm)	T_{dep} $(°C)$
NFOAr-01	STO	12	450
NFOAr-02	STO	12	500
NFOAr-03	STO	12	550
NFOAr-04	STO	6	550
NFOAr-05	STO	3	550
NFOAr-06	STO//LSMO/STO	12	450
NFOAr-07	STO//LSMO/STO	6	450
NFOAr-08	STO//LSMO/STO	3	450

Table 5.2: Table of the samples used for the study on the properties of $NiFe_2O_4$ films grown in a pure Ar atmosphere. 'Template' denotes the growth template used for the sample (STO: $SrTiO_3$, LSMO: $La_{2/3}Sr_{1/3}MnO_3$), t the $NiFe_2O_4$ film thickness and T_{dep} the deposition temperature.

reflections, so the out-of-plane orientation of the films is the same as the one of the substrate.

The rocking curves (a typical is shown in the inset of Figure 5.14(a)) show a con-

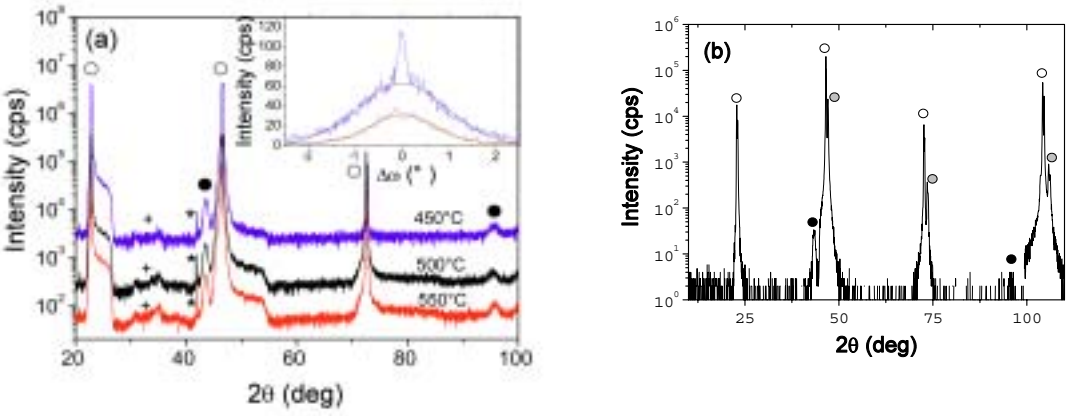

Figure 5.14: XRD $\theta - 2\theta$ scan of (a) NFO single films for different deposition temperatures and (b)LSMO/STO/NFO heterostructure. The black, gray and white points in denote the reflections of the NFO, LSMO and STO, respectively. The + denotes the substrate peaks due to the K_β rays. The peaks denoted with * appear due to the glue which was used to stick the samples on the holder. The inset in (a) shows the rocking curve of the single film (blue curve) and the heterostructure (red curve). The black lines are gaussian fits.

tribution of the substrate and the layer, the values of $\Delta\omega$ are 0.11° for the substrate and between 1.6° and 1.9° for the NFO layer (see Figure 5.15). The decrease of $\Delta\omega$ is due to the higher mobility of the adatoms on the film surface and so the crystalline quality increases. The values are comparable to that one found for the films grown in an Ar/O_2 atmosphere although the deposition rate is much faster for these films. The rocking curve of the heterostructure has a $\Delta\omega$ of 1.3°, thus the structural properties are comparable to the single films grown on STO(001), the crystal quality is even slightly increased.

To investigate the in-plane epitaxy ϕ-scans were carried out on the (202) reflection of STO and the (404) reflection of the NFO single films (Figure 5.15). The four peaks reflect the four-fold symmetry of the {110} planes for a crystal oriented (001) out-of-plane, where the position of the film peaks are the same than for substrate peaks. Thus the NFO grows with a cube-on-cube epitaxial relationship on the substrate.

The lattice parameters of the NFO layer derived from the (004) and (008) reflections of these spectra are summarized in Figure 5.15. c is slightly smaller than the bulk value for all the films. Also a is shown. The value was derived from the position of the (404) peaks using Equation (4.2). a is larger than c, so the cubic unit cell of the spinel is

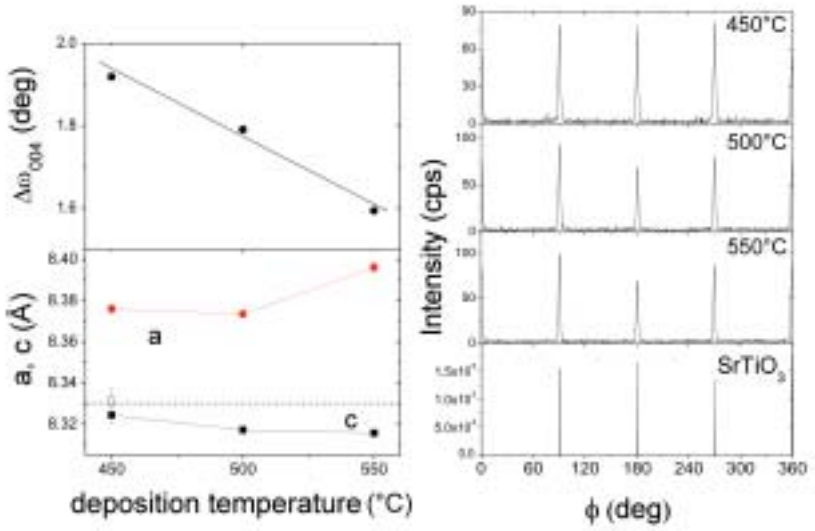

Figure 5.15: Left panel: Summary of the in-plane (a) and out-of-plane(c) lattice parameters and the FWHM of the rocking scans of the (004) NFO reflection for different deposition temperatures. The circles denote the parameters of single films, the squares of the film on a LSMO/STO heterostructure and the triangles of post-annealed single films. The dashed line indicates the NFO bulk value. The solid line is guide to the eye. Right panel: ϕ-scans of the STO(202) and the NFO(404) reflection for different deposition temperatures.

slightly tetragonally distorted. The volume of the unit cell is around 0.583 to 0.586 nm^3 and so somewhat larger than the bulk value and the value found for the films grown in an Ar/O_2 atmosphere in contrary to the expected behavior [195].

We must note that in the case of an oxygen deficiency some of the Fe^{3+} ions would be reduced to Fe^{2+} having a bigger ionic radius, thus leading to a bigger unit cell volume [201]. This is consistent with the observed higher unit cell volume and a decrease of the lattice parameter with increasing deposition temperature. The observed behavior seems to be in contradiction to the behavior of the unit cell volume of the films grown in an Ar/O_2 atmosphere. There it was found that the unit cell volume decreases with increasing deposition temperature. However, the amount of oxygen vacancies will be much lower for the films grown in Ar/O_2 than in the films grown in pure Ar. Thus in the former ones the increase of the unit cell volume due to the Fe^{2+} ions might be covered by another effect.

At this point unclear is also the change of the strain state of the unit cell. While in the case of films grown in an Ar/O_2 atmosphere $a/c < 1$ for all samples, here $a/c > 1$. This change of the geometry of the unit cell indicates a different strain state of the film. As the growth rate is substantially higher in these films, the origin can be found probably in the growth mode of the film.

In Figure 5.15 also the out-of-plane parameter of a film grown on a heterostructure is shown (indicated by the open symbol). It corresponds to the bulk value, indicating a relaxed film growth of the NFO on heterostructures. The parameter is similar to that one found for single films.

The diffraction measurements were also done for different film thickness. The (004) peak of the NFO is shown in Figure 5.16 together with the analysis of the out-of-plane

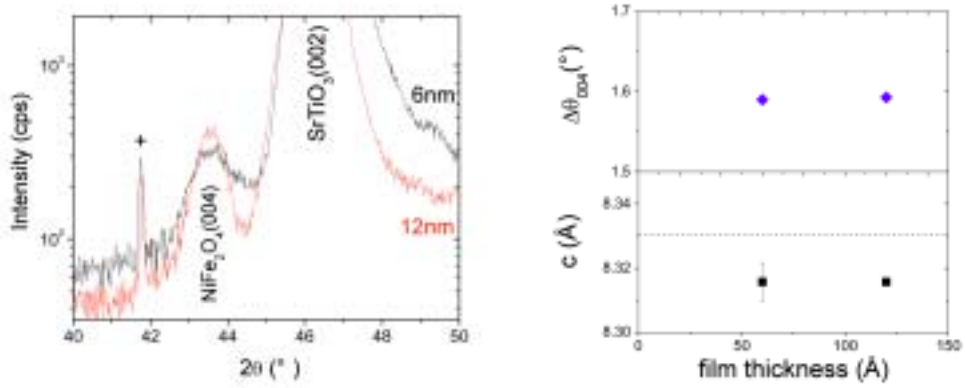

Figure 5.16: Left side: The(004) NFO peaks and the STO(002) peak in a θ-2θ scan for two different layer thickness, 6 and 12nm. The peak marked with + is the K_β reflection of the substrate. Right side: Summary of the out-of-plane lattice parameter (bottom panel) and $\Delta\omega$ (top panel) vs film thickness. The dashed line indicates the bulk value.

lattice parameter. Unfortunately for the thinnest layer of $3nm$ the reflections were too low in intensity to be visible in the spectra. However, the lattice parameter does not change with decreasing film thickness, indicating a relaxed growth also for small film thickness.

RHEED imaging

Directly after the growth of the NFO layers RHEED images were taken. A summary of the dependence on the deposition temperature for single films is shown in Figure 5.17 for a constant film thickness of $12nm$. Comparing the patterns obtained on the NFO films with the one of the substrate at $800°C$ (first column), a doubling of the lattice rods can be noticed. The change in periodicity reflects the two times bigger lattice parameter of the film consistent with the formation of a spinel structure. The RHEED pattern of the sample grown at $550°C$ corroborates this: The positions of the reflections indicate a face-centered cubic lattice.

In contrast to the samples grown in Ar/O_2 the RHEED images show spots instead of streaks reflecting a three dimensional growth mode. Regarding the shape of the reflections, at $450°C$, less-spotty lattice rods are obtained, indicative of a two dimensional growth mode. But when increasing the deposition temperature, the rods change to spots, so the films grow in a three dimensional mode.

Regarding the change of the growth mechanism, the structural peculiarities as for instance the a/c ratio > 1 of these films can be explained in terms of strain relaxation by the formation of islands (see Section 2.4.3). Due to the relaxation at the island edges the film is relaxed already at very low film thickness, although the epitaxial relationship between the substrate and the film is preserved. c corresponds to the bulk parameter, while the a is enhanced maybe due to a better fitting with the substrate.

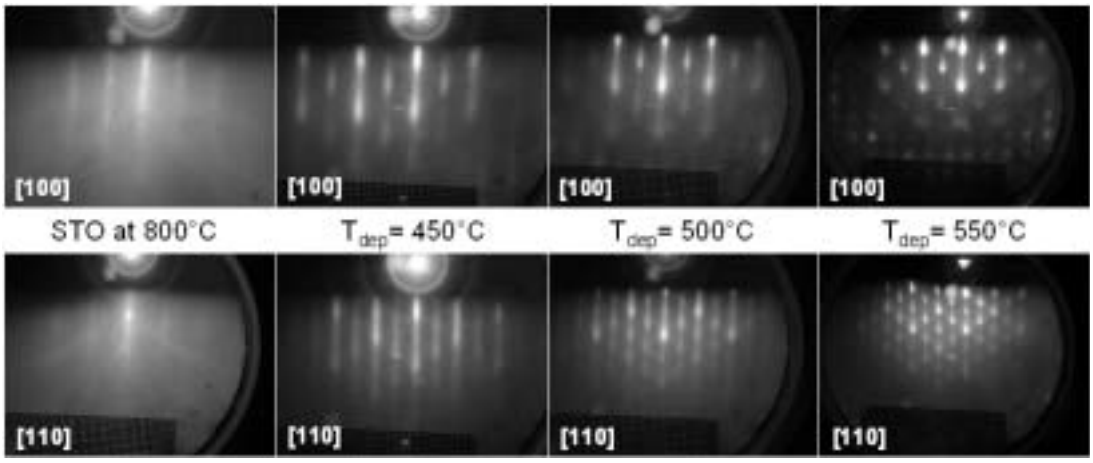

Figure 5.17: RHEED patterns for films grown at different deposition temperatures and a thickness of $12nm$. The first row shows the [100] azimuth, the second the [110] azimuth. The first column shows the pattern of the substrate.

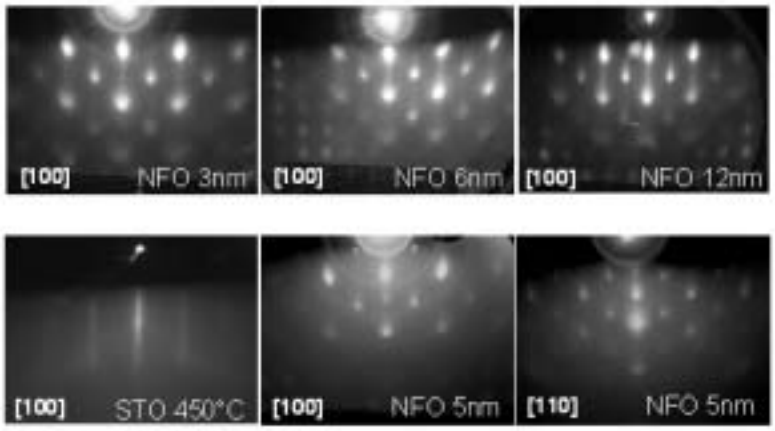

Figure 5.18: Top row: RHEED patterns for films grown at 550°C and three different layer thicknesses. Bottom row from left to right: RHEED patterns for the surface of the STO layer and a 5nm thick NFO layer along the [100] azimuth and the [110] azimuth in a LSMO/STO/NFO heterostructure, respectively.

Two azimuths are shown in Figure 5.17, the [100] located at 0° with respect to the sample edges and the [110] located at 45°. The films show reflections only at 0° and 45°, indicating that the films grow with the <110> directions oriented in the same way like in the substrate, as also observed in the XRD measurements (see Figure 5.15).

A series with samples of different thickness was prepared. The thickness was 3, 6 and 12nm at a deposition temperature of 550°C. The RHEED pictures (Figure 5.18 top row) show a three dimensional growth for all thicknesses, as well as an ordering of reflections which corresponds to a face centered cubic lattice. Even for a very low film thickness (3nm correspond to less than 4 unit cells) the doubled reflection points are clearly visible, indicating a spinel face-centered cubic lattice for this sample. This is important to note as no XRD measurement is available for this sample.

Also the NFO films grown on top of a LSMO/STO structure show a three dimensional growth of the NFO layer grown in pure Ar as observed in Figure 5.18 (bottom row). The surface of the 2 unit cell thick STO barrier is smooth, well-crystallized and clean at 450°C observed by the appearance of the well-defined streaks, which turn to points after the NFO deposition at the same temperature. The spacing of the points of half the spacing of the STO streaks confirms the spinel structure of the NFO.

5.2.2 Morphology

The impact of the three dimensional growth observed in the RHEED imaging on the morphology was investigated by AFM and TEM imaging. The growth mode results in a grain structure as can be seen in Figure 5.19, especially for the sample grown at 550°C with a peak-to-valley value of 5nm, which is nearly half of the film thickness. However, the roughness is low for low deposition temperatures, thus this temperature

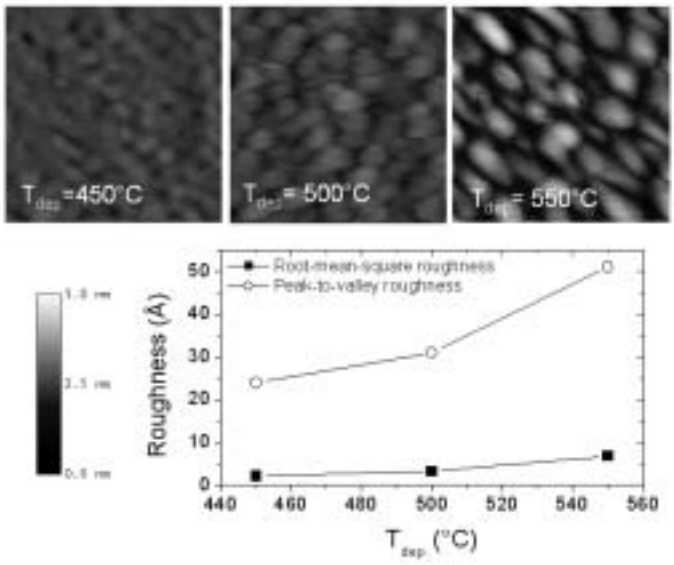

Figure 5.19: Top: AFM images (200nm x 200nm) of 12nm thick films grown at three different temperatures. Bottom: Summary of the surface rms roughness and the peak-to-valley value.

was chosen for the deposition of the NFO films on the LSMO/STO structure. The roughness increases with the deposition temperature (Figure 5.19, bottom panel), as observed already in the RHEED imaging.

AFM images were also done for different film thickness, Figure 5.20 shows the images of

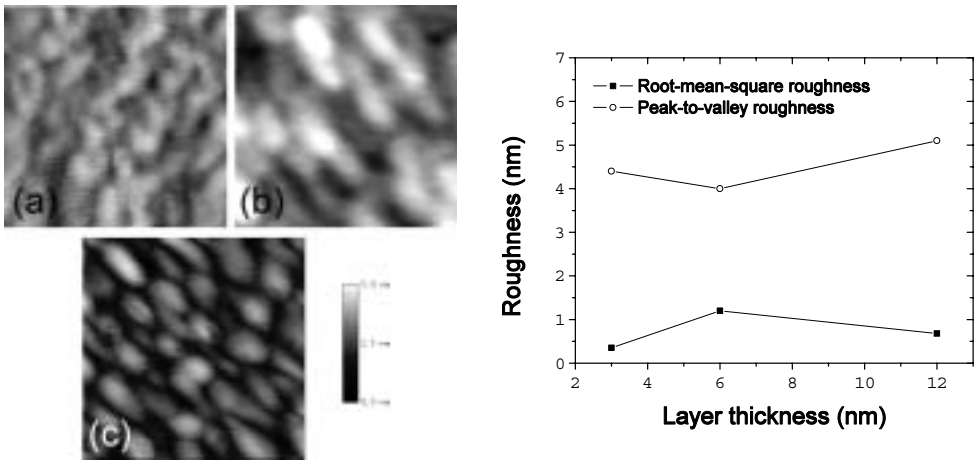

Figure 5.20: AFM images (200nm x 200nm) of a 3nm (a), 6nm (b) and 12nm (c) thick film grown at 550°C. Right: Summary of the surface rms roughness and the peak-to-valley value. The image edges correspond to the [100] directions.

NFOAr-05, -04 and -03. All films down to the thinnest one show the formation of grains, which are elongated along the [110] directions. Correspondingly the roughness of the films is high. Especially the film with nominally $3nm$ shows a peak-to-valley roughness value of $4.5nm$, which is higher than the film thickness. Thus the thickness of the film is highly inhomogeneous. The rms value and the peak-to-valley roughness stay roughly constant over all the investigated thickness range. Obviously the three dimensional grains are formed in the first stages of the growth and are overgrown homogeneously later on, without the preferred incorporation of material either in the valleys or in the hills.

To get information on the interface properties in a LSMO/STO/NFO structure with a $3nm$ NFO film (NFO-Ar08) covered by Pt, a cross-section was prepared and observed in a high-resolution TEM by J.-L. Maurice at the UMR CNRS-Thales-Université Paris-Sud at Orsay. A representative image is shown in Figure 5.21 (left). While the interface of the NFO layer with the STO is atomically smooth, the interface with the Pt is rough but continuous with a local thickness of the NFO layer ranging from 1 to about $5nm$, corroborating the high peak-to-valley roughness found in the AFM images for the single film. The in-plane interreticular spacing is $0.209nm$, which is close to 1/4 of the bulk parameter, i.e. $0.2083nm$.

5.2.3 Composition

An EELS analysis was performed on the same cross-section shown in Figure 5.21 (left) and elemental profiles crossing the interface for a representative region of the sample are shown in Figure 5.21 (right). No significant interdiffusion between the different layers is detected. The profiles for Ni, Fe and O in the NFO layer are consistent with the presence of a Fe-Ni oxide, with no evidence for metallic Ni-Fe alloys. This strongly suggests that the NFO films are single-phased, as also supported by X-ray diffraction results.

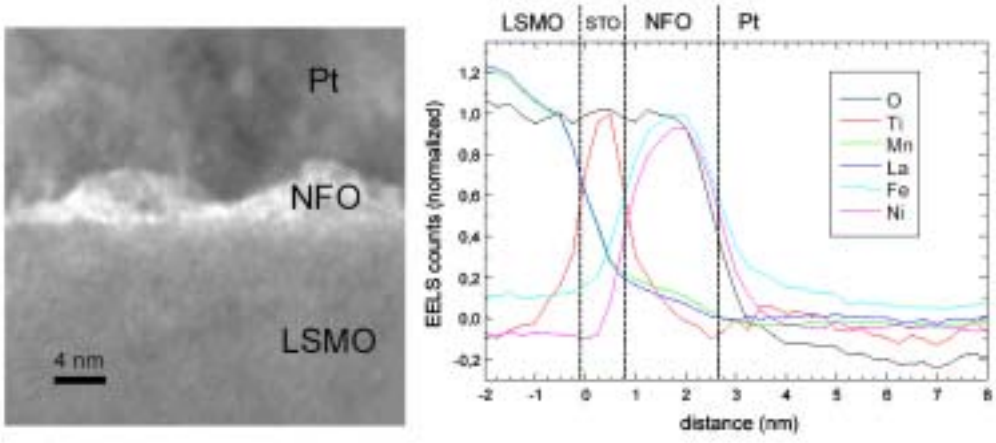

Figure 5.21: Left side: HRTEM cross section of a LSMO/STO/NFO/Pt heterostructure. Right side: EELS elemental profile across the structure.

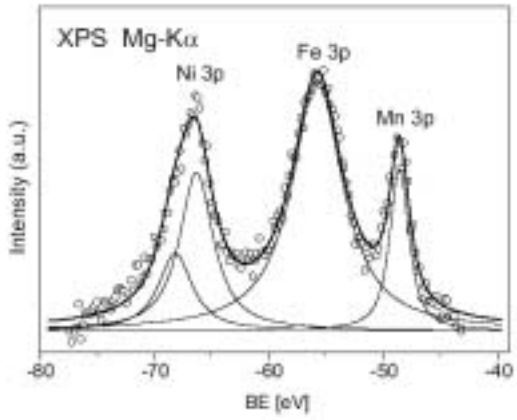

Figure 5.22: XPS spectrum of a $3nm$ thick NFO sample grown onto a LSMO/STO heterostructure in the region of Ni $3p$ and Fe $3p$. The Mn $3p$ peak arises from the LSMO underlayer.

In order to evaluate the ratio between the Ni and Fe content in the film an XPS analysis has been carried out by R. Bertacco and coworkers at the INFM and L-Ness at Como, at $10eV$ of pass energy in the region of Ni $3p$ and Fe $3p$ on a LSMO/STO/NFO($3nm$) trilayer shown in Figure 5.22. The Mn $3p$ peak, arising from the LSMO underlying film, is also visible, so that an accurate estimate of the peak area can be obtained only by means of an appropriate deconvolution, shown in the figure with continuous line. For each peak Voigt functions were used with a gaussian component taking into account the experimental resolution (FWHM of the source : $0.85eV$). For Ni $3p$ a doublet with the proper branching ratio (1.95) and spin-orbit separation ($1.85eV$) has been employed, while for Fe $3p$ and Mn $3p$ a single peak was used, due to the smaller value of spin-orbit interaction for these levels [202]. From this analysis a ratio of 0.50±0.05 between the Ni $3p$ and Fe $3p$ areas normalized to the photoemission cross sections was obtained. As the kinetic energy of photoelectrons corresponding to Ni $3p$ and Fe $3p$ peaks is essentially the same ($1182.9eV$ and $1193.5eV$) the influence of the electron escape depth and analyzer transmission on the peak intensity is also the same, so that the ratio of the areas normalized to the cross sections directly reflects the ratio between the Ni and Fe concentrations. One can then conclude that the experimental ratio between the Ni and Fe content in the investigated NFO film is in good agreement with the expected stoichiometry: $NiFe_2O_4$.

5.2.4 Magnetic properties

The magnetic properties of the films were studied with SQUID magnetometry. In Figure 5.23 the hysteresis loops of three different thicknesses of single films are summarized, measured at $10K$. Again the magnetic moment for all the films is above the NFO bulk magnetic moment of $300emu/cm^3$ and a strong dependence of the magnetization on the

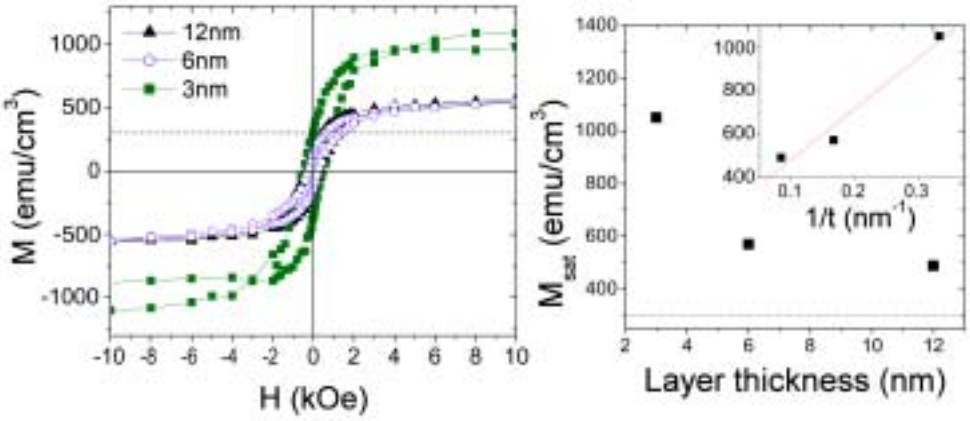

Figure 5.23: Right panel: Hysteresis loops of samples grown at 550°C for three different layer thicknesses. The dashed line indicates the magnetization of bulk NFO. Left panel: Summary of the saturation magnetization vs. the layer thickness. The inset shows the saturation magnetization vs the reciprocal layer thickness. The red line is a linear fit.

layer thickness can be observed with increasing magnetic moment for decreasing layer thickness. The inset shows the linear behavior with the reciprocal film thickness.

As the enhanced magnetic moment was already observed in the films grown in an Ar/O_2 atmosphere, the reader is refered to Section 5.1.3 for the discussion. The reason is found in a possible cation inversion between the spinel A- and B-sites. Compared with the magnetic moment in the samples grown in Ar/O_2, the values found in these films are slightly smaller. The reason can be a reduced ion inversion, thus the $3nm$ NFO film grown in pure Ar shows an ion inversion of only 88%. Another possible mechanism is the introduction of Fe^{2+} ions due to the deposition without oxygen. Here, some of the Fe^{3+} ions ($5\mu_B/ion$) are reduced to Fe^{2+} ions with only $4\mu_B/ion$, thus the total magnetic moment decreases. Assuming a total ion inversion (thus all Ni^{2+} ions on A-sites), the expected magnetic moment is $1200emu/cm^3$, but only $1050emu/ccm^3$ are measured for the $3nm$ thick film. This difference corresponds to eight Fe^{2+} ions per unit cell, thus half of the Fe^{3+} ions are reduced and the resulting molecular formula would be $NiFe_2O_{3.5}$.

Concerning the dependence of the deposition temperature (Figure 5.24), the unusual high magnetic moment is only observed for high deposition temperatures (500 and 550°C). At a deposition temperature of 450°C the saturation magnetization is slightly lower than the bulk value, as expected for a thin film. This may indicate that the origin of the formation of antisites is also influenced by the growth kinetics. The change in morphology should have only a small influence, as in the case of the samples grown in Ar/O_2 the samples show a high magnetic moment in connection with a low surface roughness.

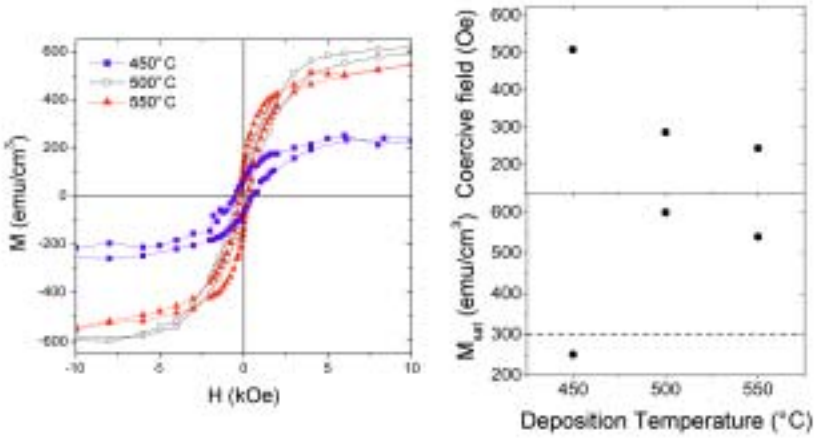

Figure 5.24: Left side: Hysteresis loops of samples grown at three different deposition temperatures for a layer thickness of $12nm$. Right side: Summary of the saturation magnetization and the coercive field vs. the deposition temperature. The dashed line in the bottom diagram indicates the magnetization of bulk NFO.

In Figure 5.25 the hysteresis loop of a $7.3nm$ thick NFO film grown in an Ar/O_2 atmosphere is compared with the loop of a $6nm$ film grown in pure Ar. The magnetization values are similar, but the shape of the loop at low field is different (see inset). The coercive field and the remanence of the film grown in an Ar/O_2 atmosphere are smaller,

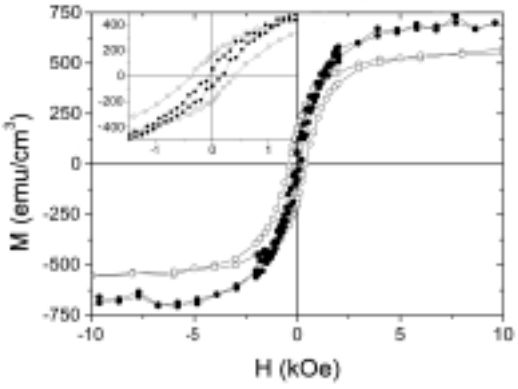

Figure 5.25: Hysteresis loops of a $6nm$ film grown in an pure Ar (NFOAr-04, open symbols) and of a $7.3nm$ film grown in an Ar/O_2 atmosphere (NFOOx-06, solid symbols). The inset shows a zoom at low applied field.

resembling the magnetization behavior of bulk NFO [58].

The influence of the deposition atmosphere is restricted to the remanence and the coercive field, the enhanced magnetic moment and its thickness dependence is not changed. Thus neither the change in the structural properties, nor the change of the growth mode or the deposition rate have a strong influence on the magnetic properties of the NFO films. However, small changes due to, for instance, the existence of Fe^{2+} or the change in the angle between the cations and the oxygen ions cannot be distinguished from a change due to a lower ion inversion.

5.2.5 Electric properties

The transport properties of the films grown in pure Ar differ very strongly from the bulk properties. The resistance of a $12nm$ thick film (NFOAr-03) was measured in an in-plane geometry, shown in Figure 5.26. It increases slowly with decreasing temperature and at around 50K the slope increases. In the plot of T/ρ vs $1000/T$ three ranges with different activation energies can be identified, one ranging from $3.4/K$ to $5/K$ ($200K$ to $295K$), a second one from $7/K$ to $26/K$ ($40K$ to $140K$) and the low temperature range for $1000/T > 37$ ($T < 30K$), approximately. Using the model of thermally activated hopping (Equation (2.33)), the activation energy for the high temperature range was found to be in the range of $65meV$ and in the middle range of $17meV$, respectively. The range for low temperature shows an activation energy of $0.4meV$.

It is well known, that the conductivity of NFO is enhanced at temperatures above room temperature due to a charge transfer mechanism (see Section 2.3.3). The activation energy was found to be $0.45eV$ [203] and the mechanism is only observed for temperatures above $500K$ [64]. As the charge transfer takes place between two B-site ions, the thermal energy of the ions must be high enough for an overlap of the wave

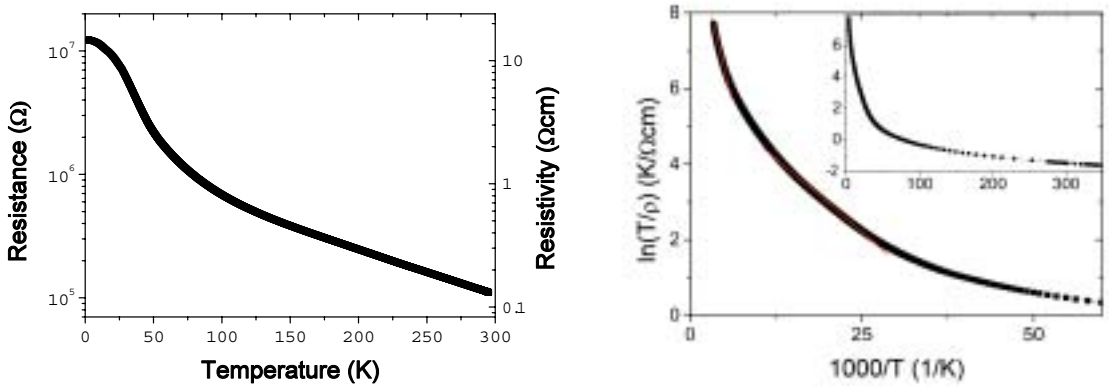

Figure 5.26: Left side: Resistance (left axis) and resistivity (right axis) vs temperature of a $12nm$ thick NFO film grown in pure Ar. Right side: Natural logarithm of T/Resistivity vs $1000/T$ of the same data. The lines are linear fits.

functions, thus the effect only appears at comparably high temperature. The temperature range measured for the films of this thesis is lower and the activation energy for the conduction mechanism was found to be an order of magnitude smaller, so that this mechanism does not hold for the enhanced conductivity of the samples grown in pure Ar.

On the other hand, the activation energy for electric transport in magnetite in the high temperature range (i.e. above the Verwey transition at $120K$) was found to be $70meV$ [204]. The conduction mechanism in magnetite is still not completely understood, but it is clear that it is a hopping mechanism of the $3d$ e_g electron of the Fe^{2+} ion, described as a polaronic transport [205]. The similarity of the activation energy with the one found for conductive NFO in this thesis suggests that a similar transport mechanism also applies for the NFO, especially because the resistivities and the crystal structures are quite similar [56]. As the conduction is found in samples grown in a pure Ar atmosphere, a possible oxygen deficiency of these films could lead to the formation of Fe^{2+} ions in a row of Fe^{3+} ions, as already discussed in connection with the enhanced unit cell volume of the films. The 'extra' $3d$ e_g electron of the Fe^{2+} ions could hop along the B-sites also in NFO and account therefore for the low resistivity.

The existence of antisites may also play a role in the electric properties. For a $12nm$ thick film the number of Ni ions on A-sites was estimated to be around 30%, so that equally the B-sites are occupied by 30% of Fe ions more than in bulk NFO. Thus a Fe^{2+} ion will have more Fe neighbors than in the bulk structure, so that the hopping of the electron is favored by the antisites. The strong rise of the resistance at $50K$ could be due to a increasing localization of the 'extra' electron. However, the rise is not comparable in amplitude with the resistance jump of several orders of magnitude observed in magnetite at the Verwey transition.

The picture of the magnetic coupling mechanism in NFO, which in the case of insulating NFO is governed by the intersite super exchange, has possibly to be modified for the conductive state, as the $3d$ electrons are the charge carriers. The enhanced resistivity in connection with the cation redistribution could result in a double exchange coupling of the mixed valence Fe ions on the B-sites and thus a ferromagnetic coupling of the Fe ions. As also in the bulk NFO spin structure the B-site ions are ferromagnetically ordered, the spin structure does not change with the double exchange mechanism.

More measurements must be done to investigate the conduction mechanism of the conductive NFO. The dependence of the resistivity on disorder in the sample, film thickness and oxygen vacancies could confirm the above described conduction mechanism. Hall-effect measurements or dynamic transport measurements could lead to more insight into the energetics of the transport and finally band structure calculations will allow to extract more knowledge about other properties of the conductive NFO.

On the heterostructures Ultraviolet Photoemission Spectroscopy measurements were carried out by R. Bertacco and coworkers at the INFM and L-NESS at Como to confirm the conducting behavior. The measured sample was a $3nm$ NFO film deposited on LSMO/STO. As the onset of the UPS spectrum from NFO is placed exactly at the Fermi level (see Figure 5.27), as determined from the edge of the Ta spectrum, the sample behaves as a conductor. Within the finite resolution of the set up ($\approx 100meV$),

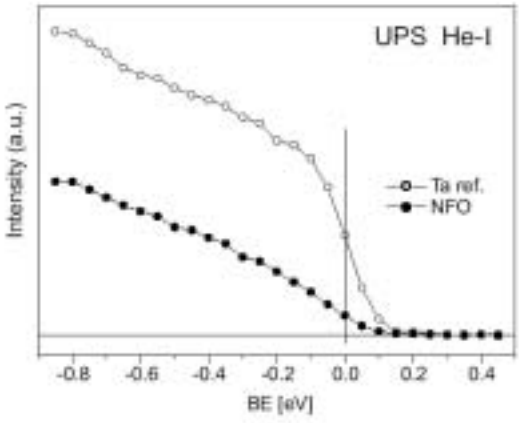

Figure 5.27: UPS spectra from the NFO sample and from a Ta foil in electrical contact with the sample.

in fact, a small but finite density of states is present at the Fermi level thus ensuring electrical conduction.

To determine the resistance behavior with different film thicknesses a resiscope study was carried out for the same heterostructures comprising the film thickness ranging from 3 to 12nm. In Figure 5.28 a resistance map of the surface of a LSMO/STO before and after the deposition of a 5nm NFO film is shown. Obviously the resistance does not change with the deposition of the NFO film, which indicates that the resistance of the STO is the governing contribution. The low resistance of the NFO is confirmed in the

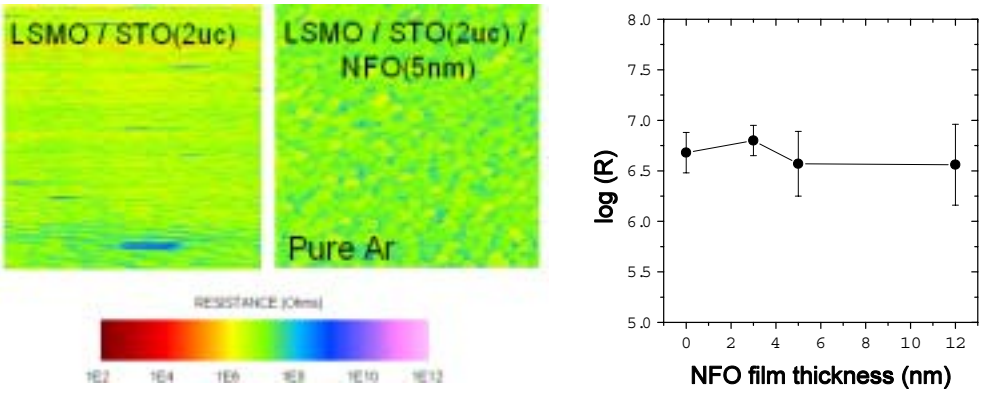

Figure 5.28: Resistance surface maps for a LSMO/STO bilayer (left) and the same LSMO/STO bilayer with 5nm NFO grown in a pure Ar atmosphere (middle). At the right the mean resistance value is plotted vs the NFO film thickness.

study of films with a different thickness (Figure 5.28): the resistance of the surface does not change with increasing layer thickness. In case that the NFO would show a sufficiently high resistance so that the electrons tunnel through the NFO layer, the surface resistance should increase exponentially with the film thickness as observed for the films grown in a Ar/O_2 atmosphere.

In summary, the NFO single films grown in a pure Ar atmosphere show also the enhanced magnetic moment, but are conducting. Thus an application as a spin filter barrier is not possible, but as the resistivity is comparable with Fe_3O_4, the integration of these NFO films as a magnetic electrode in a magnetic tunnel junction should be possible.

5.3 Postannealing experiments on $NiFe_2O_4$ films grown in pure Ar

The low resistivity of the single films grown in pure Ar is due to a possible oxygen deficiency of the films. If the films would be exposed to an atmosphere containing oxygen at an elevated temperature, an oxygen uptake of the film would be possible, so that the resistivity should raise. On the other hand, the enhanced magnetic moment of the single films of NFO was ascribed to the redistribution of the ions on the A- and B-sites. As bulk NFO shows the inverse spinel structure, the normal spinel structure of the thin films is a non-equilibrium state. Thus it should be possible to remove the non-equilibrium cation distribution by post-annealing.

To investigate the influence of a post-annealing treatment on the properties of the single films grown in a pure Ar atmosphere, the samples NFOAr-01 to -05 (see Table 5.1) were post-annealed in air at a temperature of 600 and 800°C during 1h. Parts of these samples were also post-annealed in a pure Ar atmosphere as blind samples, to investigate the influence of the possible oxygen uptake during the post-annealing in air on the magnetic properties of the films. This post-annealing was done under an Ar pressure of $1 \cdot 10^{-2} mbar$, which is the deposition pressure. The samples were post-annealed at 600°C during 1h.

5.3.1 Structural properties

XRD measurements

XRD measurements were only done on the samples post-annealed at 800°C, as the building of possible parasite phases or a change in film orientation would be the strongest in these samples. The θ-2θ scans of the samples post-annealed in air at 800°C are very similar to those of the as-grown samples. In Figure 5.29 the spectra of the sample NFOAr-01 as-grown (black line) and after the post-annealing treatment (red line) are compared. No visible parasite phase was formed during annealing.

On the other hand, the position of the reflections shifted slightly, indicating a smaller out-of-plane parameter (c). c and the in-plane parameter a are shown on the right side of Figure 5.29 for the samples of different deposition temperature as-grown (open symbols) and post-annealed in air at 800°C. Both a and c decreased during the post-annealing treatment, suggesting that the higher unit cell volume found for the as-grown films is due to a formation of Fe^{2+} ions. After the post-annealing in air the oxygen content of the films should approach the bulk content, so that the Fe^{2+} are oxidized to Fe^{3+}. Accordingly the unit cell volume decreased to around $0.580 nm^3$, which is the NFO bulk value. The post-annealing of the NFO single films leads also to a recrystallization of the films, resulting in a reduction of $\Delta\omega$ down to 1.2°.

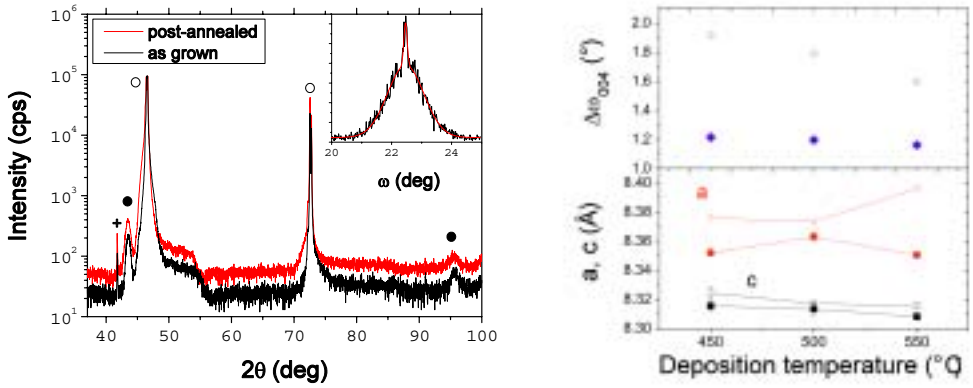

Figure 5.29: Left side: XRD θ-2θ scan of a $12nm$ NFO single film in the as-grown state (black line) and after a post-annealing treatment (red line). The black and open points in denote the reflections of the NFO and STO, respectively. The + denotes the substrate peaks due to the K_β rays. The inset shows the rocking curve of the post-annealed film, the red line is a gaussian fit. Right side: Lattice parameter (bottom panel) and $\Delta\omega$ vs deposition temperature. The solid symbols denote the values of the post-annealed films and the open symbols the values of the as-grown films.

5.3.2 Morphology

The surface morphology of the samples change strongly during the post-annealing treatment. In Figure 5.30 AFM images of sample NFOAr-05 in the as-grown state (a) and after a post-annealing at $600°C$ (b) and $800°C$ (c) are shown. As discussed in Section 5.2.2, already the as-grown film shows a high roughness. After the post-annealing at $600°C$ in both atmospheres the surface roughness increases and after the post-annealing in $800°C$ in air the formation of well-defined islands can be observed. These islands show the same features as the islands found in $CoCr_2O_4$ films on $MgAl_2O_4$ (see Section 7.1.3) and will be discussed more in detail in Section 7.2.

Tracing the roughness of the surface for the as-grown and the post-annealed samples at different temperature (Figure 5.30), a rapid increase can be observed until the peak-to-valley value is a multiple of the nominal film thickness. An important surface mass transport takes place. The three dimensional form of the islands suggests an Ehrlich-Schwoebel barrier which is smaller for upward diffusion than for downward. The driving forces of the formation of these islands are discussed in Section 7.2. The high peak-to-valley value suggests that no closed film is present, but that all the material is concentrated in isolated islands.

The island formation observed in the $3nm$ film at $800°C$ appears also for the $6nm$ film (see Figure 5.31), but not in the $12nm$ film, where smaller and less defined islands are observed. This is also reflected in the dependence of the roughness on the nominal layer

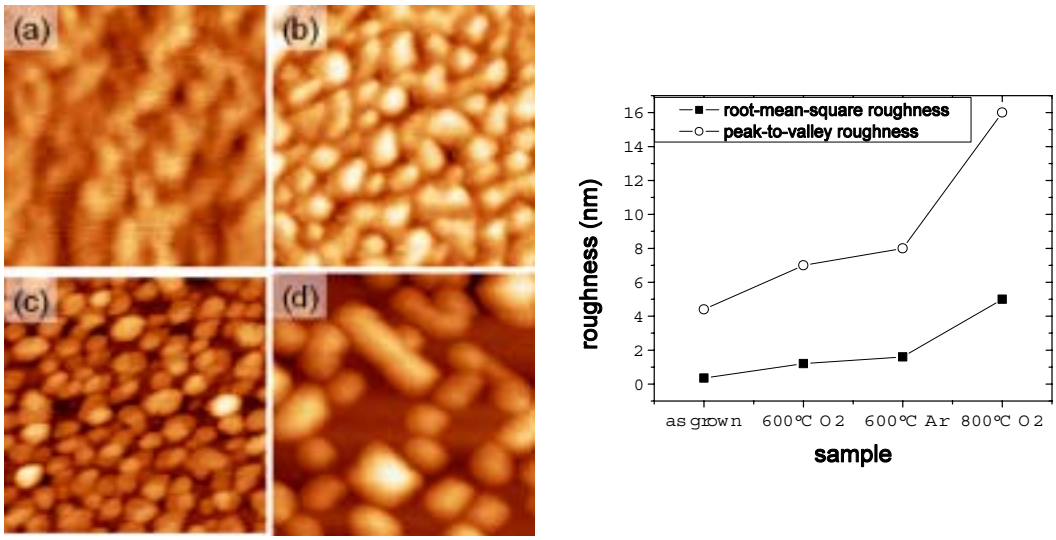

Figure 5.30: Plane view AFM images of a NFO film on STO(001) (a) in the as-grown state and after a post-annealing at (b) $600°C$ in air, (c) $600°C$ in Ar and (d) $800°C$. The size of the image is $200nm$ x $200nm$, the z-scale is $3nm$ for (a), $9nm$ for (b) and(c) and $27nm$ for (d). The edges of the images coincide with the [100] directions. Bottom panel: Roughness for the three AFM images shown on top.

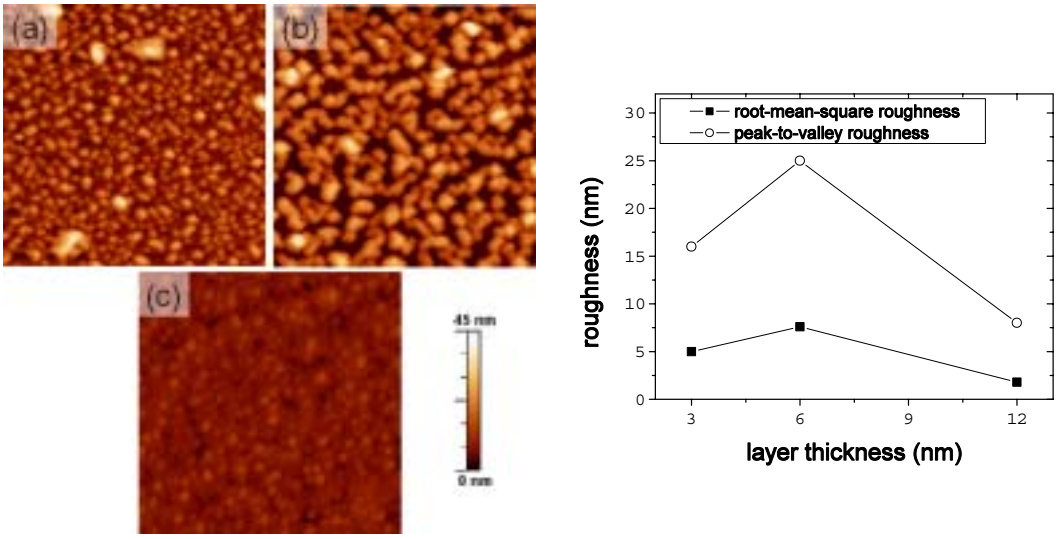

Figure 5.31: Plane view AFM images of 1 x $1\mu m^2$ of post-annealed films at $800°C$ for a thickness of (a) $3nm$, (b) $6nm$ and (c) $12nm$. The edges of the images coincide with the [100] directions. Bottom panel: Roughness vs layer thickness.

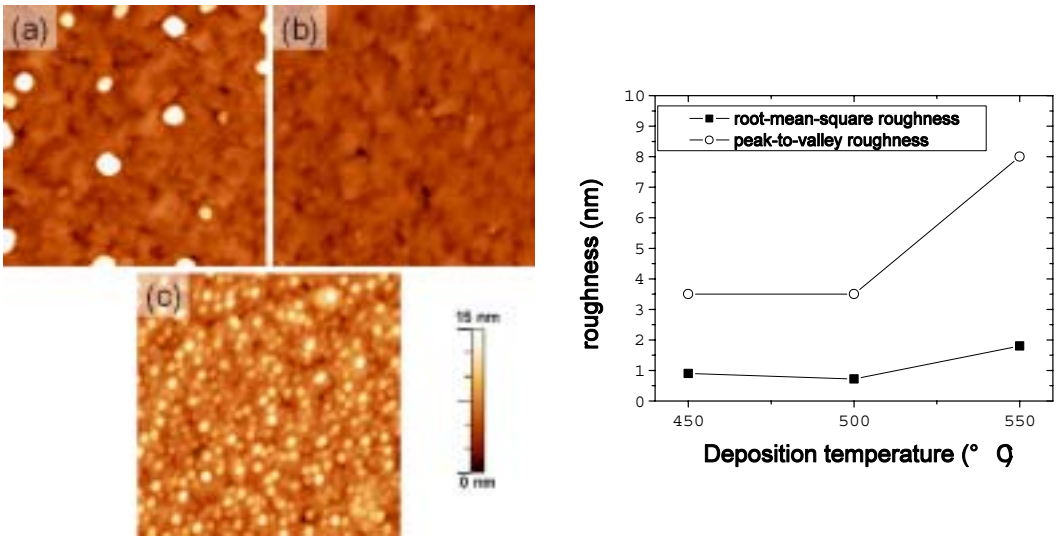

Figure 5.32: Plane view AFM images of NFO films on STO(001) deposited at (a) 450°C, (b) 500°C and (c) 550°C post-annealed at 800°C. The size of the image is 1 x 1μm^2, the edges of the images coincide with the [100] directions. Bottom panel: Roughness vs deposition temperature.

thickness: the roughness increases going from 3nm to 6nm, but decreases for the 12nm film. As stated before, an important material transport takes place in the films. On the other hand, at the relatively low temperature and the short annealing time of 1h, the transport is done preferred by surface diffusion. In the 12nm film too much material is present to be reorganised, so that only at the surface of the film the islands are formed.

AFM images of 12nm NFO films grown at three different deposition temperatures, post-annealed at 800°C in air, are shown in Figure 5.32. Here, consistent with the observation in Figure 5.31 (c), grains are formed but no islands. The surface shows a relief (best visible in picture (b), as no superimposed features are present) with a peak-to-valley value of around 2nm and a period of around 100nm. The film grown at 550°C shows an enhanced roughness due to the higher density of islands formed on the surface, but the underlying relief has the same roughness and shape as in the other 12nm thick samples.

During the post-annealing step the films recover their equilibrium surface as shown in Section 7.1.4. In case of the sample grown at 550°C the island formation is the strongest already in the as-grown film (see Figure 5.19), so that the high island density after the post-annealing step is a result of the as-grown morphology. The samples grown at lower temperature show a small density of islands, corresponding to the fact, that the as-grown surface was smoother.

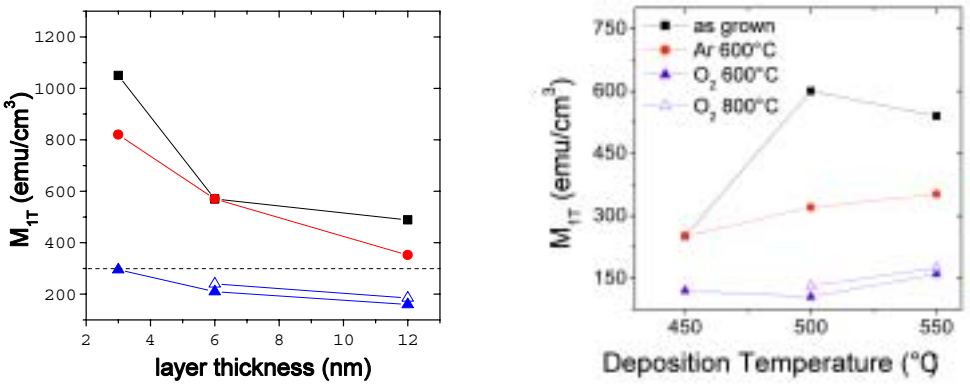

Figure 5.33: Magnetization at $10K$ vs film thickness (left side) and deposition temperature (right side) of as-grown samples (squares) and samples post-annealed in Ar (circles) and air (solid triangles) at $600°C$ and in air at at $800°C$ (open triangles). The inset of the right panel shows the magnetization vs the reciprocal film thickness.

5.3.3 Magnetic properties

The post-annealed films show a decrease of the magnetic moment in respect to the values of the as-grown films, as shown in Figure 5.33 for different film thickness (left side) and deposition temperature (right side). The magnetic moment found for the samples post-annealed in Ar are for all samples at least a factor of 2 higher than the moment of the samples post-annealed in air. While these films have a moment typically smaller than the NFO bulk value (down to half of it), the films post-annealed in Ar have a magnetic moment which is comparable to the bulk value for $12nm$ thick films. For a smaller film thickness the value is still higher than the bulk magnetic moment. Thus the post-annealing atmosphere has an effect on the evolution of the magnetic moment, although it was found that the deposition atmosphere has no influence on the magnetic moment of the as-grown films. Furthermore, the magnetic properties do not change in respect to the post-annealing temperature. The values found after a post-annealing in air at $600°C$ (solid triangles) or at $800°C$ (open triangles) are comparable.

It was found as a result of the XRD measurements, that the post-annealing in air leads to an oxygen uptake and that the unit cell volume approaches the bulk value. During a post-annealing in Ar such an oxygen uptake is not possible. On the other hand, the surface morphology is comparable after the post-annealing in the two atmospheres. So, what is the origin of the change in magnetic moment and especially the strong decrease to half the bulk-value for the samples post-annealed in air?

The first possibility to explain such a strong decrease is the redistribution of the cations towards the bulk distribution. Here, the Ni ions would change to the B-sites and, if the inverse spinel structure is reached, the bulk magnetic moment is recovered. However, the

saturation magnetization of the films with a thin film thickness post-annealed in Ar stay above the NFO bulk value, while that of the films post-annealed in air decrease to a value below the bulk magnetic moment. Thus the reduction of the saturation magnetization can be explained only in parts by a redistribution of the ions.

Second, the change in film morphology must be taken into account. In ferrite nanoparticles Kodama et al [58] showed that the magnetic structure of a particle can be described as a core with the bulk magnetic properties covered by a shell with disturbed magnetic

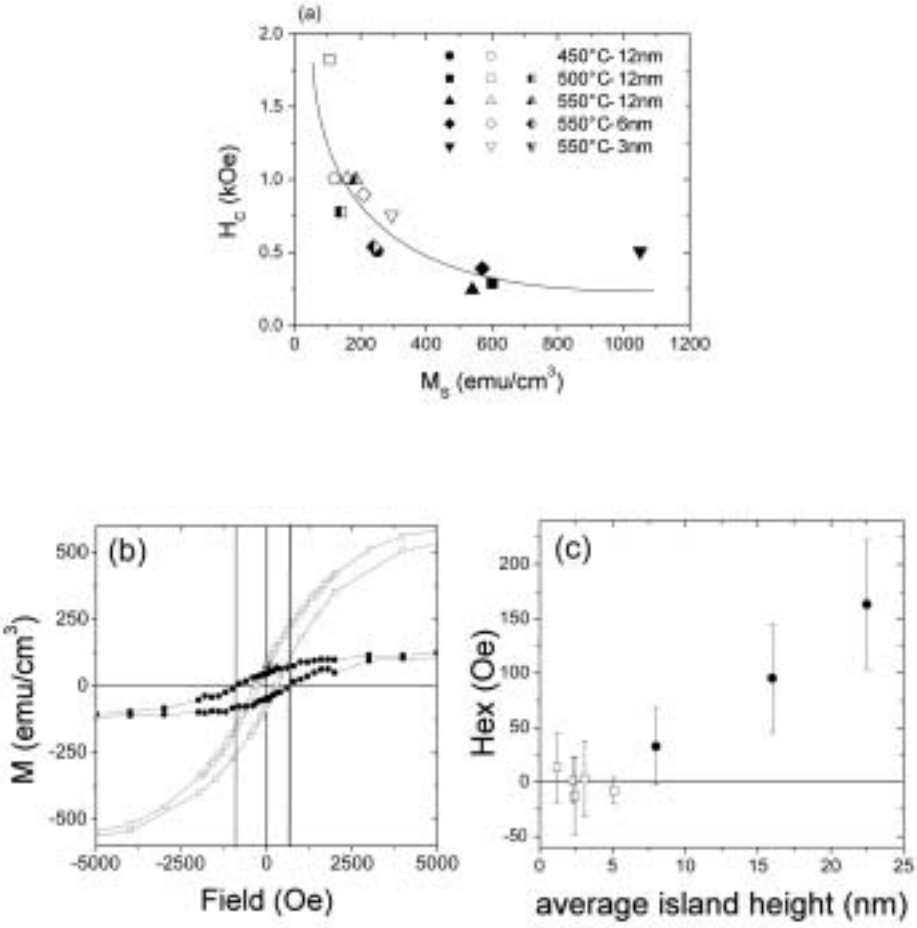

Figure 5.34: (a) Coercive field vs magnetic moment for as-grown and post-annealed films. The solid symbols denote the values found for the as-grown samples, the open for the samples post-annealed at $600°C$ in air and the half-open, half-solid symbols for the samples post-annealed in air at $800°C$. (b) Hysteresis loop at $10K$ of a $12nm$ as-grown sample (squares) and the sample post-annealed at $800°C$ in air (circles). (c) Field shift vs the average island height.

exchange coupling due to the lower coordination of the ions and the surface roughness. Numeric simulations with such a model lead to a decreased magnetic moment and a shift of the hysteresis loop along the field axis, as an exchange anisotropy is induced by the coupling of the ferrimagnetic core and the shell with a spin-glass structure.

Indeed, a strong correlation of the coercive field and the saturation magnetization was found in the films, showing a high coercive field for a low magnetic moment and vice versa (Figure 5.34a). The major part of the post-annealed samples showed even a shift of the hysteresis loop along the axis of magnetic field H_{Ex}(an example is shown in Figure 5.34b). When H_{Ex} is plotted against the average island height (Figure 5.34c) for the samples of which AFM data is available, a correlation can be found. The open symbols denote the as-grown films (NFOAr-01 to -05), while the solid symbols are extracted from NFOAr-05 post-annealed in Ar at $600°C$, NFOAr-03 post-annealed in air at 600 and $800°C$ with increasing average island height. The height of the islands on the AFM images were measured and the mean value was taken.

Thus the strong decrease of the magnetic moment can be attributed to the formation of a spin-glass state at the surface of the islands, which are formed during the post-annealing treatment. However, the difference of the evolution of the magnetic moment for the two different post-annealing atmospheres is not explained by this mechanism, as the film morphology is roughly the same for both.

The saturation magnetization of the samples post-annealed in air is reduced to approximately half the bulk value. Comparing to the samples post-annealed in Ar, the reduction of the saturation magnetization due to the island formation is in the order of 20%, suggesting that another mechanism for the decrease of the magnetic moment is present in the films post-annealed in air. As stated before (see Section 5.3.1), an oxygen uptake during the postannealing takes place. A decrease of the saturation magnetization can thus be explained by a decrease of the exchange coupling due to the oxygen uptake. The change of the geometry of the unit cell connected with the uptake is small, so that such an important decrease of the saturation magnetization seems improbable.

However, due to the interaction of an oxygen uptake, the change in crystal structure, the possible redistribution of cations and the restructuring of the film's morphology the origin of the decrease of the saturation magnetization stays unclear. More advanced measurement methods must be involved to investigate the processes in the film during the post-annealing.

5.4 $NiFe_2O_4$ grown on Pt(001) in pure Ar

The electric properties of the NFO grown in pure Ar are very interesting, but the three dimensional growth mode is a problem for the homogeneity of the film thickness and so the introduction into heterostructures. As will be discussed in Section 7.2, the three dimensional growth mode is due to the (001) out-of-plane induced growth of the film, though the {111} planes have a significant lower surface energy. This anisotropy in surface energy leads to important grain formation of the material to lower the surface energy. Ritter et al [193] showed that magnetite grows (111) oriented on Pt(001), so that NFO films were grown on a Pt(001) layer to investigate the structural and magnetic properties. The deposition procedure and parameters for these films are described in Section 4.1.2.

5.4.1 Structural properties

RHEED pictures shown in Figure 5.35 indicate that for Pt/NFO the growth mechanism is different as for the deposition on STO in pure Ar. The top images correspond to the MgO substrate with the electron beam parallel to the [100] (left) and [110] (right) direction; lattice rods and Kikuchi lines are clearly observed and reveal the flat surface of the substrate after annealing and prior to film growth. The middle images were taken at the end of the deposition of the Pt layer at a thickness of $20nm$. These RHEED patterns indicate that the Pt layer has grown in a bidimensional (Frank-van-der-Merwe) mode and cube-on-cube onto the MgO substrate. The bottom patterns were collected at the end of the deposition of the NFO layer, and are also consistent with a bidimensional growth.

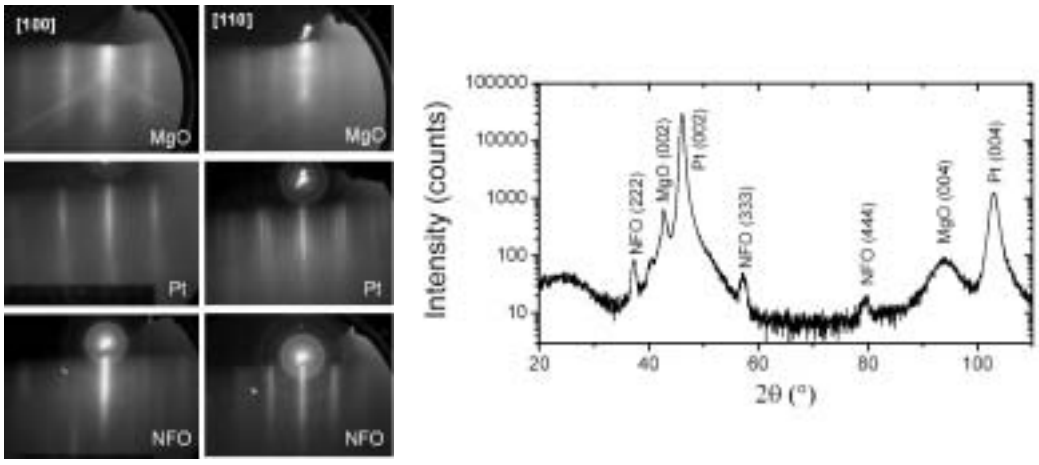

Figure 5.35: Left side: RHEED pictures of the MgO surface (upper line), the Pt surface (middle line) and the NFO surface (bottom line) of the [100] (left columm) and [110] azimuth (right column). Right side: XRD θ-2θ scan of a MgO//Pt/NFO heterostructure.

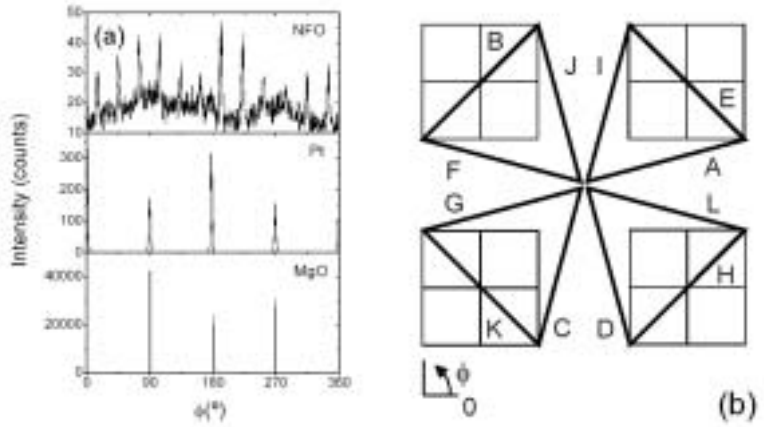

Figure 5.36: Left side: ϕ-scans of the (202) reflections of MgO (bottom panel), Pt (middle panel) and NFO (top panel). Right side: Schematic representation of the four possible orientations of the triangular mesh of the (111)-oriented NFO onto the square mesh of the (001)-oriented Pt.

At an azimuth corresponding to the [100] direction of the MgO, the RHEED pattern is quite blurry, but neat diffraction appeared at 15° off this direction, and then every 30°. The right bottom image, obtained 45° off the [100] direction of MgO (i.e. along [110] of MgO) is illustrative of this pattern. Twelve similar patterns were collected at azimuths spaced by 30°, thus indicating a twelve-fold in-plane symmetry.

Figure 5.35 and 5.36 report results from X-ray diffraction for Pt/NFO. From the θ-2θ scan (Figure 5.35) and the ϕ-scans of the (202) reflections of MgO and Pt (Figure 5.36), it is clear that the Pt grows cube-on-cube on the MgO substrate, with a (001) out-of-plane orientation. From these scans there is no indication for the presence of (111)-oriented Pt crystallites, which are often found when Pt films on (001)-MgO were gown at low temperatures and low pressure [206]. The FWHM of the (002) reflection of Pt is $\Delta\omega_{(002)}$=1.70°, in the range of what can be found in other studies (0.4° to 2.1°, depending mainly on the growth temperature) [206, 207]. The out-of-plane parameter of the Pt layer, calculated from the position of the (002) reflection, is $0.3941nm$, slightly larger than that of the bulk ($0.3923nm$).

On the $\theta - 2\theta$ scan shown in Figure 5.35, peaks that can be unambiguously attributed to (111) reflections of the NFO are also detected. The $\Delta\omega$ for the (222) reflection of NFO reflection is $\Delta\omega_{(222)}$=1.66°, almost equal to that of the (002) reflection of the underlying Pt layer. A ϕ-scan of the (202) planes of the NFO layer is shown in Figure 5.36. Twelve peaks separated by 30° are detected, in agreement with the RHEED analysis. Because of the three-fold symmetry of a (111) crystal plane, the observation of twelve peaks reflect the presence of four families of crystallites with (111) out-of-plane orientation, but different in-plane orientations rotated one to another by 90°. This kind of pattern has been observed, for instance, for (111)-STO on (001)-oriented yttria-stabilized zirconia [208]. The way the triangular mesh of (111) crystallites align on the

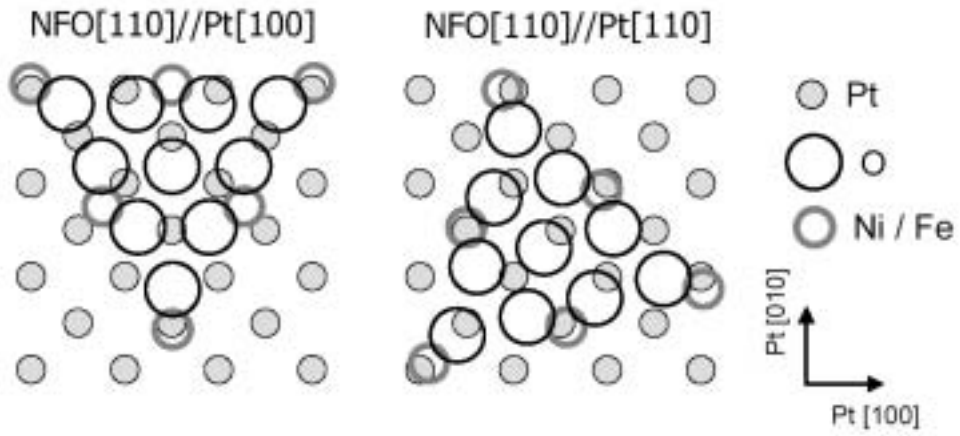

Figure 5.37: Schematic representation of two different alignments of the (111) mesh of the NFO (assuming B-site occupation either by Ni and Fe ions) onto the (001) mesh of Pt.

square mesh of the (001) Pt can be deduced by comparing the positions of the peaks in the ϕ-scans of Figure 5.36(c) and (b). By simple geometry considerations, one can deduce that if the edges of the triangular mesh of the NFO align on the diagonal of the square mesh of the Pt (see Figure 5.36(b)), the ϕ-scan of the NFO would consist of four sets of three peaks located at (i) 45° (B), 165° (F) and 285° (J), (ii) 135° (E), 255° (I) and 15° (A), (iii) 225° (H), 345° (L) and 105° (D), and (iv) 315° (K), 75° (C) and 195° (G) (the letters refer to the schematics of Figure 5.36(b)). This picture is in agreement with the position of the peaks observed in Figure 5.36(a). Summarizing, the [110]-type directions of the (111)-oriented NFO align on the [110]-type directions of the (001)-oriented Pt (we call this configuration NFO[110]//Pt[110]) . The mismatch for the growth of these crystallites is therefore equal to δ_{Pt} (-5.9%).

It is worth to discuss the implications of the observation of the NFO[110]//Pt[110] epitaxial configuration. The total energy of the system includes the elastic energy of the film and terms related to the interface energy. If the elastic energy of the growing NFO film were the only relevant parameter of the epitaxy, then it could be speculated that it would be much more favorable for the (111)-NFO crystallites to grow onto the Pt with the edges of the (111) triangular mesh parallel to the edges of the square mesh of the Pt ([100] and [010] directions), because the length of the former is $a_{NFO[110]}$=1.179nm, i.e. very close to three times that of the latter (3 x $a_{Pt[100]}$= 1.1769nm), with a mismatch of only -0.18% (NFO[110]//Pt[100] configuration). As can be seen on Figure 5.37, the atomic positions coincide better in the NFO[110]//Pt[110] configuration than in the NFO[110]//Pt[100] one, and therefore it is very likely that the former has a lower interface energy. As a result, the total energy, including the elastic energy and the interface energy terms, would be lower in the experimentally observed NFO[110]//Pt[110] configuration.

5.4.2 Magnetic properties

For NFO films grown on Pt the magnetization is also larger than that of the bulk as observed for the samples grown on STO (Figure 5.38). The ultrathin $Ni_{80}Fe_{20}$ layer intercalated between the MgO and Pt layers, if ferromagnetic, would give a signal of about $2 \cdot 10^{-6} emu$, which would represent $3 emu/cm^3$ after normalizing to the volume of the NFO layer. A similar contribution from Pauli paramagnetism of Pt can also be expected, in a field of $10 kOe$. These two layers therefore contribute negligibly to the overall magnetic signal. In conclusion, the observed large magnetization of the Pt/NFO could therefore also be due to cation disorder, thus suggesting that nanometric NFO films are also prone to partial Fe/Ni inversion in the octahedral and tetrahedral sites. In Figure 5.38 it can also be appreciated that, when the magnetic field is applied in the film plane, the Pt/NFO is harder to saturate than the NFO films grown on STO. This observation is a consequence of the magnetic anisotropy of the NFO films; in NFO as in most spinels the easy axis of the magnetization lies along the [111] direction [209]. For Pt/NFO this direction is normal to the plane, and in agreement with the experimental observation the films are harder to magnetize in plane than the films grown on STO with the [111] direction at a smaller angle.

5.4.3 Electric properties

The electric properties were measured by resiscope surface maps. A typical map is shown in Figure 5.39, showing a poor homogeneity of the resistance and hot spots, where the resistance falls of several orders of magnitude. These hot spots are not due to holes in the NFO layer, because in the RHEED images a flat surface was observed, but to diffusion of Pt to the surface along grain boundaries or other defectious film parts. This diffusion was also observed in the preparation of UPS measurements, where the flash heating of the sample led to the observation of Pt on the sample surface.

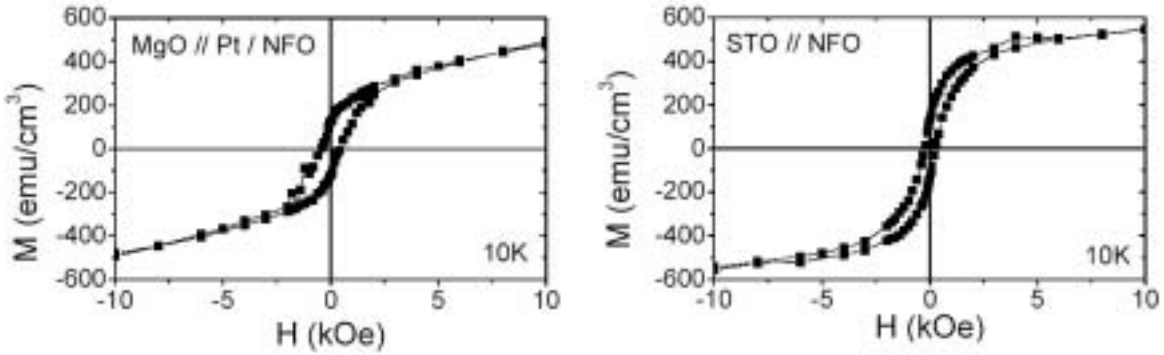

Figure 5.38: Magnetization vs field for a Pt/NFO sample (right panel) and a STO/NFO sample (left panel) grown under the same deposition conditions.

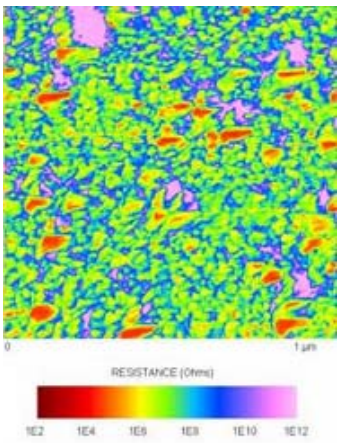

Figure 5.39: Resiscope image of a $5nm$ NFO film grown on Pt(111).

5.4.4 Discussion

It was shown in the RHEED pictures that the (111) oriented growth of the NFO film leads indeed to a two dimensional growth mode and a smooth surface. However, the fact that the [111] direction is out-of-plane leads to higher saturation field for a field applied in-plane, as the easy axis includes an angle to the film plane. In the case of the NFO grown on STO, the [111] direction is at an angle of 53.7° of the film plane, so that the easy axis is forced into the film plane by shape anisotropy.

The observation of the elevated moment comparable with the moment of the samples grown on STO confirms the observation, that it is not induced by the three dimensional growth mode neither by the exposition of a metastable surface. As the misfit resulting of the NFO[110]//Pt[110] configuration is around 6%, so equal to the misfit in the STO system, nothing can be deduced on the elastic stress as a driving force for the formation of antisites.

Although this system shows a two dimensional growth mode, spin-dependent transport on this system will not be successful due to the high density of pin-holes and the non-uniformity of the resistance of the NFO. When a barrier is deposited on the NFO layer, the current will take the pin-holes as a way of low resistance regarding the high resistance of the conducting NFO. Another problem is the easy diffusion of the Pt through the system. In an epitaxial growth the temperatures used are elevated, favoring the diffusion of the Pt and finally the NFO bottom electrode will not have the properties of the NFO films described here, but a lower magnetic moment. The NFO films grown on Pt are not useful as a base of a heterostructure.

6 Spin-dependent transport of conductive and insulating $NiFe_2O_4$

As observed during the characterization of the $NiFe_2O_4$ (NFO) thin films (see Chapter 5), integrating NFO in a heterostructure for spin-dependent transport allows the realization of two different devices: using a conductive NFO layer or an insulating one. In the first case the conductive character allows to apply the NFO as a magnetic electrode in a magnetic tunnel junction (MTJ) (Figure 6.1(a)). In the latter case the magnetic and insulating state of the NFO is used to build a spin filter device with NFO as a barrier (Figure 6.1(b) and (c)).

First describing the MTJ, the design is shown in Figure 6.1(a). Integrating the conducting NFO film as an electrode, materials for the barrier and the counter-electrode must be found. The electrode material has to fulfill two conditions: the spin-polarization must be high to achieve a high tunnel magnetoresistance (TMR), and it must allow the epitaxial growth of all components. Another condition for the design of the device results from the three dimensional growth of the NFO in pure Ar (see Section 5.2): using it as the bottom electrode would result in a rough morphology of the NFO/barrier interface and thus a structural and magnetic disorder of this region. As deduced by Slonzcewski (see Section 2.1.1) the quality of the electrode/barrier interface is of outstanding importance for the performance of the tunnel junction, thus the NFO layer should be the top electrode.

The use of metallic magnetic elements as a counterelectrode like Co or Fe was excluded. The NFO and the possible barrier materials are oxides, and connected with the elevated temperatures of the growth of NFO (Section 4.1.2) oxygen diffusion into the electrode could occur. A layer of iron oxides or the antiferromagnetic CoO at the electrode-barrier interface would alter the TMR strongly.

A bottom electrode from the group of spinel oxides is the best choice from the point of view of epitaxial growth. An obvious choice would be magnetite Fe_3O_4, which was already used as an electrode in the literature (see Section 3.2.3) and showed a reasonable spin-polarization. But also a rapidly decreasing spin-polarization with increasing temperature was found, so that at room temperature the spin-polarization of the magnetite layer was nearly zero (see Section 3.2.3).

Supposing however the choice of magnetite as the bottom electrode, a possible spinel barrier, resulting in an isostructural MTJ design, would be $CoCr_2O_4$ [181]. However, the characterization of the thin films in Chapter 7 shows very rough surfaces of the films, thus a $CoCr_2O_4$ is not adaptable. Another possible barrier material is MgO. It is one of the most-used substrates for the growth of spinels (see Section 3.2), but the spinel films are known to show degraded magnetic properties (see Section 3.2.2) due to the rock salt

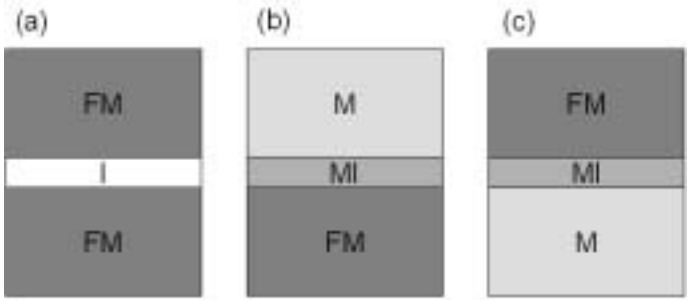

Figure 6.1: Schematical drawing of the heterostructures of (a) a magnetic tunnel junction, and (b) and (c) two different possibilities for the realization of a spin filter. FM denotes a ferromagnetic metal, M a non-magnetic metal, I a non-magnetic insulator and MI a magnetic insulator, respectively.

structure of MgO and the easy Mg interdiffusion in the range of deposition temperatures used for the growth of NFO.

As the growth of NFO single layers on $SrTiO_3$ (STO) substrates results also in an epitaxial growth in spite of the high misfit (see Chapter 5), an electrode from the perovskite family is possible, too. Widely used perovskite electrodes for magnetic tunnel junctions are $La_{2/3}Sr_{1/3}MnO_3$ (LSMO) and $La_{2/3}Ca_{1/3}MnO_3$, as they are half-metals and in case of the LSMO with a T_C above room temperature (see appendix A1-1). As the high T_C of NFO allows the operation of the MTJ at room temperature, LSMO is chosen. Regarding the choice of the barrier material, STO is the most adequate one, as the growth on LSMO is well controlled and it is an insulator well-studied for the application as a barrier in MTJs [181, 210–212]. The physical properties of LSMO and the characterization of the LSMO/STO heterostructures are found in the Appendix A1-1 and A1-2. The results of the spin-dependent transport measurements of the MTJ applying NFO as an electrode will be described in Section 6.1.

Turning to NFO with insulating character, the film is integrated as a magnetic barrier in a spin filter device (see Section 2.1.2). Experimentally two set-ups are possible as shown in Figure 6.1(b) and (c), with the ferromagnetic electrode in the bottom or on top of the heterostructure. In case (b) magnetite, Co or Fe as the magnetic electrodes are eliminated as discussed above, but even more, the close contact with the NFO and the elevated temperature during growth favors the interdiffusion of Ni, Co or Fe throughout the heterostructure. Thus the same reasoning as for the MTJ applies and LSMO is chosen as the electrode. As the top electrode a noble metal like for instance Au can be used, which does not attract the oxygen of the NFO film. The results of this heterostructure will be described in Section 6.2.

In case (c) the bottom electrode is the non-magnetic electrode. The advantage compared with design (b) is the easier choice of material for the magnetic top electrode, as the restriction of epitaxial growth is relaxed for this layer. For the non-magnetic electrode a noble metal like Au or Pt would be possible, but these materials diffuse very easily through the structure [213], as observed for the NFO films on top of Pt (see

Section 5.4).

Also some materials with spinel structure are conducting and non-magnetic, as for instance the stannates Cd_2SnO_4 [214], Zn_2SnO_4 [215], and $ZnCo_2O_4$ [86]. Electrodes of these materials would provide the possibility to be a perfect growth template for the NFO barrier. However, Cd_2SnO_4 contains the toxic Cd and in the case of Zn_2SnO_4 and $ZnCo_2O_4$ again the interdiffusion of Zn is likely, as $(Ni, Zn)Fe_2O_4$ is a stable spinel. In the perovskite family some non-magnetic metallic materials can be found like La or Nb doped STO. $(La, Sr)TiO_3$/NFO heterostructures were made, but were found to be insulating possibly due to problems during the deposition process. On these heterostructures, as the design (c) shows advantages to design (b), work is in progress.

6.1 Conductive $NiFe_2O_4$: Magnetic tunnel junction

As stated in Section 5.2.5, the NFO films grown in pure Ar are conducting with a resistivity of around $0.14\Omega cm$, which is comparable to the resistivity of magnetite, so that the NFO could be used as an electrode in magnetic tunnel junctions. The films were grown on top of a LSMO/STO heterostructure, for the deposition process see Section 4.1.2, and for the characterization of the perovskite films appendix A1-2 and for the characterization of the NFO films Section 5.2. For a NFO thickness of $3nm$ and a junction diameter of $20nm$, the resistance of the electrode alone is around to $1M\Omega$ increasing linearly with the electrode's thickness. Thus the NFO thickness is held as small as possible and a thickness of $3nm$ was chosen.

Spin-dependent measurements were done on two samples with a 3nm NFO electrode. The design of the heterostructure, the lithography process, the measured junctions and the obtained maximum values are listed in Table 6.1. While the junctions made by

Sample	Lithography	Junction	Maximum TMR(%)
LSMO(35nm)/STO(0.8nm)/ NFO(3nm)	nanojunctions	B1	5
		C1	no TMR
		C3	8
		D1	2
		D2	4
		D3	18
		E3	115
LSMO(35nm)/STO(1.2nm)/ NFO(3nm)	macrojunctions	F03	0.5
		F05	0.2
		F07	0.3
		J06	0.3

Table 6.1: Table of the maximum TMR values measured for the different samples. "nanojunctions" and "macrojunctions" denote junctions made by nanoindentation (see Section 4.5.2) and by optical lithography (Section 4.5.1), respectively.

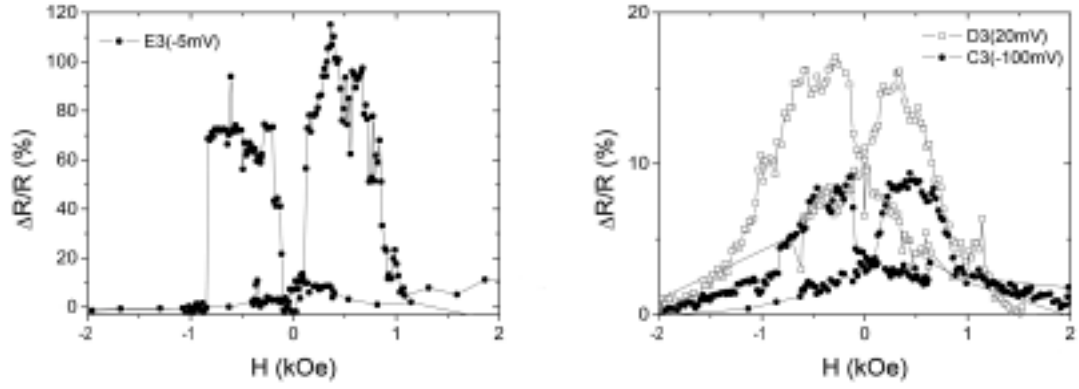

Figure 6.2: Resistance vs field curves of different junctions of a LSMO/STO/NFO heterostructure at $4K$. The bias voltage of the curves are specified in brackets in the legend.

nanolithography showed a TMR effect ranging from some percent to 115%, the junctions prepared by optical lithography showed a small TMR of less than 1%. The low TMR observed can be explained by the three dimensional growth mode of the NFO leading to a poor thickness uniformity of the NFO over the junction area. Thus in the following only the results obtained by nanojunctions will be discussed.

In Figure 6.2 different R(H) curves for three samples are shown. All curves show an increase of the resistance between ± 50 and $100Oe$, which is in agreement with the coercive field measured for the LSMO film (see appendix A1-2). The second switching field, where the resistance decreases to the high field value is around $\pm 800Oe$, thus slightly higher than coercive field of $500Oe$ observed in the single films (see Section 5.2.4). While the curve of junction E3 shows very sharp resistance jumps, the other junctions show a much slower reversal behavior.

The observed differences in the TMR curves is firstly due to the local character of the measurement because of the small junction area. Furthermore, the angle of the magnetizations of the LSMO and the NFO layers in the low field is maybe not 180°, but a smaller angle leading to a smaller TMR value. This is also corroborated by the less abrupt resistance jumps and the round shape of the TMR of the junctions D3 and C3.

The spin-polarization of the NFO, calculated from the TMR value of junction E3 with Julliére's formula (Equation (2.24)) and assuming a spin-polarization of the LSMO electrode of 90% [7], is 40%. This value is similar to the values observed in the Ni or Co, but even more interesting is the comparison with magnetite, as the conduction mechanism and the magnetic interactions are similar (see Sections 2.3.2 and 5.2.5). The highest spin-polarization measured by magnetic tunnel junctions was found to be 43% [180], so in the same range in spite of the half-metallic character of magnetite.

Taking into account the similar conduction mechanism for magnetite and NFO, the positive sign of the spin-polarization found for NFO is worth a discussion. Band cal-

culations of magnetite predict a negative spin-polarization [5]. Different signs of spin-polarization were found for magnetite in MTJs, as described in Section 3.2.3. Parkin et al [216] showed that the measured spin-polarization is depending on the thickness and the orientation of the magnetite electrodes. Evenmore, the sign of the spin-polarization is also influenced by the barrier material [212].

Therefore the observed positive TMR value of the junctions in this thesis does not allow the deduction of the sign of the spin-polarization in the conductive NFO. However, as discussed in Section 5.2.5 a double exchange mechanism of the mixed valence $Fe^{2+/3+}$ ions located at the B-sites is possible and thus a similar transport mechanism as in magnetite could be present. For this reason a negative spin-polarization and, even more, a half-metallic character of the conductive NFO can be expected. But for the experimental proof measurements like spin-polarized photo emission are necessary. Band calculations of the conductive, normal NFO could give insight into the theoretically expected spin-polarization.

6.1.1 Dependence on bias voltage

The bias voltage dependence of the TMR is shown in Figure 6.3. The low bias regime was measured for the junction E3 and the high bias regime for the junction C3. The high TMR value observed at low bias voltages decreases fast at a voltage of around $\pm 50mV$. For higher bias voltages the TMR value stays roughly constant at a low level.

A decrease of the TMR value with increasing bias was also found for MTJs including manganite electrodes [217]. The effect was investigated theoretically by Gu et al [22],

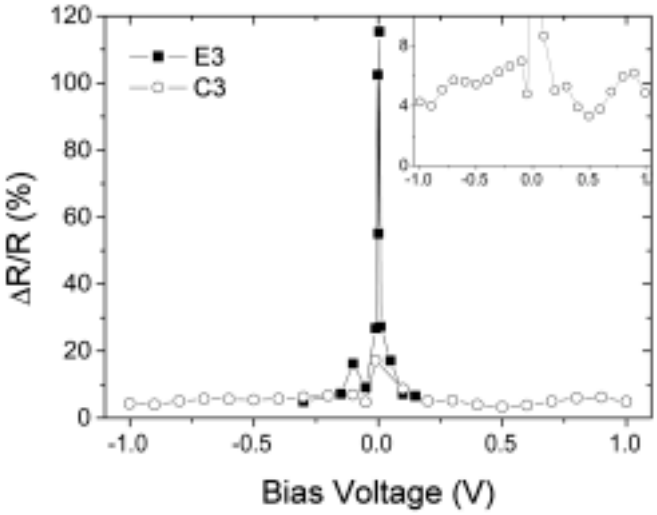

Figure 6.3: $\Delta R/R$ vs bias voltage for two different junctions at 4K. The inset shows a zoom at low TMR values.

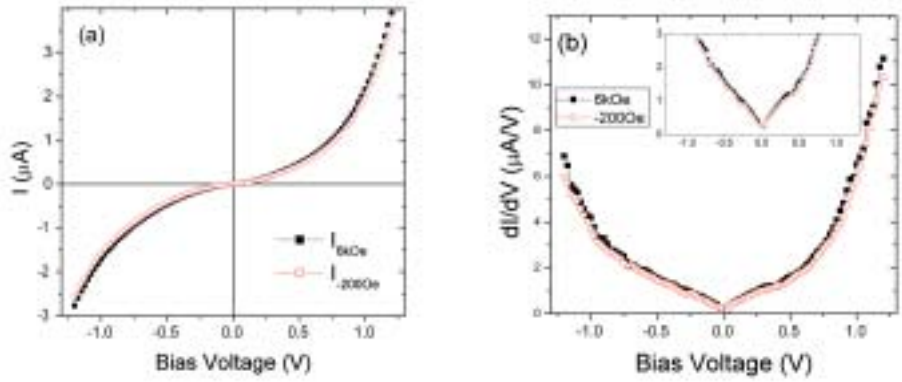

Figure 6.4: Current(a) and conductance (b) vs bias voltage of a LSMO/STO/NFO heterostructure at $4K$. The inset shows a zoom at low conductance. The solid symbols (open symbols) denote the curve measured in $6kG$ (-$200G$).

who found that a finite tunnel current is present in the antiparallel state of two half-metallic electrodes due to spin excitation in the electrodes. The manganites are double exchange systems (see appendix A1-1) and so a magnon emitted at the barrier-electrode interface can travel throughout the electrode, in contrast to systems containing itinerant magnets, where the spin excitations are basically confined to the interface. This small, but finite tunnel current for the antiparallel state leads to a decrease of the TMR value above a certain bias voltage. The observation of strong bias dependence of the TMR value in the conductive NFO is thus consistent with the hypothesis, that the magnetic coupling in this material is due to a double exchange mechanism at the B-sites.

Also an effect of the density of states at the Fermi energy of the NFO could lead to a dependence on the bias voltage of the TMR as observed in the present case. In tunnel junctions containing magnetite, peaks in the bias dependence were found at $\pm 50mV$ [182] emerging below $120K$ and explained by the existence of a band gap in the insulating state below the Verwey transition. As discussed before in Section 5.2.5, a rise of the resistance at around $50K$ is observed in the NFO related to the increasing localization of the conduction electrons. Unfortunately no data on the bias voltage dependence of the TMR above $50K$ is available, so that a possible relation cannot be confirmed.

In the inset of Figure 6.3 a zoom of the high bias regime is shown and oscillations of the TMR value with increasing bias voltage can be observed. Those oscillations in the TMR value for higher bias voltages are commonly observed in the case of defect states in the barrier [218]. Depending on the bias voltage the states allow resonant tunneling, so that the conduction of one of the spin channels is increased due to sequential tunneling.

An I(V) curve and its derivative of junction C3 is shown in Figure 6.4(a) and (b), respectively. In the inset of (b) a zoom of the conductance at low bias shows a zero bias anomaly consistent with the peak observed in the bias dependence deduced from the R(H) curves.

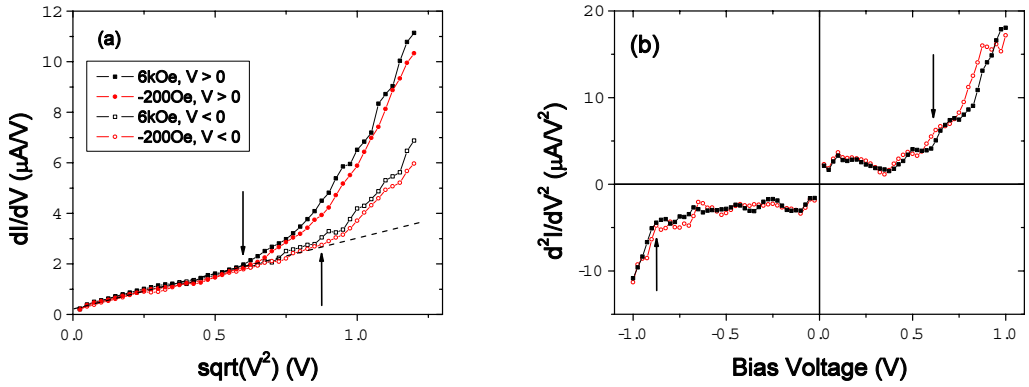

Figure 6.5: dI/dV(a) and d^2I/dV^2(b) vs bias voltage of a LSMO/STO/NFO heterostructure at $4K$. In (b) the solid symbols (open symbols) denote the curve measured in $6kG$ (-$200G$). The dashed line in (a) indicates the slope at low bias voltages and the arrows the position of the change of slope.

To extract the barrier height of the STO at the interface with LSMO and with NFO, the conductance for negative and positive bias are plotted on the positive bias axis (Figure 6.5(a)). The dashed line indicates the slope at low bias. An increase of the slope for the curves measured at positive bias voltage can be observed at $0.6V$, indicated by the arrow. As the change of slope occurs at the same voltage for the curves collected in the parallel and antiparallel alignment of the electrodes, it is not due a change of the spin-dependent tunneling, but due to the transport mechanism. The positive voltage corresponds to the transport of electrons from the NFO into the LSMO, so that the barrier height at the LSMO/STO interfaces equals $0.6eV$. At higher bias voltages also the curves measured at negative bias voltage increases. The position is at $0.88V$, thus the barrier height of the STO/NFO interface is $0.88eV$. In the derivative of the conductance curves (Figure 6.5(b)) the values for the barrier height indicated by the arrows are corroborated.

The difference in barrier height at the both interfaces suggests a trapezoidal shape of the barrier. Another origin can be the Schottky effect at the interface. As the material of the both electrodes are different, the band curvature at the interface with STO differs so that a difference of the barrier height is measured, although the barrier has a square shape.

However, assuming a trapezoidal barrier shape, a schematical drawing of the MTJ in terms of energy can be made as shown in Figure 6.6. The Fermi energy of the two electrodes is at the same level, as they are in electric contact. But the different work functions of the two electrodes results in a locally varying vacuum level of the barrier, as the vacuum level matches at the interface between the barrier and the two electrodes, so that also the barrier height differs at the interfaces. Using a value of the work function of LSMO of $4.7eV$ [219] and a difference of the barrier height ($\Delta U_0 = 0.28eV$, the work

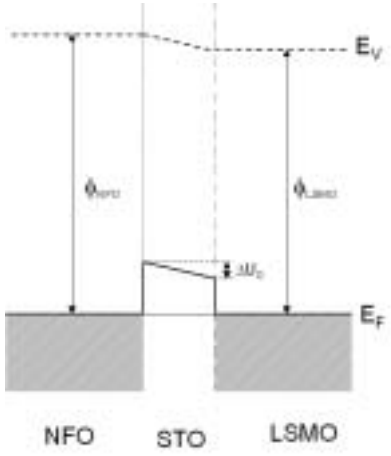

Figure 6.6: Schematic representation of the magnetic tunnel junction. E_F and E_V denote the Fermi energy and the vacuum level, respectively.

function of the conductive NFO is calculated with $\phi_{NFO} = \phi_{LSMO} + \Delta U_0 = 4.98eV$.

With the work function ϕ_{STO} derived from band structure measurements of STO single crystals is $2.6eV$ [220], the expected barrier height $(E_V - \phi_{STO})$ is thus around $2eV$, higher than the experimentally observed value. On the other hand the used barrier thickness of $0.8nm$ is very small, so that interface effects change the electronic structure of the STO. Also impurities in the barrier can lead to a small observed barrier height. In the thesis of M. Bowen [210] on tunnel junctions of LSMO with a barrier of STO a similar barrier height was observed. The samples were made in the same way like those

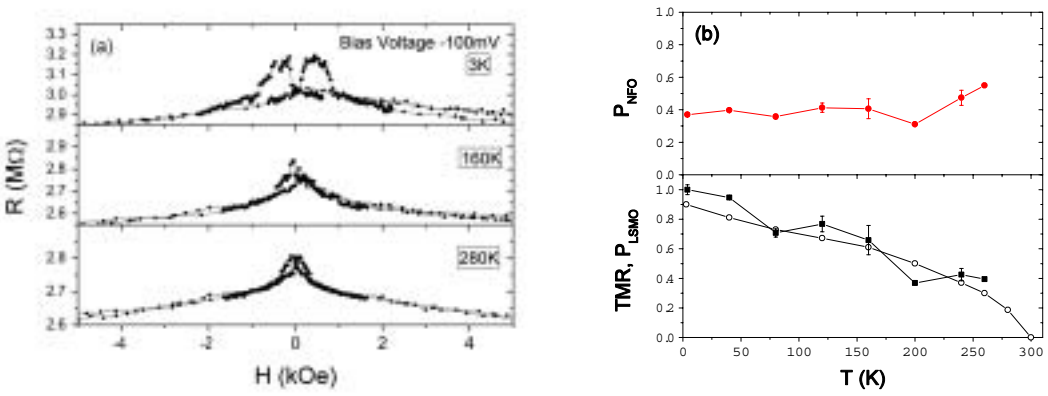

Figure 6.7: (a) Resistance vs field at three different temperatures of a LSMO/STO/NFO heterostructure and (b) bottom panel: $\Delta R/R$ (solid symbols) and the spin-polarization of the LSMO/STO interface (open symbols) after [211] vs temperature. Upper panel: spin-polarization of NFO.

in this thesis.

6.1.2 Temperature dependence

In Figure 6.7(a) R(H) curves are shown for three different temperatures for the junction C3. The curve taken at $280K$ still shows some TMR effect as expected from the magnetization measurements (see Section 5.2.4). The symmetric background of the curves is due to the Colossal Magnetoresistance (CMR) effect of the LSMO electrode (see appendix A1-2).

The summary of the TMR dependence on the temperature is shown in Figure 6.7(b, bottom panel: solid symbols), showing a smooth decrease of the TMR. The slope of the normalized TMR vs temperature is the same as observed for the temperature dependence of the polarization of the LSMO/STO interface (bottom panel: open symbols) [211] indicating a constant spin-polarization of the NFO. Indeed, when the polarization of the NFO is calculated with Julliere's formula (Equation (2.24)) for the different temperatures, it is found to be constant in temperature. The decrease of the TMR value to 0 at room temperature is only due to a decrease of T_C of the LSMO interface [211]. The spin-polarization shown in Figure 6.7(b, top panel) was renormalized to the spin-polarization of 40% found for the junction E3, as junction C3 shows a smaller TMR value.

6.2 Insulating $NiFe_2O_4$: Spin filter

From the transport measurements on single films one can deduce that the NFO films grown in an Ar/O_2 are insulating (see Section 5.1.4), so they were integrated as a barrier into heterostructures with a LSMO and a Au electrode. As in a spin filter the two magnetic layers are in close contact, in a part of the samples a thin STO film was introduced between the LSMO and the NFO layer to favor the magnetic decoupling in the antiparallel state. On the other hand the additional barrier will result in an enhanced resistance of the junction without influencing directly the TMR value. A list of the samples, the lithography technique and the maximum TMR value of the measured junctions is given in Table 6.2. The optical lithography was possible in these samples as the two dimensional growth mode provides homogeneous and flat NFO layer.

Sample	Lithography	Junction	Maximum TMR(%)
LSMO(35nm)/STO(0.8nm)/ NFO(3nm)/Au *SF1*	nanojunctions	B1	5
		B3	no TMR
		C1	no TMR
		C3	no TMR
		D3	5
LSMO(35nm)/STO(0.8nm)/ NFO(3nm)/Au *SF2*	nanojunctions	B1	25
		B3	15
		C1	27
		D2	20
LSMO(35nm)/STO(0.8nm)/ NFO(5.5nm)/Au *SF3*	macrojunctions	F01	50
		F03	18
		F08	9
LSMO(35nm)/ NFO(3.3nm)/Au *SF4*	nanojunctions	B2	no TMR
		B3	no TMR
		B4	no TMR
		D2	-7
LSMO(35nm)/ NFO(5nm)/Au *SF5*	nanojunctions	B1	35
		C2	8
LSMO(35nm)/ NFO(5.5nm)/Au *SF6*	nanojunctions	B3	no TMR
		C2	-7
		C4	55
		D2	no TMR
		D3	20
		D4	no TMR

Table 6.2: Table of the maximum TMR values measured for the different samples. "nanojunctions" and "macrojunctions" denote junctions made by nanoindentation (see Section 4.5.2) and by optical lithography (Section 4.5.1), respectively.

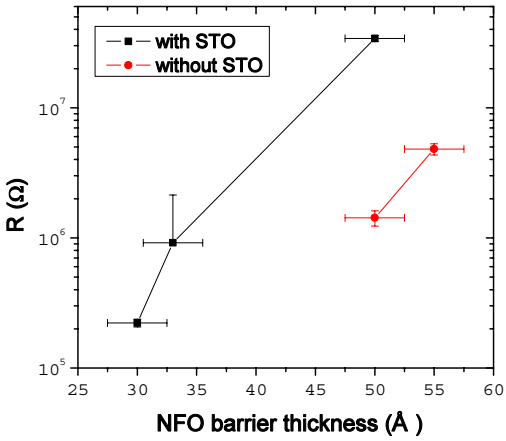

Figure 6.8: Resistance vs NFO barrier thickness at $4K$ and $100mV$. The values for STO/NFO hybrid and single NFO barriers are denoted by squares and circles, respectively.

To investigate the role of the NFO layer, the junction resistance was plotted over the NFO barrier thickness (Figure 6.8). The exponential increase confirms the tunneling transport through the NFO layer. Furthermore, the curve for the STO/NFO hybrid barrier show a similar slope, so that indeed the STO increases only the resistance of a factor of 2.

From the slope of the curve, the NFO barrier height can be extracted using the dependence of the transmission coefficient of the tunnel effect on the barrier thickness (Equation (2.6)). The tunnel current is proportional to the transmission coefficient, so that the relation with the resistance of the junction is

$$\ln(R) = C + \frac{2}{\hbar}\sqrt{2m(U_0 - E_x)}d \tag{6.1}$$

where C is a constant. So $\ln(R)$ vs d was fitted with a linear function to extract the slope B. From the above given equation and the slope, the barrier height can be calculated with

$$U_0 = \frac{(\hbar B)^2}{8m} + E_x \tag{6.2}$$

The calculated NFO barrier height is $160meV$ for the single NFO barrier and $155meV$ for the junctions with a STO/NFO barrier. The resistance values were collected in a field of $6kOe$, so that a parallel alignment of the magnetic layers is verified, and at positive bias voltages. The calculated value is thus the lower height of the exchange-split barrier for tunneling into the LSMO electrode.

Turning to the spin-dependent transport measurements, R(H) curves of different samples are shown in Figure 6.9. Two types of R(H) curves were observed. The curves of

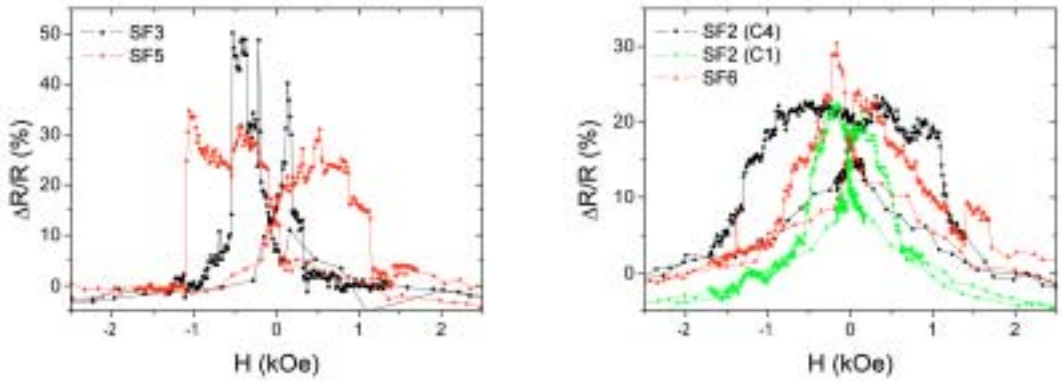

Figure 6.9: Resistance vs magnetic field for different spin filter samples at $4K$.

two samples (shown in the right panel) show a resistance increase between ± 50 and $100Oe$, which coincides with the coercive field of the LSMO layer. The position of the second switching varies between 400 and $1100Oe$, but is well-defined and is attributed to the magnetic reversal of the NFO barrier. This observation in relation with the fact, that the NFO layer forms a tunnel barrier (see Figure 6.8), point unambiguously toward a spin filtering effect of the NFO layer.

The other observed shape is shown in Figure 6.9 in the right panel. It shows a symmetric resistance increase approaching zero field, which is due to the intergrain magnetoresistance of the LSMO electrode (see appendix A1-2), so that the samples showing this contribution were excluded from the analysis. Only the data of SF3 and SF5 will be discussed in the following, although similar properties were found for SF2 and SF6. The samples with a $3nm$ NFO barrier (SF1 and SF4) did not show a TMR effect, possibly due to a coupling of the two magnetic layer and the small layer thickness of NFO.

All samples show a positive TMR effect, thus the barrier for the spin-up channel is smaller than for the spin-down channel. This is in contrast to band calculations, which predict a larger gap for the spin-up bands than for the spin-down bands [115, 120, 221]. Calculations were also done for a normal spinel structure of the NFO [120] with the same results. However, a simple band structure model based on the complete localization of the electrons can explain a positive TMR.

The model assumes a normal spinel structure (i.e. Ni^{2+} on A-sites and Fe^{3+} on B-sites) and completely localized electrons, so that the ionic electron configuration can be used. It must be noted that the Ni^{2+} ions on the A-sites have a tetrahedral coordination, so that the e states are lower in energy than the t_2 states. The spin-dependent electronic occupancy of the d-states is shown in Figure 6.10(a). Thus a spin-up t_2 state is found just below the Fermi energy. The degeneration of the t_2 states is lifted possibly due to a Jahn-Teller effect for the Ni^{2+} [200].

To place the bands in the band structure shown in Figure 6.10(b), a crystal field split-

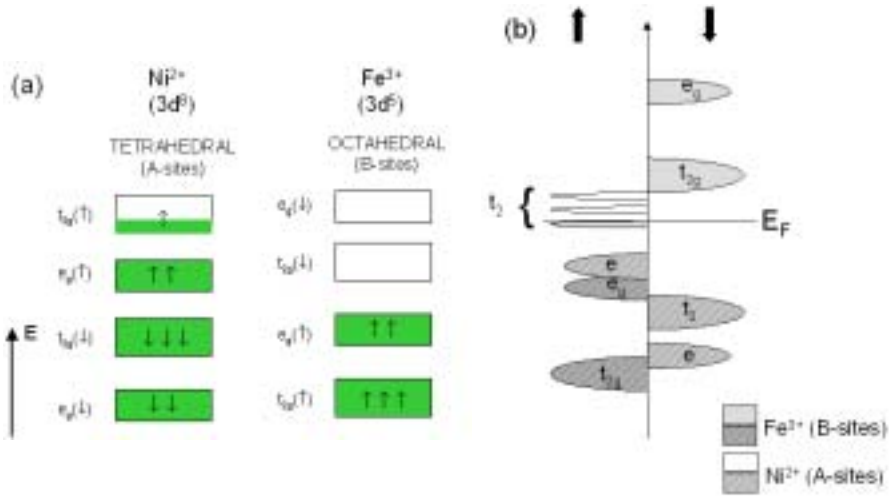

Figure 6.10: (a) Schematic electron occupation of the $3d$ states of a Ni^{2+} ion on a tetrahedral and a Fe^{3+} ion on an octahedral site. (b) Schematic band structure of normal NFO based on the complete localization of the $3d$ electrons.

ting of $\Delta_{cf} = 0.7eV$ and an exchange splitting of $\Delta_{Ex} = 1.4eV$ as found for tetrahedral Ni^{2+} ions in $(La, Sr)_2NiO_4$ [222] was used. The position in energy of the Fe^{3+} t_{2g} states was extracted from a site-resolved band calculation of inverse NFO [223] and is $0.45eV$ above the Fermi energy. With $\Delta_{cf} = 1.3eV$ and $\Delta_{Ex} = 3eV$ [205] for Fe^{3+} ions in an octahedral site, the band structure as shown in Figure 6.10(b) is deduced. The structure has a smaller gap for the spin-up bands than for the spin-down bands and provides thus an explanation for the positive sign of the observed TMR.

Based on the model of Jullière a filter efficiency of the magnetic barrier can be extracted from the TMR value [26] and compared with the predictions of the free electron picture of the tunneling process (see Section 2.1.2). The maximum TMR value was measured for the sample SF3 and is about 50% at 4K. Treated with Julliere's model assuming a spin-polarization of the LSMO of 90% [7], a filter efficiency of 22% can be extracted.

To compare with the theoretically expected filter efficiency, the value was calculated with the same model and a lower (higher) barrier height of $0.16eV$ ($0.45eV$). The result is a filter efficiency of 51%, higher than the observed value. However, the theoretical value is estimated with the assumption that a perfect antiparallel state is reached, i.e. the angle between the magnetization directions of the two magnetic layers is 180°. Regarding the close contact of the NFO and the LSMO layer, this is possibly not the case.

6.2.1 Dependence on bias voltage

The bias dependence of the TMR of sample SF3 and SF5 is shown in Figure 6.11. The curve shows a peak at zero bias and a steep decrease, which changes to a smaller slope at a bias of 50 to $100mV$ for both samples, though SF3 comprises a STO layer. Obviously

the influence of the hybrid barrier on the bias dependence is minimal.

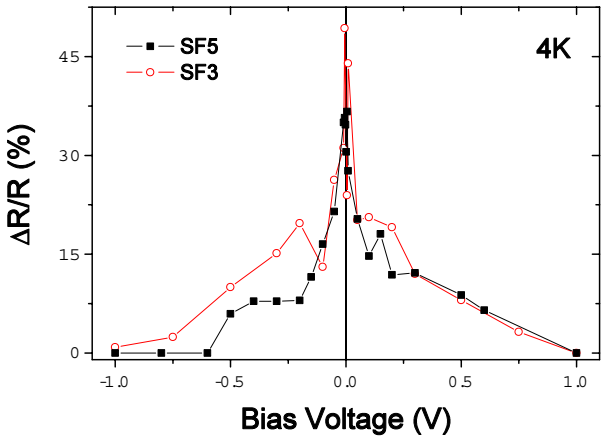

Figure 6.11: $\Delta R/R$ vs bias voltage for two different samples at $4K$.

The observed behavior resembles the curve measured for the MTJ (see Figure 6.3), but the decrease of the TMR value is not as fast. A different bias dependence was predicted for the spin filter. In the model of Saffarzadeh, described in Section 2.1.2, a maximum of the TMR at finite bias voltage results from the calculations. This maximum is not observed in the R(H) curves for different bias voltages, neither in the other reported spin filtering systems like Al/EuS/Gd or LSMO/$(La, Bi)MnO_3$/Au [224]. Indeed, the model by Saffarzadeh is a simple one, not taking into account effects of inelastic tunneling or

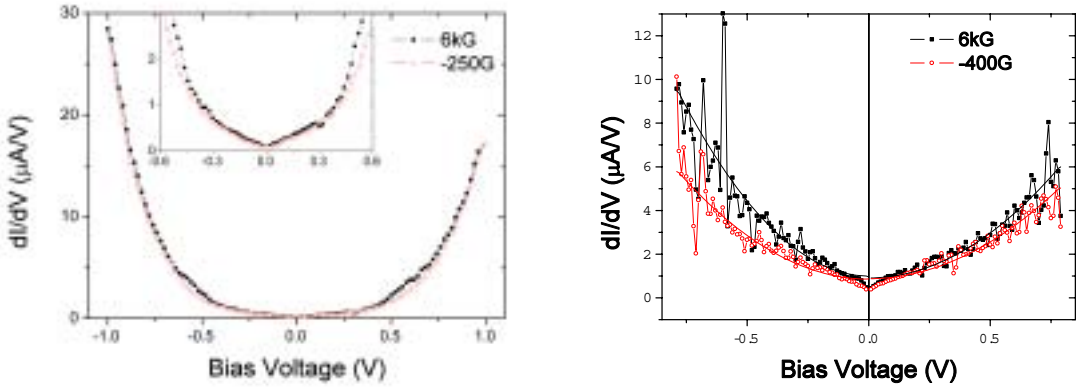

Figure 6.12: Conductance vs bias voltage for the sample SF3 (left panel) and sample SF5 (right panel). The inset in the left panel shows a zoom at low bias voltages.

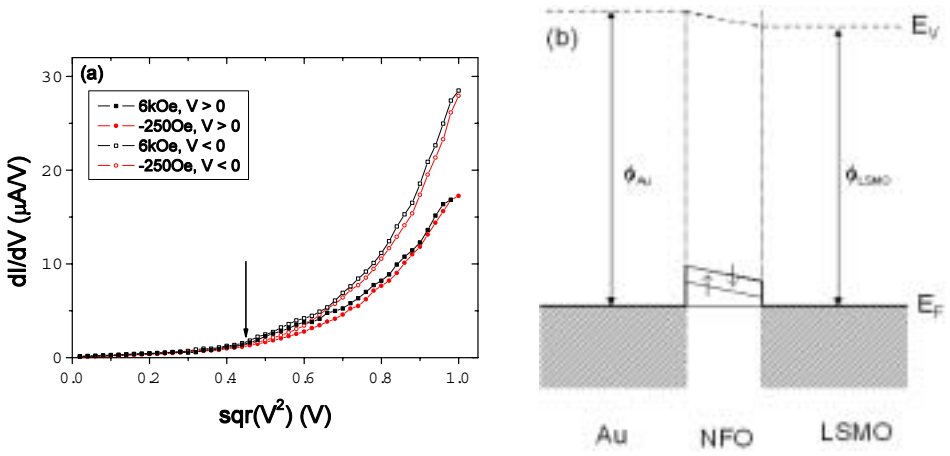

Figure 6.13: (a) $\mathrm{d}I/\mathrm{d}V$ vs bias voltage for the sample SF3 at $4K$. The solid (open) symbols denote the curve measured at positive (negative) bias voltage. (b) Schematic representation of the spin filter. E_F and E_V denote the Fermi energy and the vacuum level, respectively.

of the density of states of the barrier. As the maximum is expected at the bias voltage corresponding to the lower barrier height, the effect is possibly covered by inelastic effects. The conductance curves show a zero-bias-anomaly (see Figure 6.12), indicating that effects like magnon emission or absorption alter the bias dependence for low bias voltages.

In the magnetic tunnel junctions, the magnon absorption and emission is confined to the electrodes, but in a spin filter, these processes can also occur in the barrier. The impact on the bias dependence is still under investigation [225], but as the tunnel current depends exponentially on the height of the barrier, it can be expected to be high.

The asymmetry of the conductance curve indicate a trapezoidal shaped barrier. The barrier height of the STO on the side of Au can be extracted from the deviation of the slope of the conductance curves for negative and positive bias voltages (shown in Figure 6.13(a)). The deviation occurs at $0.46V$, which is in excellent accordance with the shear of the barrier due to the difference of the work functions of the two electrodes ($\Phi_{LSMO} = 4.7eV$ [219] and $\Phi_{Au} = 5.1eV$ [226]). The corresponding energetic schema is shown in Figure 6.13(b).

6.2.2 Temperature dependence

The TMR value decreases rapidly with increasing temperature (shown in Figure 6.14) and disappears at a temperature of approximately $140K$. In the right part R(H) curves at different temperatures are shown. Tracing the switching fields of the NFO, they diminish with the same temperature dependence and are at $200Oe$ at $140K$, so that a connection between the diminishing of the TMR and of the switching field is established. In the temperature range between $90K$ and $120K$, sample SF3 shows a very noisy TMR

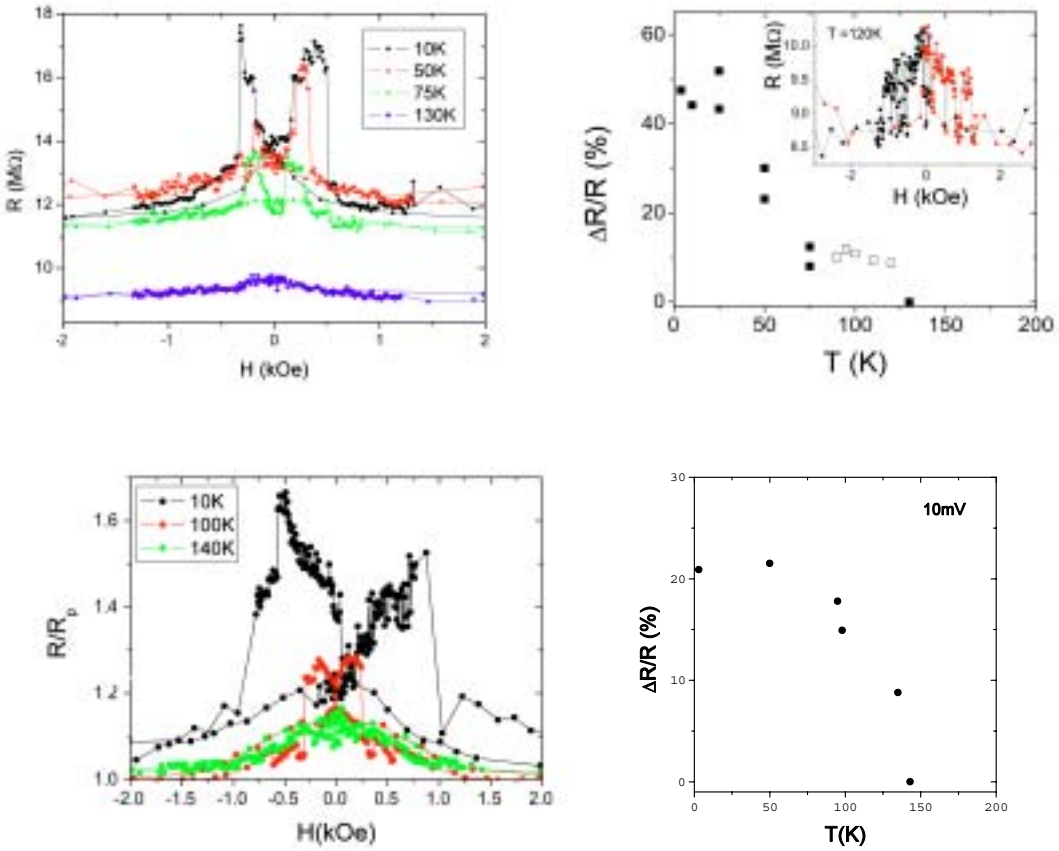

Figure 6.14: $\Delta R/R$ vs temperature for a bias voltage of $10mV$ (left panel) and normalized resistance vs field for three different temperatures (right panel) for SF3 (top row, $5.5nm$ NFO) and SF5 (bottom row, $5nm$ NFO). The top row is data collected for SF3, in the bottom line for SF5. The inset in the panel in the right top corner shows a R(H) curve at $120K$ of the same sample.

(shown in the inset), where the resistance jumps between two states. The noise appears in the range of field, where at lower temperature a TMR effect was measured, so that the noise is due to a badly defined antiparallel state. The STO layer intercalated between LSMO and NFO for this sample does not have an influence on the maximum temperature at which a TMR is observed.

The disappearance of the TMR effect is normally due to a decrease of the spin-polarization of one of the magnetic layers connected with the approach to the Curie temperature, but in the magnetic measurements of the heterostructures (Section 5.1.3) it was shown that the T_C of both materials is above room temperature. Also a lowering of the T_C of the LSMO interface cannot explain the effect, as it drops typically to room temperature [211].

Another mechanism, which leads to the disappearance of the TMR effect, is a coupling

of the magnetic layers, so that during the reversal of the magnetic layers the antiparallel state is not gone through. Regarding the close contact of the NFO and the LSMO, a similar process is possible. The coercive field of the NFO layer at $380K$ was measured to be below $100Oe$ (Figure 5.11), very similar to that one of the LSMO, accompanied by a low remanence. A diminishing of the second switching field with increasing temperature was observed, as well as a badly defined antiparallel state at elevated temperatures in the sample SF3. Evidently, the increase of temperature leads to a decrease of the coercive field of the NFO, thus the two magnetic layers do not reverse independently, but they are coupled due to stray fields.

7 Self-organized islands in spinel oxides

In the advent of ever increasing memory densities and decreasing size of high-end electronic devices, new techniques for surface structuring must be found. The classical way of structuring a surface or a multilayer, photolithography, has an intrinsic lower size edge of some $50nm$ due to the wavelength of the used light. The length scale was pushed even further by electron lithography down to some nanometers, but the technical setup gets more and more complicated. While the various lithography techniques are reducing the size of the original structure, self-organized or self-assembled growth of material allows to control the size of the structure directly during the deposition process. If the shape, size, orientation and location of the self-assembled objects can be controlled, nanostructures for (spin-)electronic devices can be grown directly on the substrate, without a subsequent shape forming treatment.

However, for the large scale application the growth and the properties of these materials must be very well controlled, but only some materials show self-organized growth. One example is the Si-Ge system [227–229], on which one can find strong scientific activity in the last 15 years. The self-assembled growth of this system is ascribed to the strain relaxation by the island edges [228–232]. Although this system has a strong inconvenience, which is the shape transition with increasing size, which the islands undergo [233, 234], it was possible in the last years to prepare ordered arrays of these islands [235, 236], which is very interesting for electronics [237]. Other materials in which a similar kind of islands were observed are Cu_2O [238], CeO_2 [239] and $CoSi_2$ [240].

For a comparable system for spinelectronics, the islands must be metallic and magnetic. A very interesting article was published in Science [88], where a multiferroic composite of $CoFe_2O_4$ and $BaTiO_3$ was grown, showing spinel nanostructures in the perovskite matrix. The samples are made by codeposition of the two materials, indicating a strong preference of the $CoFe_2O_4$ to form clusters. There are also some groups working with the magnetic transition metals (Ni, Fe, Co) (for a review see for instance [241–243]), using the formation of islands in a sub-monolayer coverage of the surface. The problem is to control the shape and the location of these islands, as well as the magnetic properties. As the islands are only some nanometers in size they become superparamagnetic at high temperature (the typical blocking temperature is about $50K$). But no magnetic oxide material was found which exhibits self-assembled or self-organized growth of islands comparable to that found in the Ge-Si system above.

We found self-assembled islands of magnetic spinel oxides. Single films of $CoCr_2O_4$ (CCO) show strong three dimensional growth, forming faceted islands, oriented uniformly, which do not show any shape transition or closing of the surface up to a size of a micrometer. It will be shown, that the interesting features of these islands, like the size and the density, can be controlled by the deposition parameters. The most impor-

tant conclusion drawn from these observations is the possibility to grow similar islands of all of the spinel oxides having a strong anisotropy of the surface free energy and so the possibility of making nanostructures out of materials with high Curie temperatures and different magnetic properties. This idea was confirmed by the formation of similar islands in $NiFe_2O_4$ thin films.

7.1 Epitaxial islands of $CoCr_2O_4$

Epitaxial films of $CoCr_2O_4$ (CCO) were grown on two different substrates: the spinel $MgAl_2O_4$(001) (MAO) and the rock salt MgO(001). The most important difference is the structure and the misfit. While the MAO substrate allows a homostructural growth of the spinel CCO, MgO with its rock-salt structure has a unit cell with one eighth of the volume of the spinel unit cell. From the growth of spinel ferrites on this substrate [35, 55, 56] it is known, that antiphase boundaries can lead to modified magnetic properties. On the other hand MgO is used widely as a substrate for spinel films because the mismatch is extremely low (around 0.3%), while MAO has a smaller lattice parameter than most of the spinels, including CCO, leading to a mismatch of 3%.

The films were grown as described in Section 4.1.1. The sample used for the study of this chapter are listed in Table 7.1. The structure was characterized by X-Ray diffraction (XRD, see Section 4.2.1), and the magnetic properties by SQUID magnetometry (Section 4.3.1). The most important tool to characterize the size and the shape of the islands were the images of Scanning electron microscopy (SEM, see Section 4.4.1), as it allows in contrast to Atomic Force Microscopy (AFM) undistorted views of the island shape. However, for islands smaller than a certain size, AFM pictures were used due to the high spatial resolution and the height information.

Due to the three dimensional growth of the films it is difficult to determine the growth

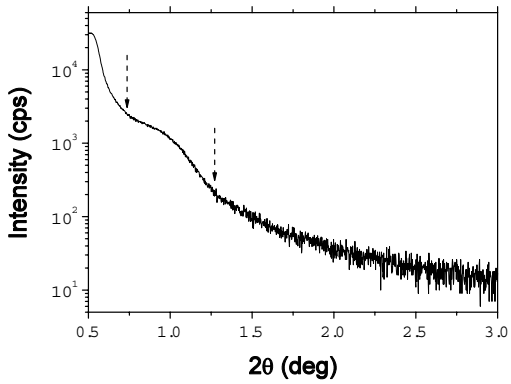

Figure 7.1: XRR measurement of a 15*min* CCO sample on MAO(001). The arrows indicate the minima of the oscillation.

rate of the CCO properly. The use of X-ray reflectivity (XRR) measurements was possible only for very thin films, as the intensity of the oscillations decreases quickly with increasing surface roughness. The growth rate could be only deduced from a sample, where no islands were formed, so a sample with $15min$ deposition time was taken (for the surface see Figure 7.11(b)). The corresponding measurement is shown in Figure 7.1. The film thickness was estimated to be $12nm$ and the corresponding growth rate around $0.8nm/min$ (for the analysis see Section 4.2.1). Due to the fact that only one oscillation is visible, the deduced growth rate has a high error bar and so in this chapter the deposition time will be used to characterize the thickness dependence of the films. When comparing films I will refer to a thicker film as that obtained with a longer deposition time.

7.1.1 Structural properties

The structural properties do not depend strongly on the substrate, although the crystal structure and the lattice parameter of the two used substrates is different. In Figure 7.2

Sample	Substrate	T_{dep} ($^\circ C$)	t_{dep} (min)
CCO-01	MAO	550	200
CCO-02	MAO	600	10
CCO-03	MAO	600	15
CCO-04	MAO	600	25
CCO-05	MAO	600	50
CCO-06	MAO	600	100
CCO-07	MAO	600	200
CCO-08	MAO	600	400
CCO-09	MAO	650	200
CCO-10	MAO	700	200
CCO-11	MAO	750	50
CCO-12	MAO	750	100
CCO-13	MAO	750	200
CCO-14	MAO	750	400
CCO-15	MAO	800	200
CCO-16	MgO	600	50
CCO-17	MgO	600	150
CCO-18	MgO	600	300
CCO-19	MgO	750	50
CCO-20	MgO	750	150
CCO-21	MgO	750	300

Table 7.1: Table of the samples used for the investigation of the properties of $CoCr_2O_4$ films. The substrate was $MgAl_2O_4$ (MAO) or MgO. T_{dep} denotes the deposition temperature and t_{dep} the deposition time.

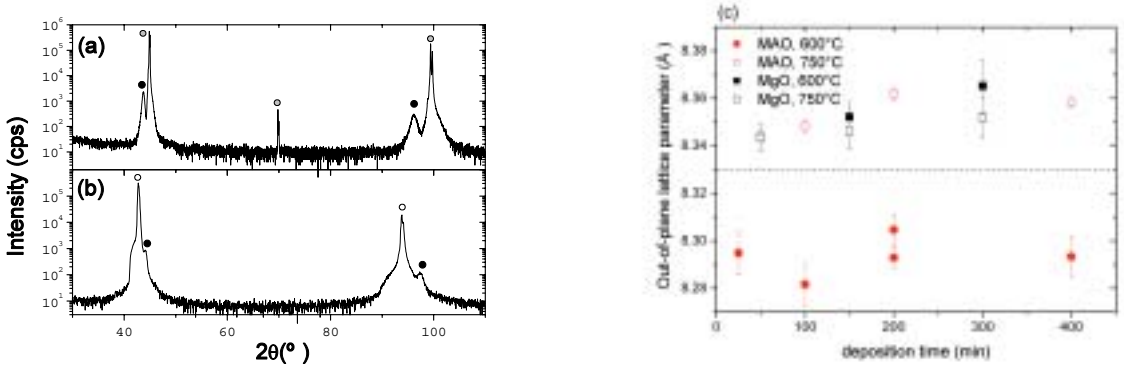

Figure 7.2: Typical θ-2θ scans of a CCO film on (a) MAO(001) (600°C, 200min) and (b)MgO(001) (600°C, 50min). The gray points indicate the reflections of MAO, the white points of MgO and the black points of CCO. (c) Summary of the out-of-plane parameters of films grown on MAO(circles) and MgO(squares). Solid symbols are the values for a deposition temperature of 600°C and open symbols for 750°C.

θ-2θ scans of a film grown on MAO (CCO-07) and of a film grown on MgO (CCO-16) are shown. Only peaks corresponding to the (00l) reflections are visible, the films are out-of-plane textured following the substrate.

For a comparative analysis of all the films we determined the c-axis (i.e., the out-of-plane) lattice parameters from the θ-2θ scan. The thickness dependences for films grown at two different temperatures (600°C and 750°C) on MAO and MgO substrates are summarized in Figure 7.2(c). The data indicate that all films grown at the highest temperature (750°C) have similar cell parameters (c = 0.834 - 0.837nm) irrespectively on the substrate and only a weak thickness dependence. Films grown at low temperature on MAO have the c-axis cell parameter somewhat reduced. In fact, whereas the films grown at 750°C on MgO and MAO have the c-axis slightly larger than that of the bulk CCO ($a = c = 0.833nm$), the films on MAO grown at 600°C have the c-axis cell parameter smaller than the bulk value. A possible relation with an elastic deformation due to the misfit of the system could not be established, as CCO on MgO has a small, compressive misfit, while CCO on MAO has a large and tensile one. The origin of the variation of the lattice parameter must be found in another mechanism, for example the interdiffusion of Mg (see Section 7.1.2).

The full width at half maximum ($\Delta\omega$) of the rocking curve of the (004) reflection of CCO is typically below 0.6° for films grown on MAO and 0.20° for the films grown on MgO. Both substrates show a $\Delta\omega$ of smaller than 0.02°. The smaller $\Delta\omega$ values on MgO can be explained by the smaller mismatch of CCO with rock salt MgO (-1.2%), while the mismatch with the spinel MAO is 3%.

XRD ϕ-scans of the (113) reflection (Figure 7.3) were performed to determine the epitaxial relationships. The results indicate, independently on the substrate, an in-plane epitaxy with the [100] direction of the CCO film parallel to the same direction of

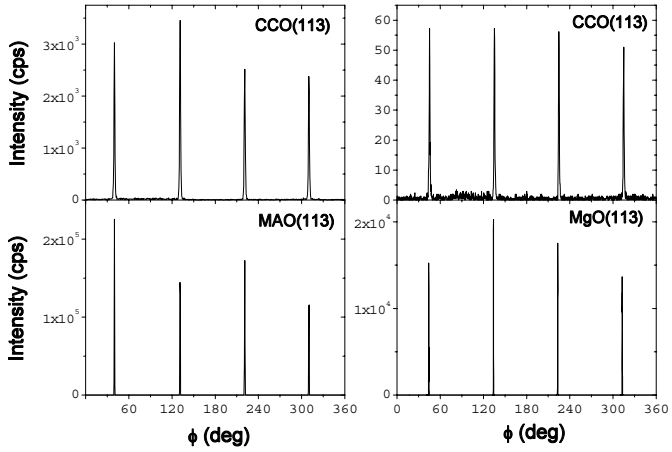

Figure 7.3: ϕ-scans of the (113) reflections of a CCO film on MAO (left panel) and on MgO (right panel).

the substrate, so that the epitaxial relationship can be described as [100]CCO(001)||[100]MAO(MgO)(001).

The state of lattice coherence/relaxation of the thin CCO films on MAO has been investigated. The XRD reciprocal space maps around the (115) spinel reflections of the 25 and 50min samples are shown in Figure 7.4(a) and (b), respectively. The map of the $25min$ sample allows determining that the in-plane lattice parameter of $0.809nm$

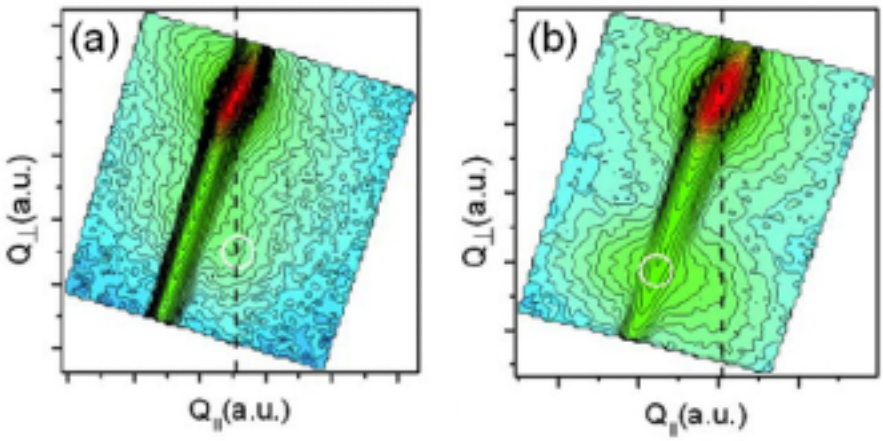

Figure 7.4: XRD reciprocal space maps of the (115) reflections of CCO (lower peak) and MAO (upper peak) corresponding to the samples deposited during (a) $25min$ and (b) $50min$. The dashed line indicates the $Q_{\|}$ value corresponding to the substrate peak, and the circles the position of the CCO(115) reflection.

is coincident with that of the substrate, which implies that the CCO is strained. c is calculated to be $0.286nm$ corresponding to c found for thicker films (see Figure 7.2 (c)), so that the cubic spinel cell is tetragonally distorted with $a/c = 0.98$. In contrast, the analysis of the peak position of the $50min$ sample indicates that this film is not strained, the in-plane lattice parameter determined from the map is $\approx 0.835nm$, which is approximately the bulk lattice parameter. c is $0.831nm$, so that in this sample, the unit cell is cubic. Summarizing, while the out-of-plane parameter is approximately constant even for very thin films, the in-plane parameter adapts to the smaller parameter of the substrates for films with a deposition time of $25min$ or smaller leading to a tetragonally distorted unit cell.

7.1.2 Magnetic properties

Figure 7.5(a) shows the temperature dependence of the magnetization -measured under a field of $10kOe$- of $200min$ films on MAO and MgO substrates deposited at $600°C$. For comparison the magnetization curve of the CCO sputtering target used for the deposition of the films is also included (right axis). The onset of magnetization of the target, occurring at T = $100K$ and the maximum of magnetization around $80K$ are in agreement with earlier data for bulk material [53] explained by a non-collinear magnetic structure and a small magnetic moment per unit cell, which has been reported to be between 0.1 and $0.2\mu_B$ per unit cell in agreement with the measurements.

In Figure 7.5(a), the data indicate that for films on both substrates the onset of magnetization occurs at about $100K$. As the volume of the film can not be well defined, the magnetization curves of two films with the same thickness have been normalized at

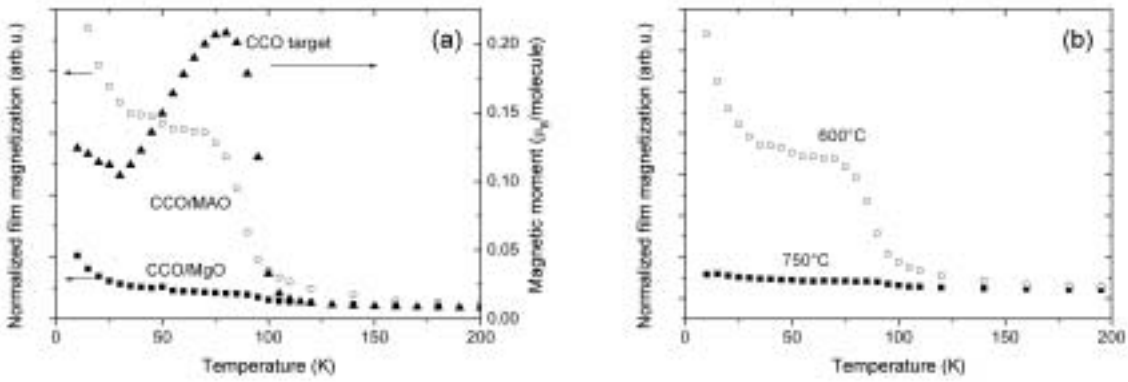

Figure 7.5: (a) Normalized magnetization vs temperature in a field of $10kOe$ for two CCO films of similar thickness grown on MAO (open circles) and MgO (filled squares) at $600°C$ and magnetic moment per formula unit vs temperature for the CCO target (filled triangles). (b) Normalized magnetization vs temperature in a field of $10kOe$ for two CCO films of the same thickness grown on MAO at $600°C$ (open circles) and at $750°C$ (filled squares).

the magnetization at $300K$ and the amplitude of the jump of magnetization occurring at T_C can be taken as a measure of the film magnetization. The magnetization close to T_C of the CCO/MAO film follows the same behavior as the bulk magnetization. However, a superimposed paramagnetic-like component becomes visible at T $\approx 50K$. The CCO/MgO film, on the other hand, shows a reduced magnetization and the features associated to the inset of magnetic ordering at $100K$ are only hardly visible. In Figure 7.5(b) the magnitude of the magnetization of the CCO/MAO grown at $600°C$ and $750°C$ can be compared. A reduction of the magnetization is clearly visible in the film deposited at the higher temperature, which is even more apparent in films grown on MgO: indeed no trace of magnetic ordering was visible for films grown at $750°C$ on this substrate.

The magnetization data reported above clearly indicate that high temperature deposition ubiquitously produce a reduction of the magnetization of the CCO films, which is more apparent -that is, it becomes relevant even at lower deposition temperature- when using MgO substrates. A possible reason for the reduction of magnetization of the CCO/MgO could be the existence Mg diffusion from the substrate. Indeed, Mg segregation was observed [145, 151], when growing Fe_3O_4 on MgO. The cell parameters variation presented in Figure 7.2(c) is compatible with this possibility. The c-axis cell parameters of films grown at the highest temperature become independent on the substrates, whereas for CCO/MAO films grown at lower temperature the c-axis is significantly shorter. This would imply that atomic interdiffusion may expand the c-axis.

7.1.3 Surface morphology

A SEM image (Figure 7.6) of the surface of a film deposited during $200min$ at $600°C$ shows the typical surface morphology of the CCO films. Islands are present with dimensions reaching about one micrometer and having a very well-defined shape with square or rectangular base, i.e. pyramids or huts. The apex and the edges are better visible in the derivative image (right panel). The well-defined shape strongly suggests the island

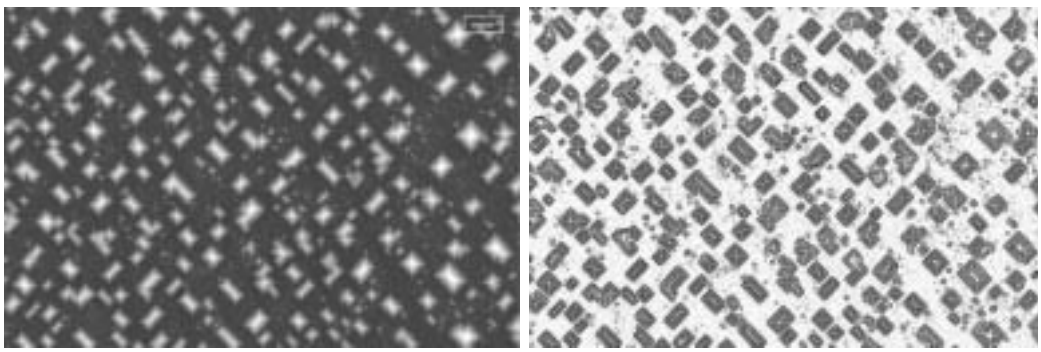

Figure 7.6: Morphology of a film deposited at $600°C$ during $200min$: the left panel shows a 0° view, the right panel the same image after applying a derivative filter. The edges of the images correspond to the [100] directions, the scale in the upper right corner is $1\mu m$.

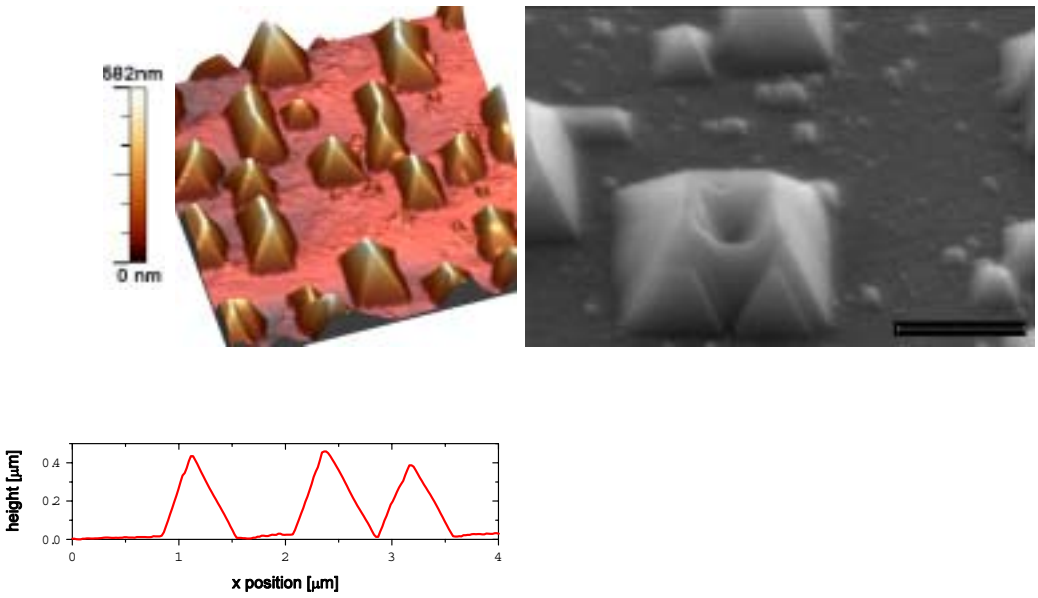

Figure 7.7: Left side: 3D view of an 5 x 5 μm^2 AFM image of the same sample like in Figure 7.6. The image edges correspond to the [110] directions. Bottom panel: Height profile of the same sample, measured by AFM. Right side: SEM image (45° view) of some islands of the same sample. The scale corresponds to $1\mu m$.

surfaces to be crystalline facets. In addition to having such particular individual shape (see also Figure 7.7), the islands show a collective order: they are perfectly oriented along the $\langle 110 \rangle$ crystal directions and are usually around 1μm apart. Closer inspection of the SEM image also shows the presence of a collection of smaller islands (100-200nm) having the same shape as the large ones.

More precise information on the island morphology and height values was obtained from AFM scans. Figure 7.7 shows an AFM image (3D view) corresponding to the same sample. The height profile shows that the height of the square-based pyramids and rectangular-based hut clusters is up to $400nm$. Even more noticeable than such large values is that the lateral surfaces of the islands form an angle $\theta \approx$50-55° with the substrate plane. The dispersion in the measured angles is due to the convolution of the film topography and the AFM tip. Also, the finite size of the AFM tip explains that some islands have a not perfectly symmetric shape. Within the experimental error in the AFM measurement, the lateral surfaces are likely to be {111} facets, which form an angle θ=54.7° with the (001) plane. The AFM image also emphasizes the existence of smaller islands, 10-100nm high and 70-200nm base dimension, as already observed in the SEM picture.

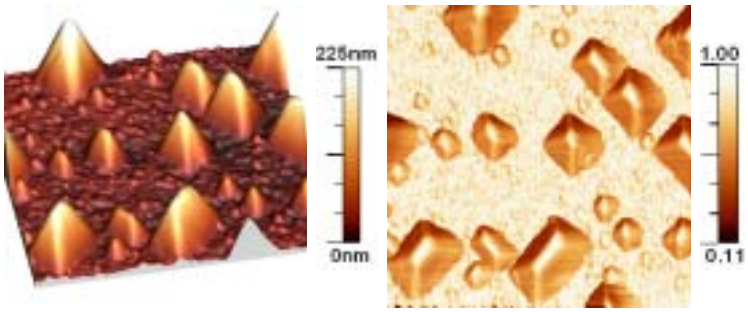

Figure 7.8: 3D view (left side) and the cosine filter (right side) of an 2 x 2μm^2 AFM image of a 50min sample grown at 600°C. The image edges correspond to the <100> directions.

Evolution with thickness

In order to explore the morphology evolution with the deposition conditions four samples were prepared at the same substrate temperature (600°C) and with 50, 100, 200 and 400min of sputtering time (samples CCO-05 to -08). In Figure 7.8 the corresponding a AFM image of the 50min sample is shown. It can be noted that the film presents a

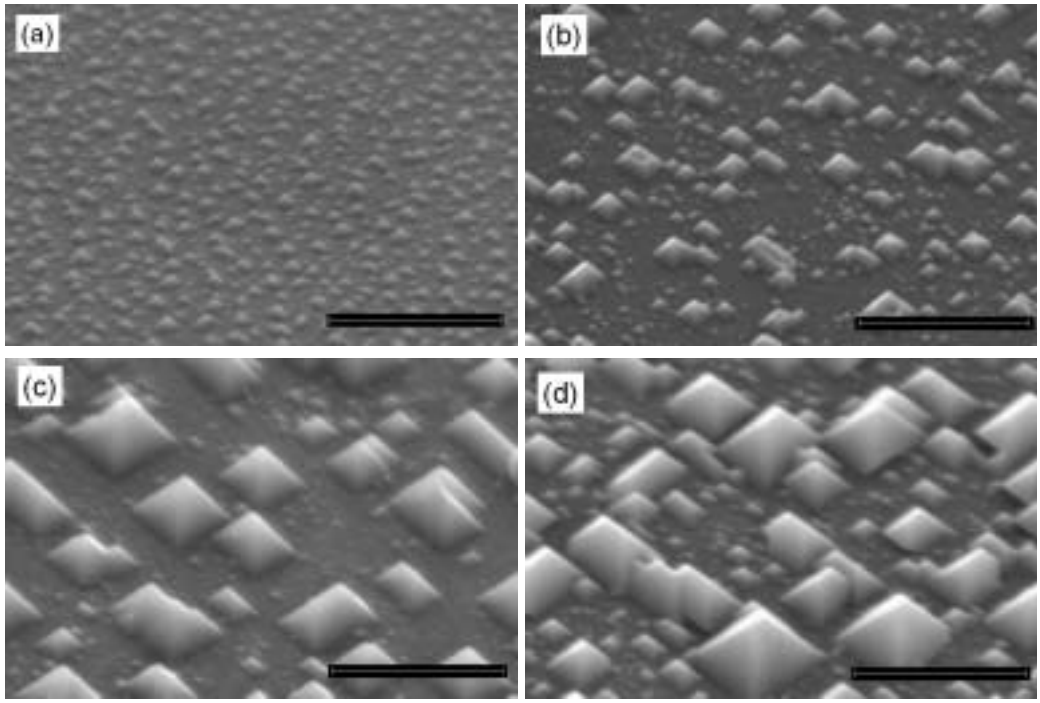

Figure 7.9: SEM images (45° view) of films deposited at 600°C during (a) 50min, (b) 100min, (c) 200min and (d) 400min. The scale corresponds to 2μm. The image edges are aligned along the [100] directions.

structure similar to that described in Figure 7.6 ($600°C$ and $200min$) although the size of the islands is smaller. The biggest islands at $50min$ have dimensions up to $400nm$. In spite of the small size, their faceted morphology and pyramidal shape (quadratic or hut type) is clearly resolved in the cosine filter image (Figure 7.8 right side). The cosine filter represents the cosine of the surface normal at each image point. Moreover, a collection of smaller islands, having dimensions around $100nm$ are also visible. We note that all objects are {111}-faceted irrespectively of size.

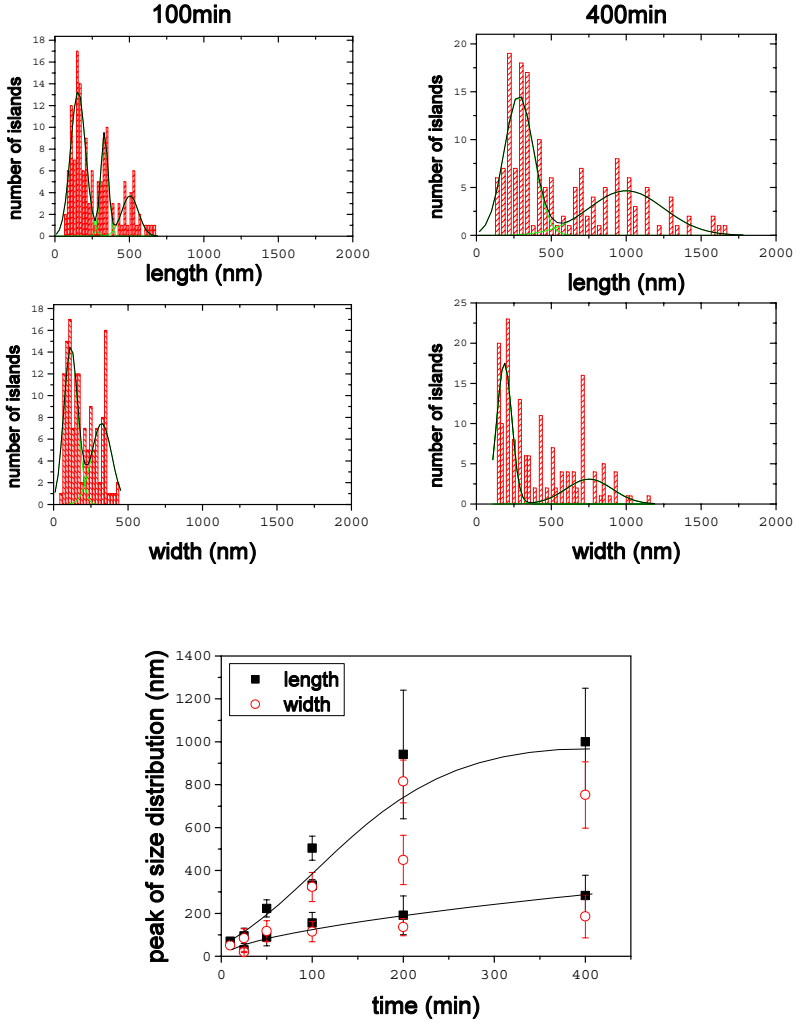

Figure 7.10: Histograms and the gaussian fits (lines) of the length of the islands (upper panel) and the width of the islands (bottom panel) for $100min$ (left panel) and $40min$ (right panel), the deposition temperature is $600°C$. In the bottom the peaks of the size distribution are shown as a function of the deposition time, the lines are guide to the eye. The error bars indicate the FWHM of the fits.

Comparing the evolution of the film's morphology (Figure 7.9) we observe that the size of the larger islands increases with the deposition time, while a family of islands with dimensions around $200nm$ is found in all the samples. These observed trends were confirmed with a quantitative analysis of the evolution of the dimensions of the objects. It was performed by measuring the length (long axis of the island base) and the width (short axis of the island base) of around 150 islands from each sample and fitting Gauss functions to the histograms of the measured island dimensions. In Figure 7.10 the histograms of the $100min$ and $400min$ samples are shown and the fitted Gauss functions. As a summary in the same figure the maxima of the distributions are indicated by points, whereas the bars correspond to the full width at half maximum (FWHM) of the Gauss functions corresponding to each family. This plot clearly shows that the bimodal size distribution develops progressively, i.e. the difference of the size of the two island families increases with deposition time (whereas for the thinner films the maxima of length distribution are at about 200 and $100nm$, they grow up to 1000 and $300nm$, respectively, for the thicker ones). Note also that increasing the sputtering time causes the distributions to become notably broader.

The left top panel of histogram in Figure 7.10 shows three peaks for the length of the island, corresponding roughly to the length of the square based pyramids (second maximum) and the rectangular based hut cluster (third maximum). However, the size distribution stays bimodal as the islands showing the same width, but a different length, belong to the same family of islands.

Initial stages of growth

Regarding the initial stages of growth of the islands, samples with much less deposited material, i.e. smaller deposition times, were made. Figures 7.11(a) to (d) show SEM images corresponding to the 10, 15, 25 and $50min$ deposition time samples, respectively (samples CCO-02 to -05). As stated before, although the thickest film of this family ($50min$, panel (d)) is still in an early growth stage in comparison with the $400min$ sample (see Figure 7.9(d)), the principal features like the pyramidal shape, long range order, and bimodality are already well perceived. However, such features are absent in the thinnest film ($10min$ deposition, panel (a)). The entire surface of the thinnest film is very homogeneous, showing a relatively smooth, dense, granular-like structure. In the image we can detect only one slightly contrasted grain-like object, maybe indicative of a close transition to the three-dimensional growth. Such close transition is apparent in the sample prepared with $15min$ sputtering time (panel(b)). In this image, the contrast is not determined by a dense structure of very small grains, but by a few of them that have grown more than the rest. In fact, the shape of the biggest one observed in the image (located close to the top left of the image) seems to be pyramidal and oriented along the [110] direction.

The three-dimensional growth becomes obvious in the $25min$ sample (panel(c)): there is a high number of pyramids, having all of them a quadratic base (i.e., there are no hut clusters) with a lateral dimension below $100nm$. We note that the islands prefer to be aligned along the $\langle 110 \rangle$ directions, although the long range order is much less

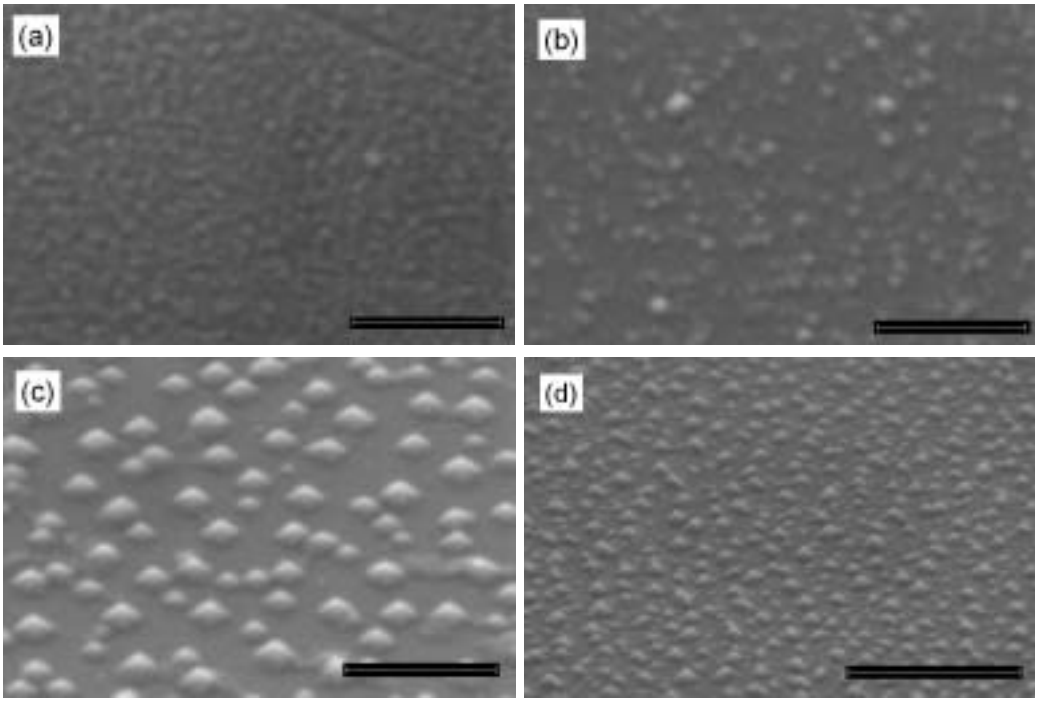

Figure 7.11: SEM images (45° view) showing the formation process of the CCO objects. The deposition times were (a) $10min$, (b) $15min$, (c) $25min$ and (d) $50min$. Note that the magnification in (d) is less than in the other panels: The scale of (a) - (c) corresponds to $500nm$, while the scale of (d) corresponds to 2μm. The image edges are aligned along the [100] directions.

apparent than in the thicker films. Indeed, in panel(d) in Figure 7.11, corresponding to the $50min$ sample, the long range order of the pyramidal objects can be clearly identified. Moreover, the islands in this sample already display a bimodal size distribution. This is a feature to be remarked, because in a previous growth stage ($25min$, panel(c)) the pyramids were present, but having a single size distribution. The observed bimodality in the $50min$ sample implies that a part of the already formed objects have experienced an abnormal high growth rate. Consequently, it is of interest to determine the reason of the three-dimensional growth and also to determine the reason of the higher growth rate of a part of the islands that produces the bimodality in the $50min$ sample and thicker films.

The closed granular film, which was observed in the $10min$ sample, was also observed in cross section SEM images, as shown in Figure 7.12. The samples were cut after the deposition with a diamond saw and sticked vertically on the SEM sample holder, so that it was possible to observe the cross section of the sample. The samples treated in this way were CCO-06 and CCO-08 with a CCO deposition time of 100 and $400min$, respectively, and deposited at $600°C$.

While in the film of $100min$ (left image) the granular layer only gives a shallow dark

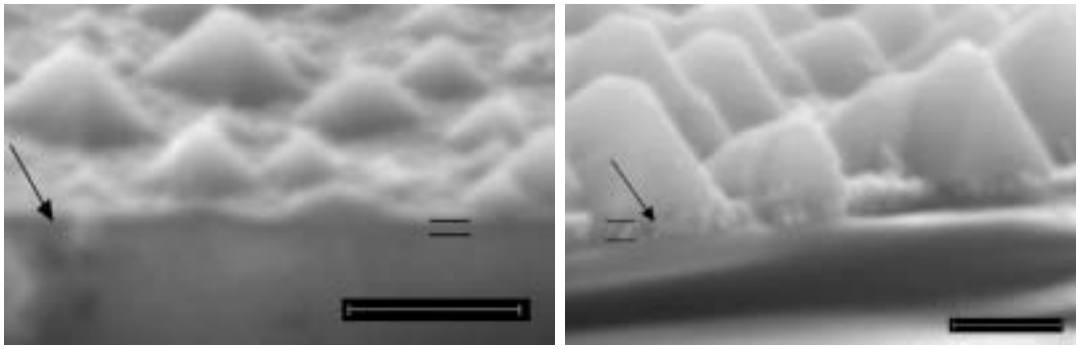

Figure 7.12: Cross section SEM images (0° view) along the [100] direction of films deposited at $600°C$ during $100min$ (left image) and $400min$ (right image). The scale corresponds to $500nm$. The arrows indicate the underlying CCO film, the lines the location at which the thickness of the film was measured.

contrast (indicated by the arrow), it can be observed very well in the $400min$ sample (right image). Here the granular structure of the underlying film is very well distinguishable from the smooth facets of the islands on top. From the images a thickness of the underlying film can be estimated. The black lines indicate the position, where the thickness was measured. For the $100min$ film a thickness of roughly $45nm$ was found, while for the $400min$ the thickness is around $90nm$. The deposition time of the thin film, at which the transition to the three dimensional growth mode seems to be adjacent (Figure 7.11 (b)) corresponds to a thickness of roughly $25nm$, thus much smaller than the observed thickness in the cross section, which would correspond to a deposition time of at least $30min$. However, for this deposition time islands are already observed (Figure 7.11 (c)).

Also after taking into account the uncertainty of the deposition rate as well as that of the measured thickness due to the shallow contrast of the SEM image, the thickness of the underlying film measured from the cross-section deviates from that observed directly by varying the deposition time. The origin of this deviation is not clear. As the measured underlayer thickness increases with deposition time, the incorporation of material into the underlying layer at higher deposition times could be one possibility. However, this can be ruled out, as the observed underlying film thickness is the same whether an island is located on top or not (as can be observed in the right image in Figure 7.12). As the islands are formed in a later stage of film growth, no material can be incorporated under an island.

Evolution with deposition temperature

I turn now to the dependence of the film morphology on the growth temperature. Figure 7.13 shows SEM images of films prepared during the same sputtering time ($200min$) but at different substrate temperatures from 600 to $800°C$ (samples CCO-07, -10, -13 and CCO-15). Visual inspection of these images immediately reveals that, in the explored

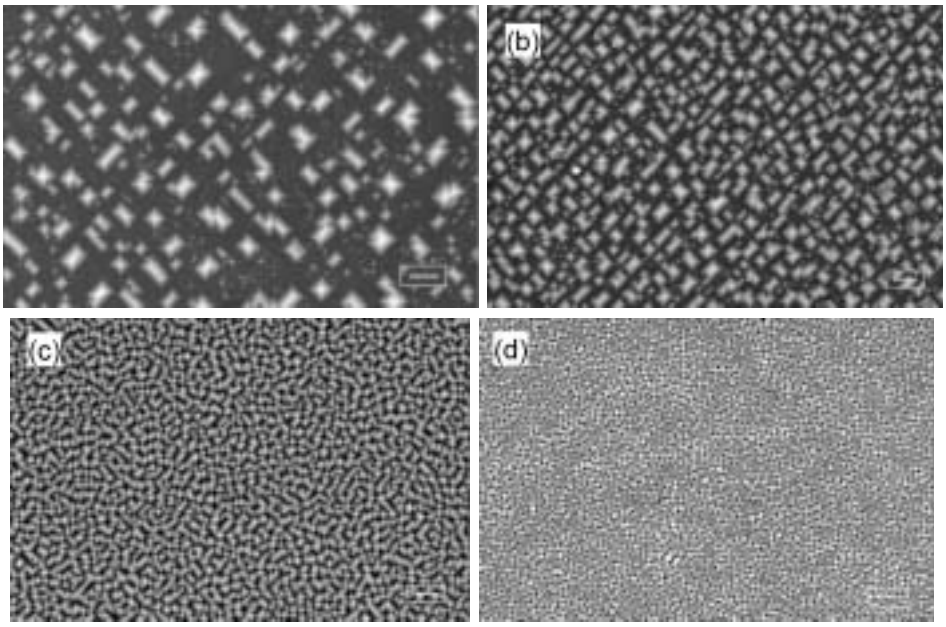

Figure 7.13: SEM images (0° view) of films deposited during $200min$ at (a) $600°C$, (b) $650°C$, (c) $700°C$ and (d) $800°C$. The scale in the right bottom corner corresponds to $1\mu m$. The image edges are aligned along the [100] directions.

temperature range, the size of the islands is reduced progressively as the deposition temperature increases. Even more, when the deposition temperature rises, not only is the size of the objects reduced to around $200nm$, but also the size distribution becomes notably narrower and the bimodal distribution is no longer observable. In Figure 7.15 (left side) the histograms of length and of width (top and bottom panel, respectively), corresponding to the sample prepared at $750°C$ are plotted. The quantitative analysis of these images has been performed as indicated above. The strong influence of the

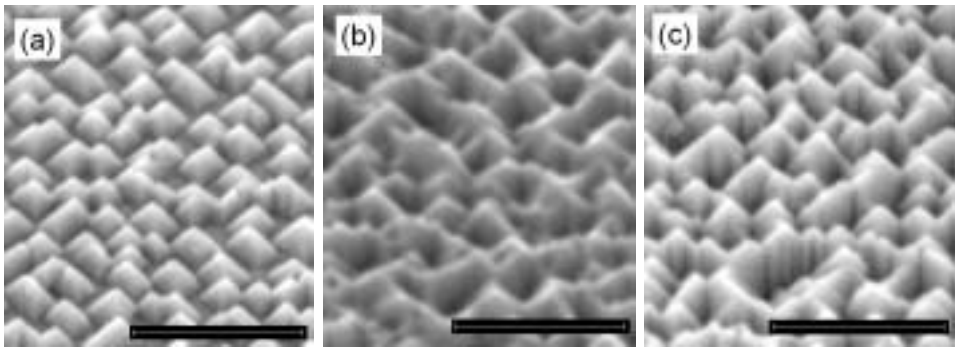

Figure 7.14: SEM images (45° view) of films deposited at $750°C$ during (a) $100min$, (b) $200min$ and (c) $400min$.

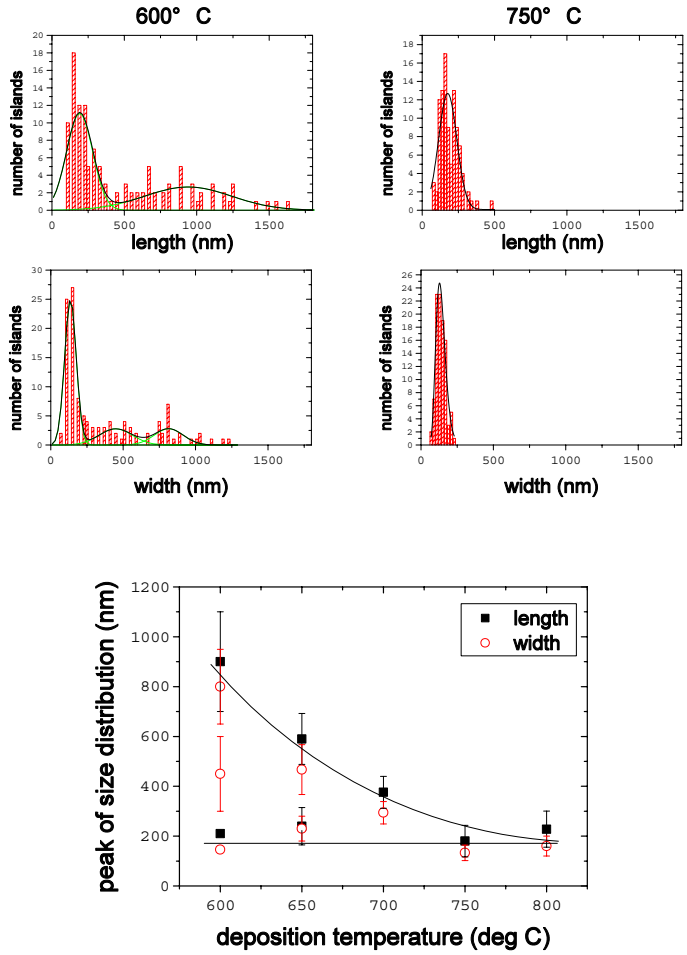

Figure 7.15: Histograms of the length of the islands (upper panel) and the width of the islands (bottom panel) for two different deposition temperatures: $600°C$(left part) and $750°C$(right part). The deposition time of both samples is $200min$. In the bottom the peaks of the size distribution are shown as a function of the deposition temperature. The lines are guide to the eye. The error bars indicate the FWHM of the fit.

temperature is evidenced with a comparison between these histograms and that of the sample grown at $600°C$ (middle panel). It can be also appreciated in Figure 7.13 that the degree of coverage of the film surface with CCO pyramids becomes higher when rising the deposition temperature. In fact, most of the islands are in contact, and so they form a {111} fully-faceted surface. The same morphology is evidenced in the sample prepared at $750°C$.

Films were also prepared at high temperature ($750°C$) during longer and shorter sputtering times (samples CCO-11 to -14) to investigate the formation and evolution of the {111} fully-faceted surface. In an earlier stage ($100min$ sputtering time) the surface

is not yet fully faceted but there is a well ordered structure of small islands that have similar sizes (Figure 7.14(a)). Note that although the coverage is nearly complete most of the islands remain isolated. With additional incorporation of material this surface becomes {111} fully-faceted after the deposition during $200min$ (b), which is kept even at the highest deposition time of $400min$ (c). This implies that the {111} fully-faceted CCO surface constitutes a highly stable system.

CCO on MgO

The islands appear also for the growth of CCO on MgO(001), as can be observed in the SEM images in Figure 7.16. The pyramidal (or hut cluster) shape and the {111}

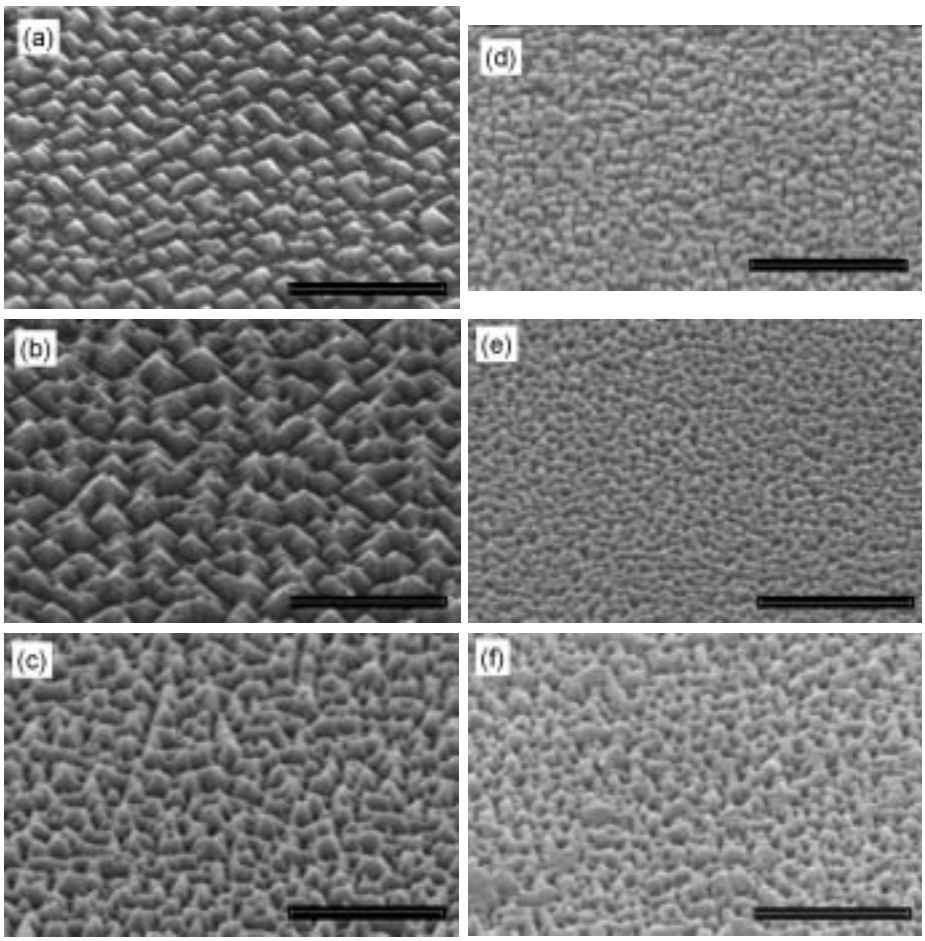

Figure 7.16: SEM images (45° view) of films deposited on MgO(001) at $600°C$ and a deposition time of (a) $50min$, (b) $150min$ and (c) $300min$. (d), (e) and (f) show the morphology of samples prepared at $750°C$ for $50min$, $150min$ and $300min$, respectively. The scale corresponds to $2\mu m$. The image edges are aligned along the [100] directions, only for panel (c) along the [110] directions.

faceting are identical to the islands observed for the CCO/MAO system, as well as the orientational order along the [110] direction. The influence of the substrate is restricted to the size and the density of the islands. The scale in Figure 7.16(a) is the same as in Figure 7.9(a), so the pictures are directly comparable. The histograms of the height, length and width of the $50min$ sample is shown in Figure 7.17(a) to (c), respectively, showing a monomodal, gaussian distribution. For comparison the histograms of the sample on MAO are shown in panel (d) to (e), showing a bimodal distribution in an early stage. Obviously the growth mechanisms of the islands on MgO are different to that on MAO.

Regarding the dependence of the island size on time, a SEM image of a film grown at

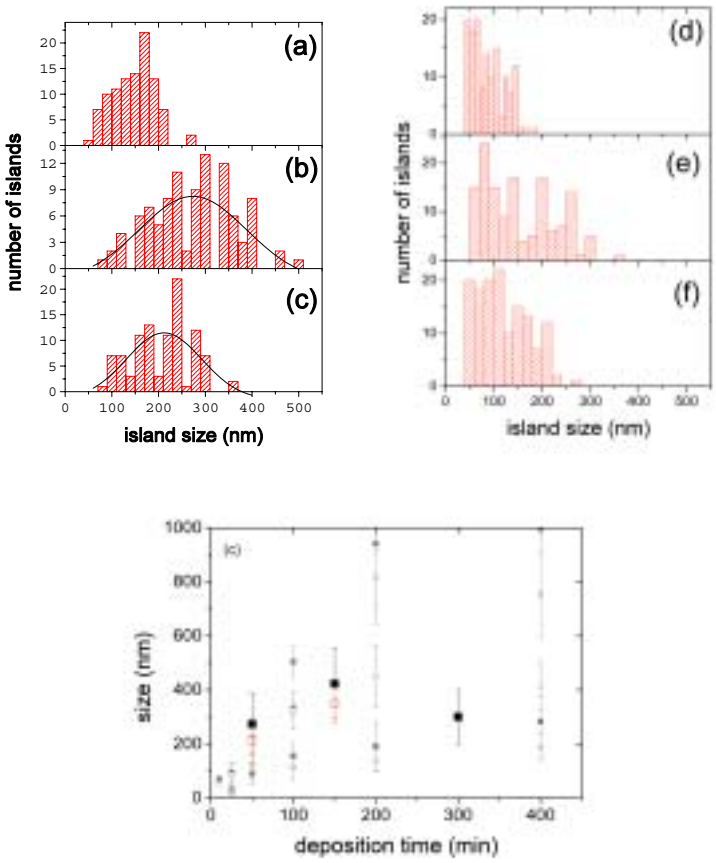

Figure 7.17: Histograms of the height (a), width (b) and length (c) of the islands grown on MgO at $600°C$ during $50min$ and (d), (e) and (f), respectively, of the islands grown on MAO with the same deposition parameters. Panel (g): peaks of the size distribution are shown as a function of the deposition time (solid square: length, open circles: height) of the samples grown on MgO. The small points in gray are the peaks of the size distribution for the samples grown on MAO.

$600°C$ during $50min$ (Figure 7.16(a)), $150min$(b) and $300min$ (c) is shown. While at a deposition time of $50min$ the islands are dense but isolated, the islands begin to touch after $150min$ and show a fully {111}-structured surface for a deposition of $300min$ (c). The summary of the island size in Figure 7.17(g) indicates that the island size does not change with deposition time due to the high density of the islands, so that they cannot grow in the plane, but only in z-direction.

Changing the deposition temperature to $750°C$ leads to a even higher density and a smaller island size for the $50min$ sample (panel (d)). Again, the islands are dense, but remain isolated. Increasing the deposition time to $150min$ (panel (e)) at this high temperature results in a morphology comparable to the $300min$ sample grown at $600°C$.

7.1.4 Discussion

The observation of 3D objects with a micrometric size and well-defined shape and facets is quite unusual in thin film deposition processes. The basic question to start the discussion of the origin of this island formation is, if the surface morphology is thermodynamically stable, or if it is formed due to the non-equilibrium deposition technique and the kinetics of the incoming atoms. It is to be noted that when islands are in contact, they remain {111} faceted, i.e. no other facets are introduced at the contact zone (see e.g. Figure 7.14(b)). We also note that the spatial distribution of the family of smaller islands is not affected by the presence of the large islands, i.e., there is not a zone denuded of small islands around the larger ones. This indicates that small islands, also {111} faceted, have to be very stable and hence a migration of their atoms is not expected. In fact, SEM images (Figure 7.18(a)) show islands a few tens of nanometers base dimensions very close to the big ones, i.e. those with hundreds of nanometers of base dimensions. The stability of the CCO objects was demonstrated by an additional experiment: a film deposited during $100min$ at $600°C$ was cut into two pieces; one of those was afterwards annealed during $120min$. The SEM images did not reveal appreciable differences between the as-grown film (Figure 7.18(a)) and the annealed one (Figure 7.18(b)).

As the surface morphology is thermodynamically stable and due to the observation, that the islands have the same faceting for all deposition conditions and for at least two different substrates, the origin of the {111} faceting should be due to intrinsic driving forces of the CCO. The appearance of these facets, which are strongly enhancing the free surface of the film compared to a flat (001) surface, can be explained by an anisotropy of the surface energy γ. It has to be noted that γ in spinels is strongly anisotropic [42, 44] with the {111} planes having minimum energy. In fact, the calculations of Mishra and Thomas [42] indicate that the surface energy of the {111} planes of some spinel ferrites is around five times lower than that of the {100} planes, and close to ten times lower than that of the {110} planes. Such extreme difference explains the shape of the CCO crystallites, since the total energy, which depends on the free surface area and the surface energy, can be minimized with the formation of minimum energy surfaces, although the free surface is enlarged. According to the Wulff construction, the equilibrium shape of a crystal with such extreme anisotropy is a {111} faceted octahedra as calculated

for $MgAl_2O_4$ [43]. As the faceting is observed on two different kind of substrates, differences in the interface energy CCO(001)//MAO(001) or CCO(001)//MgO(001) do not play a role for the shape of the objects and the equilibrium Wulff construction can be successfully applied to account for the observed shapes of CCO crystallites. In agreement with the theoretical predictions the spinel octahedral shape is commonly seen in single crystals also for other spinels [45] including the chromites [46].

The faceted morphology of the islands produces the clear orientational order, since the {111} facets intersect the (001) substrate plane in the ⟨110⟩ directions (Figure 7.19). As the films grow epitaxial, the orientation of the [110] directions is spatially fixed for all the islands.

The strong anisotropy of γ explains therefore that the facets of the islands are {111} planes, but not the process of emergence of the islands. Regarding the high surface energy of the {100} plane in the spinel system, a hypothesis would be, that the islands emerge to reduce the high surface energy of a primary (001) oriented film. This possibility will be excluded, as the underlying CCO film (the surface is visible in Figure 7.11(a)) is not a smooth (001) oriented film, but shows a rough surface. Also the existence of a critical thickness (i.e. the observation of a Stranski-Krastanov growth mode) is hard to explain in this picture, as the inset of the energy minimization would be advantageous already in the first monolayer of CCO and a Volmer-Weber growth mode would be expected.

A second scenario would be the emergence of the islands to reduce the elastic energy, which was identified as the main driving force of the island formation in the SiGe system [229]. Islands allow to partially release the stress at the surface and the edges of the island. The elastic energy is cumulative with the film thickness, so that a critical thickness is expected in this scenario. Also the observation of the strain state of the film with reciprocal space maps for very thin films (Figure 7.4) is consistent: in the reciprocal space map of the $25min$ sample, which shows a fully strained film, only the underlying film is measured. Due to the small volume of the islands the intensity of this part of the

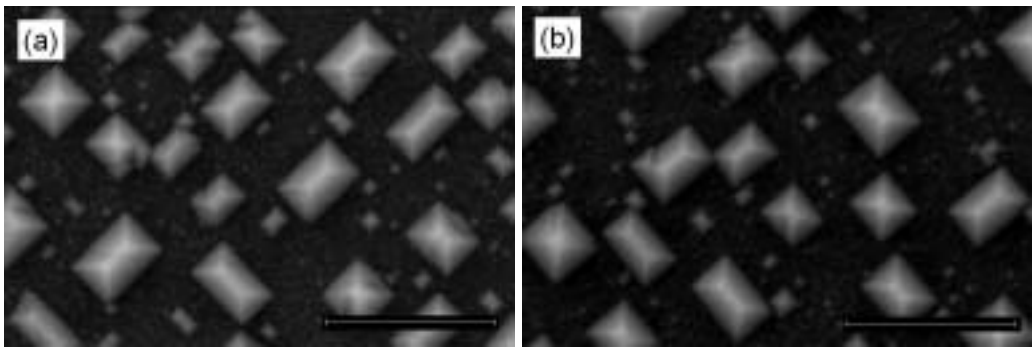

Figure 7.18: SEM images (0° view) of a film deposited during $100min$ at $600°C$ (a) as-grown and (b) after a post-annealing during $120min$ at $600°C$ and $250mtorr$ ($25\%0_2$-75%Ar).

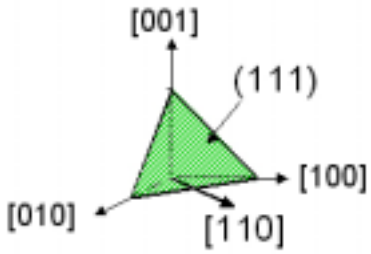

Figure 7.19: Schematical view of the location of the (111) plane in the cubic crystal lattice.

film is a factor of ten smaller than the intensity of the underlying film and because of the low count rate, the former contribution is in the order of the noise. No conclusion can be drawn of the strain state of the islands. On the other hand the $50min$ film shows a relaxed film. Here the volume of the islands is much bigger in respect to the $25min$ samples, and the contribution of the islands and the underlying layer will be roughly equal. In fact, a slight shoulder of the film peak on the right side can be observed in Figure 7.4(b), indicating that a part of the film is still strained, while another one is relaxed. The strained part was already observed in the $25min$ sample and attributed to the underlying film, so that it is suggestive to attribute the relaxed part to the newly emerged islands. The islands would therefore grow because they allow a partial strain relaxation of the film.

However, the observed higher density and bigger island size observed on the MgO substrate for the same amount of deposited material does not fit in this picture in a simple way. Taking into account only the different misfit of the CCO film with the two substrates, the strain relaxation in the CCO/MgO system would be expected in a later stage than in the CCO/MAO system due to the lower misfit in the former system, and so a thicker critical thickness before the formation of islands. On the other hand, it is not only the misfit which changes going from MAO to MgO, but also the crystal structure. The rock salt structure will result in different growth kinetics of the film, as it has more energetically equal sites for the two different transition metal cations. The straight forward reasoning is also difficult, as the film is not a elemental film, but consists of three different ions. Furthermore a possible interdiffusion of Mg was observed in the magnetic measurements, resulting in a change of the lattice parameter. The change of the substrate can result in more complex changes, so that taking into account only the change in misfit can lead to wrong conclusions.

The second step of the growth - the evolution of a bimodal size distribution - is caused by an abnormally high growth rate of some of the islands. In semiconductors the bimodal distributions are explained as due to phase transitions associated with the shape evolution from pyramids to domes. In contrast, the CCO structures present bimodal size distributions in spite they are {111} faceted during all the stages of their growth. The samples for deposition times above $25min$ are fully relaxed (as deduced from the

XRD measurements in Section 7.1.1) and allows the hypothesis that in an early growth stage the plastic (i.e. via dislocations) relaxation of the islands was non-simultaneous. This assumption implies that during a time of the film growth, dislocated and elastically strained islands coexisted. In the $25min$ sample a monomodal distribution is observed, so that this morphology can be attributed to the state before the relaxation of some islands, although the strain state was not determinable.

The coexistence of relaxed and coherently strained islands provide a driving force for the observed bimodal size distribution, as it could trigger a higher incorporation of adatoms of the dislocated islands, since the chemical potential of the dislocated objects has to be lower than that of the still elastically strained ones. In fact, a similar scenario was used to account for the spectacular growth of some SiGe domes at high coverage as related to their plastic deformation [233, 244]. Furthermore the CCO island size distribution is single-modal and narrower in films prepared at the highest deposition temperatures. This behavior is consistent with the hypothesis of non-simultaneous relaxation as the origin, since the energy barriers for the nucleation and propagation of dislocations should be more easily overcome at high temperature. Indeed, the simultaneous island growth that is expected at high temperature explains the smaller size of the structures.

The third island family observed in the sample grown at $600°C$ and during $200min$ (Figure 7.15) cannot be explained in this model. However, the length histogram does not show a third maximum, and it is observed only for this sample. The appearance could be due to a later growth of a part of the small islands, also triggered by a non-simultaneous relaxation at a later time.

Finally a certain long range order can be observed in the samples. The islands show an alignment of the edges or the apex, as can be appreciated for example in Figure 7.13(b) or 7.6(b). The AFM image of the surface of a MAO substrate, shown in Figure 7.20, indicates the origin of this behavior: the surface shows polishing streaks some nanometers in depth. At these streaks the CCO film will be able to release the strain

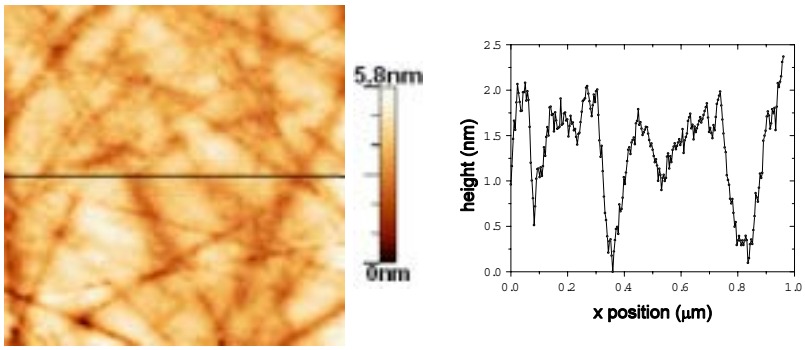

Figure 7.20: Plane view of an AFM image of a MAO(001) substrate. The size of the image is 1 x $1\mu m^2$. The black line indicates the position of the height profile shown in the right panel.

elastically, so that islands will be formed preferably at these sites and the long-range order is due to the initial substrate morphology. The image shows the surface of a substrate as-received and the annealing of the substrate might lead to a smoothing of the surface, as material is redistributed. The closed film, which is build before the emergence of the first islands, keeps the same morphology like the substrate, as can be appreciated in the $200min$ closed film, which was grown at $550°C$ (see Figure 7.21).

However, in the images of the surface covered by islands, the long range order is preferably along lines in the <110> direction, indicating that also a long range order inherent of the island growth is existent, which could have its origin for example in an interaction between the islands mediated by the underlying layer. The surface morphology of samples grown at higher temperatures underlines this, as the size of the islands is much smaller than the period of the streaks observed in Figure 7.20.

Summarizing, epitaxial pyramidal shaped islands with a {111} faceting and a orientational order were observed for different deposition times and temperatures on two different substrates. The observed morphology of the films grown on MAO(001) is summarized as a phase diagram in Figure 7.21. For temperatures of $600°C$ and above isolated islands were found. The evolution with the deposition time shows a closed, rough layer for small times, on top of which isolated islands start to appear after a critical thickness. At temperatures above $700°C$ the islands form after a second critical thickness a fully {111} structured surface of coalesced islands. The origin of this morphology was found in the possibility to release strain elastically by forming islands. The faceting of the

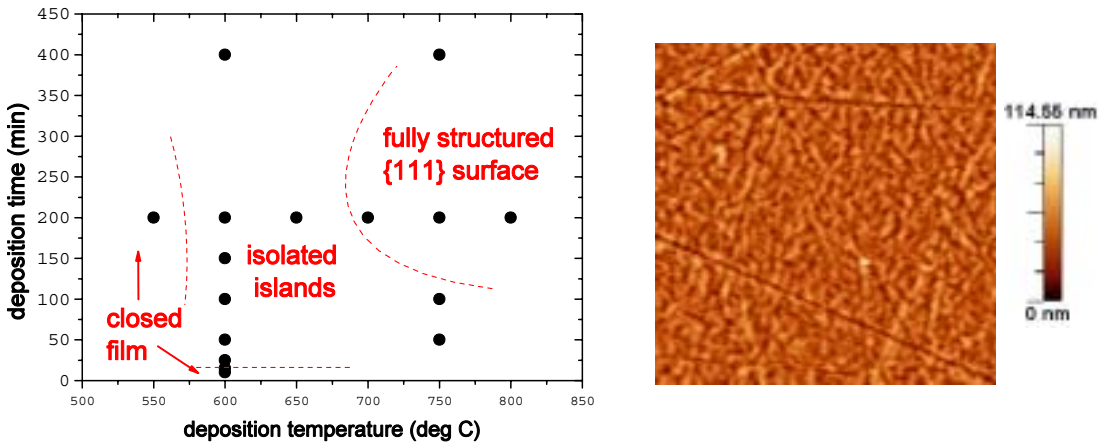

Figure 7.21: Phase diagram of the observed CCO film morphology on MAO(001) as a function of the deposition time and temperature. On the right side an AFM picture of a typical surface of a film grown at $550°C$ and $200min$ is shown. The dimensions are 10 x $10\mu m^2$ and the image edges are oriented along the [100] direction.

islands is due to the high anisotropy of the surface energy typical of the spinels favoring strongly a {111} surface although the free surface area will be increased. The bimodal size distribution of the islands in samples at low deposition temperature and high deposition times is likely due to an enhanced material incorporation by plastically relaxed islands. The long-range order of the edges was assigned partly to the morphology of the substrate, so that the growth of the islands is intrinsically self-assembled.

7.1.5 Other phenomena and open questions

Some phenomena of island growth were observed in individual samples, thus they were not included into the discussion of the general island growth. However, the observed features are interesting and are worth to be discussed. In Figure 7.22 two examples are shown. In the left image a feature formed in a sample grown at $600°C$ during $200min$ is shown. Four islands encircle a number of much smaller islands. The four encircling islands were formed during the earlier growth and in the moment, that they touched and formed a closed rectangle, the adatoms incident in this area were confined to this area, building smaller islands.

In the right image a detail of a sample grown at $750°C$ during $50min$ is shown. In an homogeneously covered area some parts are not covered by islands. While in the holes on the left side no islands are present, on the right side smaller islands are formed in the area. The surrounding islands form a kind of spiral, taking into account the elongation of the islands. A possible explanation is that in the middle of these areas defects, which inhibit the island formation, are formed. To decide, which kind of defects have this effect, the nucleation behavior must be closer investigated.

In Figure 7.23 the surface morphology of a sample grown at $600°C$ during $100min$ after a post-annealing treatment of $2h$ at $600°C$ in air is shown. Already on the large scale image (left image) inhomogeneities of the island coverage can be appreciated. In the zoom it becomes visible, that the different areas show different island sizes and density. The different areas are divided by long, straight lines without islands, which seem to follow different crystalline directions of the substrate. The origin of this behavior is

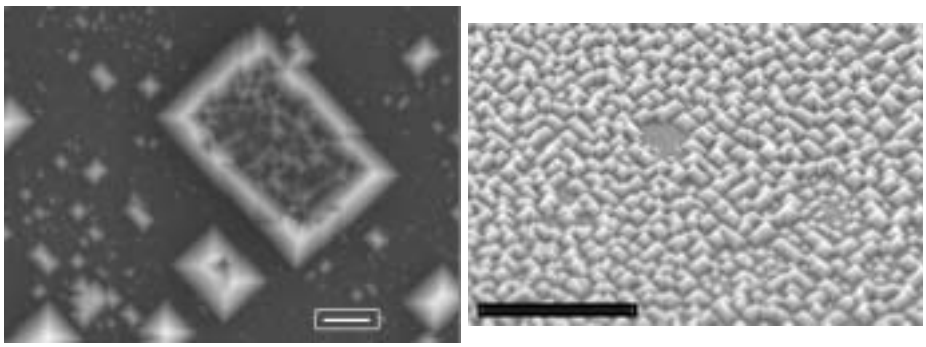

Figure 7.22: SEM images of details of sample CCO-07 (left image) and CCO-11 (right image). The scale bars correspond to $1\mu m$ and $2\mu m$, respectively.

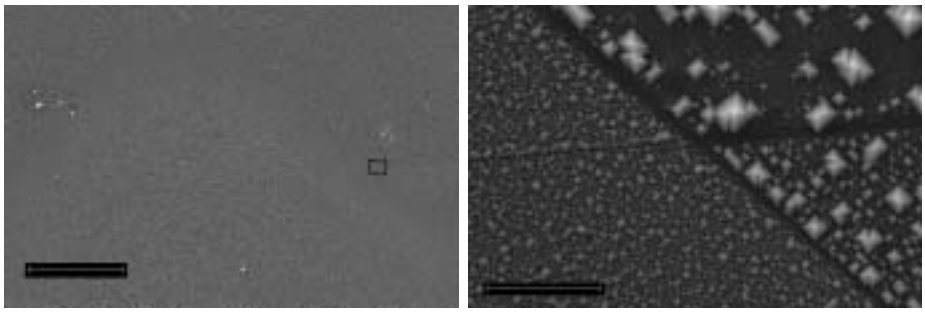

Figure 7.23: SEM image of a sample ($600°C$, $100min$) post-annealed at $600°C$ during $2h$ and a zoom of the same area. The scale bars correspond to $50\mu m$ and $2\mu m$, respectively. The rectangle in the left image indicates the zoom area.

unclear, as well as the origin of the streaks. They are possibly borders between parts of the substrate monocrystals which are slightly misoriented. Evidently, this sample was not used for the analysis of the island growth in the previous part. For the other samples the homogeneity of the samples were controlled.

Although we are able to explain the basic aspects of the growth of the islands, certain features remain unclear. The untypically big islands and their large spacing for lower deposition temperatures poses the question on the mobility of the adatoms. In the simple picture, that the islands are formed by surface diffusion of the adatoms, the way to travel to incorporate to the nearest island is quite long, up to $200nm$. Even more, the adatom density is not negligible, so that the scattering is possible. The incoming particles are ions, thus the formation of dimers or trimers cannot be excluded. Thus the mobility of the adatoms is extraordinarily high, or the mass transport takes place by other means.

A possible mechanism would be, for example, that the underlying closed CCO layer forms a kind of reservoir. In this case the islands would grow from the adjacent adatoms and the atoms already incorporated into the underlying layer. However, in this case a depletion of the underlying layer next to the islands would be expected, which was not observed for example in the cross section images (Figure 7.12). Furthermore the bulk diffusion in the underlying layer is supposedly slower than the surface diffusion of the highly energetic adatoms.

A correlated aspect is the large height of the islands. To build islands up to $400nm$ in height, the upward diffusion of adatoms must be more favorable than the downward diffusion, which would be the case of a large Ehrlich-Schwoebel-barrier. It was shown recently for the homoepitaxy of metals, that indeed the upward diffusion can be energetically more favorable than the downward diffusion at steps [245], leading to island growth. The mechanism on the atomistic level is a replacement by an adatom of an edge atom, which is pushed into the higher lying plane. A chain process throughout the islands could thus lead to a mass transport to the top of the island.

The elongation of the quadratic pyramids into hut clusters is a topic, which was discussed for the Si/Ge system. A model was proposed by Tersoff and Tromp [231],

which describes the optimal shape of the base area as a trade off between the surface energy and the strain relief at the island edges (see the discussion in Section 7.3). As will be shown, this theory does not describe the elongation of the islands in the case of the CCO islands. The reasons for the elongation are unknown.

7.2 Islands in $NiFe_2O_4$

As the formation of {111} faceted islands is due to the strong anisotropy of the surface energy as discussed in the previous part, these kind of islands should be visible also in other spinels, presuming that the film is strained and the by epitaxy induced surface is a {001} plane. Mishra and Thomas [42] calculated the surface energies for some spinels, including $NiFe_2O_4$ (NFO), and showed the strong anisotropy for these materials. Consequently the pyramidal islands could be observed in NFO, too. Indeed, as already stated in Section 5.3.2, post-annealed samples of the NFO films grown in pure Ar atmosphere on $SrTiO_3$(001) show the formation of three dimensional islands for 3 and 6nm thick films. In Figure 7.24 AFM images in a three dimensional view are shown.

The morphology of the samples show well-defined islands, aligned with their edges along the [110] directions. The mean value of the angle between the facet and the surface is 51.5°, which is near to the value of {111} planes in a cubic crystal of 54.7°. The deviation is due to the finite size of the AFM tip, which distorts the objects. The size of the islands is typically some 20 to 30nm, which is the same length scale like the ripples in the as-grown samples or the grains in the sample post-annealed at 600°C. The aspect ratio of the islands is typically 0.8, thus approximately the value expected for {111} faceted islands.

The observed islands in the post-annealed samples corroborate the thesis, that the observed faceting of the islands is a result of the strong anisotropy of the surface energy. Also in this system with STO as the substrate, the misfit is high (6.2% compressive) and the flat surface would be a {001} surface, so that the islands should appear. Even more, the post-annealing experiments show, that the relatively flat surface of the as-grown film is a metastable state, while the islands appearing after the heat treatment form the stable surface. Here, effects of the growth kinetics can be strictly excluded to be the origin of the island formation. The islands were formed on a third substrate after MAO

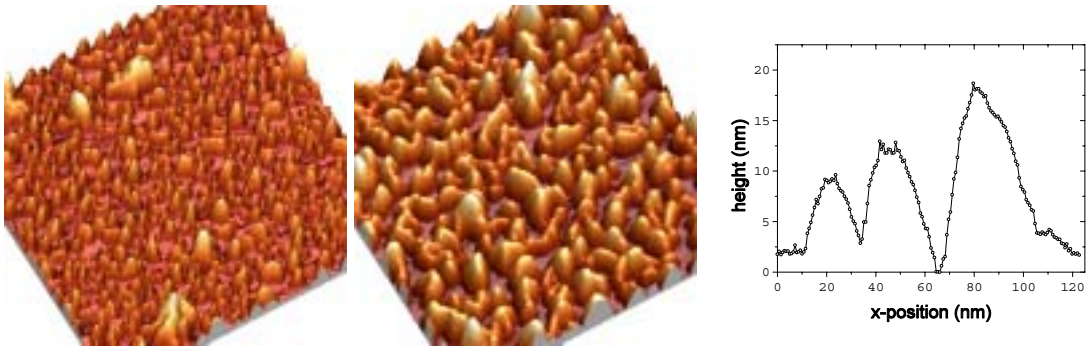

Figure 7.24: 3D AFM images of a 3 (left image) and 6nm (right image) thick NFO film grown in pure Ar and after a post-annealing at 800°C. The images have a size of 1μm x 1μm. The image edges are aligned with the STO [100] directions. In the panel on the right a height profile of a part of the left image is shown.

and MgO. The STO does not influence the shape of the islands, for the influence of the size and the density more experiments must be made on thicker films.

The formation of the flat, metastable surface morphology of the as-grown films is comparable to the underlying layer build in the CCO system. The thickness of the NFO samples is much lower than that of the discussed CCO samples. Furthermore the growth parameters will have an influence, for instance the growth rate, which was much smaller for the NFO films. The lower supersaturation results in a slower incorporation of the material into the islands. Also the deposition technique was different (see Section 4.1): the off-axis geometry in the case of the NFO films leads to low bombardment of the surface by the ions in the plasma.

However, the appearance of the islands in this system is not due to a strain relief, because the films in the as-grown state are already relaxed. The introduction of {111} facets is only due to the interplay between the enhancement of the free surface energy due to the higher surface and the decrease due to the introduction of the minimum energy facets. Evidently the energy gain in introducing the {111} facets is higher than the cost of the large free surface of the high aspect-ratio islands.

7.3 Comparison to Si/Ge

Regarding the shape of the observed islands, the semiconductor system Ge on Si(001) shows a similar growth behavior. In Figure 7.25, a typical surface morphology for thin films is shown. This system was investigated theoretically very intensively, so that a comparison of the CCO system to this one can lead to insights in the growth of the CCO islands.

Description of Si/Ge islands

The discovery in 1990 [246] of the growth of Ge pyramids and hut clusters on Si(001) triggered an enormous interest in the self-assembled growth of semiconductors. It was observed that these islands, having a size of a few nanometers, appeared by a Stranski-Krastanov mechanism induced by the 4% lattice mismatch. These objects are coherent (dislocation free) and their size distribution is narrow (i.e., growth is self-assembled). Moreover they can show self-organization and some of their characteristics as number and size can be partially tuned by growing SiGe alloys of a varied stoichiometry [247], changing the amount of deposited material, or adjusting processing parameters such as growth rate or temperature [228, 229, 232]. The lateral surface of the Ge pyramids are {105} facets forming an angle of only 11.3° with the substrate surface. There are still important problems in the reproducible fabrication of organized SiGe structures, some of these difficulties arise from the shape transition to multifaceted domes that the objects undergo during growth [227, 230]. The transition complicates the fabrication of objects having a single shape, limits the range of attainable sizes, and the faster growth rate of domes compared to {105} pyramids results in bimodal size distributions.

On the other hand, theoretical work was carried out to elucidate the energetical landscape of the islands. A relatively simple model [231], where the extra surface and interface energy was compared to the energy gain due to elastic relaxation at the edges of the island, was able to explain the formation and shape of the islands of pyramids and hut clusters, where the latter were observed only above a critical amount of material.

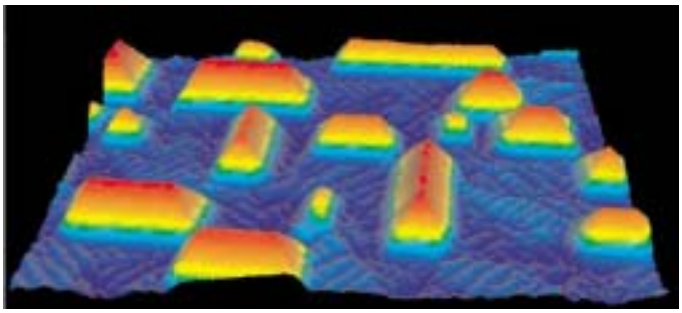

Figure 7.25: 3D view of a scanning tunneling micrograph of the morphology of a 1.81 monolayer thick Ge film on Si(001) after Voigtländer [228]. The image size is 130nm x 100nm.

Goryll et al [233] observed in their experiments in addition to the coherently strained islands described by [231] relaxed islands with a different faceting and a larger size, as did Medeiros-Ribeira et al [227]. The difference in size between the coherently strained and the relaxed islands was ascribed to a discontinuity in the chemical potential of the relaxed islands leading to an enhanced adatom incorporation. Later on this behavior was confirmed theoretically by Ross et al [248].

The important role of the elastic energy makes the surface morphology strongly dependent on the misfit. By adding Si to the Ge layer, the misfit can be varied and with it the morphology [229, 249]. Another mechanism to order the islands was found in the $Ge_{1-x}Si_x$ islands: the two atoms have different surface diffusion coefficient on the Si surface, so that the islands should form a regular pattern on the surface [250, 251].

With the same approach of thermodynamic equilibrium, a model was developed taking into account also the interaction between the islands in the form of a stray field mediated by the substrate [74, 252, 253]. It was shown, that the islands can form a spontaneous ordered array with a narrow size distribution due to a minimum in the chemical potential as a function of the island volume [74, 254]. Only after this minimum is reached, the islands will start to introduce dislocations and grow further [255]. Daruka et al developed from this a phase diagram for different growth modes including bimodal size distributions [252] and showed that the island shape is basically material independent, which was proved experimentally for the Ge/Si system and the InAs/GaAs system [256].

Comparison with CCO islands

In the growth of Si/Ge islands basically two states are found: coherently strained pyramids and hut-clusters with {105} facets and relaxed domes with a different faceting and a larger size. In the growth of the CCO no such shape transition with increasing size was observed due to the high anisotropy of the surface energy with a minimum for the {111} planes. In the Si/Ge system a lower anisotropy is present, so that other facets can be introduced above a critical size.

Regarding the driving forces of the island formation and shape transition the two systems are not too different. The base of both is the same: the islands form due to strain relief. The gain in elastical energy overcomes the higher surface energy, so that islands are introduced. The stage of coherently strained islands in the CCO system was not observed directly (see Figure 7.4 and the discussion in Section 7.1.4), but could be attributed to the monomodal size distribution observed in the $25min$ sample. The strong growth rate of some of the islands in the Ge/Si system is due to the change of the chemical potential, when a pyramid becomes a dome, which is a result of the lower energy state of the less strained dome [244]. A similar mechanism is proposed to take place in the CCO system. Here the strong growth rate of one part of the islands is thought to be due to the introduction of dislocations of some islands depending on their size.

Most of the experiments and theories in the Si/Ge system were done for the stage of coherently strained islands. This stage was observed only for very small islands in the CCO system and the emphasis of the study was put on the investigation of later

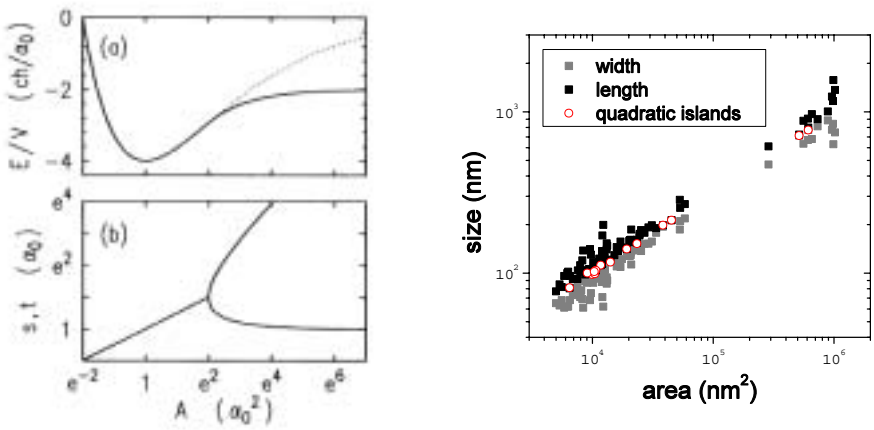

Figure 7.26: Top panel: Total energy per unit volume of an island versus the base area (dotted line: when island keeps a square base) after [231]. Bottom panel: Width and length of an island versus base area. Right side: Length and width vs area for CCO on MAO ($600°C$, $200min$).

growth stages. However, one study on Si/Ge allows the direct comparison regarding the introduction of hut clusters. The paper by Tersoff and Tromp [231] proposes a very general explication for this: at a critical area a_0 the optimal size of a pyramidal island (i.e. with a square base) as a trade-off between the enhanced surface energy and the possible strain relief is reached. If the island grows further, the minimum energy shape is a hut-cluster (i.e. a pyramid with a rectangular base area). Due to the crossover in energy, one of the base axis will grow larger than the other one (see Figure 7.26). As the theory relies only on the surface energy and the elastic energy, the critical area should be material dependent, but the formation of hut clusters after a critical area should be observed also in other systems.

To compare the behavior of the islands found in the CCO/MAO with this theory, the length and the width of the islands of a film grown at $600°C$ during $200min$ was plotted versus the area. The quadratic islands are plotted with open circles. The pyramids coexist with the hut clusters for all the measured range, so also in a stage of coherently strained islands in the CCO system pyramids existed with the same size as the hut cluster. Comparing different deposition temperatures and times, we found a part of 20 to 40% of quadratic islands coexisting in the same area range with the hut-clusters. Only the sample grown at $600°C$ and $25min$ shows a population nearly exclusively of pyramids. Thus the theory of Tersoff and Tromp does not describe the emergence of hut clusters in the CCO system, so the origin must be found in other aspects than the proposed ones.

7.4 Discussion

The growth of two different spinel materials on three different oxide substrates shows a three dimensional island formation as the thermodynamically stable morphology. As pointed out before, the reason is to be found in the low energy of the {111} planes, which overcomes together with the minimization of the elastic energy at the island edges the higher surface energy of the islands. As the anisotropy of the surface energy is typical for the spinels, these kind of islands should be expected in most of the spinel materials assuming the growth on a substrate with a misfit and which imposes a (001) surface.

The choice of the spinel material following the results of this thesis can be made in the group of the ferrites and the chromites, but supposedly the choice is even wider. However, the growth of these kind of islands was not published until now, although this special morphology should be the thermodynamically stable surface. Suzuki et al [157] published a very interesting AFM picture of the surface of a CCO film. The roughness is extremely high: in a film of $100nm$ a peak-to-valley value was found of $80nm$. Furthermore the grains are elongated in one direction. Although the grains do not show a pyramidal shape (or it was not resolved in the measurement), the morphology reminds strongly the morphology found for the CCO films of this thesis.

Recently, ferrites were codeposited together with ferroelectric materials resulting in ferrite columns in a ferroelectric matrix [88], and the authors claimed that this is possible with a row of ferrites. Possibly the columnar growth of the ferrites reflects the island growth of these materials. It also has to be pointed out, that in the NFO films the island morphology in the as-grown state was a flat, metastable surface (see Section 5.2.2). Even more, for the films grown in a Ar/O_2 atmosphere a very smooth surface was found (see Section 5.1.2), so the resulting surface of an oxide film is dependent on the deposition conditions.

Regarding the possible substrate, the influence of it is confined to the size and the density of the islands. As pointed out before, the important factor is the (001) out-of-plane orientation and the epitaxial growth. On the other hand, the influence on the density and size can be used to control the size distribution and the nucleation sites. For the samples on MAO and low deposition times, the size distribution was comparatively narrow and the islands had a regular distance. The observed long-range order in the samples due to the polishing streaks on the surface of the MAO (as well as the study by Kim et al [235], where Ge islands were grown on a surface with buried dislocation lines) shows a possibility to control very effectively the nucleation sites by prepatterning the surface [257]. A possibility would be to use the steps of an annealed STO(001) surface (see appendix A1-2) to create preferred nucleation sites. The density could be controlled with the miscut angle.

The particularities of the spinel islands make this system valuable for application. The ferrites have interesting magnetic and electric properties, including a high spin-polarization combined with a Curie temperature far above room temperature. If the growth can be controlled, small ferrite islands could be grown epitaxially on a surface to form a high density memory device. A way to control the uniformity of this material was proposed already: using relatively low deposition temperature, few deposited material

and a prepatterned substrate to control the nucleation sites. But the study of these islands is not only interesting for application. The islands form a model system to investigate for example the surface diffusion and growth mechanism in materials, which consist of atoms of more than one element. The theory of the growth of oxides is very complex, as different cations are involved and an ordering of the ions must be reached. Investigating the growth of a single island, interesting insights into the growth mechanism of oxides can be gained.

8 Main results and remaining questions

8.1 Properties of $NiFe_2O_4$ thin films

Thin spinel oxide films of $NiFe_2O_4$ (NFO) were grown by RF sputtering on $SrTiO_3$(001) to study the magnetic and electric properties in order to integrate them into heterostructures for spintronics devices. An epitaxial growth of the films was observed with a cube-on-cube relationship with the substrate.

It is found that the epitaxial growth allows the stabilization of novel spinel $NiFe_2O_4$ phases that do not exist in its bulk form, having remarkable distinct properties, such as a dramatic enhancement of the magnetic moment. The magnetic moment of ultrathin films is found to be up to $1200 emu/cm^3$, which is 4 times the bulk value of $300 emu/cm^3$. We argue that the enhanced moment results from a partial cation inversion of NFO, in which Ni^{2+} ions are distributed among the two available sites -octahedral and tetrahedral- of the spinel structure.

It was also found, that a change of the oxygen partial pressure in the deposition atmosphere leads to the ability to tune the electrical properties of the films, changing from insulating in an Ar/O_2 atmosphere as in bulk to conductive in a pure Ar atmosphere. Oxygen vacancies are likely to promote the metallic behavior by inducing mixed-valence $Fe^{2+/3+}$ states at the octahedral sites.

8.1.1 Magnetic structure of ultrathin $NiFe_2O_4$ films

The enhanced magnetic moment was explained by an ion redistribution on the spinel A- and B-sites. A part of the Ni^{2+} ions, in the bulk material only found on B-sites, are located on A-sites substituting the Fe^{3+} ions, which in turn are located on the B-sites. In very thin films for a thickness of 3 to $4nm$ all Ni ions were found on A-sites, thus constituting the normal spinel structure.

To clarify the magnetic structure of these films it is fundamental to have a direct proof of the cation redistribution and the existence of Fe^{2+} ions. In nanoparticles Mössbauer spectroscopy was chosen to measure the ion distribution (see Section 3.1.1), as the coordination of the Fe ions can be measured by this technique. By comparing the intensity of the lines observed for octahedrally coordinated Fe ions with that of tetrahedrally coordinated Fe ions, the site occupation of the Fe can be deduced with a low error bar. However, for thin films this experiment is difficult to realize, as a certain amount of ^{57}Fe in the sample is needed. The films must be made with an enriched

iron, thus also the target. As two targets are necessary, which are quite big, the sample preparation will be too expensive.

In scattering techniques like Extended X-ray Absorption Fine Structure (EXAFS) (for references see Section 3.1.1) or X-ray Magnetic Circular Dichroism (XMCD) [110, 258, 259], the repartition of the ions can be studied, too. In XMCD the magnetic moment of one element is deduced from the dichroism at the absorption edge. The location of the Ni ions on both A- and B-sites can be observed by a negative and a positive contribution to the XMCD signal, as the A- and B-sublattice are coupled antiferromagnetically. Furthermore a pre-edge feature of the Fe K-line is attributed to Fe ions on tetrahedrally coordinated sites [259], so that an eventual cation inversion from the inverse to the normal spinel structure can be observed in XMCD measurements. As XMCD is a surface sensitive technique, even smallest amounts of magnetic ions can be detected [260], so that also the properties of films with a small thickness can be measured. A project to measure the cation distribution of the NFO films was accepted at Eletra, Trieste.

Regarding the preference of Ni^{2+} ions for octahedral sites as found in bulk [40], the origin of the observed cation inversion has to be investigated. As cation inversion is promoted by the interfaces (see Section 5.2.4), it would be interesting to study the interface of STO and NFO. Also here a theoretical description of the influence of the interface (for instance due to strain or deformation of the film, binding energy and local surrounding of the ions) would be highly appreciated. From the experimental point of view the initial stages of the growth of NFO can be studied by deposition of very few amounts of NFO on a substrate and investigate by spectroscopy techniques the coordination and site occupation of the Ni and Fe ions, as was done for instance for magnetite by Ritter et al [193]. Probably the normal spinel structure is favored by the change of the energetics at the interface.

8.1.2 Conducting phase of $NiFe_2O_4$

For the films grown in the pure Ar atmosphere, a conductive phase of NFO was found. The conduction mechanism was proposed to be electron hopping along a chain of mixed valence $Fe^{2+/3+}$ ions located at the B-sites. Furthermore, this conduction mechanism leads to a double exchange coupling of the B-sites. Thus the magnetic and electric properties are strongly correlated: the ion redistribution leads to an enhanced number of Fe ions on B-sites, so that the hopping conduction gets possible.

This conductive phase of NFO is very interesting from the point of view of application in spintronics. But also from the point of view of the fundamental magnetic and electric structure of this material. Besides magnetite it is the only conducting ferrite, so insight into still discussed topics of magnetite can be won by studying NFO.

To evidence the proposed conduction mechanism, the valence state of the Fe ions must be determined. With XMCD it is also possible to distinguish between Fe^{3+} and Fe^{2+} ions, as the L-edge absorption peak of Fe^{2+} occurs at a lower energy than that of the Fe^{3+} [111]. Thus with a comparison of the Fe L-edge spectra between NFO films grown in pure Ar and in a mixed Ar/O_2 atmosphere, the existence of Fe^{2+} ions can be studied.

If the hypothesis of electron hopping along chains of mixed valence Fe ions on B-sites is confirmed, the conductive NFO phase can be used to investigate the properties of conducting ferrites. As a half-metallic behavior is found for other double-exchange systems (as magnetite or doped manganites [5]), a high spin-polarization can be expected for the conductive NFO, too. Spin-dependent photo emission is the adequate technique to measure the spin-polarization of the normal spinel, conductive NFO phase. Band structure calculations would give insight into the transport properties and the highest, theoretically possible spin-polarization.

8.2 Spin-dependent transport measurements of $NiFe_2O_4$ thin films

We have taken advantage of our ability to obtain epitaxial ferromagnetic $NiFe_2O_4$ films of metallic or insulating character to integrate them in two different spintronics devices, namely a magnetic tunnel junction and a spin filter.

The conductive NFO films were used as ferromagnetic electrodes in a magnetic tunnel junction. A substantial tunnel magnetoresistance has been measured up to a temperature as high as $280K$, with values corresponding to a spin polarization of NFO of about 40%, essentially constant up to the highest measured temperature. These results suggest that this novel metallic phase is an interesting candidate for highly spin-polarized materials for spintronics.

The insulating NFO was successfully implemented as a ferrimagnetic tunnel barrier into a spin filter device and is thus the first spin filter realized with a complex oxide barrier. A filtering effect has been observed and signaled by a tunnel magnetoresistance reaching values up to about 50%. From the experimental barrier height we were able to extract a qualitative sketch of the band structure of normal spinel NFO.

8.2.1 Magnetic tunnel junction containing conductive $NiFe_2O_4$

The conductive NFO can be applied for the realization of high magnetoresistive magnetic tunnel junctions. As problems due to antiphase boundaries (see Section 2.3.2) can be avoided, a full spinel tunnel junction promises a good performance, which could be a tunnel junction with magnetite and NFO as electrodes. A tunnel junction with two NFO electrodes is possible, too, and promises a high magnetoresistive effect even at room temperature, as the conductive NFO phase does not show the decrease of spin-polarization approaching room temperature as reported for magnetite (see Section 3.2.2). The coercive field of the electrodes can be varied via the level of cation inversion, i.e. by the thickness, as the coercive field and the saturation magnetization are correlated (see Figure 5.34 on page 94). Another possibility to vary the coercive fields of the two electrodes would be an exchange coupling with an antiferro- or ferrimagnetic material, as for example $CoFe_2O_4$ [165].

As the barrier material preferably a spinel is chosen. $CoCr_2O_4$ was used by Hu et al [181], but the problems of three dimensional growth mode must be carefully investigated.

On the other hand, other non-magnetic spinels can be found, which are insulating.

8.2.2 Spinfilters with a spinel barrier

It was shown that NFO, in the insulating phase, is an adequate material for a spin filter barrier. However, the spin filter effect was observed only below $140K$, although the Curie temperature of the LSMO and the NFO are above room temperature. Therefore a coupling between the two layers was invoked (see Section 6.2.2).

To develop a spin filter working at room temperature, the coupling of the magnetic layers must be reduced. For this reason the introduction of a non-magnetic insulating layer ($0.8nm$ STO) between LSMO and NFO was already investigated and resulted in a similar temperature dependence of the TMR (see Section 6.2) as without the STO layer. The temperature dependence of the TMR for thicker STO layers has to be investigated. However, the hybrid barrier has to allow the tunneling transport, so that the layer thickness of the STO cannot be chosen too thick.

The coupling results from the similar coercive fields of the LSMO and the NFO layer at higher temperatures, thus another possibility to reach an antiparallel state would be to increase the coercive field of the NFO or even to shift the hysteresis loop along the field axis by the exchange coupling with an antiferromagnetic material. But the realization of such kind of heterostructure is difficult, as the NFO has the role of the barrier. The choice of conducting antiferromagnetic oxides is small, so the easier way would be to introduce a hybrid barrier with a antiferromagnetic insulator between the nonmagnetic electrode and the NFO, as for example NiO [175]. However, an antiferromagnetic barrier could depolarize the tunnel current.

A pinning of the LSMO electrode would be easier to realize, especially as it was shown that it is possible for example by an underlying $(La, Ca)MnO_3$(LCMO) layer [261–263]. This works only up to the Néel temperature of the antiferromagnetic LCMO, which is in the range of $220K$ for the antiferromagnetic phase. But a slight enhancement of the coercive field of the LSMO would lead to a decrease of the working temperature of the spin filter, as the LSMO is the material with the lower coercive field. By a magnetic hardening of the LSMO the coercive fields of the NFO and LSMO would approach.

Thus, the most adequate way is a revision of the choice of the materials. Keeping the NFO barrier, the choice of the electrode material was already discussed at the beginning of Chapter 6. The alternatives for the bottom electrode are few, but if the bottom electrode would be chosen non-magnetic, a magnetic metal with a high T_C could be used as the top electrode. One possibility is doped STO, for example with Nb, which results in a semiconducting STO. As the growth of NFO on STO was already investigated, the development of this kind of heterostructure could lead quickly to results. On the other hand NbO would be an adequate candidate, too. It is a metallic, non-magnetic material with a cubic structure and a lattice parameter of $0.42nm$. First experiments on the growth of NFO on this material are started.

But also the barrier material can be revised, as many insulating, magnetic materials exist in the group of the ferrites. For instance $CoFe_2O_4$ shows a high coercive field [165] as a result of the strong magnetocrystalline anisotropy [10] due to the Co^{2+} ions on the

octahedral sites [258]. Its high Curie temperature allows as well as NFO a spin filter working at room temperature. The band structure of this material was calculated by Jeng [221], showing a gap of $1eV$ for the minority spins and $2eV$ for the majority spins. With Equation (2.1.2) the spin filter efficiency is calculated to be 30%, which would lead in case of a LSMO magnetic electrode to a magnetoresistance of 75%. Thus $CoFe_2O_4$ would be an adequate barrier material.

Another possible barrier material is $CoCr_2O_4$ (CCO), as it was already used as a barrier in magnetic tunnel junctions [181]. The Curie temperature of CCO is $100K$ (see Section 2.3.2), which allows the investigation of the spin filter effect near to the transition to the paramagnetic state of the barrier. Even more, band structure calculations for this material do not exist, so that the investigation of it by spin-dependent transport can give insight into the electronic structure of the CCO. Although it was shown that CCO layers have a strong tendency to form three dimensional islands (Chapter 7), thin films of this material were grown on $La_{2/3}Ca_{1/3}MnO_3$ in this thesis. The results are summarized in appendix A2, showing that it is not possible to suppress the three dimensional growth mode, at least not in the chosen range of deposition parameters. To develop a CCO film which can be used as a tunnel barrier, more experimental work has to be carried out.

Due to the few theoretic and experimental works on the spin filter effect (for an overview see Section 2.1.2) also fundamental investigation of the effect is important. First, the dependence of the magnetoresistance on the applied bias voltage is not clear. While the theory predicts an initial increase with increasing voltage, the experimental data do not show this feature. The origin of this deviation between theory and experiment is not clear. Also effects like the creation of magnons in the barrier has not been investigated until now. In case of the spin filters realized in this thesis, the contribution to the voltage dependence of the LSMO electrode inhibits a careful investigation of the voltage dependence. It is therefore important to change the electrode (see discussion above). If the magnetic electrode can be chosen among the magnetic metals, parasite effects like the creation of magnons in the electrodes can be avoided.

8.3 Self-organized growth of spinel islands

A self-organized structure of isolated pyramids and hut clusters with {111} facets develops in (001)-oriented epitaxial CCO films on MAO and MgO substrates. It was shown that varying the deposition conditions the size of the objects can be tuned, and that a {111} fully faceted surface can be obtained. As the driving force for the growth of the {111} faceted objects, the anisotropy of the surface energy in spinels and the possibility of stress relaxation at the island edges was found, and possible mechanisms were proposed to explain the observed size distributions and long range order. The same type of islands were found also for NFO showing that the formation of islands is independent on the spinel material and on the strain state of the film.

Our findings have evidenced that the growth of complex oxides can promote a variety of self-organized morphologies not necessarily predictable from the widely investigated growth of semiconductors and, perhaps leading to a more reproducible and simpler fab-

rication process. Even more, the combination of the rich physical properties of complex oxides and the long range ordering of nano/micro single-faceted objects might lead to novel functionalities.

To apply the CCO film as it was thought originally, thus as a barrier in a spin filter, it is crucial to avoid the three dimensional growth mode. For this reason the growth of CCO on LCMO was investigated for very low film thickness (see appendix A2), but island growth was found to take place for a film thickness as low as $3nm$. The surface resistance of the samples is highly inhomogeneous, indicating that the CCO has, however, an insulating character. The deposition of a CCO film on a {111} oriented growth template could lead to the desired effect. In this way the low energy surface of the spinel system is the film surface. This effect was already investigated for the NFO films grown with an Ar atmosphere, which show on a STO(001) substrate a three dimensional growth and on a Pt(111) surface a smooth two dimensional growth.

There are other possibilities to impose a two-dimensional growth mode, but they are far harder to realize for a heterostructure with CCO as a barrier. The growth on vicinal substrates could lead to a smooth film, as the heterogeneous nucleation at the steps is energetically favorable for the adatoms. The resulting step flow mode can avoid the formation of three dimensional grains, at least for small film thicknesses. However, the vicinality of the substrate surface must be kept by the bottom electrode morphology, thus the growth of this layer must be very well controlled.

Also, the CCO films could be grown with deposition parameters, which do not allow the surface diffusion of the adatoms, for instance a high supersaturation or low deposition temperatures. It was observed for CCO films grown at $550°C$, that a continuous layer was formed, although it was very rough. On the other hand, this way will lead to poorly crystalline films, as the adatoms are basically confined to the place where they are incident on the surface. Thus a low epitaxial quality, as well as inhomogeneities of the composition can be the result. Furthermore, the films will still show a substantial roughness, which is undesirable for tunnel barriers.

However, the three dimensional growth mode, forming islands or fully (111)-structured surfaces, constitutes a new area of research, as this growth mode was not observed for complex oxides before. Besides the possibility to investigate the growth processes involved, the islands are also interesting from the point of view of application.

One interesting aspect of these islands is their magnetic properties. In thin film growth the dimensions can be reduced only in one dimension, while the island growth allows the reduction in all three dimensions. The effects of the reduced dimensions of ferrite nanoparticles on their magnetic properties were investigated and a surface shell of disordered spins was found [58], as it was found also in this thesis for the magnetic properties of the NFO islands. An exchange biasing of the hysteresis loop was observed, ascribed to the coupling between a magnetically disordered part at the island surface and an ordered part in the island's core.

However, while NFO has a Néel structure (see Section 2.3.2), CCO has a spin cone structure. Thus the disorder at the surface can have another effect on the magnetic properties as observed for the ferrites. For the CCO islands it was shown, that they are also magnetic, but hysteresis loops were not collected due to the small signal of the

CCO. With an adequate technique like, for instance, the magneto-optical Kerr effect, which is surface-sensitive, or the tracing of hysteresis loops with XMCD, the hysteresis loops could be measured and the effect of the surface spin disorder could be investigated.

Also the domain structure of very small islands would be interesting. Pan et al [264] investigated the domain structure of patterned squares of magnetite and found an unusual domain structure, which was ascribed to the strong influence of antiphase boundaries on the magnetic properties of the islands. As the CCO islands do not coalesce during the growth, the density of antiphase boundaries should be drastically reduced and the domain structure independently on the antiphase boundaries can be investigated.

As the magnetic properties are size dependent, the strongest challenge is the preparation of samples with a uniform size distribution. The control of the island size is crucial to investigate the physical properties of an ensemble of islands. Unfortunately the observed bimodality of the size distribution at lower deposition temperatures leads to an ensemble of islands with two families of different size. At higher deposition temperatures the bimodality vanishes, but the islands touch each other. Thus to investigate the magnetic properties of single islands, a possible way to decrease the width of the size distribution is to avoid the bimodality at low deposition temperatures. It was suggested that the bimodality arises as the chemical potential of already relaxed islands is much smaller than the one of coherently strained islands, thus the adatoms are incorporated preferably into the relaxed islands.

Following this model there must exist a stage of growth, where all islands are still strained and thus the size distribution is monomodal. Such a morphology can be observed in Figure 7.11 (c) on page 130. The islands are all quadratic and have a homogeneous size. It would be interesting to investigate this stage of growth further, for example to determine the influence of deposition temperature and deposition rate on the size and density of these islands. By adjusting the deposition time it is possible to prepare samples with islands sizes below $100nm$ and a narrow size distribution.

Recently the control of the spatial distribution of self-assembled nanoobjects was investigated for the application to nanoelectronics. In case that the nanoparticles are magnetic, they could serve as a high density magnetic memory. For this application not only a narrow size distribution is important, but also a homogeneous spatial distribution. For the islands of CCO it was found that the spatial distribution is strongly influenced by the substrate surface morphology. This allows to control the spatial distribution by a controlled patterning of the substrate. It was shown that $MgAl_2O_4(001)$ (MAO) surfaces reorganize after a thermal and etching treatment to a stepped surface with terraces along the [110] direction [265]. Even more, the shape of the terraces can be controlled by the miscut of the substrate. If the islands nucleate preferred at the steps or on the terraces, the spatial distribution can be very well controlled.

The application as magnetic nanodots of the CCO islands for magnetic storage for example is not evident. The low magnetic moment as well as possible surface spin disorder are the drawback of these islands. However, $NiFe_2O_4$ or $CoFe_2O_4$ could be appropriate alternatives, as they have a high T_C and a high magnetic moment. On the other hand, very interesting experiments of optical pumping were made on GaN pramids [266]. The emission spectra of the islands after individual optical pumping

show single- or multi-mode peaks due to the reflection of the light on the pyramid walls. Thus the pyramid acts as a cavity and the wavelength of the emission peak can be controlled by the size of the island. As the CCO islands are insulating, a similar experiment could lead to similar results.

The fully {111}-structured surface found for higher deposition temperatures can be applied as a growth template, which permits to form well-defined pyramids and hut clusters of materials, which do not show a spontaneous three dimensional growth mode. The valleys of the surface can be filled with another material to produce quantum dots. If a magnetic material is used, this can provide a way to develop magnetic storage media, under the prerequisite of a spatially controlled growth of the CCO template. Or, for an optically active material, laser arrays can be build. Thus the self-organization of the CCO surface can be used to organize another, functional material.

Bibliography

[1] G. A. Prinz, *J. Mag. Mag. Mat.*, **200**, 57 (1999).

[2] S. A. Wolf, D. D. Awschalom, R. A. Buhrmann, J. M. Daughton, S. von Molnar, M. L. Roukes, A. Y. Chtchelkanova, and D. M. Treger, *Science*, **294**, 1488 (2001).

[3] I. Zutic, J. Fabian, and S. D. Sarma, *Rev. Mod. Phys.*, **76**, 323 (2004).

[4] R. A. de Groot, F. M. Mueller, P. G. v. Engen, and K. H. J. Buschow, *Phys. Rev. Lett.*, **50**, 2024 (1983).

[5] R. A. de Groot and K. H. J. Buschow, *J. Mag. Mag. Mat.*, **54**, 1377 (1986).

[6] J.-H. Park, E. Vescovo, H.-J. Kim, C. Kwon, R. Ramesh, and T. Venkatesan, *Nature*, **392**, 794 (1998).

[7] M. Bowen, M. Bibes, A. Barthélémy, J.-P. Contour, A. Anane, Y. Lemaitre, and A. Fert, *Appl. Phys. Lett.*, **82**, 233 (2003).

[8] M. B. Salamon and M. Jaime, *Rev. Mod. Phys.*, **73**, 583 (2001).

[9] A. Fairweather, F. F. Roberts, and A. J. E. Welch, *Rep. Prog. Phys.*, **15**, 142 (1952).

[10] R. A. McCurrie, Ed., *Ferromagnetic Materials: Structure and Properties*, Academic Press, 1994.

[11] M. Ziese, *Rep. Prog. Phys.*, **65**, 143 (2002).

[12] M. Ziese and M. J. Thornton, Eds., *Spin Electronics*, Springer, 2001.

[13] M. Julliére, *Physics Letters*, **54**, 225 (1975).

[14] J. S. Moodera, L. R. Kinder, T. M. Wong, and R. Meservey, *Phys. Rev. Lett.*, **74**, 3273 (1995).

[15] R. Meservey and P. M. Tedrow, *Physics Reports*, **238**, 173 (1994).

[16] J. C. Slonczewski, *Phys. Rev. B*, **39**, 6995 (1989).

[17] R. Meservey and P. M. Tedrow, *Phys. Rev. Lett.*, **26**, 192 (1971).

[18] J. Bardeen, *Phys. Rev. Lett.*, **6**, 57 (1960).

[19] J. G. Simmons, *J. Appl. Phys.*, **34**, 1793 (1963).

[20] J. G. Simmons, *J. Appl. Phys.*, **34**, 2581 (1963).

[21] Y. Xu, D. Ephron, and M. R. Beasley, *Phys. Rev. B*, **52**, 2843 (1995).

[22] R. Y. Gu, L. Sheng, and C. S. Ting, *Phys. Rev. B*, **63**, 220406 (2001).

[23] L. Esaki, P. J. Stiles, and S. von Molnar, *Phys. Rev. Lett.*, **19**, 852 (1967).

[24] N. Mueller, W. Eckstein, W. Heiland, and W. Zinn, *Phys. Rev. Lett.*, **29**, 1651 (1972).

[25] E. Kisker, G. Baum, A. Mahan, W. Raith, and K. Schroeder, *Phys. Rev. Lett.*, **36**, 982 (1976).

[26] J. S. Moodera, X. Hao, G. A. Gibson, and R. Meservey, *Phys. Rev. Lett.*, **61**, 637 (1988).

[27] A. Saffarzadeh, *J. Mag. Mag. Mat.*, **269**, 327 (2004).

[28] J. S. Moodera, R. Meservey, and X. Hao, *Phys. Rev. Lett.*, **70**, 853 (1993).

[29] T. S. Santos and J. S. Moodera, *Phys. Rev. B*, **69**, 241203 (2004).

[30] P. LeClair, J. K. Ha, H. J. M. Swagten, J. T. Kohlhepp, C. H. van de Vin, and W. J. M. de Jonge, *Appl. Phys. Lett.*, **80**, 625 (2002).

[31] C.-R. Chang and S.-P. Chen, *J. Mag. Mag. Mat.*, **209**, 61 (2000).

[32] A. Saffarzadeh, *Phys. Lett. A*, **270**, 353 (2000).

[33] A. Saffarzadeh, *J. Phys.: Condens. Matter*, **15**, 3041 (2003).

[34] D. C. Worledge and T. H. Geballe, *J. Appl. Phys.*, **88**, 5277 (2000).

[35] F. C. Voogt, T. T. M. Palstra, L. Niesen, O. C. Rogojanu, M. A. James, and T. Hibma, *Phys. Rev. B*, **57**, 8107 (1998).

[36] J. B. Goodenough, *Metallic oxides*, Pergamon Press Ltd., 1973.

[37] P. Anderson, *Phys. Rev.*, **79**, 350 (1950).

[38] D. S. McClure, *J. Phys. Chem. Solids*, **3**, 311 (1957).

[39] P. O'Handley, *Modern Magnetic Materials: Principals and Applications*, Wiley, 2000.

[40] A. N. Cormack, G. V. Lewis, S. C. Parker, and C. R. A. Cattlow, *J. Phys. Chem. Solids*, **49**, 53 (1988).

[41] K. Tsukimura, S. Sasaki, and N. Kimizuka, *Jpn. J. Appl. Phys.*, **36**, 3609 (1997).

[42] R. K. Mishra and G. Thomas, *J. Appl. Phys.*, **48**, 4576 (1977).

[43] R. Dekkers, C. F. Woensdregt, and P. Wollants, *J. Non-Cryst. Solids*, **282**, 49 (2001).

[44] R. Dekkers and C. F. Woensdregt, *J. Cryst. Growth*, **236**, 441 (2002).

[45] M.-R. Huang, C.-W. Lin, and H.-Y. Lu, *Appl. Surf. Sci.*, **177**, 103 (2001).

[46] M. Bayhan, T. Hashemi, and A. W. Brinkman, *J. Mat. Sci.*, **32**, 6619 (1997).

[47] L. Néel, *Ann. Phys.*, **3**, 167 (1948).

[48] D. G. Wickham and J. B. Goodenough, *Phys. Rev.*, **115**, 1156 (1959).

[49] Y. Yafet and C. Kittel, *Phys. Rev.*, **87**, 290 (1952).

[50] J. M. Hastings and L. M. Corliss, *Phys. Rev. Lett.*, **126**, 556 (1962).

[51] D. H. Lyons, T. Kaplan, K. Dwight, and N. Menyuk, *Phys. Rev.*, **126**, 540 (1962).

[52] T. R. McGuire, L. N. Howard, and J. S. Smart, *Ceram. Age*, **60**, 22 (1952).

[53] K. Dwight and N. Manyuk, *J. Appl. Phys.*, **40**, 1156 (1969).

[54] E. Whipple and A. Wold, *J. Inorg. Nucl. Chem*, **24**, 23 (1962).

[55] D. T. Margulies, F. T. Parker, F. E. Spada, R. S. Goldmann, J. Li, and R. Sinclair, *Phys. Rev. B*, **53**, 9175 (1996).

[56] W. Eerenstein *Spin-dependent transport across anti-phase boundaries in magnetite films* PhD thesis, Rijksuniversiteit Groningen, (2003).

[57] A. H. Morrish and K. Haneda, *J. Appl. Phys.*, **52**, 2496 (1981).

[58] R. H. Kodama, A. E. Berkowitz, E. J. McNiff, and S. Foner, *J. Appl. Phys.*, **81**, 5552 (1997).

[59] G. F. Goya, H. R. Rechenberg, and J. Z. Jiang, *J. Appl. Phys.*, **84**, 1101 (1998).

[60] C. N. Chinnasamy, A. Narayanasami, N. Ponpandian, K. Chattopadhyay, H. Guerault, and J.-M. Greneche, *J. Phys.: Condens. Matter*, **12**, 7795 (2000).

[61] C. N. Chinnasamy, A. Narayanasamy, N. Popandian, K. Chattopadhyay, K. Shinoda, B. Jeyadevan, K. Tohji, K. Nakatsuka, T. Furubayashi, and I. Nakatani, *Phys. Rev. B*, **63**, 184108 (2001).

[62] Y. D. Zhang, S. H. Ge, H. Zhang, S. Hui, J. I. Budnick, W. A. Hines, M. J. Yacaman, and M. Miki, *J. Appl. Phys.*, **95**, 7130 (2004).

[63] S. Chkoundali, S. Ammar, N. Jouini, F. Fiévet, P. Molinie, M. Danot, F. Villain, and J.-M. Greneche, *J. Phys.: Condens. Matter*, **16**, 4357 (2004).

[64] N. Ponpandian, P. Balaya, and A. Narayanasamy, *J. Phys.: Condens. Matter*, **14**, 3221 (2002).

[65] P. Nicolau, I. Bunget, M. Rosenberg, and I. Belciu, *IBM J. Res. Develop.*, **14**, 248 (1970).

[66] E. Bauer, *Z. Kristallogr.*, **110**, 372 (1958).

[67] H. Brune, *Surf. Sci. Rep.*, **31**, 121 (1998).

[68] D. R. Frankl and J. A. Venables, *Adv. Phys.*, **19**, 409 (1970).

[69] J. A. Venables, *Philos. Mag.*, **27**, 697 (1973).

[70] M. Zinke-Allmang, *Thin Solid Films*, **346**, 1 (1999).

[71] G. Ehrlich and F. G. Hudda, *J. Chem. Phys.*, **44**, 1039 (1966).

[72] R. L. Schwoebel, *J. Appl. Phys.*, **40**, 614 (1969).

[73] D. J. Eaglesham and M. Cerullo, *Phys. Rev. Lett.*, **64**, 1943 (1990).

[74] V. Shchukin, N. N. Ledentsov, P. S. Kop'ev, and D. Bimberg, *Phys. Rev. Lett.*, **75**, 2968 (1995).

[75] V. A. Shchukin, N. N. Ledentsov, M. Grundmann, P. S. Kop'ev, and D. Bimberg, *Surf. Sci.*, **352**, 117 (1996).

[76] C. Ratsch and A. Zangwill, *Surf. Sci.*, **293**, 123 (1993).

[77] H. C. Galloway, J. J. Benitez, and M. Salmeron, *J. Vac. Sci. Technol. A*, **12**, 2302 (1994).

[78] J. Wollschlaeger, D. Erdoes, and K.-M. Schroeder, *Surf. Sci.*, **402**, 272 (1998).

[79] J. W. Matthews and E. Klokholm, *Mat. Res. Bull.*, **7**, 213 (1972).

[80] S. A. Chambers, *Surf. Sci. Rep.*, **39**, 105 (2000).

[81] A. Atkinson, *Rev. Mod. Phys.*, **57**, 437 (1985).

[82] T. Kodama, H. Kato, S. G. Chang, N. Hasegawa, M. Tsuji, and Y. Tamaura, *J. Mater. Res.*, **9**, 462 (1994).

[83] J. F. Marco, J. R. Gancedo, M. Gracia, J. L. Gautier, E. I. Rios, H. M. Palmer, C. Greaves, and F. J. Berry, *J. Mater. Chem.*, **11**, 3087 (2001).

[84] R. M. Anderson, C. R. Vestal, A. C. S. Samia, and Z. J. Zhang, *Appl. Phys. Lett.*, **84**, 3115 (2004).

[85] P. J. van der Zaag, J. J. M. Ruigrok, and M. F. Gillies, *Philips J. Res.*, **51**, 173 (1998).

[86] H. J. Kim, I. C. Song, J. H. Sim, H. Kim, D. Kim, Y. E. Ihm, and W. K. Choo, *J. Appl. Phys.*, **95**, 7387 (2004).

[87] A. F. Bakuzis, K. S. Neto, P. P. Gravina, L. C. Figueiredo, P. C. Morais, L. P. Silva, R. B. Azevedo, and O. Silva, *Appl. Phys. Lett.*, **84**, 2355 (2004).

[88] H. Zheng, J. Wang, S. E. Lofland, Z. Ma, L. Mohaddes-Ardabili, T. Zhao, L. Salamanca-Riba, S. R. Shinde, S. B. Ogale, F. Bai, D. Viehland, Y. Jia, D. G. Schlom, M. Wuttig, A. Roytburd, and R. Ramesh, *Science*, **303**, 661 (2004).

[89] M. I. Bichurin, D. A. Filippov, V. M. Petrov, V. M. Laletsin, N. Paddubnaya, and G. Srinivasan, *Phys. Rev. B*, **68**, 132408 (2003).

[90] Y. R. Dai, P. Bao, J. S. Zhu, J. G. Wan, H. M. Shen, and J. M. Liu, *J. Appl. Phys.*, **96**, 5687 (2004).

[91] X. M. Chen, Y. H. Tang, I.-W. Chen, Z. C. Xu, and S. Y. Wu, *J. Appl. Phys.*, **96**, 6520 (2004).

[92] Y. Suzuki, *Ann. Rep. Mat. Res.*, **31**, 265 (2001).

[93] W. Jiang, H. C. Yang, S. Y. Yang, H. E. Horng, J. C. Hung, Y. C. Chen, and C.-Y. Hong, *J. Mag. Mag. Mat.*, **283**, 210 (2004).

[94] E. J. W. Verwey, *Nature*, **144**, 327 (1939).

[95] E. J. Verwey and P. W. Haayman, *Physica*, **9**, 979 (1941).

[96] H. Seo, M. Ogata, and H. Fukuyama, *Phys. Rev. B*, **65**, 085107 (2002).

[97] J. P. Wright, J. P. Attfield, and P. G. Radaelli, *Phys. Rev. B*, **66**, 214422 (2002).

[98] I. Leonov, A. N. Yaresko, V. N. Antonov, M. A. Korotin, and V. I. Anisimov, *Phys. Rev. Lett.*, **93**, 146404 (2004).

[99] H.-T. Jeng, G. Y. Guo, and D. J. Huang, *Phys. Rev. Lett.*, **93**, 156403 (2004).

[100] I. V. Shvets, G. Mariotto, K. Jordan, N. Berdunov, R. Kantor, and S. Murphy, *Phys. Rev. B*, **70**, 155406 (2004).

[101] G. Subias, J. Garcia, J. Blasco, M. G. Proietti, H. Renevier, and M. C. Sanchez, *Phys. Rev. Lett.*, **93**, 156408 (2004).

[102] G. Subias, J. Garcia, M. G. Proietti, J. Blasco, H. Renevier, J. L. Hodeau, and M. C. Sanchez, *Phys. Rev. B*, **70**, 155105 (2004).

[103] Z. Szotek, W. M. Temmerman, A. Svane, L. Petit, G. M. Stocks, and H. Winter, *Phys. Rev. B*, **68**, 054415 (2003).

[104] N. Guigue-Millot, N. Keller, and P. Perriat, *Phys. Rev. B*, **64**, 012402 (2001).

[105] L. A. Kalev, P. Schurer, and L. Niesen, *Phys. Rev. B*, **68**, 165407 (2003).

[106] N. Berdunov, S. Murphy, G. Mariotto, I. V. Shvets, and Y. M. Mykovskiy, *J. Appl. Phys.*, **95**, 6891 (2004).

[107] N. Berdunov, S. Murphy, G. Mariotto, and I. V. Shvets, *Phys. Rev. B*, **70**, 085404 (2004).

[108] Y. S. Dedkov, M. Fonin, D. V. Vyalikh, J. O. Huach, S. L. Molodtsov, U. Ruediger, and G. Guentherodt, *Phys. Rev. B*, **70**, 073405 (2004).

[109] L. Braicovich, G. van der Laan, G. Ghiringhelli, A. Tagliaferri, and N. B. Brookes, *Phys. Rev. B*, **66**, 174435 (2002).

[110] V. N. Antonov, B. N. Harmon, and A. N. Yaresko, *Phys. Rev. B*, **67**, 024417 (2003).

[111] J. Chen, D. J. Huang, A. Tanaka, C. F. Chang, S. C. Chung, W. B. Wu, and C. T. Chen, *Phys. Rev. B*, **69**, 085107 (2004).

[112] M. Taguchi, L. Braicovich, E. Annese, C. Dallera, G. Ghiringhelli, A. Tagliaferri, and N. B. Brookes, *Phys. Rev. B*, **69**, 212414 (2004).

[113] G. van der Laan, G. Ghiringhelli, A. Tagliaferri, N. B. Brookes, and L. Braicovich, *Phys. Rev. B*, **69**, 104427 (2004).

[114] D. J. Huang, C. F. Chang, H. T. Jeng, G. Y. Guo, H.-J. Lin, W. B. Wu, H. C. Ku, A. Fujimori, Y. Takahashi, and C. T. Chen, *Phys. Rev. Lett.*, **93**, 077204 (2004).

[115] M. Penicaud, B. Siberchicot, C. B. Sommers, and J. Kuebler, *J. Mag. Mag. Mat.*, **103**, 212 (1992).

[116] D. J. Singh, M. Gupta, and R. Gupta, *Phys. Rev. B*, **65**, 064432 (2002).

[117] H.-T. Jeng and G. Y. Guo, *J. Mag. Mag. Mat.*, **240**, 436 (2002).

[118] F. F. Fava, I. Baraille, A. Lichanot, C. Larrieu, and R. Dovesi, *J. Phys.: Condens. Matter*, **9**, 10715 (1997).

[119] X. Zuo and C. Vittoria, *Phys. Rev. B*, **66**, 184420 (2002).

[120] Z. Szotek, W. M. Temmerman, A. Svane, L. Petit, P. Strange, G. M. Stocks, D. Koedderitzsch, W. Hergert, and H. Winter, *J. Phys.: Condens. Matter*, **16**, 5587 (2004).

[121] M. C. Warren, M. T. Dove, and S. A. T. Redfern, *J. Phys.: Condens. Matter*, **12**, 43 (2000).

[122] V. A. M. Brabers, Y. G. Proykova, N. Salerno, and T. E. Whall, *J. Appl. Phys.*, **61**, 4390 (1987).

[123] Y.-C. Chung and H.-I. Yoo, *J. Mater. Res.*, **16**, 774 (2001).

[124] A. Pavese, D. Levy, and A. Hoser, *Am. Min.*, **85**, 1497 (2000).

[125] K. Haneda and A. H. Morrish, *J. Appl. Phys.*, **63**, 4258 (1988).

[126] R. H. Kodama, *J. Mag. Mag. Mat.*, **200**, 359 (1999).

[127] C. N. Chinnasamy, A. Narayanasamy, N. Ponpandian, R. J. Joseyphus, B. Jeyadevan, K. Tohli, and K. Chattopadhyay, *J. Mag. Mag. Mat.*, **238**, 281 (2002).

[128] V. Sepelak, D. Baabe, D. Mienert, D. Schultze, F. Krumeich, F. J. Litterst, and K. D. Becker, *J. Mag. Mag. Mat.*, **257**, 377 (2003).

[129] P. Perriat, *Lettre des sciences chimiques*, **67** (1998).

[130] Z. H. Zhou, J. M. Xue, J. Wang, H. S. O. Chan, T. Yu, and Z. X. Shen, *J. Appl. Phys.*, **91**, 6015 (2002).

[131] C. Rath, N. C. Mishra, S. Anand, R. P. Das, and K. K. Sahu, *Appl. Phys. Lett.*, **76**, 475 (2000).

[132] C. Rath, S. Anand, R. P. Das, K. K. Sahu, S. D. Kulkarni, S. K. Date, and N. C. Mishra, *J. Appl. Phys.*, **91**, 2211 (2002).

[133] S. Calvin, E. E. Carpenter, B. Ravel, V. G. Harris, and S. A. Morrison, *Phys. Rev. B*, **66**, 224405 (2002).

[134] B. Jeyadevan, K. Tohji, and K. Nakatsuka, *J. Appl. Phys.*, **76**, 6325 (1994).

[135] S. A. Morrison, C. L. Cahill, E. E. Carpenter, S. Calvin, R. Swaminathan, M. E. McHenry, and V. G. Harris, *J. Appl. Phys.*, **95**, 6392 (2004).

[136] D. Pajic, K. Zadro, R. E. Vanderberghe, and I. Nedkov, *arXiv:cond-mat 0403358v1* (2004).

[137] B. Baruwati, K. M. Reddy, S. V. Manorama, R. K. Singh, and O. Parkash, *Appl. Phys. Lett.*, **85**, 2833 (2004).

[138] C. Upadhyay, H. C. Verma, and S. Anand, *J. Appl. Phys.*, **95**, 5746 (2004).

[139] L. Schreyeck, A. Wlosik, and H. Fuzellier, *J. Mater. Chem*, **11**, 483 (2001).

[140] J. B. Yang, X. D. Zhou, W. B. Yelon, W. J. James, Q. Cai, K. V. Gopalakrishnan, S. K. Malik, X. C. Sun, and D. E. Nikles, *J. Appl. Phys.*, **95**, 7540 (2004).

[141] H. Wang, T. Zhu, K. Zhao, W. N. Wang, C. S. Wang, Y. J. Wang, and W. S. Zhan, *Phys. Rev. B*, **70**, 092409 (2004).

[142] K. Parvin, J. Ma, J. Ly, X. C. Sun, D. E. Nikles, K. Sun, and L. M. Wang, *J. Appl. Phys.*, **95**, 7121 (2004).

[143] H. Zeng, S. Sun, J. Li, Z. L. Wang, and J. P. Liu, *Appl. Phys. Lett.*, **85**, 792 (2004).

[144] D. M. Lind, S. D. Berry, G. Chern, H. Mathias, and L. R. Testardi, *Phys. Rev. B*, **45**, 1838 (1992).

[145] B. Handke, J. Haber, T. Slezak, M. Kubik, and J. Korecki, *Vacuum*, **63**, 331 (2001).

[146] Y. X. Chen, C. Chen, W. L. Zhou, Z. J. Wang, T. Jang, D. X. Wang, and J. M. Daughton, *J. Appl. Phys.*, **95**, 7282 (2004).

[147] S. A. Krasnikov, A. S. Vinogradov, K.-H. Hallmeier, R. Hohne, M. Ziese, P. Esquinazi, T. Chasse, and R. Szargan, *Mat. Sci. Eng. B, to be published* (2004).

[148] S. Kale, S. M. Bhagat, S. E. Lofland, T. Scabarozi, S. B. Ogale, A. Orozco, S. R. Shinde, T. Venkatesan, B. Hannoyer, B. Mercey, and W. Prellier, *Phys. Rev. B*, **64**, 205413 (2004).

[149] Y. Zhou, X. Jin, and I. V. Shvets, *J. Appl. Phys.*, **95**, 7357 (2004).

[150] N. Wakiya, K. Shinozaki, and N. Mizutani, *Appl. Phys. Lett.*, **85**, 1199 (2004).

[151] K. A. Shaw, E. Lochner, and D. M. Lind, *J. Appl. Phys.*, **87**, 1727 (2000).

[152] S. Venzke, R. B. van Dover, J. M. Phillips, E. M. Gyorgy, T. Siegrist, C.-H. Chen, D. Werder, R. M. Fleming, R. J. Felder, E. Coleman, and R. Opila, *J. Mat. Res.*, **11**, 1187 (1996).

[153] J. F. M. Cillessen, R. M. Wolf, J. B. Giesbers, P. W. M. Blom, K.-O. Grosse-Holz, and E. Pastoor, *Appl. Surf. Sci.*, **96**, 744 (1996).

[154] W. Eerenstein, T. T. M. Palstra, T. Hibma, and S. Celotto, *Phys. Rev. B*, **68**, 014428 (2003).

[155] W. Eerenstein, T. Hibma, and S. Celotto, *Phys. Rev. B*, **70**, 184404 (2004).

[156] W. Eerenstein, L. Kalev, L. Niesen, T. T. M. Palstra, and T. Hibma, *J. Mag. Mag. Mat.*, **258**, 73 (2003).

[157] Y. Suzuki, R. B. van Dover, E. M. Gyorgy, J. M. Phillips, V. Korenivski, D. J. Werder, C. H. Chen, R. J. Cava, J. J. Krajewski, J. W. F. Peck, and K. B. Do, *Appl. Phys. Lett.*, **68**, 714 (1996).

[158] Y. Suzuki, R. B. van Dover, E. M. Gyorgy, J. M. Phillips, V. Korenivski, D. J. Werder, C. H. Chen, R. J. Felder, R. J. Cava, J. J. Krajewski, and J. W. F. Peck, *J. Appl. Phys.*, **79**, 5923 (1996).

[159] M. T. Johnson, P. G. Kotula, and C. B. Carter, *J. Cryst. Gr.*, **206**, 299 (1999).

[160] R. J. Kennedy and P. A. Stampe, *J. Phys. D: Appl. Phys.*, **32**, 16 (1999).

[161] D. Reisinger, M. Schonecke, T. Brenninger, M. Opel, A. Erb, L. Alff, and R. Gross, *J. Appl. Phys.*, **94**, 1857 (2003).

[162] C.-H. Lai, P.-H. Huang, Y.-J. Wang, and R. Huang, *J. Appl. Phys.*, **95**, 7222 (2004).

[163] S. Jain, A. O. Adeyeye, and D. Y. Dai, *J. Appl. Phys.*, **95**, 7237 (2004).

[164] S. M. Watts, K. Nakjima, S. van Dijken, and J. M. D. Coey, *J. Appl. Phys.*, **95**, 7465 (2004).

[165] Y. Suzuki, R. B. van Dover, E. M. Gyorgy, J. M. Phillips, and R. J. Felder, *Phys. Rev. B*, **53**, 14016 (1996).

[166] Y. Suzuki, G. Hu, R. B. van Dover, and R. J. Cava, *J. Mag. Mag. Mat.*, **191**, 1 (1999).

[167] G. Hu, J. H. Choi, C. B. Eom, V. G. Harris, and Y. Suzuki, *Phys. Rev. B*, **62**, 779 (2000).

[168] Y. C. Wang, J. Ding, J. B. Yi, B. H. Liu, T. Yu, and Z. X. Shen, *Appl. Phys. Lett.*, **84**, 2596 (2004).

[169] L. A. Kalev and L. Niesen, *Phys. Rev. B*, **67**, 224403 (2003).

[170] J.-B. Moussy, S. Gota, A. Bataille, M.-J. Guittet, M. Gautier-Soyer, F. Delille, B. Dieny, F. Ott, T. D. Doan, P. Warin, P. Bayle-Guillemaud, C. Gatel, and E. Snoeck, *Phys. Rev. B*, **70**, 174448 (2004).

[171] J. F. Bobo, D. Basso, E. Snoeck, C. Gatel, D. Hrabovsky, J. L. Gauffier, L. Ressier, R. Mamy, S. Visnovsky, J. Hamrle, J. Teillet, and A. R. Fert, *Eur. Phys. J. B*, **24**, 43 (2001).

[172] W. L. Zhou, K.-Y. Wang, C. J. O'Connor, and J. Tang, *J. Appl. Phys.*, **89**, 7398 (2001).

[173] F. C. Voogt *Spin-dependent transport across anti-phase boundaries in magnetite films* PhD thesis, Rijksuniversiteit Groningen, (1998).

[174] G. J. Strijkers, J. T. Kohlhepp, P. A. A. van der Heijden, H. J. M. Swagten, W. J. M. de Jonge, and J. M. Gaines, *J. Appl. Phys.*, **85**, 5294 (1999).

[175] B. Negulescu, L. Thomas, Y. Dumont, M. Tessier, N. Keller, and M. Guyot, *J. Mag. Mag. Mat.*, **242**, 529 (2002).

[176] S. Capdeville, P. Alphonse, C. Bonningue, L. Presmanes, and P. Tailhades, *J. Appl. Phys.*, **96**, 6142 (2004).

[177] W. Eerenstein, T. T. M. Palstra, and T. Hibma, *Thin Solid Films*, **400**, 90 (2001).

[178] Y. S. Dedkov, U. Ruediger, and G. Guentherodt, *Phys. Rev. B*, **65**, 064417 (2002).

[179] X. W. Li, A. Gupta, G. Xiao, W. Qian, and V. P. Dravid, *Appl. Phys. Lett.*, **73**, 3282 (1998).

[180] P. Seneor, A. Fert, J.-L. Maurice, F. Montaigne, F. Petroff, and A. Vaures, *Appl. Phys. Lett.*, **74**, 4017 (1999).

[181] G. Hu and Y. Suzuki, *Phys. Rev. Lett.*, **89**, 276601 (2002).

[182] G. Hu, R. Chopdekar, and Y. Suzuki, *J. Appl. Phys.*, **93**, 7516 (2003).

[183] J. Y. T. Wei, N.-C. Yeh, R. P. Vasquez, and A. Gupta, *J. Appl. Phys.*, **83**, 7366 (1998).

[184] C. Srinitiwarawong and G. A. Gehring, *J. Phys.: Condens. Matter*, **13**, 7987 (2001).

[185] S. V. Dijken, X. Fain, S. M. Watts, and J. M. D. Coey, *Phys. Rev. B*, **70**, 052409 (2004).

[186] M. Bibes *Creixement i estudi de capes primes de manganites de valencia mixta* PhD thesis, Universitat Autonoma de Barcelona, (2001).

[187] R. Lyonnet, J.-L. Maurice, M. J. Hytch, D. Michel, and J.-P. Contour, *Applied Surface Science*, **162**, 245 (2000).

[188] R. Lyonnet *Heteroepitaxie d'oxydes en ablation laser pulsee pour la realisation de dispositifs a magnetoresistance tunnel* PhD thesis, Universite Paris-Sud, (2001).

[189] F. Petroff private communication, 2002.

[190] J. Eberhardt, *Methodes physiques d'etude des mineraux et des materiaux solides*, 1976.

[191] F. Houze, R. Meyer, O. Schneegans, and L. Boyer, *Appl. Phys. Lett.*, **69**, 1975 (1996).

[192] K. Bouzehouane, S. Fusil, M. Bibes, J. Carrey, T. Blon, M. L. Du, P. Seneor, V. Cros, and L. Vila, *Nanoletters*, **3**, 1599 (2003).

[193] M. Ritter, H. Over, and W. Weiss, *Surf. Sci.*, **371**, 245 (1997).

[194] M. Kawasaki, M. Izumi, Y. Konishi, T. Manako, and Y. Tokura, *Mat. Sci. Eng. B*, **63**, 49 (1999).

[195] W. D. Westwood, H. K. Eastwood, and A. G. Sadler, *J. Vac. Sci. Techn.*, **8**, 176 (1971).

[196] K. L. Chopra, *Thin Film Phenomena*, McGraw-Hill Book Company, 1969.

[197] A. E. Paladino, *J. Amer. Ceram. Soc.*, **42**, 168 (1959).

[198] J. M. Robertson and A. J. Pointon, *Solid State Comm.*, **4**, 257 (1966).

[199] K. J. Kim, H. S. Lee, M. H. Lee, and S. H. Lee, *J. Appl. Phys.*, **91**, 9974 (2002).

[200] F. J. Schnettler and E. M. Gyorgy, *J. Appl. Phys.*, **35**, 330 (1964).

[201] H. M. O'Bryan, F. R. Montforte, and R. Blair, *J. Amer. Ceram. Soc.*, **48**, 577 (1965).

[202] J. H. Scofield, *J. Electro. Spectrosc. Relat. Phenom.*, **8**, 129 (1976).

[203] A. M. Abdeen, *J. Mag. Mag. Mat.*, **192**, 121 (1999).

[204] U. D. Lanke, *Bull. Mater. Sci.*, **24**, 35 (2001).

[205] Z. Zhang and S. Satpathy, *Phys. Rev. B*, **44**, 13319 (1991).

[206] B. M. Lairson, M. R. Visokay, R. Sinclair, S. Hagstrom, and B. M. Clemens, *Appl. Phys. Lett.*, **61**, 1390 (1992).

[207] M. Morcrette, A. Gutierrez-Llorente, W. Seiler, J. Perriere, A. Laurent, and P. Barboux, *J. Appl. Phys.*, **88**, 5100 (2000).

[208] V. Trtik, C. Ferrater, F. Sanchez, M. Varela, J. Fontcuberta, M. Bibes, and B. Martinez, *J. Cryst. Growth*, **209**, 842 (2000).

[209] S. E. Harrison, C. J. Kriessman, and S. R. Pollack, *Phys. Rev*, **110**, 844 (1958).

[210] M. O. Bowen *Experimental insights into spin-polarized solid state tunneling* PhD thesis, Université Paris XI, (2003).

[211] V. Garcia, M. Bibes, A. Barthélémy, M. Bowen, E. Jacquet, J.-P. Contour, and A. Fert, *Phys. Rev. B*, **69**, 052403 (2004).

[212] J. M. de Teresa, A. Barthélémy, A. Fert, J. P. Contour, F. Montaigne, and P. Seneor, *Science*, **286**, 507 (1999).

[213] N. Keller private communication, 2004.

[214] X. Wu, W. P. Mulligan, and T. J. Coutts, *Thin Solid Films*, **286**, 274 (1996).

[215] D. L. Young, H. Moutinho, Y. Yan, and T. J. Coutts, *J. Appl. Phys.*, **92**, 310 (2002).

[216] S. Parkin In *International Conference of Ferrites 9, San Francisco*, 2004.

[217] M. Bowen, A. Barthélémy, M. Bibes, E. Jacquet, J.-P. Contour, A. Fert, F. Ciccacci, L. Duo, and R. Bertacco, *to be published in Phys. Rev. Lett.* (2005).

[218] A. Barthélémy private communication, 2004.

[219] M. P. de Jong, V. A. Dediu, C. Taliani, and W. R. Salaneck, *J. Appl. Phys.*, **94**, 7292 (2003).

[220] W. Maus-Friedrichs, M. Frerichs, A. Gunhold, S. Krischok, V. Kempter, and G. Bihlmayer, *Surf. Sci.*, **515**, 499 (2002).

[221] H.-T. Jeng, Introduction to lda+u method and applications to transition-metal oxides , Contribution to the Summer Course on First-principles Computational Materials Research held at the National Center for Theoretical Sciences of Taiwan, an on-line version can be found at http://phys.cts.nthu.edu.tw/workshop/summer/cmr/CMR20030828/NDHU.LDA+U.ppt, 2003.

[222] J. H. Jung, D.-W. Kim, T. W. Noh, H. C. Kim, H.-C. R. ans S. J. Levett, M. R. Lees, D. M. Paul, and G. Balakrishnan, *Phys. Rev. B*, **64**, 165106 (2001).

[223] Z. Szotek private communication, 2004.

[224] M. Bibes private communication, 2004.

[225] A. Fert and P.Levy private communication, 2004.

[226] H. B. Michaelson, *Handbook of Chemistry and Physics*, CRC Press, Cleveland, Ohio, 58 ed., 1977.

[227] G. Medeiros-Ribeiro, A. Bratkovski, T. Kamins, D. Ohlberg, and R. Williams, *Science*, **279**, 353 (1998).

[228] B. Voigtlaender, *Surf. Sci. Rep.*, **43**, 127 (2001).

[229] C. Teichert, *Phys. Rep.*, **356**, 335 (2002).

[230] R. E. Rudd, G. A. D. Briggs, A. P. Sutton, G. Medeiros-Ribeiro, and R. S. Williams, *Phys. Rev. Lett.*, **90**, 146101 (2003).

[231] J. Tersoff and R. M. Tromp, *Phys. Rev. Lett.*, **70**, 2782 (1993).

[232] B. Voigtlaender, M. Kawamura, N. Paul, and V. Cherepanov, *J. Phys.: Condens. Matter*, **16**, 1535 (2004).

[233] M. Goryll, L. Vescan, K. Schmidt, S. Mesters, H. Lueth, and K. Szot, *Appl. Phys. Lett.*, **71**, 410 (1997).

[234] E. Sutter, P. Sutter, and J. E. Bernard, *Appl. Phys. Lett.*, **84**, 2262 (2004).

[235] H. J. Kim, Z. M. Zhao, and Y. H. Xie, *Phys. Rev. B*, **68**, 205312 (2003).

[236] Z. Zhong and G. Bauer, *Appl. Phys. Lett.*, **84**, 1922 (2004).

[237] Z. Yuan, B. E. Kardynal, R. M. Stevenson, A. J. Shields, C. J. Lobo, K. Cooper, N. S. Beattie, D. A. Richie, and M. Pepper, *Science*, **295**, 102 (2002).

[238] G. Zhou and J. C. Yang, *Phys. Rev. Lett.*, **89**, 106101 (2002).

[239] S. N. Jacobsen, U. Helmersson, R. Erlandsson, B. Skarman, and L. R. Wallenberg, *Surf. Sci.*, **429**, 22 (1999).

[240] S. H. Brongersma, M. R. Castell, D. D. Perovic, and M. Zinke-Allmang, *Phys. Rev. Lett.*, **80**, 3759 (1998).

[241] J. Shen and J. Kirschner, *Surface Science*, **500**, 300 (2002).

[242] W. Eberhardt, *Surface Science*, **500**, 242 (2002).

[243] C. R. Henry, *Surf. Sci. Rep.*, **31**, 231 (1998).

[244] R. S. Williams, G. Madeiros-Ribeiro, T. I. Kamins, and D. A. A. Ohlberg, *Annu. Rev. Phys. Chem*, **51**, 527 (2000).

[245] W. Zhu, F. B. de Mongeot, U. Valbusa, E. G. Wang, and Z. Yang, *Phys. Rev. Lett.*, **92**, 106102 (2004).

[246] Y. W. Mo, D. E. Savage, B. S. Swartzentruber, and M. G. Lagally, *Phys. Rev. Lett.*, **65**, 1020 (1990).

[247] W. Dorsch, H. P. Strunk, H. Wawra, G. Wagner, J. Groenen, and R. Carles, *Appl. Phys. Lett.*, **72**, 179 (1998).

[248] F. M. Ross, J. Tersoff, and R. M. Tromp, *Phys. Rev. Lett.*, **80**, 984 (1998).

[249] M. A. Lutz, R. M. Feenstra, P. M. Mooney, J. Tersoff, and J. O. Chu, *Surf. Sci. Letters*, **316**, 1075 (1994).

[250] B. J. Spencer, P. W. Voorhees, and J. Tersoff, *Appl. Phys. Lett.*, **76**, 3022 (2000).

[251] P. Venezuela and J. Tersoff, *Phys. Rev. B*, **58**, 10871 (1998).

[252] I. Daruka and A.-L. Barabási, *Phys. Rev. Lett.*, **79**, 3708 (1997).

[253] I. Daruka, J. Tersoff, and A.-L. Barabási, *Phys. Rev. Lett.*, **82**, 2753 (1999).

[254] D. E. Jesson, T. P. Munt, V. A. Shchukin, and D. Bimberg, *Phys. Rev. Lett.*, **92**, 115503 (2004).

[255] H. T. Johnson and L. B. Freud, *J. Appl. Phys.*, **81**, 6081 (1997).

[256] G. Costantini, A. Ratelli, C. Manzano, R. Songmuang, O. G. Schmidt, K. Kern, and H. von Kanel, *Appl. Phys. Lett.*, **85**, 5673 (2004).

[257] G. M. Francis, L. Kuipers, J. R. A. Cleaver, and R. E. Palmer, *J. Appl. Phys.*, **79**, 2942 (1996).

[258] J. F. Hochepied, P. Sainctavit, and M. P. Pileni, *J. Mag. Mag. Mat.*, **231**, 315 (2001).

[259] F. Saito, T. Toyoda, T. Mori, M. Tanaka, K. Hirano, and S. Sasaki, *Physica B*, **270**, 35 (1999).

[260] G. Schuetz and P. Fischer In K. Juelich, Ed., *24. Ferienkurs des Instituts fuer Festkoerperforschung: Magnetismus von Festkoerpern und Grenzflaechen*, 1993.

[261] D. Magnoux, D. Hrabovsky, P. Baules, M. J. Casanove, E. Snoeck, A. R. Fert, and J. F. Bobo, *J. Appl. Phys.*, **91**, 7730 (2002).

[262] D.-W. Kim, T. W. Noh, H. Tanaka, and T. Kawai, *Sol. State Comm.*, **125**, 305 (2003).

[263] L. M. B. Allredge and Y. Suzuki, *Appl. Phys. Lett.*, **85**, 437 (2004).

[264] Q. Pan, T. G. Pokhil, and B. Moskowitz, *J. Appl. Phys.*, **91**, 5945 (2002).

[265] S. V. Yanina and C. B. Carter, *Surf. Sci. Lett.*, **513**, 402 (2002).

[266] S. Bidnyk, B. D. Little, Y. H. Cho, J. Krasinski, J. J. Song, W. Yang, and S. A. McPherson, *Appl. Phys. Lett.*, **73**, 2242 (1998).

[267] M. Imada, A. Fujimori, and Y. Tokuta, *Rev. Mod. Phys.*, **70**, 1039 (1998).

[268] H. Y. Hwang, S.-W. Cheong, N. P. Ong, and B. Batlogg, *Phys. Rev. Lett.*, **77**, 2041 (1996).

[269] J.-H. Park, E. Vescovo, H.-J. Kim, C. Kwon, R. Ramesh, and T. Venkatesan, *Phys. Rev. Lett.*, **81**, 1953 (1998).

[270] F. Ott, M. Viret, R. Borges, R. Lyonnet, E. Jacquet, C. Fermon, and J.-P. Contour, *J. Mag. Mag. Mat.*, **211**, 200 (2000).

[271] S. Zhang, P. M. Levy, A. C. Marley, and S. S. P. Parkin, *Phys. Rev. Lett.*, **79**, 3744 (1997).

[272] C. A. Dartora and G. C. Cabrera, *J. Appl. Phys.*, **95**, 6058 (2004).

Résumé

Des couches minces à base de $NiFe_2O_4$ et $CoCr_2O_4$ ont été réalisées par pulvérisation cathodique sur des substrats d'oxydes, dans le but de les intégrer dans des hétérostructures pour l'électronique de spin, en tant que jonctions tunnel magnétiques ou bien structures de type "filtre à spin".

Il a été montré que la croissance épitaxiale permet la stabilisation de nouvelles phases de $NiFe_2O_4$ qui n'existent pas sous forme massive. Ces phases présentent des propriétés remarquables telles qu'une augmentation forte du moment magnétique ou la possibilité d'ajuster les propriétés électriques du matériau (le faisant passer d'un état isolant, comme sous sa forme massive, à un état conducteur) . Ainsi, selon les conditions de croissance, il est possible de stabiliser soit un état isolant ferromagnétique soit un état conducteur ferromagnétique. Une étude systématique et approfondie a été menée sur les propriétés de magnétotransport et les mécanismes de croissance de ces oxydes en relation avec l'influence de l'épaisseur des couches et de l'environnement gazeux lors du dépôt.

Nous expliquons l'augmentation du moment magnétique par une inversion partielle des sites cationiques du $NiFe_2O_4$, matériau dans lequel les ions Ni^{2+} sont répartis entre les deux sites -octaédriques et tetraédriques- de la structure spinelle. Les lacunes en oxygène sont susceptibles de favoriser un comportement conducteur en induisant des états de valence mixte $Fe^{2+/3+}$ dans les sites octaédriques.

Nous avons tiré profit de notre capacité à fabriquer des couches épitaxiales et ferromagnétiques de $NiFe_2O_4$ conducteur ou isolant, afin de les intégrer respectivement dans des jonctions tunnel magnétiques et des filtres à spin.

Des couches minces de $NiFe_2O_4$ conducteur ont été utilisées comme électrodes ferromagnétiques dans des jonctions tunnel. Une magnétorésistance significative a été mesurée jusqu'à la température de 280K, correspondant à une polarisation de spin de 40% du $NiFe_2O_4$, pratiquement constante en température. Ces résultats suggèrent que cette nouvelle phase conductrice constitue un matériau intéressant pout l'électronique de spin car il présente une forte polarisation de spin.

Le $NiFe_2O_4$ isolant a été incorporé avec succès en tant que barrière tunnel ferrimagnétique au sein de jonctions de type "filtre à spin", ce qui en fait la première structure de ce type réalisée avec des oxydes complexes. L'effet de filtrage a été mis en évidence par une magnétorésistance tunnel, atteignant les 50%. A partir des valeurs mesurées, nous avons pu déduire la structure de bandes du spinelle normal $NiFe_2O_4$ et apporter un nouvel aperçu de la structure électronique de ces oxydes.

Il a été mis en évidence que les couches minces de $CoCr_2O_4$ déposées sur MgO(001) et $MgAl_2O_4$(001) ont une tendance forte à croître de manière tridimensionnelle. Par conséquent, la surface des couches n'est pas assez plane pour l'intégration dans des

hétérostructures nanométriques telles que les jonctions tunnel ou les filtres à spin, le matériau est donc difficilement intégrable dans des héterostructures.

En revanche, nous avons tiré parti de ce mode de croissance tridimensionnel afin de montrer que sous certaines conditions, il est possible de faire croître des objets pyramidaux aux facettes parfaitement définies. Nous avons étudié en détail cette croissance auto-organisée de nano-objets et sa dépendance à l'égard des conditions de dépôt. Nous avons montré qu'il est possible d'obtenir des matrices présentant des facettes et discuté des perspectives d'applications.

List of Publications

Publications in international journals

- U. Lüders, F. Sánchez and J. Fontcuberta
Initial stages in the growth of {111} faceted $CoCr_2O_4$ clusters: mechanisms and strained nanometric pyramids
Appl. Phys. A **79**, 93 (2004)

- U. Lüders, F. Sánchez and J. Fontcuberta
Tunable faceted growth in $CoCr_2O_4$(001) thin films: from pyramidal clusters to a {111} fully structured surface
Phys. Rev. B **70**, 045403 (2004)

- U. Lüders, M. Bibes, J.-F. Bobo and J. Fontcuberta
Tuning the growth orientation of $NiFe_2O_4$ films by appropriate underlayer selection
Appl. Phys. A **80**, 427 (2004)

- U. Lüders, F. Sánchez and J. Fontcuberta
Self-organized growth of pyramidal clusters in epitaxial spinel $CoCr_2O_4$ films on rock salt MgO(001) substrates
Appl. Phys. A **81**, 103 (2005)

- U. Lüders, M. Bibes, J.-F. Bobo, M. Cantoni, R. Bertacco and J. Fontcuberta
Enhanced magnetic moment and conductive behavior in $NiFe_2O_4$ spinel ultrathin films
Phys. Rev. B **71**, 134419 (2005)

Publications in conference proceedings

- U. Lüders, F. Sánchez and J. Fontcuberta
Growth and magnetic properties of $CoCr_2O_4$ epitaxial films
Proceedings of the European Materials Research Society, spring meeting 2003
Mat. Sci. Eng. B **109**, 200 (2004)

- M. Bibes, U. Lüders, A. Barthélémy, K. Bouzehouane, J.-L. Maurice, J.-F. Bobo and J. Fontcuberta
Combining perovskite and spinel oxides for spintronics
Proceedings of the Ninth International Conference on Ferrites 2004
to be published by the American Ceramics Society

- F. Sánchez, U. Lüders, G. Herranz, I. C. Infante and J. Fontcuberta
  Self-organization in complex oxide thin films: From 2-D to 0-D nanostructures of $SrRuO_3$ *and* $CoCr_2O_4$
  Proceedings of TNT 2004 Trends in Nanotechnology Conference
  to be published in Nanotechnology (2005)

- U. Lüders, F. Sánchez and J. Fontcuberta
  Self-organized growth of nanometric pyramids in ferrimagnetic epitaxial $CoCr_2O_4$ *films*
  Proceedings of the European Materials Research Society, spring meeting 2005
  to be published in Mat. Sci. Eng. B

- F. Sánchez, I. C. Infante, Ll. Abad, U. Lüders, Ll. Balcells, B. Martínez, and J. Fontcuberta
  Control of the surface roughening in the epitaxial growth of manganite films
  Proceedings of the European Materials Research Society, spring meeting 2005
  to be published in Thin Solid Films

Invited seminar talks

- Laboratoire de Magntisme et Optique de Versailles, June 2004: *Epitaxial growth of spinel oxide films: Stabilizing non-equilibrium properties*

- Unit Mixte de Physique Thales-CNRS-Universit Paris-Sud, December 2004: *Epitaxial growth of NiFe2O4: Stabilizing non-equilibrium properties*

Oral Contributions to meetings

- M2TPS workshop, Zaragoza, December 2003: U. Lders, M. Bibes, J.F. Bobo, K. Bouzehouane, A. Barthelemy and J. Fontcuberta *Oxide spin filters*

- GDR Sesame/Relax meeting, Paris, March 2004: U. Lders, M. Bibes, A. Barthlmy, K. Bouzehouane, E. Jacquet, J.-P. Contour, S. Fusil, J.F. Bobo, J. Fontcuberta, A. Fert *Spin transport in Ferrite/Manganite heterostructures*

- Colloque Louis Nel, Autrans, April 2004: U. Lders, M. Bibes, A. Barthlmy, K. Bouzehouane, E. Jacquet, J.-P. Contour, S. Fusil, J.F. Bobo, J. Fontcuberta, A. Fert *Spin transport in Ferrite/Manganite heterostructures*

- Joint European Magnetism Symposium, Dresden, September 2004: U. Lders, M. Bibes, A. Barthlmy, K. Bouzehouane, E. Jacquet, J.-P. Contour, S. Fusil, J.F. Bobo, J. Fontcuberta, A. Fert *Spin transport in Ferrite/Manganite heterostructures*

- European Materials Research Society, Spring meeting, Strasbourg, May 2004: U. Lders, M. Bibes, A. Barthlmy, K. Bouzehouane, E. Jacquet, J.-P. Contour, S.

Fusil, J.F. Bobo, J. Fontcuberta, A. Fert *Tunable transport properties of NiFe2O4 epitaxial thin films: Integration in magnetic tunnel junctions and spin filter*

Gracias! Merci! Thanks!

First of all I want to thank Rudolf Gross, Jacobo Santamaria and Marie-Jose Casanove to have accepted to be a part of the jury and to have taken the long way to Barcelona. Furthermore Josep Nogués and Jean-Claude Ousset for the representation of the two universities involved in my thesis.

As this thesis was done at three different institutes, the list of people I am indepted to is long. After all a comparable work would have been impossible without the support and helpfulness of many different persons, in all the institutes and even apart from them. I cannot express the deep gratefulness for this help.

First in the line is Pep Fontcuberta, who offered me this thesis, although it was never clear, why I wanted to come to Barcelona. I thank you warmly for the support, the disposition for discussion and the highlighting of red lines in tangled mass of data.

The other part of the thesis was taken over by Jeff Bobo. Thank you for introducing me to the Plassys, for the neverending search for money and the support in this complicated time. Although the lab moved and I was only with breaks in Toulouse, there was always a desk for me there.

Special thanks to Agnés Barthélémy, that you made it possible for me to stay at the UMR during several months, taking full advantage of the experimental and personal possibilities of the institute. And for the taxi service after long days of measurements.

Although Manuel Bibes was not involved officially in this thesis, he is one of the most important supporters, not only with scientific help and discussions, but also with an open ear for the problems of a PhD student, with a basic class of music for beginners and cigarets. It was a pleasure to work with you and thanks a lot!

Muchas gracias a todo el ICMAB de haberme hecho una bienvenida tan calida. Aunque algunas ideas de la cocina alemana y los alemanes en general estaban un poco dudosas, en total era un clima de trabajo incomparable. Muchas gracias a Florencio Sánchez por aguantar discussiones fuertes, horas delante del SEM y para la ayuda con las islas verdes. Gracias a Benjamin Martínez por la ayuda durante las pescadas en el SQUID y los cursos de español. Era una lastima que Lluís Balcells estaba en Madrid, justamente cuando yo tenia que trabajar con el sputtering. Muchas gracias por la ayuda invalorable. Pero el mayor parte del trabajo era con los otros becarios de mi grupo: Muchas gracias a Jose Navarro para sus esfuerzos en ingles y la introduccion en el sistema ICMAB, a Gervasi Herranz por su incansable disposición, algunas palabras alemanas y medidas de MOKE, a Sergi Valencia por la introduccion en las diferentes technicas y por enseñar que un espanyol puede sobrevivir en Alemania, a Llibertat Abad por su ayuda con las capas de LCMO y el mantenimiento del sputtering, a Diego Rubí por el tiempo al SQUID y el suporte general y a Ingrid Cañero por algunas medidas y el divertimiento durante los meetings. Tambien gracias a Carlos Frontera por trucos

impresionantes para los fittings. En el grupo de los superconductores muchas gracias a Andrea Cavallaro, el mejor compañero de despacho del mundo, Anna Palau por las urgencias del SQUID, Juan Carlos Gonzales por el pescado al peruano, Oscar Castaño por la ayuda del lado químico, Simona Iliescu por la confianza en mis posibilidades con la sierra, Neus Romá por su personalidad misma, Joffre Gutiérrez por estar mas alto que yo y David Bastidas por la vida social del grupo.

Despues muchas gracias al personal technico y administrativo, porque sin ellos estamos perdidos. Especialmente: Trinitat Palomera por su disposicion de ayudar los becarios con todo sus posibilidades, los azules del mantenimiento y Toni Pons por un curso de espanyol de las herramientas y la ayuda durante las diferentes urgencias que hay en la vida de un becario experimental, el personal de los Rayos X y Maria Jesus Polo por su disposicion al AFM. Muchas gracias tambien a Pep Bassas de la Universidad de Barcelona por su ayuda technica y cientifica con los rayos X.

Pour la part de Toulouse, aussi la j'ai trouvé d'aide sciéntifique y hors de la science, spécialment de les autres membres de mon groupe. Un merci cordialment a Boucar Diouf, qui etait mon sauveur, a Laurianne Gabillet pour l'aide a côté administrative et pour les cafés, a Davidof Hrabovsky, qui etait toujours lá et le maitre de MOKE, a Cristophe Gatel et Thomas Blon pour l'aide experimentel et les cafés au CEMES et Pierre Baules pour les mesures de Rayons X. Aussi un merci a David Serrate de Saragosse pour le support hors du labo.

Finalment il y a aussi l'UMR de Orsay. Merci pour m'avoir donné l'impression, que je n'etais pas seulement une visitante, mais une thésarde du labo. D'abord je veux remercier Jean-Paul Contour et Eric Jacquet pour avoir fait les hétérostructure à base de perovskite. Après il y a eu l'aide inoubliable de Karim Bouzehouane, au résiscope, pour le nanolithografie et au mi-champs. Merci mille fois pour les dicussions, le scepticisme, mais d'abord pour ton soutien sans fin. Merci beaucoup aussi pour l'aide tèchnique et pour le depôt de quelques couches a Annie Vaures, Josette Humbert et Cyrile Deranlot. Et, last but not least, un merci très cordial a: Martin Gajek pour l'aide infatigable et quelques discussions pendant le café et la bière au Guichet, Karsten Rode pour l'aide pour toutes les facets d'une thèse, Marc Elsen, le grand maître de lithografie et des TMR petits mais jolies, Nathalie Lidgi pour les jours au mi-champs, Vincent Garcia pour l'aide avec la lithographie y les resultats déjà obtenus, Olivier Boulle pour son ordinateur, Henri Jaffres pour le Jazz dans la vie, Manuel Muñoz por el lado español en Paris, Madjid Anane pour avoir été un source sans fond par les problèmes techniques, Pierre Seneor pour le discussion sur le signe de TMR et encore Gervasi Herranz, maintenant post-doc, pour toutes les mesures.

Ich möchte mich ausserdem aus tiefstem Herzen für die Unterstützung (sowohl mental als auch finanziell) von meinen Eltern bedanken. Wenn nichts mehr ging, habt ihr mich aus der Scheisse gezogen und wieder auf meine Beine gestellt. Ich kann meinen Dank nicht in Worten ausdrücken.

Ganz herzlich möchte ich mich auch bei Annie Dahlheimer für das Bereitstellen der Wohnung in Paris bedanken. Ich wusste es ausserordentlich zu schätzen!

Una tesis no solo se hace en el laboratorio, pero tambien fuera durante una cervezita al bar o una cena. Por una vida social inolvidable, por orejas abiertas para quejas sobre

las bajas de una tesis y sonrisas sobre las alturas, por un suporte incansable tambien en la parte personal y divertimiento a su maximo, un gracias de todo corazon a: Andrea Cavallaro, Martin Gajek, Aurelie Friang, Diego Rubi, Elisenda Rodriguez, Neus Romá y David Muñoz. Y especialmentisimo a Jérôme Poupinet.

With the risk of repeating myself: without all this help this thesis would not have been written in it's form as it has now. Thanks a lot!

A1 Appendix 1: Properties of the $(La, Sr)MnO_3$ base layer

A1-1 Introduction to $La_{2/3}Sr_{1/3}MnO_3$

$La_{2/3}Sr_{1/3}MnO_3$ (LSMO) is a magnetic conductor [267] and was used as electrodes for oxide spin electronics [181, 211, 217] due to its high spin-polarization [5, 7]. The growth of LSMO is well-controlled [187,188] and the theory of this material is quite well understood, although some mechanisms are still under discussion. For a review of the properties of the manganites in general see [8] and especially on the transport properties see [12, 186].

Crystal structure

The crystalline structure of LSMO is the perovskite structure, shown in Figure A1-1, where the ion A is La^{3+} or Sr^{2+} and B is a Mn^{3+} or Mn^{4+}. Due to the different size of the ion radius of the ions involved, the structure is normally not the cubic one shown in Figure A1-1, but a orthorombic or rhombohedrally distorted one. The lattice parameters of the pseudocubic unit cell of bulk LSMO is a=0.387nm with an angle of 89.74°.

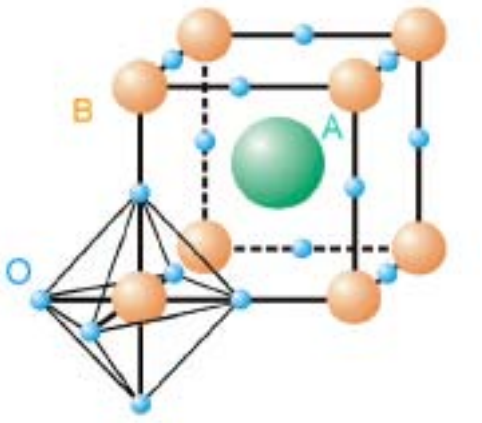

Figure A1-1: Schematic view of the cubic perovskite structure ABO_3.

Magnetic and electric properties

In LSMO the Mn ions have two different valence states due to the doping with Sr. Substituting a La^{3+} ion by a Sr^{2+} ion leads to a valence Mn^{4+}, so that the Mn ions are present as a mixture $Mn^{3+}(3d^4)/Mn^{4+}(3d^3)$. The fourth $3d$ electron of the Mn^{3+} is the first electron populating one of the two e_g bands thus Mn^{3+} is a Jahn-Teller ion (see Section 2.2.2). This e_g electron leads to a ferromagnetic coupling via the double exchange mechanism as described in Section 2.2.2, which is stronger than the antiferromagnetic super exchange coupling. As this e_g electron mediates the magnetic coupling and constitutes at the same time the conduction electron, the magnetic and electric properties of LSMO are strongly coupled. The magnetic moment of the manganites is due to the Mn ions, so in a Sr doped $La_{(1-x)}Sr_xMnO_3$ the magnetic moment is $4\mu_B/f.u. - (1-x)$.

Band calculations show, that for a doping range of $0.16 \leq x \leq 0.5$ the e_g electrons are itinerant and form a band [267], which crosses the Fermi energy. On the other hand the e_g or t_{2g} bands of the minority spins are not filled due to the first Hund's rule and show a gap at the Fermi energy, so LSMO is a half-metal. Indeed, experimentally the spin polarization of LSMO was found to be 100% by spin-resolved photo-emission experiments [6] and 95% in magnetic tunnel junctions [7].

Going through the T_C at $350K$, the break-down of the magnetic coupling leads to an insulating state (see Figure A1-2). At temperatures above T_C the paramagnetic state, i.e. no magnetic coupling of the Mn^{3+}/Mn^{4+} ions, results in a localization of the e_g electrons at the Mn^{3+} sites and thus an insulating behavior. The conduction mechanism is thermally assisted hopping, so that the conduction in this region can be described with

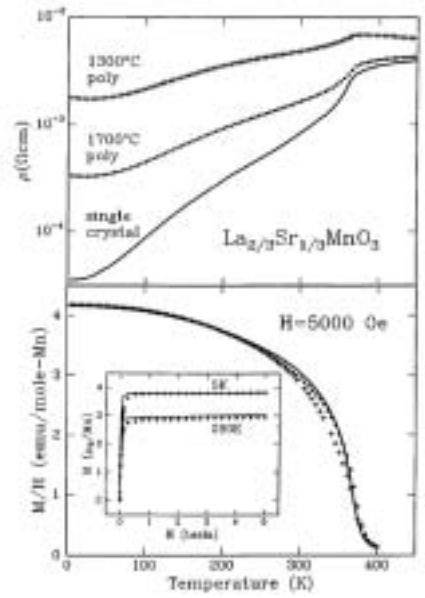

Figure A1-2: Resistivity (upper panel) and magnetization (bottom panel) vs temperature for LSMO after [268].

an Arrhenius law or variable range hopping.

For the temperature range $T_C/2 \leq T \leq T_C$ the resistance of the conducting state rises very strongly, resulting in a resistance peak at T_C. The rise of the resistance below T_C was ascribed to magnetic disorder, leading to parts of the material where the e_g conduction electron is localized. However, the magnetically ordered parts still show a high conductivity. The conduction mechanism between the still conducting regions is due to hopping through the insulating regions. Applying a magnetic field, the magnetic disorder will vanish gradually with the field, so that the resistance of the LSMO at high applied magnetic field is lower than the resistance at low magnetic field. This effect was called Colossal Magnetoresistance (CMR), as the effect can be as large as 100% of resistance change.

A structural disorder will also lead to a magnetic disorder as the double exchange coupling is strongly dependent on the Mn-O-Mn angle. This effect manifests at the surface/interface of a film, here the resistance is much higher and the T_C is reduced. For the surface the reduction of T_C was experimentally shown by Park et al [269], who found a decrease of the magnetic moment with the temperature much faster for the interface in comparison with the bulk behavior. Neutron diffraction measurements for the interface of LSMO/STO showed also a strong reduction of the magnetic moment [270].

Another region of structural disorder are the grain boundaries. For polycrystalline films the contribution of the grain boundaries to the resistance of the film was found to be the governing one [268]. Here, the coupling between the different grains is disturbed resulting in a misalignment of their magnetization at zero field. The thickness of the grain boundary region is in the nm range so that these insulating parts will act as tunneling barriers, allowing the transport of electrons between the grains. The misalignment of the magnetization of the grains gives rise to a tunnel magnetoresistance [268], which is asymmetric in field and strong for low magnetic fields. If a magnetic field is applied, the magnetization of the different grains align and the grain boundary MR decreases very rapidly with the applied field.

A1-2 Properties of the LSMO(/STO) base

The base of the heterostructure, i.e. the LSMO and LSMO/$SrTiO_3$(STO) layers on STO(001), were done by pulsed laser deposition at the UMR Thales - CNRS - Université Paris-Sud. For the complete study of the growth see the thesis of R. Lyonnet [188], here only the properties for a fixed LSMO layer thickness of $35nm$ and relevant for the growth of the heterostructure and its transport properties are discussed.

Structural and surface properties

The structural properties were measured by XRD (see for example Figure 5.2 or 5.14). The LSMO grows (001) out-of-plane oriented on the STO. The LSMO films are fully strained on the STO substrate [188] with a lattice parameter of $0.385nm$. The RHEED images show at low temperature no diffraction due to a degradation of the surface during

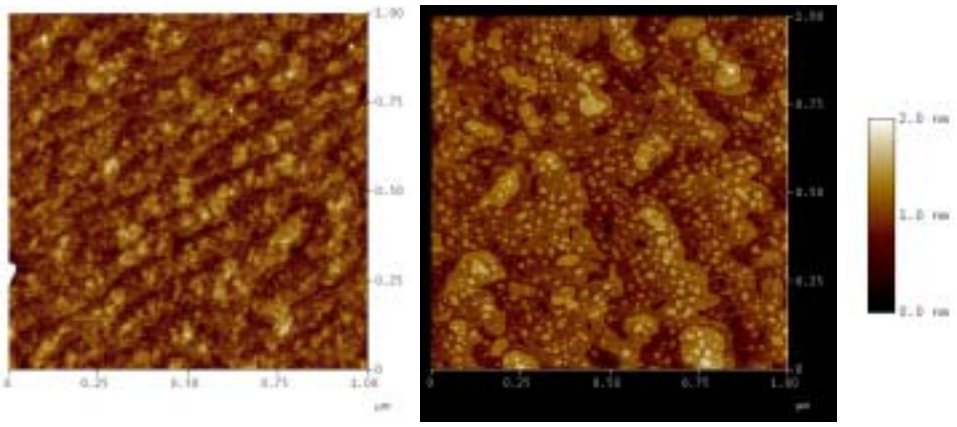

Figure A1-3: AFM images of the surface of $35nm$ thick LSMO film grown on STO(001) without (left image) and with (right image) a $0.8nm$ STO overlayer.

the transport of the films, but approaching the deposition temperature of $450°C$ streaks start to show up and at the deposition temperature, the surface has recovered a smooth and well-crystalline state as can be observed in Figure 5.7 (left column).

The surface morphology of LSMO and the LSMO/STO bilayer were measured by AFM, the images show a layer-by-layer growth which conserves the steps formed on the surface of the STO substrate (Figure A1-3 left image: $35nm$ LSMO, right image: $35nm$ LSMO / $0.8nm$ STO). The surfaces are atomically flat in the wide terraces build between the steps of the substrates.

Magnetic properties

The magnetic properties of the LSMO layer are shown in Figure A1-4. The hysteresis loop at $10K$ (left side) shows a coercive field of $50Oe$ and a saturation magnetization of $450emu/cm^3$, which is similar to the expected bulk magnetic moment of $3.6\mu_B/f.u.$. The temperature dependence (right side) was measured in a field of $2kOe$ to ensure the saturation of the film. The T_C is with $330K$ slightly lower than in bulk due to the reduced dimensions of the material.

Electric properties

The homogeneity of the resistance of the $0.8nm$ thick STO layer was measured by the resiscope to make sure the proper coverage of the LSMO surface. The images (Figure A1-5) show the resistance of the surface of a $35nm$ thick LSMO layer (left image) and of a $0.8nm$ STO layer on top of $35nm$ LSMO (right image). The resistance is elevated in respect to the LSMO surface and without hot spots, thus two unit cells of STO are enough to form a barrier. The insulating character was tested by measuring the surface resistance of two STO layer with different thickness (Figure A1-5 right side).

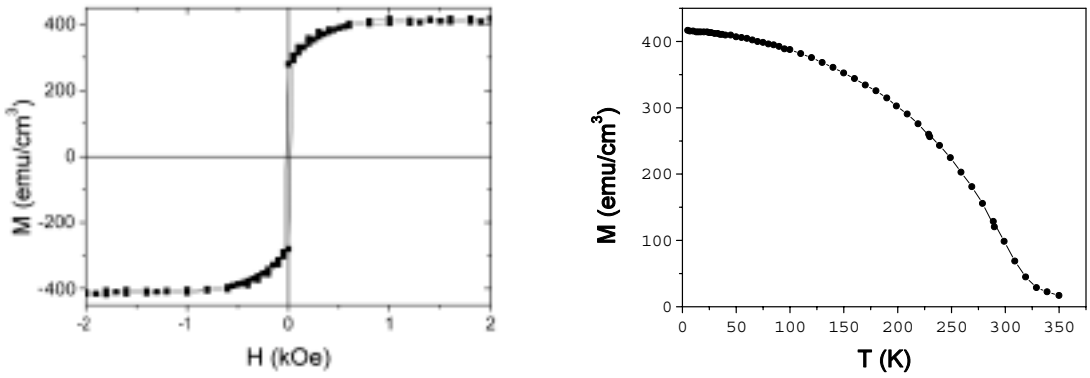

Figure A1-4: Magnetization vs magnetic field at $10K$ (left side) and vs temperature in a field of $2kOe$ (right side) for a $35nm$ thick LSMO film.

The resistance shows an exponential dependence on the layer thickness, indicating a tunneling transport through the STO layer, a sign of an insulating state of the film.

The temperature dependence of the resistance of the LSMO was checked by measuring the resistance of a LSMO($35nm$)/STO($0.8nm$)/Au heterostructure perpendicular to plane. The sample was processed by the nanoindentation process to form tunnel junctions with STO as the barrier. The resistance of the LSMO film decreases monotonously with decreasing temperature (Figure A1-6), as expected for the LSMO. The maximum of R is at $300K$ or higher consistent with the T_C measured in the magnetic measurements. The perpendicular-to-plane geometry was chosen to test the interface properties of the LSMO layer, however, the interface seems to have a T_C comparable to that of the bulk,

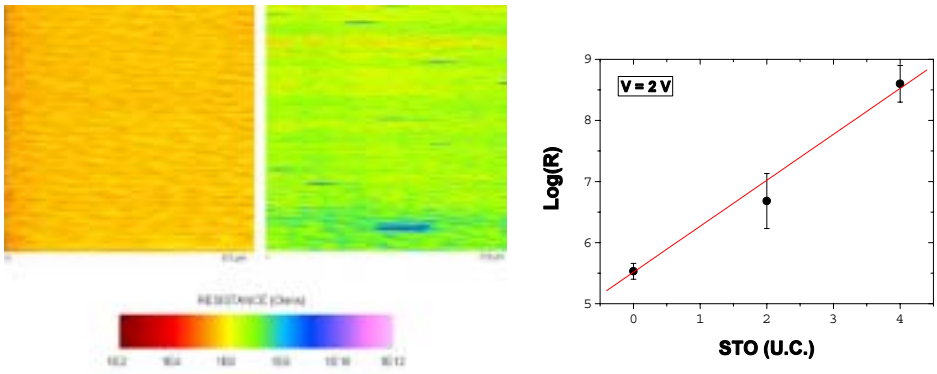

Figure A1-5: Resiscope images of the surface of $35nm$ thick LSMO film grown on STO(001) without (left image) and with (right image) a $0.8nm$ STO overlayer. The graph on the right side shows the mean value of the resistance vs the STO layer thickness in unit cells, the line is a linear fit.

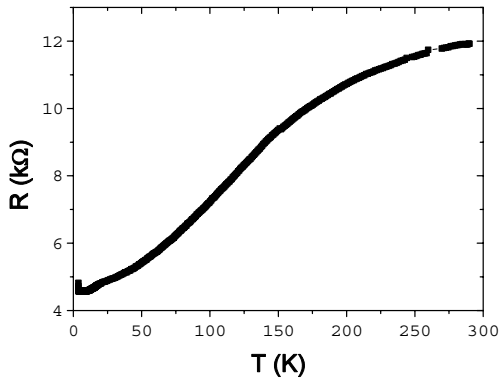

Figure A1-6: Resistance vs temperature perpendicular to plane for a LSMO($35nm$)/STO ($0.8nm$)/Au heterostructure for a bias voltage of $100mV$.

i. e. above room temperature.

Spin-dependent transport

A LSMO($35nm$)/STO($0.8nm$)/Au heterostructure was prepared to carry out transport measurements to estimate the contribution of the LSMO electrode to the magnetoresistance (MR) of the heterostructure with an integrated NFO layer. A typical R(H) curve is shown in Figure A1-7(a). Starting at the maximum positive field the resistance increases slowly with decreasing magnetic field until a field of $1kOe$, where the slope of

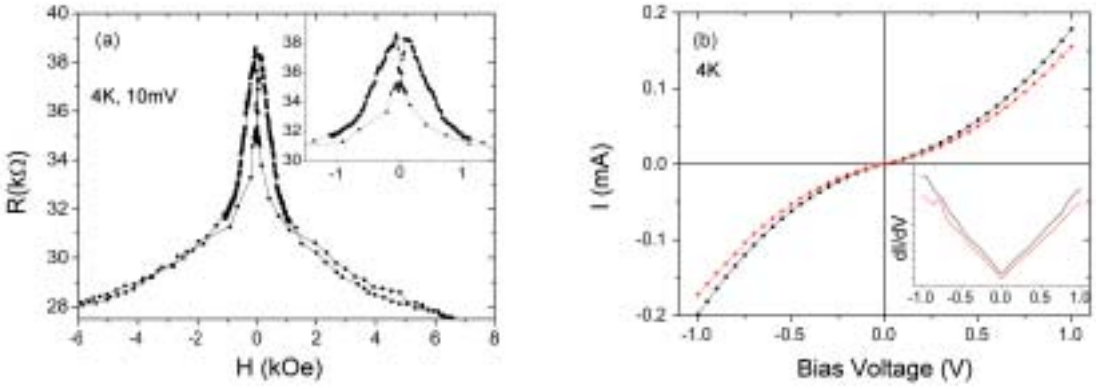

Figure A1-7: (a) Resistance vs magnetic field (the inset shows a zoom of the low field region) and (b) I(V) curve (the inset shows the derivative dI/dV) of a LSMO/STO/Au heterostructure.

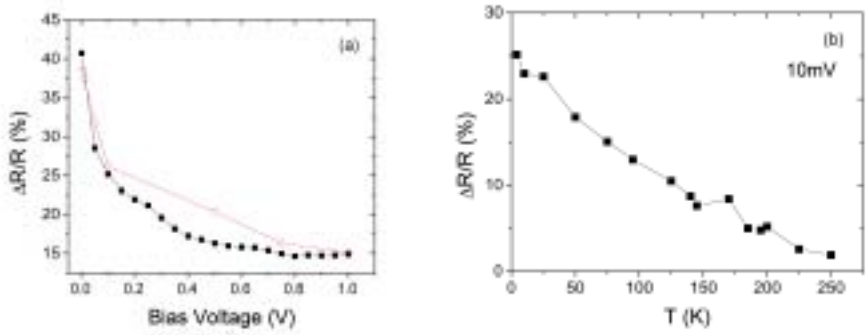

Figure A1-8: (a) $\Delta R/R$ vs bias voltage of two different junctions at $4K$ and (b) $\Delta R/R$ vs temperature of a LSMO/STO/Au heterostructure.

the increase gets steeper. The resistance raises to a maximum at -90Oe before decreasing with increasing negative magnetic field. Again a change of slope is observed at a field of -600Oe and the resistance decreases further with the slow dependence like for big positive fields. The same behavior is observed cycling back to the maximum positive field.

Thus both of the typical MR contributions can be observed. As the sample has only one magnetic layer, the asymmetric MR at low fields can only be due to the intergrain MR of the LSMO reaching an effect up to 35%. The maxima of the R(H) curves are below 100Oe, as expected for the coercive field of LSMO. The I(V) curves (Figure A1-7(b)) show a parabolic behavior due to the tunnel character of the electron transport across the domain walls. As the tunneling takes place between two LSMO grains, the derivative of the I(V) curve is symmetric.

The dependence of the MR on the bias voltage (Figure A1-8(a)) shows also the typical behavior of tunneling transport: a slow decrease with applied bias voltage. The strong decrease at low bias is due to the zero-bias-anomaly often observed in magnetic tunnel junctions including LSMO electrodes. The origin of the slow decrease at higher bias voltages is so far not very well understood, but the voltage dependence of the density of states of the electrodes or the lowering of the effective barrier height was proposed [271, 272].

The MR decreases slowly with increasing temperature (Figure A1-8(b)). Again the T_C of the interface is confirmed to be near room temperature. At around 185K the intergrain MR becomes symmetric with field, as the thermal energy of the grains is enhanced and they reverse nearly at the same field. However, the CMR is still visible and shows a less important variation with temperature.

Also the in-plane spin-dependent transport was measured. In Figure A1-9 a typical R(H) curve is shown. It shows a similar behavior like the curve measured for current perpendicular to plane, but the observed effect is much smaller, showing a maximum of only 7%. The origin of the smaller effect in-plane is to be found in the number of grains involved in the conduction path. In the in-plane measurement the distance between the

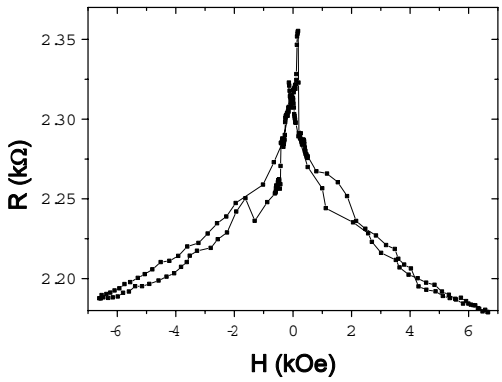

Figure A1-9: Resistance vs field parallel to plane for a LSMO($35nm$) film for a bias voltage of $10mV$.

contacts is large and the current lines will pass by the way of lowest resistance, i.e. the fewest grain boundaries to pass. On the other hand in the nanojunctions the junction area is very small, comparable to the mean grain size of around 40 to $50nm$ [187], so that the junction will act as a direct contact on the grain boundary 'tunnel junction'.

A2 Appendix 2: Results on $CoCr_2O_4$ based spin filter heterostructures

$CoCr_2O_4$ (CC0) is a ferrimagnetic insulator (see Section 2.3.2), thus also a possible candidate for the application as a magnetic barrier in a spin filter heterostructure. However, as described in Chapter 7, CCO tends to form three dimensional islands during the growth, but a continuous layer was found for very thin films or for low deposition temperatures (see Figure 7.21 on page 140), so that it may be possible to prepare closed CCO films, which can serve as a barrier. As an electrode $La_{2/3}Ca_{1/3}MnO_3$ (LCMO) was chosen, as it is a half-metal and its properties are well-characterized.

In this appendix the results are described which were obtained for heterostructures containing a LCMO electrode and an overlayer of CCO. In the first part of this chapter the characterization of the LCMO single films will be discussed, in the second part the characterization of LCMO/CCO bilayer.

A2-1 Characterization of $(La,Ca)MnO_3$ single films

LCMO is as $La_{2/3}Sr_{1/3}MnO_3$ (LSMO) a half metal with a T_C of around $270K$. The saturation magnetization is the same as for LSMO, thus $4\mu_B/f.u.-(1-x) = 3.66\mu_B/f.u.$. Its magnetic and electric properties are similar to LSMO, which was described in Section A1-1. A complete overview on the properties as well as the research can be found in the thesis of M. Bibes [186].

The LCMO samples were deposited by RF magnetron sputtering in the chamber of the ICMAB in Barcelona (description see Section 4.1.1) from a stoichiometric LCMO target. The growth parameters for the LCMO in this thesis were chosen following

Sample	t (nm)
LCMO-01	7.9
LCMO-02	24.8
LCMO-03	27.0
LCMO-04	33.8
LCMO-05	49.6
LCMO-06	64.0

Table A2-1: Table of the samples used for the investigation of the properties of $La_{2/3}Ca_{1/3}MnO_3$ films. t is the film thickness.

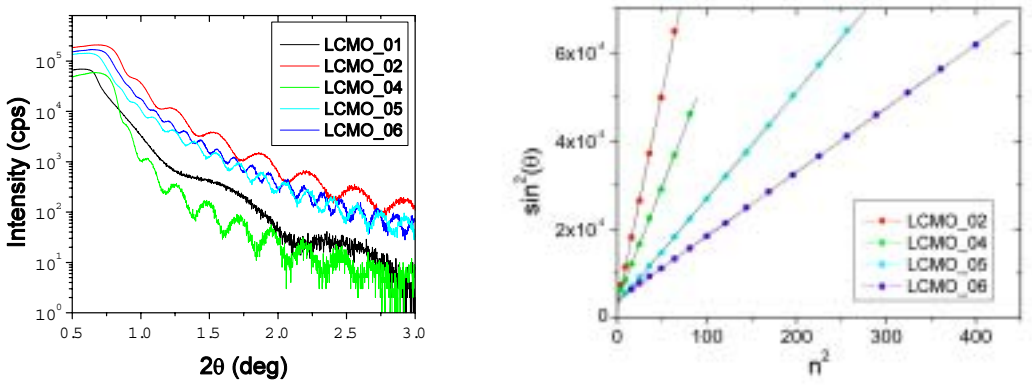

Figure A2-1: X-Ray Reflection measurement of the LCMO single films on the left side. On the right side: $sin^2(\theta)$ vs n^2 of the position of the maxima. The black lines are linear fits.

those determined in the PhD thesis of M. Bibes [186] to yield a film with a smooth surface. The substrate was $SrTiO_3(001)$, which was heat-treated before the deposition at $1000°C$ in air during $2h$, so that the surface of the substrate shows well-defined steps. The deposition was carried out at $800°C$ in a pressure of $330mtorr$. The deposition atmosphere is an Ar/O_2 mixture with 80% Ar and 20% O_2. After the deposition the films were hold at the deposition temperature under a high oxygen pressure ($1.1 \times 10^5 torr$) during one hour to guaranty the oxidation of the film. For the bilayers the CCO was deposited directly after the annealing of the LCMO film as described in Section 4.1.1.

The prepared samples are listed in Table A2-1. Due to aging effects of the target, the deposition rate differed between $0.17nm/min$ and $0.27nm/min$ for the different samples. The thickness of the films was determined by X-Ray Reflection. In Figure A2-1 the reflection curves (left side) and the $sin^2(\theta)$ analysis (right side) together with the linear fit (black lines) are shown. The derived thicknesses are summarized in Table A2-1.

Structural characterization

The structural characterization was carried out by X-ray diffraction. A typical θ-2θ scan is shown in Figure A2-2 (sample LCMO-04). The LCMO shows a single phase and is, like the substrate, (001) oriented out-of-plane. The out-of-plane parameter c varies only slightly with the film thickness.

In order to investigate the strain state of the film, reciprocal space maps were collected. Two of them can be seen in Figure A2-3, which were collected for the perovskite (103) reflection of a bilayer with a $40nm$ (left side) and $100nm$ (right side) thick LCMO layer (samples LCMO-CCO-01 and LCMO-CCO-07, see Table A2-2 on page 198). Indicated by the black line, the $Q_{||}$ position of the substrate and the film are the same, thus the

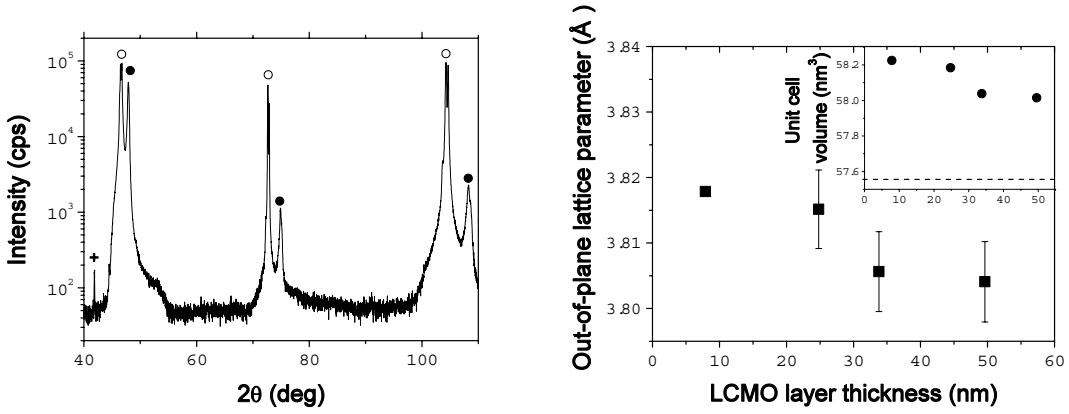

Figure A2-2: Left side: θ-2θ scan of a $33.8nm$ thick LCMO single film. The black points indicate LCMO$(00l)$ reflections, the white points the STO$(00l)$ reflections. Right side: c vs LCMO layer thickness. The inset shows the unit cell volume vs the LCMO layer thickness. The dashed line indicates the LCMO bulk value.

LCMO film is strained in-plane and has the same in-plane parameter a like the substrate up to a thickness of $100nm$.

Thus the slight decrease of c is not related to a partial relief of the strain, as the a corresponds to the a_{STO} up to a thickness of at least $100nm$. When the unit cell volume calculated from the measured c and a_{STO} is plotted vs the film thickness (Figure

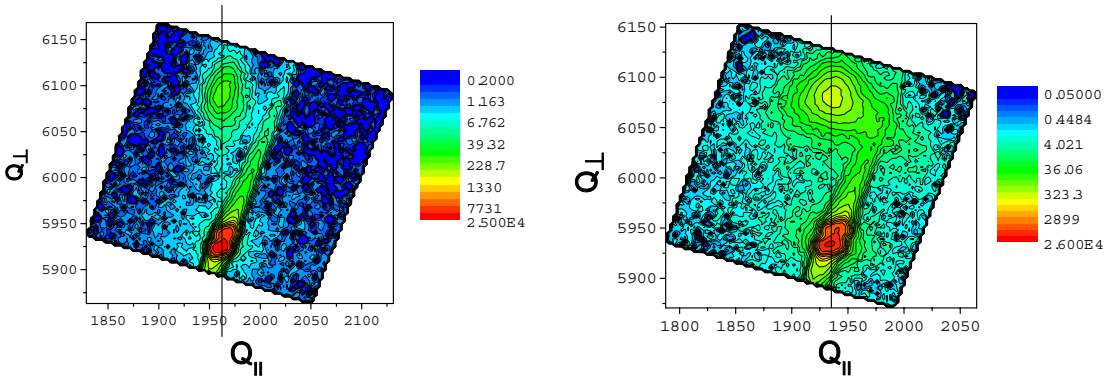

Figure A2-3: Reciprocal space maps of the (103) perovskite reflection of a $40nm$ (left side) and a $100nm$ (right side) thick LCMO film. The top peak is from the LCMO, the bottom one from the STO. The black line indicates the $Q_{||}$ position of the substrate peak.

A2-2, inset on the right side), it can be observed that the unit cell volume of the film is elevated in comparison to the LCMO bulk value. It decreases slightly with increasing film thickness. Therefore the decrease in c is related to another effect, probably an increase of the oxygen content of the film with enhanced deposition time.

Morphology

The morphology of the samples was measured by AFM. The surface morphology of samples (LCMO-02 and LCMO-04 to -06) with four different layer thickness is shown in Figure A2-4. For the samples with a layer thickness of 24.8nm (a) and 33.8nm (b) the surface shows steps, the height of which is approximately one unit cell of LCMO, as can be observed in the height profile in the right bottom panel of Figure A2-4. For the thickness of 24nm the layer grows in the step-flow mode (see Section 2.4) indicated by the atomically flat terraces. For the sample with a thickness of 38.8nm nucleation on top of the terraces can be observed (image (b)). Here the transition from the step flow growth to a two dimensional growth by homogeneous nucleation takes place.

Accordingly, in the images (c) and (d) the steps cannot be observed anymore. Here the surface morphology is governed by a layer-by-layer growth due to nucleation on the surface. The height profile of image (d), shown in the right top panel of Figure A2-4, shows that the grains have a height of only three unit cells of LCMO. The root-mean-

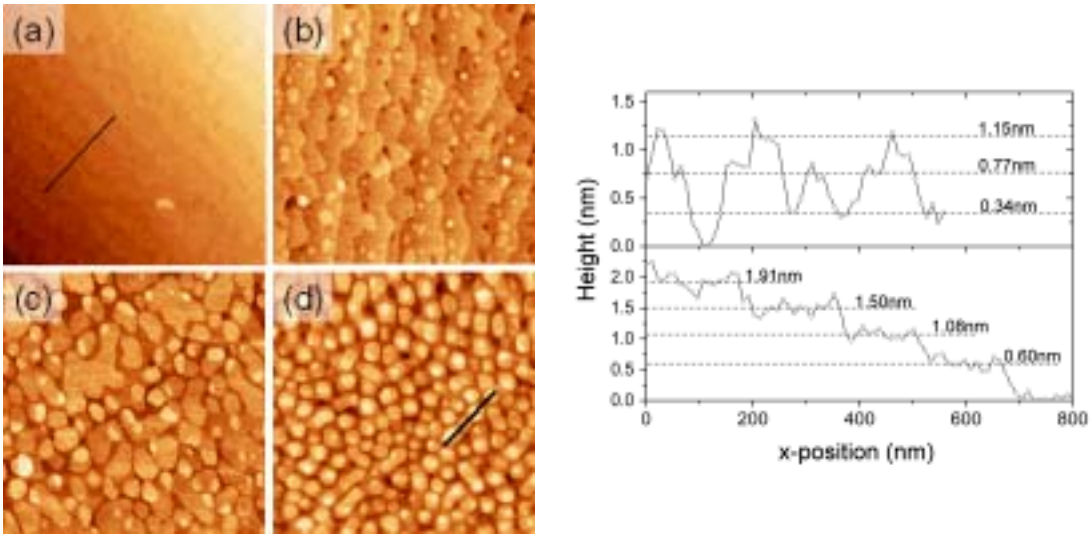

Figure A2-4: AFM images of LCMO single films with a layer thickness of (a) 24.8nm, (b) 33.8nm, (c) 49.6nm and (d) 64.0nm. The z-range of the images is 9.8nm, 3nm, 2.6nm and 2nm, respectively. The size of the samples is 2μm x 2μm, except image (b) with the size of 2.5μm x 2.5μm. The panels on the right show height profiles of (a) (bottom panel) and of (d) (top panel), which position is indicated by the black lines in the corresponding AFM images.

square roughness of image (c) and (d) is 0.4 and 0.3nm, respectively.

Magnetic properties

To check the magnetic properties of the single films, SQUID measurements were carried out. The magnetization dependence on the applied field and the temperature can be seen in Figure A2-5 on the left and on the right, respectively, for a film thickness of 24.8nm (LCMO-02), 27.0nm (LCMO-03), 33.8nm (LCMO-04) and 64.0nm (LCMO-06). The hysteresis loops show a sharp transition at the coercive field, which is typically around 230Oe. Only the thinnest film shows a reduced coercive field of 70Oe. The saturation magnetization depends on the film thickness as shown in the inset on the left. While the film of 24.8nm shows the bulk saturation magnetization of 3.66$\mu_B/f.u.$, the thicker films have a reduced saturation magnetization. The observed thickness dependence is surprising, as it is expected that the saturation magnetization is reduced with decreasing film thickness. However, the films are magnetic, so that they can be used as magnetic electrodes for the spin filter. Also the Curie temperature was measured. For all films it is decreased to a value of around 200K.

A2-2 Characterization of $(La, Ca)MnO_3/CoCr_2O_4$ bilayer

In the previous section it was shown, that the LCMO layers are smooth, so that a CCO film was grown on top. The main questions are, if the CCO grows epitaxial, as the misfit with LCMO is relatively high (6.7%), and if the CCO film is a closed film and does not show the three dimensional island growth as observed in the films grown on $MgAl_2O_4$ and MgO. As for these substrates for a low film thickness a rough, but continuous CCO

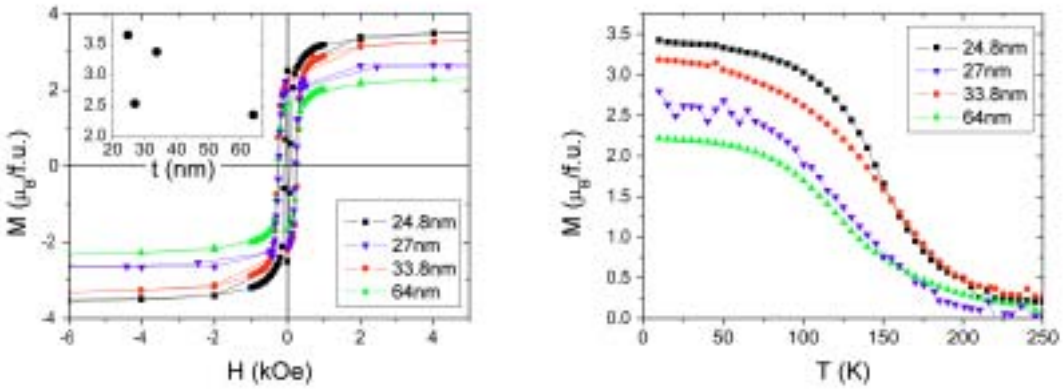

Figure A2-5: Magnetization vs applied magnetic field (left side) and vs temperature (right side) for samples with different film thickness. In the inset on the right: Saturation magnetization vs LCMO film thickness.

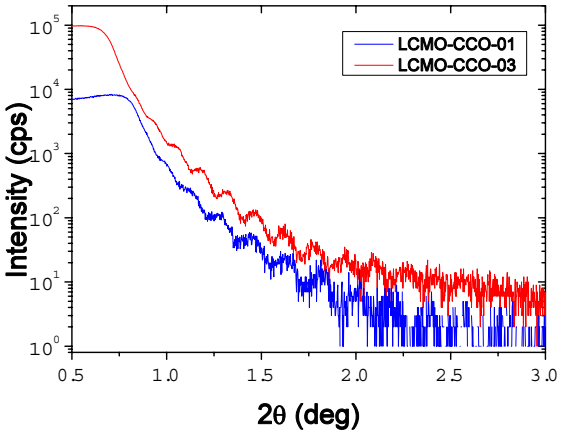

Figure A2-6: XRR curves of LCMO/CCO bilayers for a $40nm$ (blue line) and a $60nm$ (red line) LCMO thickness and a fixed CCO thickness of $3nm$.

layer was found (see Section 7.1.3), the film thickness of the CCO overlayer on LCMO was held in the range of a few nm. The samples prepared for this part are listed in Table A2-2.

To determine the growth rate of the CCO, XRR measurements were carried out for the bilayers. In Figure A2-6 the curves of the samples LCMO-CCO-01 and -03 are shown. The oscillations of the LCMO are clearly visible, while no second oscillation due to the CCO is visible. The first possibility to interpret this observation is, that no CCO was deposited on the surface. This is highly improbable, however, it will be proved by AFM and Resiscope, that CCO is present on the surface of the LCMO. The second possibility is that the CCO film does not give rise to oscillations due to a high surface roughness.

Sample	t_{LCMO}/t_{CCO} (nm)	T_{dep} $(°C)$
LCMO-CCO-01	40 / 3	600
LCMO-CCO-02	60 / 3	550
LCMO-CCO-03	60 / 3	600
LCMO-CCO-04	60 / 3	650
LCMO-CCO-05	60 / 6	600
LCMO-CCO-06	60 / 15	600
LCMO-CCO-07	100 / 3	600

Table A2-2: Table of the samples used for the investigation of the properties of $La_{2/3}Ca_{1/3}MnO_3/CoCr_2O_4$ bilayers. t_{LCMO}/t_{CCO} denotes the $La_{2/3}Ca_{1/3}MnO_3$ and the nominal $CoCr_2O_4$ film thickness. T_{dep} is the deposition temperature of the $CoCr_2O_4$ layer.

XRD measurements were carried out on the samples, but show only peaks corresponding to LCMO reflections, probably due to the small amount of material. The SQUID measurements showed properties similar to the LCMO single films, as the magnetization of the deposited CCO is too small to be distinguishable from the LCMO contribution.

Morphology

AFM images were collected for different samples. In Figure A2-7 images are shown for a nominal CCO film thickness of $3nm$ (CCO-LCMO-03, a), $6nm$ (CCO-LCMO-05, b) and $15nm$ (CCO-LCMO-06, c). The surface of all three samples show a granular morphology. The root-mean-square roughness of (a), (b) and (c) are $1.3nm$, $2nm$ and $4.3nm$, respectively, thus enhanced in respect to the roughness found for a $64nm$ LCMO single film ($0.3nm$). This suggests that the grains visible in the images are formed by the CCO. Indeed, in the images (b) and (c) a certain orientation of the films along the [110] direction can be observed. The round shape of the grains could be due to a tip-convolution effect.

As it was found that the formation of islands is also influenced by the deposition temperature (see growth diagram 7.21 on page 140), $3nm$ thick CCO films were grown on $60nm$ LCMO at $550°C$, $600°C$ and $650°C$. The AFM images are shown in Figure A2-8 (a), (b) and (c), respectively. In (c) the typical morphology of {111} faceted islands can be observed, thus at $650°C$ the CCO forms islands already for a film thickness of $3nm$. In (a) and (b) grains can be observed, but the morphology does not indicate the formation of islands. This suggests that at lower deposition temperature the CCO forms a rough, but continuous overlayer on the CCO with a root-mean-square roughness of $0.74nm$ for the sample grown at $550°C$ and $1.66nm$ at $600°C$.

The shape and orientation of the islands observed for the sample grown at $650°C$ shows that the CCO grows also in LCMO with a cube-on-cube relationship. The pyramidal form of the islands indicate a {111} faceting, although the islands could not be well enough resolved to measure the facet angle. The {111} faceting in turn indicates a

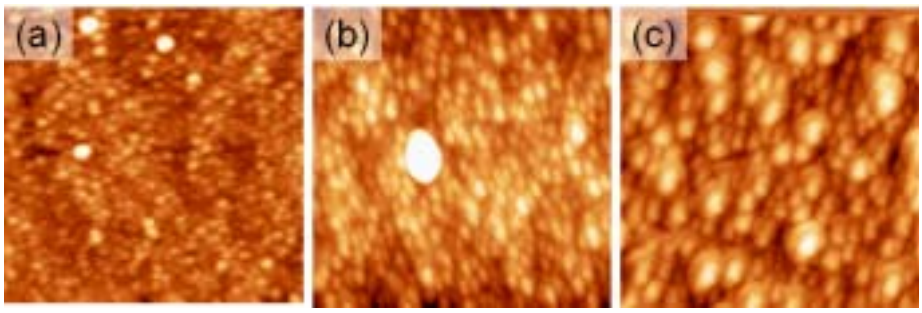

Figure A2-7: AFM images of the surface of LCMO/CCO bilayers with a nominal CCO layer thickness of (a) $3nm$, (b) $6nm$ and (c) $15nm$. The size of the images is $1\mu m$ x $1\mu m$, the z-range is $12nm$ for (a) and (b), and $30nm$ for (c). The edges of the images are aligned with the [110] direction of the STO.

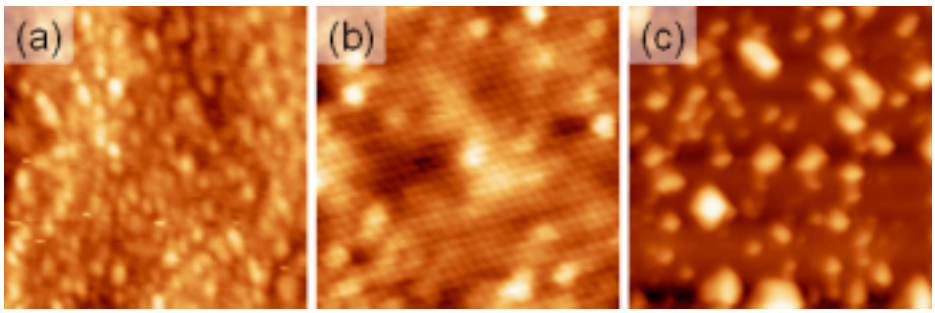

Figure A2-8: AFM images of the surface of LCMO/CCO bilayers with a nominal CCO layer thickness of $3nm$, deposited at a temperature of (a)$550°C$, (b) $600°C$ and (c) $650°C$. The size of the images is $400nm$ x $400nm$, the z-range is $5.65nm$, $11.7nm$ and $22.2nm$, respectively. The edges of the images are aligned with the [110] direction of the STO.

(001) out-of-plane texture of the film. The orientation of the island edges along the (110) directions of the LCMO film can be ascribed to an in-plane texture of the film, corresponding to that one of the LCMO.

Electric properties

As the CCO will have the role of the barrier in the spin filter, an homogeneous resistance is crucial. Therefore the surface resistance of the samples CCO-LCMO-02 to -05 was measured with a resiscope. In Figure A2-9 the topography and resistance images of the surface of CCO-LCMO-02 to -04 are shown. (a), (c) and (f) are the topology images and (b), (d) and (g) are the resistance images. The first observation is, that the surface resistance is strongly inhomogeneous. For the resistance images, the bright contrast indicates a high resistance, while the dark contrast shows the areas of low resistance. All images show white spots over all the surface. Thus the CCO does not form a film homogeneous in thickness.

Even more, the white contrast resembles the shape of the {111} faceted islands observed for thicker CCO films. Due to the exponential dependence of the resistance on the thickness in case of an insulator[1], the shape of the islands is better resolved in the resistance images than in the topography images.

In Figure A2-9 (e) and (h) local I(V) curves are shown for a place of dark contrast (red line) and of bright contrast (black line). They show clearly a insulating behavior for the places of bright contrast. For the dark contrast the I(V) curves do not show an ohmic behavior, but the conduction gap is much smaller than in the case of a bright contrast. This suggests that between the islands no continuous CCO layer is formed on the surface of the LCMO.

[1] As stated before, for a high surface resistance the current tunnels through the resistive film and the resistance depends thus exponentially on the film thickness

Resiscope images were also taken from a sample with a $6nm$ thick CCO overlayer (LCMO-CCO-05), which are shown in Figure A2-10. Also for a thicker film the surface resistance stays inhomogeneous indicating a non-continuous CCO film.

In the resiscope images it was shown, that in the investigated range of deposition parameters it is not possible to grow a continuous CCO film with a homogeneous surface

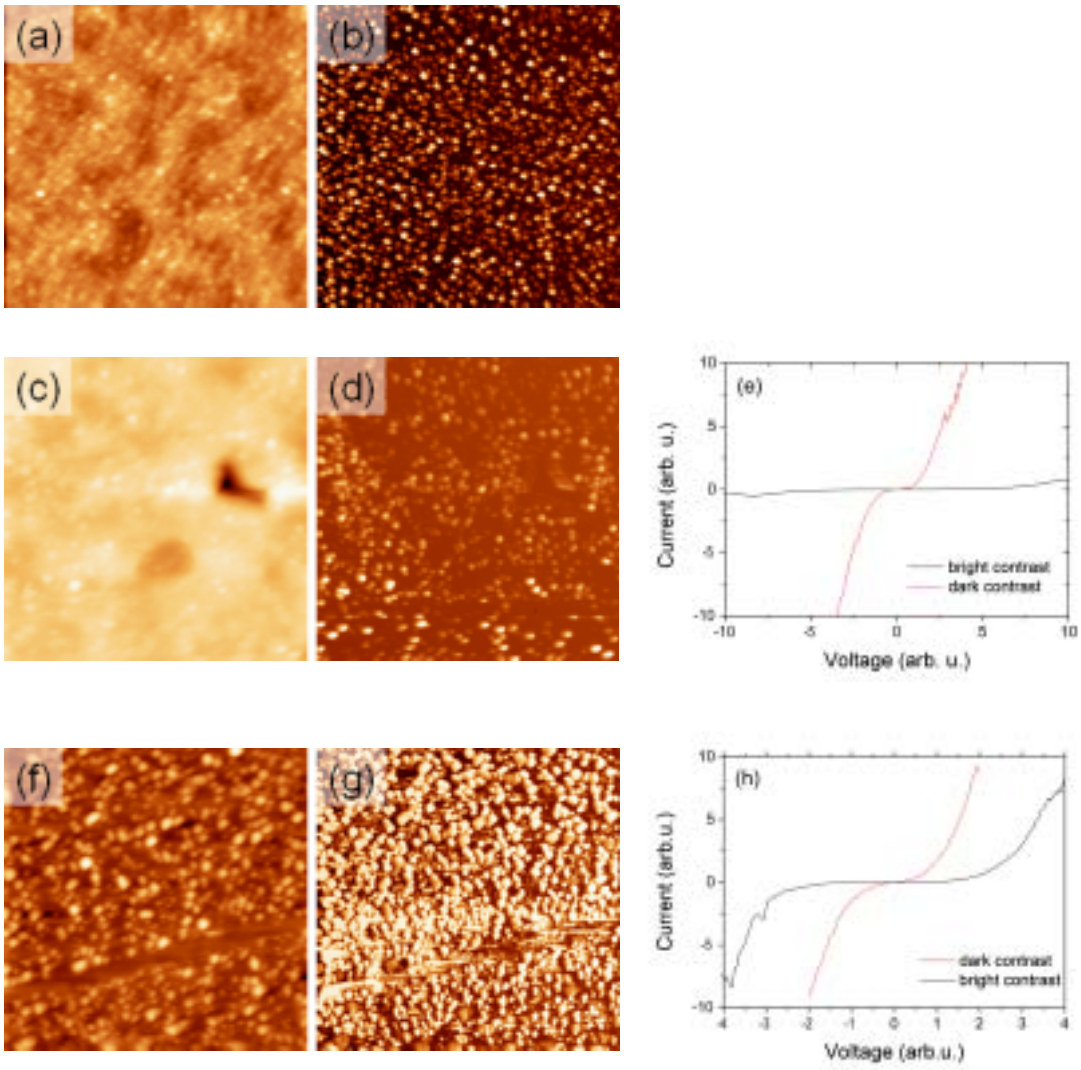

Figure A2-9: Resiscope measurements of LCMO/CCO bilayers for a $3nm$ thick CCO film and a deposition temperature of $550°C$ (topography (a) and resistance (b) mapping) , $600°C$ (topography (c) and resistance (d) mapping and local I(V) curve (e)) and $650°C$ (topography (f) and resistance (g) mapping and local I(V) curve (h)). The images have a size of $1\mu m$ x $1\mu m$. In the resistance images a dark contrast denotes a low resistance and the bright a high resistance. In the I(V) curves the red lines denote curves taken on top of a bright contrast and the black ones taken on top of a dark contrast.

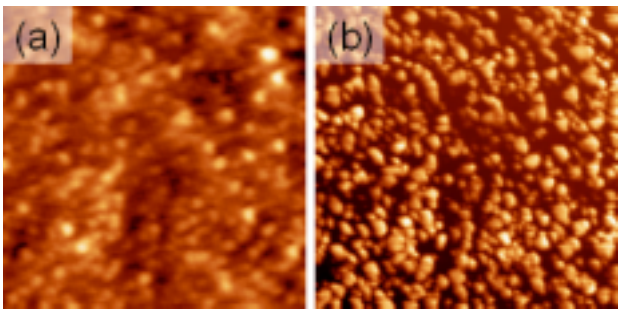

Figure A2-10: Resiscope measurements of a LCMO/CCO bilayer with a $6nm$ thick CCO film and a deposition temperature of $600°C$ (topography (a) and resistance (b) mapping). The images have a size of $500nm$ x $500nm$. In the resisitance images a dark contrast denotes a low resistance and the bright a high resistance.

resistance. Therefore the CCO layers are not adequate to be introduced into a spin filter. Evidently, the close CCO layer for small film thickness observed in the growth on $MgAl_2O_4$ does not occur in the growth on LCMO. This might be due to the high misfit, as the strain exerted by the substrate can be relaxed by introducing islands (see Section 2.4).

However, as was observed in the growth of CCO on $MgAl_2O_4$, the deposition temperature plays a crucial role. If the deposition temperature is decreased, the adatoms have a smaller energy and rest at a sufficiently low deposition temperature at their impinging position. As the formation of islands is connected with a massive mass transport on the surface, the island growth could be avoided by choosing a low deposition temperature. Therefore it could be possible to grow a continuous CCO layer at deposition temperatures lower than $550°C$.